International Centre for Innovation & Development
-ICID-

New approaches and applications on Control & computer Science

Proceedings of Engineering & Technology
-PET-

Editors:

Dr. Ali Haddi (Morocco)

Dr. Ahmed Rhif (Tunisia)

-PET- Vol. 56

ISSN : 1737-9934

ISSN: 1737-9334
-PET- Vol. 56

ICID

International Centre for Innovation & Development

Proceedings of Engineering & Technology
-PET-

New approaches and applications on Control & computer Science

Editor:

Dr. Ali Haddi (Morocco)

Dr. Ahmed Rhif (Tunisia)

International Centre for Innovation & Development

–ICID–

Summary

Substrate Integrated Waveguide bandpass filter Using Complementary Split Ring Resonators

Soufiane ACHRAOU[#1], Alia ZAKRITI[*2]Abdelkarim FARKHSI[#3] ,Souhaila BEN HADDI[*4]

[#]Information systems and telecommunications laboratory, Faculty of Sciences, BP.2121 M'Hannech II, 93030 Tetuan, MOROCCO

*Sciences and Advanced Technology Team, National School of Applied Sciences,BP.2222 M'Hanech II, 93030 Tetuan, MOROCCO

Address Including Country Name

[1]sachraou6@gmail.com

[2]azakriti@uae.ac.ma

[3]farkhsi@gmail.com

[4]souhabenhaddi2@gmail.com

***Abstract*— This article presents band-pass filter based on Substrate Integrated Waveguide (SIW) technology with Complementary Split Ring Resonators (CSRRs). The filter is designed for the pass band from 3.5 GHz to 4.3 GHz. The bandwidth of the filter is about 20%. The physical dimension for the proposed structure is of 45 mm x 22 mm. The insertion loss is low than 0.28 dB and the return loss is about 75 dB. These results show that the proposed filter is most suitable for telecommunication application like WiMAX system. The filter design was made by using the electromagnetic Simulator CST – MWS.**

***Keywords*—**SIW technology, CSRR, Bandpass.

I. INTRODUCTION

Recently, renewed attention of researchers to efficient features of rectangular waveguides including high-quality factor, high-power transmission capability and low losses. However, the demand for integration with other planar circuits has led to the advent of a new technology called substrate integrated waveguide SIW [1]. This technology has been proposed as an alternative solution to meet the great demand of high performance of compact devices which are operating in microwaves [2]. The concept of the SIW is to guide the electromagnetic waves by using rows of metallic vias which operates like a metallic wall. So many structures were reported in this technology like antennas, filters, couplers and power dividers. Reduction of the sizes, low costs of fabrication and reduction of losses in the SIW devices are major factors of making this technology a strong alternative of non-planar waveguides. It combines between the high performance of the waveguides and the compact size of the planar circuits [3],

The concept of double negative (DNG) Metamaterials (MTM) has been first introduced by Veselago in 1968 [4]. Thirty years later, the initial DNG MTM has been realized by Smith et al. [5]. It is an artificial material realized by negative values of permittivity and permeability simultaneously at special frequencies, which includes the split-ring resonators (SRRs) and thin copper wires (TWs. Analysis and proper simulation of these structures showed that TWs and SRRs produce the negative permittivity and permeability, respectively [6]. Then according to the argument duality, complementary SRRs (CSRRs) were propounded by Falcone [7]. The characteristics of SRRs and CSRRs have been investigated in detail [8-10]. The CSRRs behave similar to the electric dipole which can be excited by an axial electric field and provide the negative permittivity [7]. The open SRR (OSRR) has been introduced as an improved SRR [11] and subsequently the open complementary SRR (OCSRR) has been first proposed in [12]. The OSRRs and their Supplement, OCSRRs, are opening resonators which originated from SRR and CSRR, respectively. The OSRRs and OCSRRs are described by means of series and shunt resonant tanks, respectively [12]. Seeking to further reduce size, the new perspective of the OSRRs, fractal open SRR (FOSRR), and following that the fractal open complementary SRR (FOCSRR) has been

ISSN 1737-9334

introduced. It has been shown that the FOCSRR particle has a lower resonant frequency than the conventional OCSRR particle with similar dimensions [13]. Since these resonance structures are compact and keep the LH-handed features, they are useful for the synthesis of planar metamaterials and microwave components.

In this paper, we present a new SIW BPF combined with specific CSRR.

II. DESIGN PROCESS

A. *Design of SIW structure*

SIW structure is a combination of top and bottom metallic plates and dielectric material embedded with two linear arrays of metal vias connecting top and bottom metallic plates. To find out the cutoff frequency in TE10 mode, the key parameter of the SIW, we use following equations:

$$f_{cTE01} = \frac{C_0}{2\sqrt{\varepsilon_r}}\left(a - \frac{4R^2}{0.95P}\right)^{-1} \quad (1)$$

$$w_{siw} = w_{eff} + \frac{D^2}{0.95p} \quad (2)$$

$$w_{eff} = \frac{a}{\sqrt{\varepsilon_r}} \quad (3)$$

$$d < \frac{\lambda g}{5} \quad (4)$$

$$P \leq 2d \quad (5)$$

Where:

f_{cTE01} IS cutoff frequency in TE10 mode.
C_0 is the speed of light in vacuum.
εr is the relative permittivity of dielectric.
P is the spacing between two adjacent vias, also called pitch.
a is the width rectangular waveguide.
w_{siw} is the central distance between via arrays also called. integrated waveguide width.
w_{eff} is the width of equivalent SIW.
d is the diameter of via.

and:

$$\lambda g = \frac{c}{f\sqrt{\varepsilon_r}}$$

λg is the guide wavelength of SIW

where:

c is the speed of light in vacuum
f is the design frequency
εr is the relative permittivity of dielectric

In order to increase performance and quality of our proposed filter, we add the slots, that are characterized by the length of $\frac{\lambda g}{4}$. Their positions are adjusted to have the desired frequency.

B. *Microstrip Part Design*

To get high connection between Microstrip circuits and SIW structure, an intermediate transition should be developed by forming series combination of quarter-wave. Its role is to adapt the fundamental mode of the substrate integrated waveguide to the quasi-TEM mode of the Microstrip line. By this transition we can put easily the interconnection of the I/O connectors. The two keys parameters of the tapered transition are the width and the length and they could be calculated by the following equations [14]:

$$\frac{120\pi}{\eta H\left(\frac{w_t}{h}+1.393+0.66\ln\left(\frac{w_t}{h}+1.444\right)\right)} = e^{-0.627\frac{\varepsilon_r}{\frac{\varepsilon_r+1}{2}+\frac{\varepsilon_r-1}{2\sqrt{1+\frac{12H}{w}}}}} \quad (6)$$

Where $\boldsymbol{\eta}$ is the free space intrinsic impedance and its value is 377ohm. And the length taper is given by [14]:

$$l_t = \frac{n\lambda_g}{4}, \quad n=1,2,3,4\ldots \quad (7)$$

The tapered have some characteristics such as to be simply designed, with a minimum of losses and perfectly matched [15].

Proposed SIW filter has diameter of all the metallic vias is 2 mm, pitch of the vias is 3.5 mm and width of the SIW filter is about 17.6 mm calculated using Equations 1-3, which is shown in the Figure 1 (a). The dimensions of the designed filter are given in Table 1. The simulated result of the SIW filter is as shown in Figure 1(b).

ISSN 1737-9334

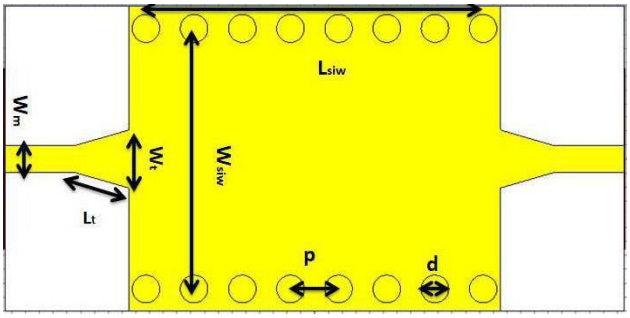

(a)

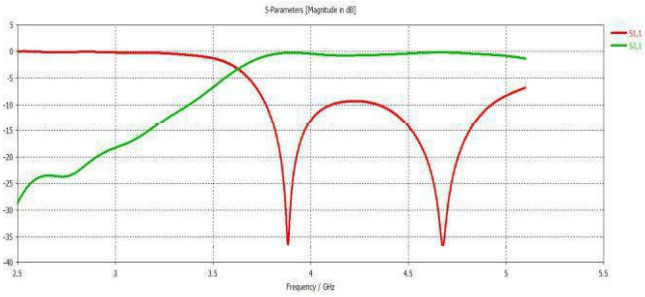

(b)

Fig. 1 (a) Configuration of the SIW bandpass filter (b) Simulated S-Parameter of the filter.

TABLE I: DIMENSIONS OF THE DESIGNED FILTER

Parameter	Values in mm
D	2
P	3.5
Tm	0.035
Wm	1.87
Lsiw	24.5
Wsiw	18.83
Wt	4.14
Lt	2.3

The proposed SIW structure works as a highpass filter. The insertion loss is of 0.7 dB with a cut off frequency is 3.6 GHz and the return loss is approximately 9.3dB.

III. THE BANDPASS FILTER WITH CSRR STRUCTURE

As mentioned previously, SIW structure works as a highpass filter as shown in Figure 1(B). In order to achieve the band pass response, CSRR are etched on the top metal plane. This structure works as bandstop filter providing high out of band rejection due to negative permeability of the CSRRs. Then, combination of SIW structure and CSRRs etched on the top metal surface forms a bandpass filter.

When a magnetic field is applied perpendicular to the plane of the ring, the ring begins to conduct and gives rise to current flow. The current flowing through the rings will enable it to act as an inductor and the dielectric gap (g) between the rings will lead to mutual capacitance. Hence the equivalent circuit of the CSRR will be a parallel LC tank circuit as shown in Fig.2 (b).

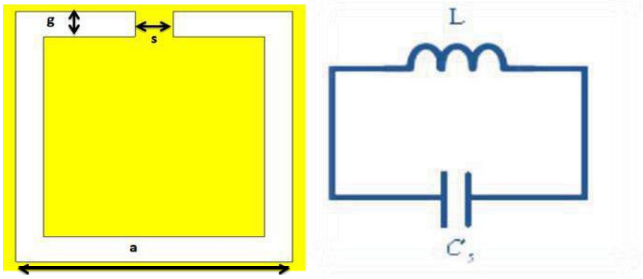

(a) (b)

Fig.2. (a) Structure of Square Complementary split ring resonator and it's circuit equivalent (B)

From this, we can calculate the resonant frequency.

$$f_r = \frac{1}{2\pi\sqrt{LC_s}} \qquad (8)$$

The SIW structure with etched top metal plane is shown in Figure 3, then we insered three parallel CSRR in the filter which are illustrated in Figure 4 (yellow zone represents metal). The dimensions of the CSRR structure are mentioned in the Table 2.

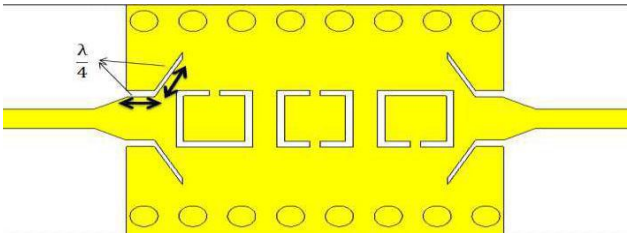

(a)

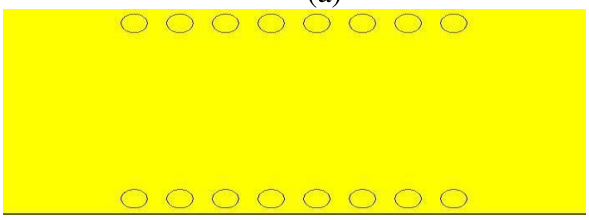

(b)

Fig. 3 Configuration of the SIW bandpass filter loaded by the CSRR cellule (a) (top view) (b) (bottom view)

ISSN 1737-9334

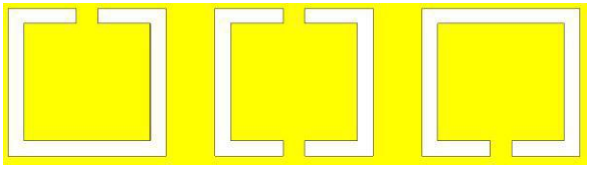

Fig. 4 layout of CSRR structure

TABLE 2
DIMENSIONS OF THE DESIGNED FILTER SHOWN IN FIGURE 3(A)

Parameter	Values in mm
g	0.55
s	0.75
a	5.50

IV. RESULTS AND DISCUSSION

In the proposed structure, bandpass filter is designed on Rogers RO4003C substrate with a thickness of 0.813 mm, relative permittivity of 3.38 and loss tangent of 0.0027. Firstly, SIW based filter is designed, which act as a high pass filter in the desirable operating frequency band. To obtain the band pass response, CSRR are inserted on the top metal surface of the SIW structure, which can work as parallel LC resonator and has high band rejection characteristics.

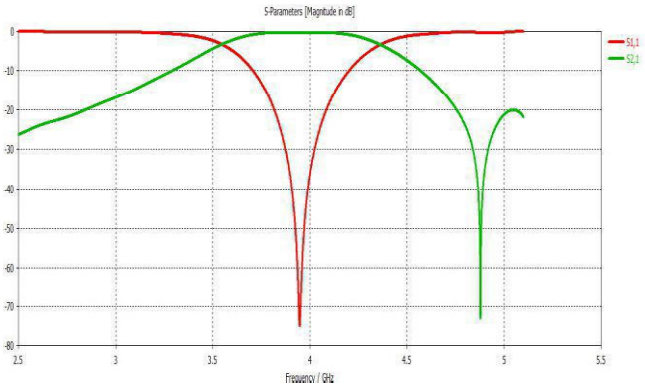

Fig. 5 Simulated S-Parameter of the filter with CSRR

The filter is designed for the pass band from 3.5 GHz to 4.3 GHz. The bandwidth of the filter is about 20%. The physical dimensions of the proposed structure is of 45 mm x 22 mm. The insertion loss is low than 0.28 dB and the return loss is about 75dB.

V. CONCLUSION

In this paper, a bandpass SIW filter based on Complementary Split Ring Resonators (CSRRF) is designed by using the electromagnetic Simulator CST – MWS. The simulated results of this filter have shown that the passband is from 3.5 GHz to 4.3 GHz, while the insertion loss is -0.28dB within 20 % bandwidth around 3,9 GHz and the return loss is about 75dB. These filters are easy for integration with other planar circuit compared by using conventional waveguide. This bandpass SIW filter based on Complementary Split Ring Resonators (CSRRs) is suitable for Telecommunication application like WiMAX system.

REFERENCES

[1] Shigeki F. “Waveguide line,” Japan Patent, 1994.
[2] K. Wu, Substrate Integrated Circuits (SiCs) – A new paradigm for future GHz and THz electronic and photonic systems. IEEE Circuitsand Systems Society Newsletter, 3(2) (2009).
[3] K. Wu, “Hybrid three-dimensional planar/non-planar circuits for microwave and millimeter-wave applications: the state-of-the-art and challenges,” TELSIKS’97, Nis, Yugoslavia, Oct. 8-10, pp. 281-286 (invited paper).
[4] Veselago VG. The electrodynamics of substances with simultaneously negative values of E and m. Sov Phys Uspekhi. 1968;10 (4):517–526.
[5] Caloz C, Itoh T. Electromagnetic metamaterials: transmission line theory and microwave applications. John Wiley & Sons, Inc., Hoboken, NJ; 2005.
[6] Marques R, Ferran M, Mario S. Metamaterials with Negative Parameters: Theory, Design and Microwave Applications. Vol. 183. John Wiley & Sons, Inc., Hoboken, NJ; 2011.
[7] FalconeLopetegi FT, Baena J, Marques D, Martin RF, Sorolla M. Effective negative-epsilon stopband microstrip lines based on complementary split ring resonators. IEEE Microw Wireless Compon Lett. 2004;14(1412):280–282
[8] Baena J, Bonache D, Martin J, Marques F, Falcone R, Lopetegi FT, Laso MA, Garcia G, Gil JI, Sorolla M. Equivalent-circuit models for split-ring resonators and complementary split-ring resonators coupled to planar transmission lines. IEEE Trans Microw Theory Tech. 2005;53(4):1451–1461.
[9] Garcia J, Martin JF, Baena J, Marques DR, Jelinek L. On the resonances and polarizabilities of split rings resonators. J f Appl Phys. 2005;98:033103–033103.
[10] Bonache J, Gil M, Gil I, Garcia J, Martin F. On the electrical characteristics of complementary metamaterial resonators. IEEE Microw Wireless Compon Lett. 2006;16(10):543–545.
[11] Martel J, Marques R, Falcone F, et al. A new LC series element for compact band pass filter design. IEEE Microw Wireless Compon Lett. 2004;14(5):210–212
[12] Velez A, Aznar F, Bonache J, Vel Azquez-Ahumada MC, Martel J, Martin F. Open complementary split ring resonators (OCSRRs) and their application to wideband CPW band pass filters. IEEE Microw Wireless Compon Lett 2009;19(4):197–199.
[13] Crnojevic-Bengin V, Radonic V, Jokanovic B. Fractal geometries of complementary split-ring resonators. IEEE Trans Microw Theory Tech. 2008;56(10):2312–2321
[14] D.Dominic. “Design equations for tapered microstrip-to-substrate integrated waveguide transitions”. Microwave Symposium Digest (MTT),2010 IEEE MTT-S International. IEEE, p704 707, May 2010.
N.Keltouma, F.Mohammed, S.Adnan “Design and characterization of tapered transition and inductive window filter based on Substrate Integrated Waveguide technology (SIW)” International Journal of Computer Science Issues, Vol. 8, Issue 6, No 3, November 2011.

ISSN 1737-9334

Modeling grid-connected solar PV system with maximum power point tracking Controller

Henchiri Abdelhamid[#1], Bahi Tahar [*2], Lekhchine Salima[¤3]

[#] 20 August 1955-Skikda University, Laboratory of Mechanical Engineering and Materials Skikda 21000, Algeria
[1] ab.henchiri@gmail.com
* Automatic and Signals Laboratory LASA, Badji Mokhtar University Annaba, 23000, Algeria
[2] tbahi@hotmail.fr
[¤] *Department of Electrical Engineering, 20 August University Skikda, 21000, Algeria*
[3] slekhchine@yahoo.fr

***Abstract* – Nowadays, the installation of photovoltaic systems is attractive renewable energy sources to generate electricity. This is to satisfy the need for energy demand, which has grown steadily in recent decades. Solar energy is the most interesting renewable energy sources compared to the other energy sources. However, their operation is essentially depending on solar radiation and temperature. The main objective of this paper is to provide an early evaluation of the system performance of the studied chain of grid-connected solar photovoltaic system composed mainly by the distributed photo-voltaic (PV) generation, DC-DC boost converter, voltage source inverter (VSI) and utility grid. For each component of the system a mathematical model is developed. Otherwise, the developed control strategies have been associated with a maximum power point tracking (MPPT) technique, especially, perturb and observe (P&O) technique is used to extract PV panel maximum power. The MPPT technique that generates the control signal which feeds the boost converter.**

Keywords: **PV systems; Grid; MPPT; Control; Simulation.**

I. INTRODUCTION

The production of energy is a challenge of great importance for the years to come. Indeed, the energy needs of industrialized societies are constantly increasing. Today, renewable energies compete with fossil fuels from the point of view of cost and production performance [1]. They are currently experiencing a strong development in the world, seen its ecological character, it appears as an important source such that the amount of solar energy that reaches the surface of the earth in a day is ten times greater than that consumed [2]. Photovoltaic electricity can be produced as close as possible to its place of consumption, in a decentralized way, directly to the user, which makes it is accessible to a large part of the world's population, but in particular it will be necessary to be free from the intermittent nature of power supply. Therefore, to ensure the optimal operation of the photovoltaic generator (GPV) a control equipment must be placed between the GPV and the load whose purpose is the adaptation of the two devices (photovoltaic generator, load) for a better energy transfer to the load [3]. The last can significantly increase the power output of GPV, for this a list of DC-DC converter (chopper) is used to control of the maximum power point tracking (MPPT).

The simulation model is designed using Matlab/Simulink software environment where the corresponding I = f (V) and P = f (V) curves are illustrate and the discussions of the obtained results are given in this work. Otherwise, the model is tested under standard temperature conditions (STC): radiation 1000 W/m2 and temperature 25◦C and then after under different climatic conditions and scenarios: for validation and testing of the MPPT technique and compared with the maximum power of the array computed.

II. MODELLING AND SIMULATION

A. Photovoltaic cell

A photovoltaic cell exposed to light produces electricity thanks to the photovoltaic effect. The current obtained is proportional to the incident light power. The photovoltaic cell delivers a direct current. The maximum voltage of the cell is about 0.6 V for a zero current. This voltage is called open circuit voltage (V_{OC}). The maximum current occurs when the terminals of the cell are short-circuited (I_{CC}). Figure 1 shows the equivalent circuit of a photovoltaic cell. It corresponds to a current generator *I* connected in parallel with a diode.

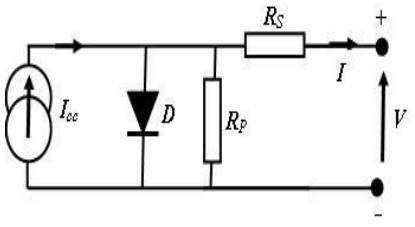

Fig 1 Equivalent electric circuit of a photovoltaic cell

ISSN 1737-9334

two parasitic resistances are introduced in this scheme. These resistances have some influence on the characteristic I = f (V) of the cell [4]: The series resistance (Rs) is the internal resistance of the cell: it depends mainly on the resistance of the semiconductor used, the contact resistance of the gates and the resistivity of these gates. The shunt resistor (Rp) is due to a leakage current at the junction; it depends on how it was done.

The mathematical model for the current-voltage characteristic of a PV cell is given by [5]. For the previous models, the expressions of the output current are, respectively, given by the following equation [6 -10].

$$I = I_{cc} - I_{01}[e^{q(\frac{V+I*R_s}{n_1 kT})} - 1] - I_{02}[e^{q(\frac{V+I*R_s}{n_2 kT})} - 1] - \frac{V+I*R_s}{R_p} \quad (1)$$

With,

I_{CC} (A), the short circuit current of the cell depending on the sun light and the temperature,

I_{01} (A): saturation current of diode1; I_{02} (A): saturation current of diode 2; K: Boltzmann constant; Tc (K): effective temperature of cell; T (K) = 273 = T (° C); q: (1.602 × 10-19 C), the charge of the electron; n_1: the non-ideality factor of the junction of the diode1; n_2: the factor of non-ideality of the junction of the diode2; I (A): current supplied by the cell; V (V): voltage across the cell; R_P (Ω): parallel resistance; R_S (Ω): series resistance.

Figures 2 and 3 show the cases of the variations of the irradiation and the temperature, respectively, for the current as a function of the voltage and the power as a function of the voltage.

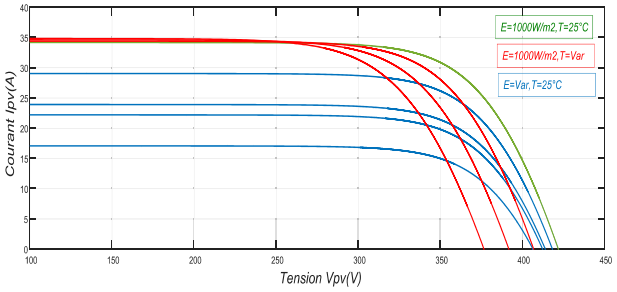

Fig 2. Zoom of the characteristic I = f (v) with variation of T and E

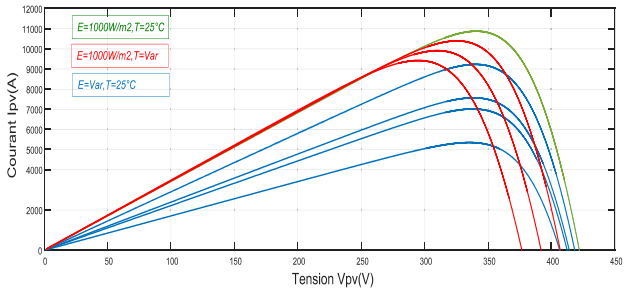

Fig 3 Characteristic P = f (v) with variation of T and E

B. *Boost converter*

The boost converters are continuous converters that cut a continuous input variable, voltage or current, and whose output quantity is also continuous or low waviness [11]. Its use is necessary to store photovoltaic energy in batteries, or to feed a continuous load [12]. The boost converter consists of capacitors, inductance and switches. In the ideal case, all these devices consume no active power, which is why we have good yields in boost converters [13]. Also known as "boost" its basic block diagram is that of Figure 2. Its typical application is to convert its input voltage to a higher output voltage [14].

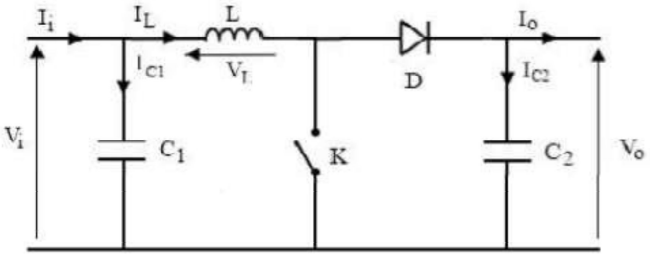

Fig 4 Circuit of a boost converter

When the switch is closed for the duration, the current in the inductor increases linearly. The voltage across K is zero. During the time, the switch opens and the energy stored in the inductor controls the flow of current in the freewheeling diode D. By writing that the voltage across the inductor is zero, we have the expression (2) by means of which the graph of FIG. 5 is schematized

$$V_O(1-\alpha) = V_i \quad (2)$$

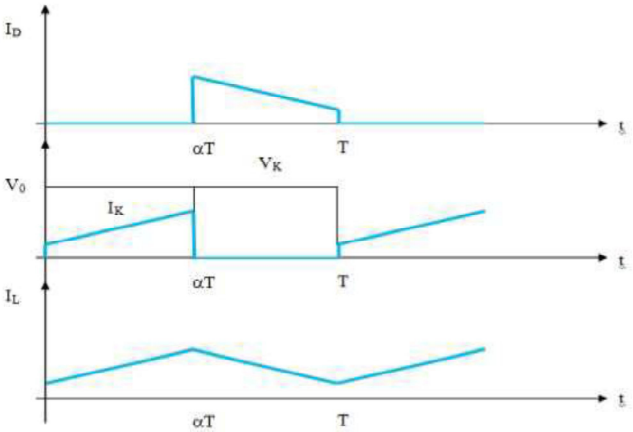

Fig 5 Sequences of operation of the boost converter

ISSN 1737-9334

C. PV- boost converter

An MPPT control, associated with an intermediate matching stage, makes it possible to operate a GPV so as to permanently produce the maximum of its power. Thus, whatever the weather conditions (temperature and irradiation), the converter control places the system at the maximum operating point (VPPM and IPPM). The photovoltaic conversion chain will be optimized through a static converter (SC) controlled by a MPPT. It can be represented by the diagram of Figure 6.

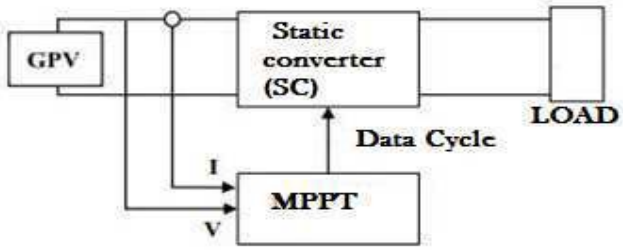

Fig 6 Solar energy conversion chain including a MPPT command

In the literature, we can find different types of algorithms performing the PPM search. In this work we use the Perturb & Observe (P & O) method, whose flowchart is presented in Figure 7.

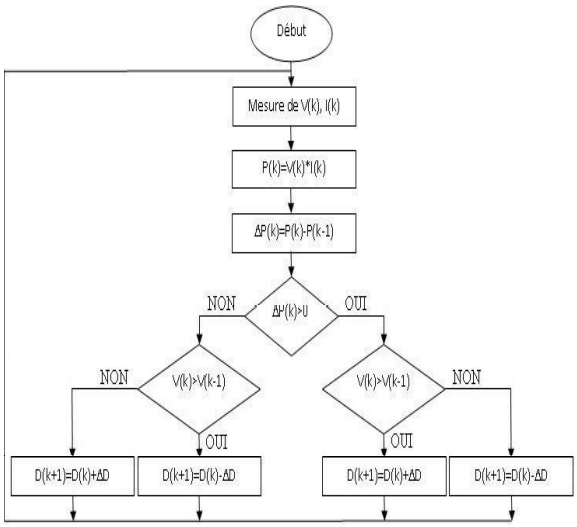

Fig 7 P & O algorithm

- *Irradiation E variable and constant temperature T=25°C*

For values of E = 1000W / m2, 850W / m2, 700W / m2, 650W / m2, 500W / m2, we presented the results of simulations (see Figures 8 and 9) which show that our panel delivers the maximum of power as shown in the panel feature figures.

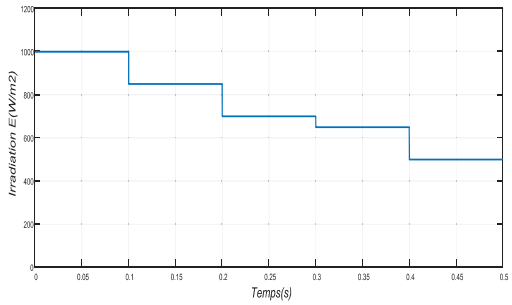

Fig 8 Variation of the irradiation E and the constant temperature T = 25 ° C.

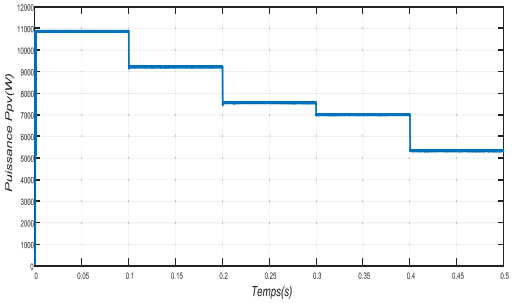

Fig 9 MPP with variation of E and T=25°C

• *Variable temperature and E=1000W / m²*

In this case we keep E constant but we change the values of the temperature: T = 25 ° C, 35 ° C, 45 ° C, 55 ° C. Figures 10 and 11 shows the evolution of the temperature and power provided by the panel.

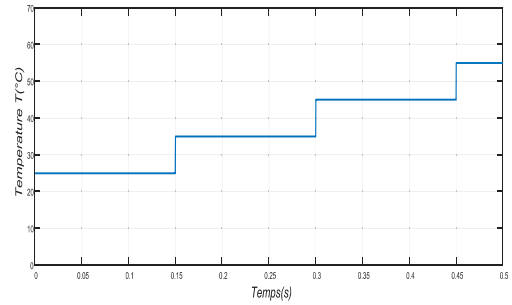

Fig 10 temperature Variation and irradiation constant E = 1000W / m²

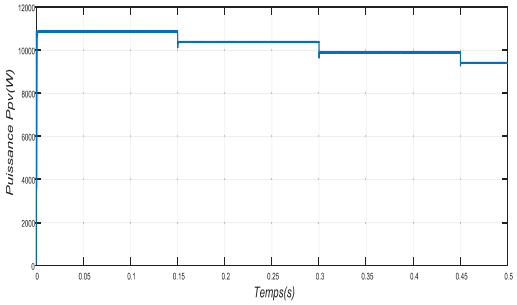

Fig 11 MPP with variation of T and E =1000W/m²

ISSN 1737-9334

III. GRID-CONNECTED SOLAR PV

The studied chain includes, mainly a photovoltaic panel, a chopper, a control MPPT, a three-phase inverter with a connection to a distribution network. The inverter and the network are simultaneously connected to a three-phase load. Figure 12 shows the structure of the global conversion chain.

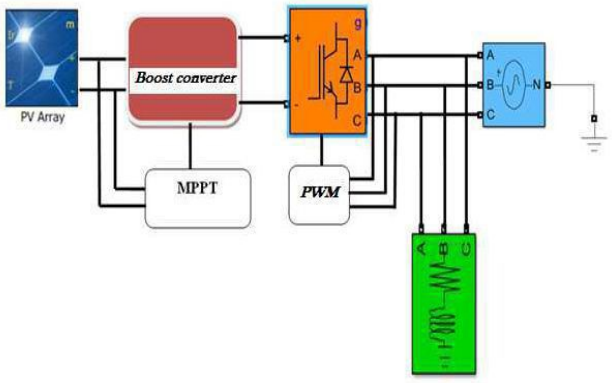

Fig 12 Structure of the conversion chain

In order to achieve the synchronization of the converter (inverter) with the electrical network, a PLL structure has been used. Its calculation principle is shown in Figure 13.

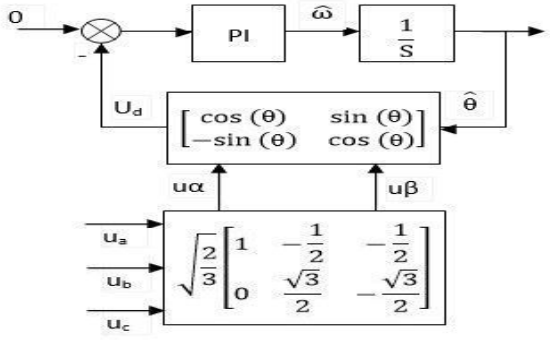

Fig 13 Schematic diagram of a PLL

The powers represented by FIG. 14: the active power of the load (Pch), the power delivered by the panel (Ppv), the power of the distribution network (Pr) and finally the appearance of the sum of the (Ppv + Pr), we notice that during the first interval (0s-0.1s) and after a transient regime, the solar panel develops a power greater than that required by the load so all the power consumed by the load is provided exclusively by the panel (current of the null network). Between 0.1s and 0.2, since the irradiation has dropped to 650W / m^2 the panel will only be able to deliver a maximum power of 7KW, thus lower than that demanded by the load. Thus, the network goes into action to deliver to the load the amount of power missing (3KW) which is found by increasing the amplitude of the phase currents of the network. For the second 0.1s-0.2s interval, there is a remarkable decrease in irradiation up to 650W / m^2, which provides a power of 7KW. In this case, the load takes the complement of its needs from the network, we notice an addition of the powers of the panel = 7KW and 3KW delivered by the network to satisfy the needs of our load, which is shown by the increase of the amplitude of the phase currents of the network. Finally for the last 0.2s-0.3s interval the irradiation level is at 0W / m^2, so the panel does not deliver power and therefore the power demanded by the load and totally ensured by the network.

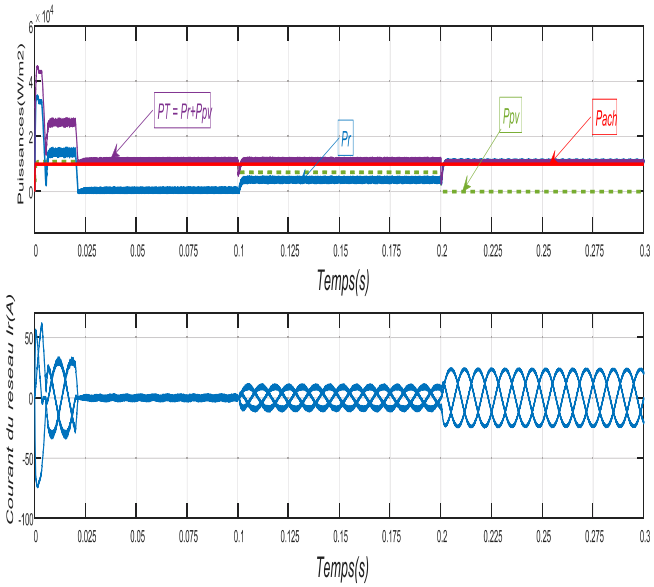

Fig 14 The exchange of power between the panel and the network

IV. CONCLUSION

This work was mainly devoted to the definition, role and modeling of the various components of a photovoltaic conversion chain. Thus, ~~that~~ the principles of operation of the solar system of energy production is amply developed in particular in terms of the influence of the meteorological conditions (irradiation and temperature). In view of applying the optimization technique for monitoring the maximum power delivered by the panel, whatever the variations of the irradiation and the temperature, we will in the rest of this work insert it for the control of the chopper Elevator of the studied chain.

REFERENCES

[1] Parida, B, Iniyan, S, Goic, R. A review of solar photovoltaic technonologie s. Renewable and sustainable energy reviews.2011, 15, 3, 1625-1636.

[2] Rasool, Fahad, et al. "PV panel modeling with improved parameter extraction technique." Solar Energy 153 (2017): 519-530.

[3] Karami, N, Moubayed, N, Outbib, R. General review and classification of different {MPPT} Techniques.Renew. Sustain. Energy Rev 2017; 68: 1–18.

ISSN 1737-9334

[4] Henchiri ,A, Bahi , T, Khochemane, L, Lekhchine,S. Control of the DC Voltage Output Photovoltaic System, 5th International Conference on Green Energy and Environmental Engineering , 28-30 April 2018 , Tunisia.

[5] Rakesh, R, Kannan, S. A, Jomy, J, Kamala, D. VJayaraju, , M. Modelling and analysis of MPPT techniques for grid connected PV systems. International journal of innovative research in electrical, electronics, instrumentation and control engineering. 2014; 2: 1031-1037.

[6] S. Pétion, « New Distributed Architectures for Energy Management and Conversion for Photovoltaic Applications ", Doctoral Thesis, University of Toulouse, 2009.

[7] Cabal C. «Energy optimization of the electronic adaptation stage dedicated to photovoltaic conversion. "Doctoral Thesis 2008.

[8] Faranda R., Leva S. “Energy comparison of MPPT techniques for PV Systems.” Wseas Transactions on Power Systems, Issue 6, Volume 3, Juin 2008.

[9] Cid Pastor A. «Design and realization of photovoltaic modules. "PhD thesis, University of Toulouse 2006.

[10] Helali K. «Modeling of a photovoltaic cell: comparative study ». Memory of Majistaire, 2012. University of Mouloud Mammeri of Tizi-Ouzou.

[11] http://dspace.univbiskra.dz:8080/jspui/bitstream/123456789/11199/1/%C3%89tude_et_simulation_0d%E2%80%99un_convertisseur_DC-CMulticellulaires.pdf

[12] https://fr.wikipedia.org/wiki/R%C3%A9gulateur_PID

[13] https://bu.univ-ouargla.dz/master/pdf/BENSACI-Wafa.pdf?idmemoire=146

[14] http://dspace.univbiskra.dz:8080/jspui/bitstream/123456789/11199/1/%C3%89tude_et_simulation_d%E2%80%99un_convertisseur_DC-DCMulticellulaires.pdf

ISSN 1737-9334

OPTIMIZING EXPOSURE PARAMETRES IN DIGITAL MAMMOGRAPHY

Talbi Mohammed[#1], Oustous Aziz[#1], Ben messaoud Mounir[#3], Sebihi Rajaa[#2], Khalis Mohammed[#1]
[#1] *The Moulay IsmailUniversity of Meknes,* Physical Sciences and Engineering, *NPT*
B.O. 11201,Zitoune Meknès, Morocco
[1]mo.talbi@uhp.ac.ma
[#2]*Mohammed V University, faculty of sciences, ESMAR*
B.O. 1014, Rabat, Morocco
[#3] *Sidi Mohamed Ben Abdellah University, faculty of sciences*
B.O. 1014, Fès, Morocco

Abstract— **Breast cancer is the leading cause of death for women around the world. Screening mammography is based mainly on mammography examinations, which is the reference examination due to its sensitivity for detecting small lesions and micro-calcifications.**
Therefore, it is essential to ensure quality examination with the lowest possible dose. These conditions depend on the choice of parameters (anode / filter, voltage and tube current). In the clinic, the majority of radiology technician use the automatic mode pre-programmed on the device.
AIM: The purpose of our research is to check that these constants are adapted. Using the manual mode and varying one parameter at a time, we were able to determine the most appropriate anode/filter , voltage and tube current.
METHODS: We performed our measurements on digital mammographic (PLANMED Sofie-classic.
A solid dosimeter (AGMS Radcal) and a MTM 100 phantom allow to quantify the dose delivered and the image quality.
For image quality assessment, scores, defined by the rate of visible inserts (MTM 100 phantom), obtained and compared for each acquisition both in manual and automatic mode.
RESULTS: The results show that the parameters of mammographic on which we have made our measurements can be improved in order to offer a better compromise between image quality and breast dose. The last one can be reduced up to 13.27% to 22.16%, while preserving comparable image quality.

***Keywords*— mammogram, image quality, breast dose**

I. INTRODUCTION

Nowadays, breast cancer is the most common cancer in women worldwide, it is the second leading cause of cancer death among women and accounts for 16% of all women's cancers[1].

In Morocco, between 30 000 and 40 000 new cases of cancer are identified each year, the most frequent localization, On the women's list, is the breast cancer which occupies the first place (36%) [2].
The chances of winning the battle for healing are the result of the progress made in this direction through multiple actions supported by the Ministry of Health, through awareness campaigns, mobilization in early detection[3].

In morocco , the Ministry of Health proceeded a screening mammography program, for women over 45 years, using mobile units [4-5].

Organized breast cancer screening recommends one mammography every 2 years for women aged 45 to 70 years in the absence of any particular symptom, which means many examinations.

One of the risks of the screening is the induction of radiation-induced cancers according to the dose received by the repetition.For 100,000 women each receiving a dose of 3.7 mGy on both breasts and examined40 to 55 years and every two years until age 74 years, it is expected that 86 cancers will be induced and 11 deaths from radiation-induced breast cancer. [6-7].

For a woman considered to be at risk [8], this can lead her to undergo more than 20 mammography, not counting other examinations that she undergoes during her life (scanners, radiology)[9]. In addition, during a mammography, a woman can undergo multiple shots, so receive repeated doses over short periods of time.[10]

Ensuring Optimization of image quality and minimizing breast dose in mammography patients is a major challenge.

several research concluded the impact of exposure parameters on the quality of image and dose radiationthey try to propose standards for imaging protocols that balance the image quality and the dose[11].

Therefore, it is essential to ensure quality examination with the lowest possible dose. These conditions depend on the choice of parameters (anode / filter, voltage and tube current). In the clinic, the majority of radiology technician use the automatic mode pre-programmed on the device

AIM: The purpose of our research is to verify that these constants are adapted. Using the manual mode and varying one parameter at a time, we were able to determine the most appropriate anode/filter , voltage and tube current.

ISSN 1737-9334

II. METHOD

We performed our measurements on mobile unit of mammograms, on the city of Temara mammographs (PLANMED:Sofie-classic).

to assess the image quality and the breast dose we are based on the European protocol for thequality control of the physicaland technical aspects ofmammography screening.[12]

For image quality assessment, we used MTM 100 phantom an artificial breast designed and dedicated to the performance test of a mammography machine it contains:

Micro-calcifications.

Masses.

Fibrous structures

Scores defined by the rate of visible inserts (MTM 100 phantom), obtained and compared for each acquisition both in manual (kVp, the tube current, the anode / filter couple) and automatic mode (AEC).

The MTM100 phantom is placed between the compression plate and the breast position base, symmetry must be achieved between the two sides of the phantom with the help of the cells drawn in the compression plate, to avoid slightly oblique images. this may subsequently cause a lack of occurrence of expected masses due to misposition. After taking the images, the cassette is injected into the digitizer, whose function is to extract the image obtained for diagnostic purposes.

for the evaluation of the glandular dose we used a small Solid State multi-parameter sensor (The AGMS-M+ Multisensor) used for single exposure . It measures dose, dose-rate, time, kVp, HVL, and beam filtration. we also used The Rapid-Gold digitizer. And through its accu-gold software that allows to visualize the result obtained. We have been able to compare the different modes of exposure, in a first time we exposed the detector by the automatic exposure control (AEC) then in a second time we exposed the detector by the manual mode by varying one parameter at a time (kVp, the tube current, the anode / filter couple).

The value of the current of the tube (mAs) is fixed (There is a stability of the image quality for the mAs between 32 and 40, then a slight improvement for the range (70-80 mAs)) and the kilo-voltage (kV) is varied for taking the images kV = [26-36];

In order to obtain an estimate close to the real case, the detector was placed directly on the MTM 100 phantom, to take into account the effect of the diffusion.

the effect of tube current (mAs) was neglected.

Score calculation

The image quality is expressed by a calculation of score obtained by the summation of the number of lesions appearing in the image taken at the end of the MTM100, the quality improves in parallel with the increase of the score and vice-versa, this is in the general case, remains to seek to optimize the dose delivered to ensure a minimum dose for good image quality in mammography.

III. RESULT

A. *IMAGE QUALITY*

In this study, we carry out several manipulations to evaluate the image quality according to the exposure mode and this for the two combinations anode-filter Mo /Mo and Mo/Rh.

For each group of [micro-calcification, mass, fiber], the number of inclusions is determined. The last visible inclusion gives the score.

We evaluate the degree of visibility of the inclusions: entirely or partially visible

The overall score is the sum of the partial scores determined for the three groups of inclusions

On this graph (Figure 1) we tried to compare the image quality via the score obtained for fibers of the phantom visualized on the image. we used the manual exposure mode, varying the kVp voltage four different kVp values (26, 28, 30, 32) while the tube current remained fixed,

For this manipulation It has been noted that the score for fibers elements increases from low voltage to 32 kVp peak voltage, the score was better for with Mo/Rh than with Mo/Mo.

The graphfigure 2 above represents the calculated score variation for the two anode-filter pairs Mo/Mo and Mo/ Rh for the visibility of masses.

in terms of the score of masses, it was the same for both target-filter combinations at kVp 26-28, with slight increase with Mo/Rh at 32 kVp.

In this graph,Figure 3 comparison of the image quality between Mo/Mo and Mo/Rh for the visibility of specks against the tube voltage (kVp).

A significant increase was observed for both combinations, at 28 kVp, no change observed between 28 and 32 kVp.

At the end we summed the total scores of the inclusions, we observed that the score increases with the increase of the voltage with a slight domination with the couple Mo/Rh than with the couple Mo/MoFigure 4.

The result of this manipulation show that the score is greater than 46 (1sd)which shows that the device is in the standards recommendations, that the score of acceptability is 32 in total of the constituent elements of the phantom. At the end of the manipulations we have chosen to compare the manual exposure mode and the automatic mode for the same device and for the same combinations and for similar peak voltages.

For the 32 kVp voltage the two modes are in the norms, since the acceptability score is 32, while the two modes are around 64 (1sd).

ISSN 1737-9334

B- Radiation Dose

At the TEMARA mobile unit, experimental measurements were made to evaluate the image quality and the level of exposure.
At the beginning for each peak voltage of the range [26 - 32] kV and for each anode-filtration pair selectable on the device, the dose at the input was raised by incrementing successively.
These different parameters of interest are presented in FIG. 26 for the anode-filtration pairs Mo / Mo, Mo / Rh, respectively.

In this graphFigure 5 we mentioned the dose at the input as a function of the voltage kVp for the two filter-anode couples.

We find on this graph that the dose at the input increases significantly by increasing the voltage kVp that for the Mo / Mo and Mo / Rh filter anode pair Examination of these two acceptability criteria makes it possible to show that the beam is in agreement with the standards.

the dose increases significantly with the voltage and it varies between 2 mGy and 8,21 mGy for the Mo / Mo couple and between 6 and 10,32 mGy for the Mo / Rh pair

When using the automatic mode, the dose is around 10,03 mGy for Mo/Mo and 11,69 mGy for Mo/Rh

Comparison between manual mode and automatic mode for the anode-filter pair, we find that the dose at the entrance for the automatic mode is higher compared to the dose in manual exposure mode.

IV. DISCUSSION

A- Image Quality

the installation are within the norms, since the acceptability criterion is 32, while the results obtained for both exposure modes are generally around 56 (1sd) except for low voltage. The analysis of the curves obtained led us to deduce that the image quality increases as a function of the voltage kV.

A. Noel and al realized the same tests on several facilities in France, with the MTM100 phantom using only the automatic mode they found The mean image quality score value (limiting value = 24) was 34 6 12 (1 sd)[13].

There is a stability of the image quality for the kVp between 30 and 32 for masses and specks, then a slight improvement for fibers. Mark B. Williams and al them result are indicating that higher tube voltages would produce no further performance improvement. For a given phantom type[14].

For this reason we must understand the relationship between radiation dose and image quality [15].

It is obvious that the image quality progresses significantly with the increase of the exposure parameters but we must not neglect the dose that progresses with, so we must look for the image that delivers the best quality with the lowest dose.

the purpose of optimizing techniques is to establish standards for imaging protocols that balance the image quality and the dose to patient [16].

B. Radiation dose

A comparison between the two pairs shows that the Mo / Rh pair is more irradiating than the Mo / Mo pair. For the manual exposure mode the dosimetric quantities are optimal while being based on the annual regulatory limits of the CIPR [17] in its publication 103 (From <10mGy), and the entrance surface dose in the automatic mode was around 10,03-11,3 wich mean is in the limit of desirable value.

if we compare our result with A. Noel and al result, they were using the mode AEC but they found in the majority of facilities the mean dose value (limiting desirable value = 10 mGy) was 8.6 mGy (1 sd).[13]

The number of photons delivered is directly dependent on the intensity of the current and the exposure time, the dose is directly related to these parameters.

we was in the range of result of Dogan Bor and al, using MTM100 phantom and CIRS phantom measuredESAK (Entrance surface air KERMA) values (can be considered equal to entrance surface dose) using the routineclinical exposure settings. The mean ESAK valuewas 10.1 mGy, with a range of 3.78 – 17.8 mGy forthe CIRS phantom. The results of the four systemswere not within the proposed tolerances.[18]

The optimization of the mammography technique should not be limited to dose reduction, but to reduce the dose and to look for an image which allows to pause the correct diagnosis.[19].

The entrance surface dose can be reduced up to 22,16% for Mo/Mo and 13.27% for Mo/Rh couple , while preserving comparable image quality.

we have concluded that for breast thickness less than 45 mm the filter/anode Mo/Mo pair is well adapted with a voltage between 28 and 30 kVp, it's slightly the same forAlkhalifah K and al, Chien-HauChu and al for each breast thicknesses of 21 mm or 32 mm thickness, a voltage of 25 kV or 28 kV and a target combination Mo / Mo / filter was optimal and for 40 mm thickness and over a voltage of 30-32 kVp and a target filter combination of Mo/Rh was recommended [20-21].

ISSN 1737-9334

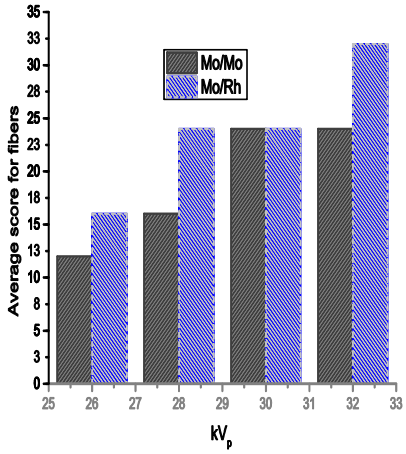

Figure 1: kVp Vs score of fibers

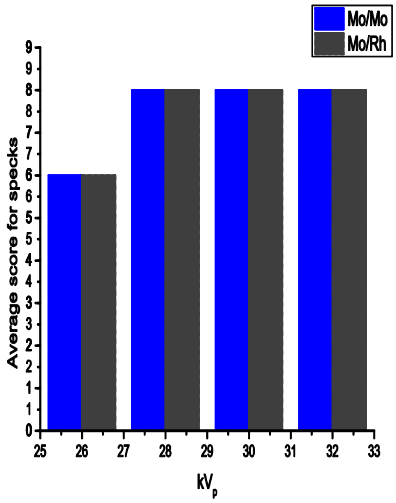

Figure 2: kVp Vs score of specks

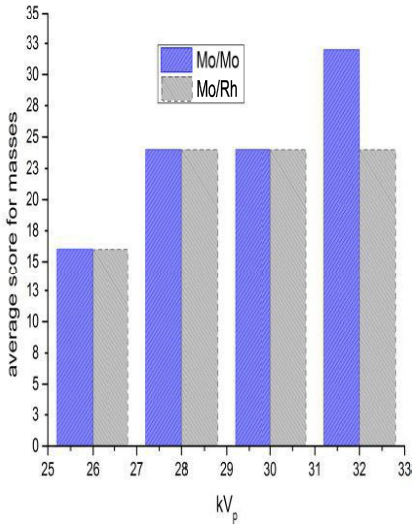

figure 3: kVp Vs score for masses

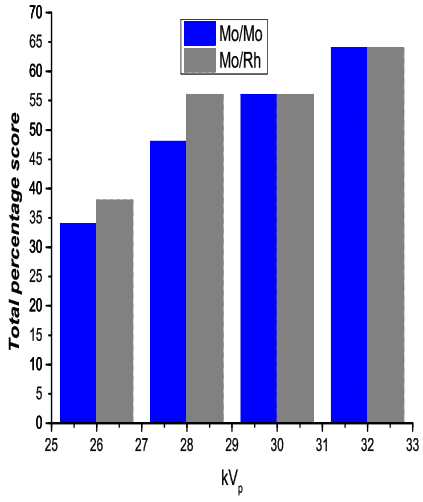

figure 4: kVp Vs Total inclusions score

ISSN 1737-9334

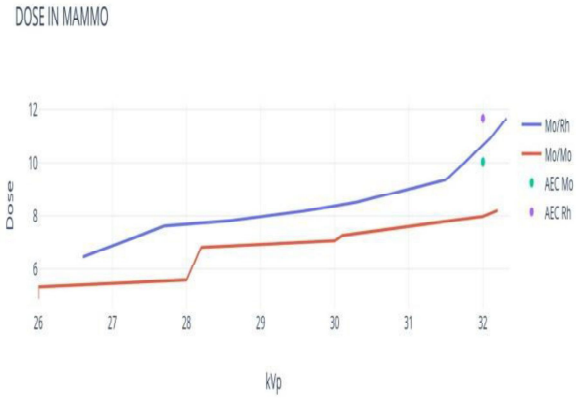

Figure 5: kVp Vs Entrance dose surface

V. Conclusions

Measurements of image quality and dose at the entrance were made on a mobile mammography unit in Morocco

the results showed that the acquisition parameters can be improved to optimize the dose to patients it's can be reduced up to 13.27% to 22.16%, while preserving comparable image quality.

The objective of optimizing the radiological techniques is to standardize the protocols that balance the image quality and the dose received by the patients.

In order to improve the functioning of the facilities, a quality control program should be applied periodically and the diagnostic reference levels (NRDs) established in MOROCCO.

References

[1] Épidémiologie des cancers chez les patients de 65 ans et plus : institut national du cancer Date de publication : 27/11/2018 MAROC

[2] laila hallaoui (Cancer: le Maroc enregistre 40.000 nouveaux cas chaque année MAROC HUFFPOST 21/11/2017)

[3] **Journée Nationale de Lutte contre le Cancer, volonté collective de combattre ce fléau dévastateur** fondation lalla salma de prévention et traitement des cancers

[4] GUIDE DE DÉTECTION PRÉCOCE DES CANCERS DU SEIN ET DU COL DE L'UTÉRUS **EDITION 2011 (Ministere de la Sante MAROC)**

[5] Plan national de prévention et de contrôle du cancer SYNTHÈSE 2010-2019

[6] Martin J. Yaffe , PhDRisk of Radiation-induced BreastCancer from MammographicScreening**Radiology:** Volume 258: Number 1—January 2011 n radiology.rsna.org

[7] R. Edward Hendrick , PhD;Radiation Doses and CancerRisks from Breast ImagingStudies, **Radiology:** Volume 257: Number 1—October 2010 n radiology.rsna.org

[8] Constance D. Lehman, M.D., Ph.D. Screening Women at High Risk for Breast Cancer with Mammography and Magnetic Resonance Imaging, 2005 American Cancer SocietyDOI 10.1002/cncr.20971Published online 30 March 2005 in Wiley InterScience (www.interscience.wiley.com).

[9] La susceptibilité individuelle aux rayonnements ionisants/ Pr. Michel Bourguignon Commissaire ASNmichel.bourguignon@asn.fr & www.asn.fr GT CIPR – 15 Mai 2014

[10] Annette LEXA, Docteur en Toxicologie, nov 2016 Mammographies et radiosensiblité : **Cancer Rose**, site d'information sur le dépistage du cancer du sein

[11] Dr. Zeina AL KATTAR,Radiation Dose Levels Assessment in Digital Mammography, 2015 International Conference on Advances in Biomedical Engineering (ICABME)©2015 IEEE

[12] N. Perry, European guidelines for quality assurance in breast cancer screening and diagnosis *Four th edition, 2013*

[13] A. Noel, use of phantoms and test objects in mammography: standardisation of quality and dose assessment in france. Radiation Protection Dosimetry Vol. 80, Nos 1–3, pp. 77–79 (1998)

[14] Mark B. Williams,[a)]Priya Raghunathan, and Mitali J. More University of Virginia, Charlottesville, Virginia 22908 **Optimization of exposure parameters in full field digital mammography Med Phys. 2008 Jun; 35(6): 2414–2423.**

[15] Daniel Bonifacio Monte Carlo simulation of X-ray spectra in diagnostic radiology and mammography using Geant4 research Gate Conference Paper · January 2005

[16] Michael P. Andre; Brett A. Spivey Optimization of tungsten x-ray spectra for digital mammography: a comparison of model to experiment .

[17] PUBLICATION 103 DE LA CIPR, Recommandations 2007 de la Commission internationale de protection radiologique

[18] Dogan Bor, performance measurements of mammographic systemsRadiation Protection Dosimetry (2008), Vol. 129, No. 1 – 3, pp. 165 – 169

[19] Young KC[1], Oduko JM, Bosmans H, Nijs K, Martinez L. Optimal beam quality selection in digital mammography Br J Radiol. 2006 Dec;79(948):981-90.

[20] Chien-HauChu[a]Ming-ChenYuan[a]Wen-ShengHuang[b] Dosimetry and kVp standarisation for quality assurance of mammography Bor-TsungHsieh[c]https://doi.org/10.1016/j.radphyschem.2013.12.013

[21] Alkhalifah K, Brindabhan A, Alsaeed R effect of exposure factors on image quality in screening mammography Radiography (Lond). 2017 Nov;23(4):e99-e102. doi: 10.1016/j.radi.2017.05.005. Epub 2017 May.

ISSN 1737-9334

Enhancement of the vibratory analysis technique by the accelerometer characteristics evolution

Zine Ghemari
Electrical Engineering Department
University Mohamed Boudiaf, M'sila
BP 166 M'sila 28000, Algeria

Abstract— **The physical behavior of the piezoelectric sensor is defined by the direct effect of the piezoelectric detection, this effect is the conversion of a mechanical force into an electrical signal. In this work; the piezoelectric sensor is modeled, and the developed model is validated by simulation tests. This model makes it possible to improve the characteristics and the performances of this sensor and to propose a new conception of this last one. A comparative study is done to show the importance of our results compared to the literature. These results showed that an appropriate choice of damping ratio developed the parameters of the sensor and improved the vibration analysis technique.**

Keywords: Precision, Damping, Piezoelectric, Measurement.

I. INTRODUCTION

Vibration analysis is the best known and the most widely used. It must be said that it alone can detect virtually all the defects that may appear in rotating machinery. An unbalance, a game, a misalignment, a worn or damaged bearing ... result in a variation of the internal forces that undergoes the machine, and thus to a modification of its vibratory behavior. The first element of the vibratory analysis is the sensor and the piezoelectric sensor will be chosen in our work because it is the most used in industries through its advantages compared to others types of sensors and their main advantage is the low cost [1-9].

Piezoelectric sensor measures the physical acceleration experienced by an object due to inertial forces or due to mechanical excitation. In this device piezoelectric technique is commonly used to convert the mechanical motion into an electrical signal. Piezoelectric accelerometers rely on piezoceramics (e.g. lead zirconate titanate) or single crystals (e.g. quartz, tourmaline) [10-11].

The piezoelectric sensor is based on the direct effect of piezoelectric material, knowing that piezoelectricity is the amplitude of certain crystalline materials to produce an electrical charge proportional to the mechanical strain that deforms them [12].

Piezoelectric vibration sensors are widely used in industry for a variety of applications; they are somewhat temperature sensitive and can work in high temperature and pressure environments. In this field of sensors, many works show new approaches to improve performances and propose new design of piezoelectric sensors [13-16].

The mechanical thermal noise and noise of the piezoelectric element are modeled in work [17] by the theory of thermodynamics and the noise characteristics of the integrated circuit. A high-shock 2,000 g accelerometer with a plate spring has been designed, fabricated, and tested in work [18]. The proposed accelerometer with a plate spring uses a device layer of an SOI (silicon on insulator) wafer. In work [19], the compression model and shear model for high temperature piezoelectric accelerometer based on the CTGS and YCOB crystal cuts were studied. Micro-electromechanical systems (MEMS) sensors designed in work [20-24] to sense fine particles on the surface apply electrical signals to identify the corresponding physical changes on the surface. These sensors have limitations when the accumulated fine particles saturate the measurement range. In this study, we have studied how to effectively remove the accumulated particles after detection, rather than measuring the sensing performance.

These works have based on the piezoelectric sensor modeling and the improvement of their performances but did not count in consequence the measurement error influence on the sensor accuracy. But, in our work, a model of the measurement error according to the accuracy is developed to propose a new design of this type of the sensors with high performances and to progress the technique of the vibratory analysis.

II. MODELING THE PHYSICAL BEHAVIOR OF THE PIEZOELECTRIC SENSOR

The principle of working of a vibration sensor can be explained by a simple mass (m) attached to a spring of stiffness (k) that in turn is attached to a casing. The mass used in sensors is often called the seismic-mass or proof-mass. In most cases the system also includes a dashpot to provide a desirable damping effect (damping factor c) (see Fig.1).

This work was supported by the Algerian general direction of research
Z. Ghemari is with the Electrical Engineering Department, University of M'sila Algeria (zine.ghemari@univ-msila.dz).

ISSN 1737-9334

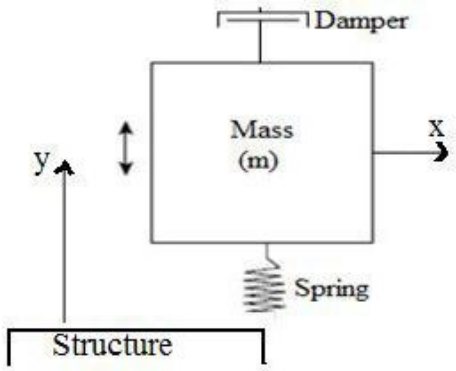

Fig.1. Model of the piezoelectric sensor

The relative movement is given by the following equation:

$$z(t) = x(t) - y(t) \quad (1)$$

y(t): the absolute movement of the vibrant structure.

z(t): the relative movement of the mass m with respect to the base of the structure (it's an equation as a function of time).

The following formula can extract by the use of the first law of movement:

$$\sum F = m\gamma = m d^2x/dt^2 = -c\,[(dx/dt) - (dy/dt)] - k(x-y) \quad (2)$$

γ : the movement acceleration

The differential equation of the system vibratory movement is given by:

$$m(d^2z/dt^2) + c(dz/dt) + k\,z(t) = -m(d^2y/dt^2) \quad (3)$$

One of the most effective methods for solving some differential equations is to use the Laplace transformation. The Laplace transform is not a function of time t, but rather a function of s. The operator will be the opposite of time, so a frequency. The Laplace transform therefore makes it possible to transform the problem of the time domain into the frequency domain.

The application of the Laplace transform on Eq. (3), we find Eq. (4) (the initial conditions are nulls).

$$m\,s^2 z + c\,s\,z + k\,z = -ms^2 y \quad (4)$$

The natural frequency of the piezoelectric sensor expressed by:

$$\omega_0 = \sqrt{(k/m)} \quad (5)$$

ω_0: the natural frequency of piezoelectric sensor

The piezoelectric damper considered here consists of piezoelectric material and a shunted circuit (resistor, inductor and capacitor). Thus, the damping factor of the damper is controllable by adjusting the frequency and electrical impedance. But the damping ratio (ξ) can be estimated by the use of Eq. (6), so the damping ratio is an estimated parameter.

$$\xi = c/(2m\omega_0) \quad (6)$$

Replacing Eq. (5) and Eq. (6) in Eq. (4), we can extract the following equation:

$$z = -y\,s^2/(s^2 + 2\xi\omega_0 s + \omega_0^2) \quad (7)$$

We know that the Laplace variable (s) is a complex number s = a + jb. In the spectral analysis, we choose for s the pure imaginary variable, not real: s = j.w (with j2 = -1).

We can write Eq. (7) as follows:

$$z = \omega^2 y/(-\omega^2 + 2j\xi\omega\omega_0 + \omega_0^2) \quad (8)$$

Eq. (8) can be expressed as follows:

$$z = \omega^2 y/\omega_0^2(1-(\omega/\omega_0)^2 + 2j\xi\omega/\omega_0) \quad (9)$$

Eq. (9) is a complex function; its module is expressed as follows:

$$Z = \omega^2 y/\omega_0^2\sqrt{[(1-(\omega/\omega_0)^2)^2 + (2\xi\omega/\omega_0)^2]} \quad (10)$$

Z: relative movement modulus (displacement value)

Eq. (10) illustrates the displacement measured by the accelerometer and the measurement precision demonstrated as follows:

$$\omega_0^2 Z = \omega^2 y/\sqrt{[(1-(\omega/\omega_0)^2)^2 + (2\xi\omega/\omega_0)^2]} \quad (11)$$

The absolute acceleration of the vibrating structure is:

$$d^2y/dt^2 = \omega^2 y \quad (12)$$

The movement relative acceleration is expressed by:

$$d^2z/dt^2 = \omega_0^2 Z \quad (13)$$

To obtain optimum precision, the sensor is chosen according to the condition ω/ω0 << 1, and then Eq. (10) becomes:

$$\omega_0^2 Z \approx \omega^2 y \quad (14)$$

So:

$$d^2z/dt^2 \approx d^2y/dt^2 \quad (15)$$

The accelerometer precision is given by:

$$P = (d^2y/dt^2)/(d^2z/dt^2) = [(y\omega^2)/(Z\omega_0^2)] \quad (16)$$

P: The accelerometer precision

Then, from Eq. (12), the accuracy is defined by the following formula:

$$P = \sqrt{[(1 - (\omega/\omega_0)^2)^2 + (2\xi\omega/\omega_0)^2]} \quad (17)$$

The new relation relating the relative movement as a function of accuracy is extracted by the use of Eq. (10), thus the expression below is obtained:

$$Z = (\omega^2 y)/P\omega_0^2 \quad (18)$$

The use of equation (18) optimizes the accelerometer characteristics and proposes a new conception of this one.

ISSN 1737-9334

The measurement error expressed as follows:

$$E=[(d^2z/dt^2)/\left(d^2y/dt^2\right)]-1=\left[\left(Z\,\omega_0^2\right)/\left(y\,\omega^2\right)\right]-1 \quad (19)$$

Replacing Eq.11 in eq. 19, the following equation is obtained:

$$E=[1/\sqrt{(1-(\omega/\omega_0)^2)^2+(2\xi\omega/\omega_0)^2}\,]-1 \quad (20)$$

According to Eq. 20 and Eq. 17, the formula relates the measurement precision and the measurement error can be extracted as illustrated by the following equation:

$$E=\left(1/P\right)-1 \quad (21)$$

Eq. 21 is a new formula of measurement error as a function of precision.

In this part, we have extracted two new models that relate the relative movement modulus and the measurement error as a function of precision through the movement law application; these two models make it possible to optimize the piezoelectric sensor parameters and propose a new design of this one.

III. SELECTION OF THE APPROPRIATE DAMPING RATIO FOR THE ACCELEROMETER

The appropriate choice of the damping ratio makes it possible to optimize the characteristics of the piezoelectric accelerometer and their performances and to achieve this objective, the model developed is simulated.

Eq. (17) and Eq. (21) shows the precision and measurement error as a function of frequency ratio and damping ratio. To maximize precision and minimize error, it must extract the appropriate values of frequency ratio and damping ratio. In this part will be focused on finding the suitable damping ratio which improves the sensor precision to its maximum value and minimize the measurement error to minimum, for this purpose Eq. (17) and Eq. (21) are simulated by using the natural frequency of piezoelectric sensor that will use for experimental validation (ω0 =2000 Hz), the variation of the movement relative frequency with respect of the condition (ω << ω0) to avoid the resonance phenomenon (the relative frequency varies from 0 to 800 Hz with a step equal 80 Hz) and takes the values of damping ratio more close to the damping ratio value of the sensor used in the experiment (damping ratio of the sensor used in the experiment ξ = 0.65). The following table shows the parameters used in the simulation (Table 1):

Table.1. Parameters of simulation of Eq. (17) and Eq. (21)

Parameters	Values
Naturel frequency (ω_0) (Hz)	2000
Movement amplitude (y) (mm)	0.35
Damping rate (ξ)	0.6, 0.62, 0.64, 0.66, 0.68, 0.7
Relative frequency (ω) (Hz)	0 to 800

The simulation results of Eq. (17) and Eq. (21) are summarized in the following figures (Fig.2 and Fig.3):

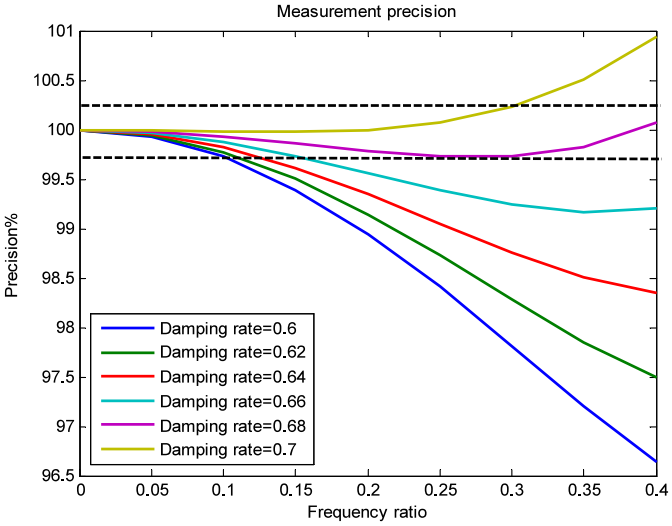

Fig.2. Measurement precision as a function of frequency ratio (Simulation results of Eq. (17))

Figure (2) shows the measurement precision according to the frequency ratio for six values of damping ratio (0.6, 0.62, 0.64, 0.66, 0.68, and 0.7), from this figure, it can be observed that the damping ratio equal to 0.68 is the appropriate choice to increase the precision to the maximum (P ≥ 99.7).

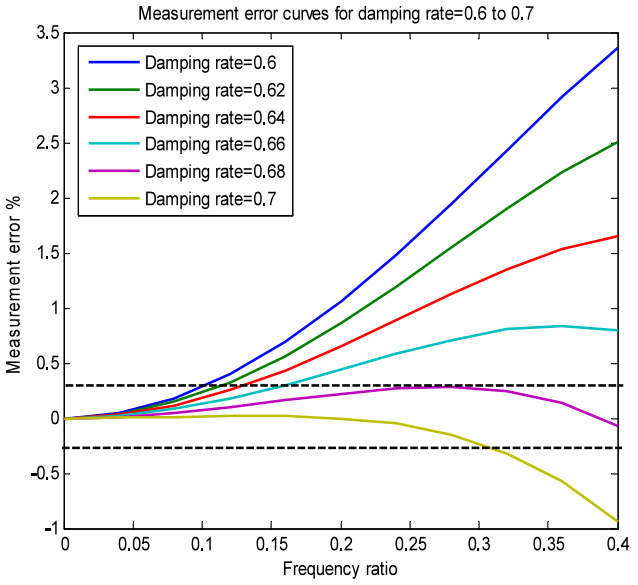

Fig.3. Measurement error as a function of relative frequency for various values of damping rate

Figure (3) shows the measurement error according to the frequency ratio for six values of damping rate (0.6, 0.62, 0.64, 0.66, 0.68, and 0.7), from this figure, it can be observed that the damping rate equal to 0.68 is the appropriate choice to reduce the error to the minimum (E ≤ 0.28).

Figure (2) and figure (3) show that the damping rate value equal to 0.68 makes it possible to increase the precision and to minimize the measurement error.

ISSN 1737-9334

IV. Comparative Study and Proposal of New Characteristics of Accelerometer

The comparison is done between a piezoelectric sensor proposed in ref [25] (damping ratio equal to 0.64), a piezoelectric sensor used in the experimental tests (damping ratio equal to 0.65), an piezoelectric a piezoelectric sensor proposed in this work (damping ratio equal to 0.68) and a piezoelectric sensor suggested in ref [26] (damping ratio equal to 0.707). The frequency is varied from 0 to 800 Hz and the measurement error (E) is simulated.

The results are presented in the following figure (Figure 4) and table (2):

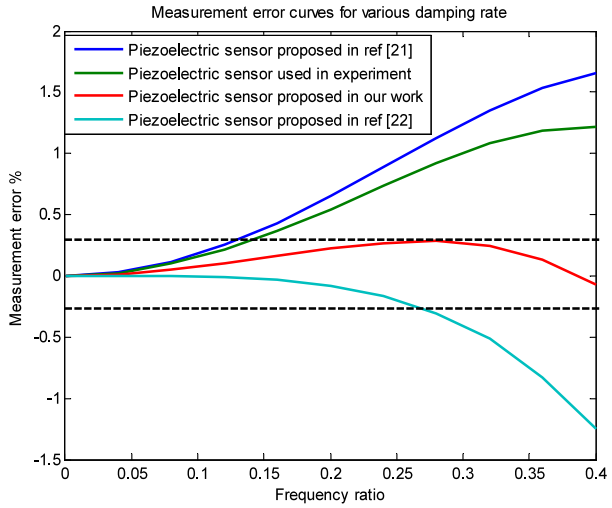

Fig.4. Measurement error as a function of frequency ratio for four damping ratios (0.64, 0.65, 0.68 and 0.707)

Figure (4) represents the measurement error as a function of frequency ratio for four sensors, the first proposed in ref [25] (damping ratio equal to 0.64), the second used in the experimental tests (damping ratio equal to 0.65), the third proposed in our work (damping ratio equal to 0.68) and the fourth proposed in ref [26] (damping ratio equal to 0.707). This figure shows a different curve of the measurement error for four value of the damping rate, which shows that the reduction or increase of the measurement error is affected by the value of damping ratio. According to this figure, we find that the damping ratio equal to 0.68 minimizes the measurement error to less than or equal to 0.3%.

Table.4. Comparison results between four sensors one used in the experimental tests and the other is the proposed sensor

Parameters	Proposed sensor in ref [25]	Sensor used in experimental tests	Proposed sensor in our work	Proposed sensor in ref [26]
Damping ratio	0.64	0.65	0.68	0.707
Precision	≥ 98.35 %	≥ 98.8 %	≥ 99.7 %	≤ 100.98%
Measurement error	≤ 1.65 %	≤ 1.2 %	≤ 0.3 %	≤ 0.98 %

From Table 2, it can be noticed that the proposed sensor is better than the proposed in ref [25], the sensor used in the experimental tests and the proposed sensor in ref [26]. We proposed new piezoelectric sensor parameters that make it more accurate and reliable compared to existing sensors.

V. Conclusion

The measurement accuracy as a function of displacement is shown by a new expression through the modeling of the physical behavior of the piezoelectric sensor. The validation of the developed model is done by simulation tests. Through these tests, an appropriate value of the damping ratio is extracted to improve the measurement accuracy of the piezoelectric sensor to an extreme value. Our results are compared with those of the results obtained in recent works to show the importance of our work.

Acknowledgment

The authors like to thank the Algerian general direction of research (DGRSDT) for their financial support.

References

[1] C. Breneur « Eléments de maintenance préventive des machines tournantes dans le cas de défauts combinés d'engrenages et de roulements » PhD Thesis from the National Institute of Applied Sciences of Lyon (France), 2002.

[2] A. Tomache, « Communication SME-ERCE, Symposium sur la maintenance industrielle » AEID-IAP. Algiers, January, 21: 23, 2001.

[3] K. A. R. Medeiros, C. R. H. Barbosa and E. C. de Oliveira "Flow Measurement by Piezoelectric Accelerometers: Application in the Oil Industry" Petroleum Science and Technology, Vol. 33, No. 13-14, (2015), PP: 1402-1409.

[4] J-C. Yu and F-H. Lai "Design and fabrication of the micro-accelerometer using piezoelectric thin films", Ferroelectrics, Vol. 263, No. 1, (2011), PP: 101-106.

[5] M F. Lumentut, K K. Teh and I. Howard "Computational FEA model of a coupled piezoelectric sensor and plate structure for energy harvesting", Australian Journal of Mechanical Engineering, Vol. 5, No. 2, (2015), PP: 199-208.

[6] Nishshanka N. Hewa-Kasakarage, Donghwan Kim, Michael L. Kuntzman, and Neal A. Hall "Micromachined Piezoelectric Accelerometers via Epitaxial Silicon Cantilevers and Bulk Silicon Proof Masses" Journal of Microelectromechanical Systems, Vol. 22, No. 6, (2013), PP: 1438-1446.

[7] H. Lv, L. Qin, and J. Liu "Principle Research on a Single Mass Six-Degree-of Freedom Accelerometer With Six Groups of Piezoelectric Sensing Elements" IEEE Sensors Journal, Vol. 15, No. 6, (2015), PP: 3301-3309.

[8] R-H. Han, J-Y. Wang, M-H. Xu and H. Guo "Design of a tri-axial micro piezoelectric accelerometer" 2016 Symposium on Piezoelectricity, Acoustic waves, and Device Applications, 21-24 Oct, 2016, Xi'an, Shaanxi, CHINA

[9] M-H. Xu, J-Y Wang, R-H Han, H. Zhou and H. Guo "analytical and finite element analysis of a new Tri-axial piezoelectric accelerometer" 2016 Symposium on Piezoelectricity, Acoustic waves, and Device Applications, Oct. 21-24, 2016, Xi'an, Shaanxi, CHINA.

[10] S. Yin, G. Niu, B. Vilquin, B. Gautier, G. Le Rhun, E. Defaÿ and Y. Robach, "Epitaxial growth and electrical measurement of single crystalline Pb(Zr0.52Ti0.48)O3 thin film on Si(001) for micro-electromechanical systems" Thin Solid Films, Vol. 520, No. 14, (2012), PP: 4572-4575.

[11] A. Lebrun « Modélisation et conception d'un capteur de vibrations à fibre optique par analyse polarimétrie : application à la sismologie » PhD Thesis, Institute of Solid State Electronics and Systems, University of Strasbourg, France, 2011.

ISSN 1737-9334

[12] J. Hu, H. Peng, T. Liu, X. Yao, H. Wu and P. Lu "A flow sensing method of power spectrum based on piezoelectric effect and vortex-induced vibrations" Measurement, Vol. 131, January 2019, PP: 473-481.

[13] A. Loghmani, M. Danesh, and M. Keshmiri "Modal structural acoustic sensing with minimum number of optimally placed piezoelectric sensors" Journal of Sound and Vibration, Vol. 363 (2016), PP: 345–358.

[14] A. Bajri and J. Høgsberg "Identification of damping and complex modes in structural Vibrations" Journal of Sound and Vibration, Vol. 431, (2018), PP: 367–389.

[15] I. Korobiichuk "Mathematical model of precision sensor for an automatic weapons stabilizer system" Measurement, Vol. 89, (2016), PP: 151–158.

[16] B. Mei, J. Lucas, S. Holé,, I. Lamarque and N. Cheronb "Origin of frequency difference between damped and sustained modes in vibrating wire sensors" Sensors and Actuators A, Vol. 241, (2016), PP: 66–73.

[17] M-H Xu et al "Noise analysis of the triaxial piezoelectric micro-accelerometer" 2017 Symposium on Piezoelectricity, Acoustic Waves, and Device Applications, Oct. 27-30, 2017, Chengdu, Sichuan, China.

[18] J-M Lee et al "High-Shock Silicon Accelerometer with a Plate Spring" International journal of precision engineering and manufacturing, Vol. 17, No. 5, 2016, pp. 637-644.

[19] L-F Kong et al "Performance improvement of CTGS and YCOB crystals for high temperature piezoelectric accelerometer applications" 2017 Symposium on Piezoelectricity, Acoustic Waves, and Device Applications, Oct. 27-30, 2017, Chengdu, Sichuan, China.

[20] M-G Kim et al "MEMS PZT Oscillating Platform for Fine Dust Particle Removal at Resonance" International journal of precision engineering and manufacturing, Vol. 19, No. 12, 2018, pp. 1851-1859.

[21] Zine Ghemari, Salah Saad: Enhancement of capacitive accelerometer operation by parameters improvement. International Journal of Numerical Modelling Electronic Networks Devices and Fields 02/2019; 32(22):e2568. DOI:10.1002/jnm.2568

[22] Zine Ghemari, Salah Saad: The use of mechanical sensitivity model to enhance capacitive sensor characteristics. Analog Integrated Circuits and Signal Processing 01/2019;, DOI:10.1007/s10470-018-01383-w

[23] Salima Khaoula Reguieg, Zine Ghemari, Tarak Benslimane, Salah Saad: Modeling and Enhancement of Piezoelectric Accelerometer Relative Sensitivity. Sensing and Imaging An International Journal 12/2019; 20(1)., DOI:10.1007/s11220-018-0222-y

[24] Zine Ghemari: Progression of the vibratory analysis technique by improving the piezoelectric sensor measurement accuracy. Microwave and Optical Technology Letters 10/2018;, DOI:10.1002/mop.31436

[25] X. Fu and W-H. Liao "Nondimensional model and parametric studies of impact piezoelectric energy harvesting with dissipation" Journal of Sound and Vibration, Vol. 429, (2018), PP: 78-95.

[26] S. Zhao and H. Fu "A novel vibration sensor system for frequency measurement based on Bias Flip technique" Measurement, Vol. 124, (2018), PP: 56–63.

ISSN 1737-9334

Energy Quality Enhancement using Power Control for Grid-Connected PV Application

Layate Zakaria [#1], Bahi Tahar [*2], Lekhchine Salima[¤3]

[#] *Department of Technology, Djilali Bounaama University*
Khemis Miliana, Ain Defla, 44001, Algeria
[1]zakarialayate@gmail.com

[*] *Automatic and Signals Laboratory LASA, Badji Mokhtar University*
Annaba, 23000, Algeria
[2]tbahi@hotmail.fr

[¤] *Department of Electrical Engineering, 20 August University*
Skikda, 21000, Algeria
[3]slekhchine@yahoo.fr

Abstract— **In the last few years, the electric power production technology has dramatically changed in terms of the sources nature adopted in this process. One of the main causes is the terrible pollution led to climate disruption because of irrational exploitation of fossil fuels in various fields, especially in power generation. According to these factors, green energy has invaded this vital field depending on new and renewable sources such as wind and solar energies, tidal energy and biofuel. Since it is distinguished of many advantages compared to other sources, the solar energy source based photovoltaic panels has currently became the most widely used and favoured power energy systems. In addition to the vast abundance of solar energy throughout the year seasons, the photovoltaic power systems are economic, no-polluted and noiseless systems due to absence of moving parts during the electricity production process. Soon before, the use of photovoltaic systems was limited on stand-alone configurations to satisfy population energy requirements in remote areas for individual applications mainly, household lighting and agricultural irrigation but actually, they exceeded this limitation and became generally available as they are also broadly, integrated on the electrical grid called grid-connected photovoltaic generator.**

This paper focuses a grid-connected distributed photovoltaic system. The considered system includes photovoltaic panels assembled and forming a photovoltaic generator, DC-DC boost converter to enhance the photovoltaic generated power and a DC-AC inverter used to adapt the power streaming between photovoltaic DC power and grid AC power. As well-known, the photovoltaic systems are non-linear systems which are easily affected by solar illumination and temperature, therefore, a maximum power point extracting system (MPPT) is inevitable task which has been implemented in this work based incremental conductance (INC) algorithm to harvest photovoltaic maximum power. Moreover, the grid injected photovoltaic energy using inverter that incorporates power electronic switches reduces the grid-side power quality, increases the reactive power and also perturbing grid balance. So, the main purpose of this article is to solve this problem where a control topology based inverter voltage control is investigated using phase and frequency control loop (PFCL) to improve grid power quality. A simulation results have been analyzed and discussed to confirm efficiency and reliability of the proposed system structure.

Keywords— **Photovoltaic, control, power, MPPT, simulation.**

I. INTRODUCTION

The growing demand for electrical energy and the excessive use of fossil fuels to generate it by classical methods causing worldwide global warming are considered as the present era problems that have acted governments and policy makers of many countries to solicit their own researchers to find alternative electricity generating techniques without greenhouse gas emissions. Consequently, renewable energy power production systems have acquired a great opportunity as the most effectiveness, free-pollution and sustainable means of electricity generation that can rapidly, reduce atmosphere harming [1].

Among different renewable energy sources, the solar photovoltaic systems presents an emergent technology which is remarkably, getting popular all over the world as it is considered a noiseless and inexhaustible mean of electric production with less maintenance requirement [2]. Today, photovoltaic installations have became the most prevalent electrical generation system due to the decreasing price of photovoltaic modules and also rising cost of conventional electricity because of acute oil crisis [3]. Recently, the photovoltaic generation technology is getting more maturity, whereas, it was confined only on autonomous mode in remote areas with relatively high investment cost due to high prices of energy storage equipments. Hence, photovoltaic technology has surpassed this limit to invade grid-connected distributed applications especially with growing evolution in electronic power technology. At present, photovoltaic grid-connected systems are more dominant and largely practical than conventional stand-alone applications and approximately covers 75% of the photovoltaic systems installed around the world [4, 5].

ISSN 1737-9334

The optimal use of the grid-connected photovoltaic systems depend not only on climatic restrictions, also they depend on technical factors such as production efficiency, reliability and stability. Moreover, from investment view point, to reach the maximum profitability in photovoltaic installation, the system have to be forced to provide its maximum output power during system life-time regardless climatic changes (temperature and solar radiation), Therefore, the use of a DC-DC boost power converter and maximum power point tracking system MPPT are necessary [6]. In case of grid integrated photovoltaic power, the DC-DC boost converter is usually used to rise-up the photovoltaic generated power even grid power level. Furthermore, the photovoltaic power is penetrated into the grid through DC-AC conversion stage to ensure alternative power delivery at the common coupling point (CCP) [7]. However, the main obsession concern such structures is the grid disruption due to the inclusion of electronic switching devices in power transfer process that often causes increasing in reactive power and an asynchronization between grid voltage and current signals. That's why in this work, we focused heavily on improvement of the grid power quality basing on quasi removed reactive power. the principle of the control strategy consists firstly of the DC link voltage control using boost converter based Perturb and Observe (P&O) algorithm which offers better performances in terms of both rapidity of transient responses and stability against weather changes. Secondly, the control of the inverter switch gates is based on grid current control in dq Park synchronous frame to regulate independently grid power using quadrature component $\boldsymbol{I_q}$ to control reactive power until extinction, while the direct component $\boldsymbol{I_d}$ controls the active power. And finally, a three phase looked loop is employed to adjust grid frequency and eliminate the synchronization problem.

II. System Description

The proposed system is composed of two energy sources that we have considered which are a primary source characterizing conventional power initially delivered to the grid which could be turbo-generator, diesel generator or gas electric power station. Otherwise, the secondary source is a photovoltaic power plant composed of a definite number of photovoltaic panels connected in a manner providing the desired power. Also, a power condition unity is introduced and is formed of two power conversion stages, a boost and three phase voltage inverter converter for photovoltaic step-up power and AC power transformation, respectively. Ultimately, a control unity is designed and contains three control subunits for MPPT, power control and synchronization.

A. Photovoltaic Power Source Model

The photovoltaic power plant is mainly based an elementary photovoltaic cells. Since photovoltaic cells are an extremely weak electric generators of power rang limited between 1 to 3 Watts and maximum voltage rate of 1 Volt [8], the use of cells directly can't be feasible in such applications. Hence, a serial and parallel connected unities have to be realized to form panels which are also combined one to the other to form arrays and plants to achieve the desired power level.

Typically, a photovoltaic solar cell is modeled as shown in electrical equivalent circuit of Fig. 1. It consists a current source presenting the photo-electric current, an inverted mounted diode expresses the P-N junction, and also serial and parallel resistances (R_s , R_p) describe electrons flow hindrance and leakage current, respectively [9].

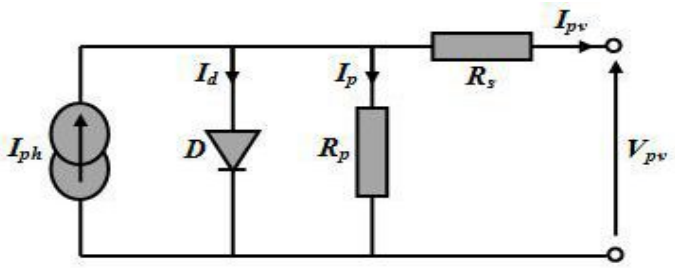

Fig. 1 Electrical equivalent circuit of photovoltaic solar cell

According to the circuit shown above, the formulation of the cell's generated current is given by [10, 11]:

$$I_{pv} = I_{ph} - I_d - I_p \tag{1}$$

With;

$$I_{ph} = \left[I_{sc} + K_0\left(T_o - T_s\right)\right] \cdot {G_o}/{G_s} \tag{2}$$

$$I_d = I_o \cdot \left(e^{\frac{V_{pv}+I_{pv}R_s}{n \cdot B \cdot T_o}} - 1 \right) \tag{3}$$

where,

I_{sc}: Short-circuit current;
K_0: Empiric current/temperature coefficient;
n: Diode's ideality factor (comprises between 1 and 2)
B: Boltzmann constant (1,38 . 10^{-23} j/K);
T_o,T_s: Operating and standard temperature;
G_o,G_s: Operating and standard solar radiation.

Hence, by substituting (2) and (3) in (1), it's obviously that the resulted current and voltage are strongly correlated with the ambient temperature and solar radiation as depict the I-V and P-V curves in Fig. 2 and Fig. 3 where the augmentation in sun irradiance level increases the generated power. However, the increment of temperature decreases cell's output power. Thereafter, to operate in independence of these factors an MPPT control have to be added to achieve the max-efficiency of the cell.

ISSN 1737-9334

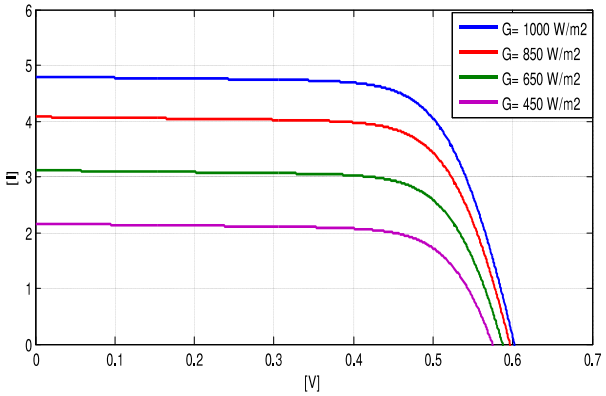

Fig. 2 I=f(V) solar cell characteristics

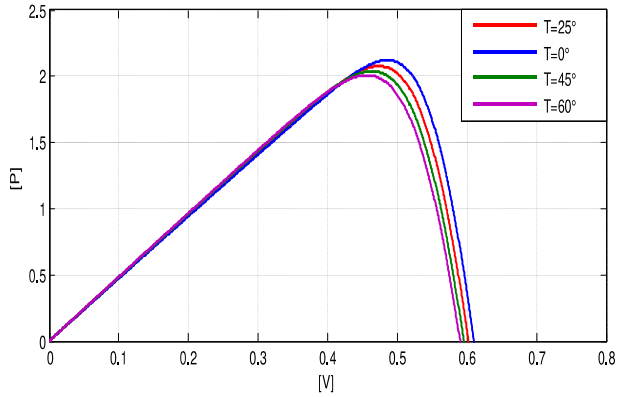

Fig. 3 P=f(V) solar cell characteristics

B. *Boost and MPPT Control Design*

A DC-DC power boost converter converts an input DC level voltage to another output higher level. As illustrated in Fig. 4, the power boost converter is composed of a static IGBT switch with an inverted diode and passive elements which are resistance, an entry and exit capacitors (C_{in} , C_{out}) and inductor. Indeed, two states are possible during its operation, ON state and OFF state that are depend on the IGBT dealing.

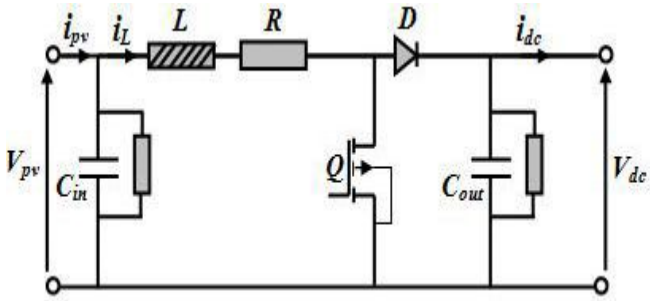

Fig. 4 Power boost converter diagram

The boost output voltage and current are depending to IGBT switching frequency characterized the duty ratio (D) according to below expressions [12]:

$$C_{in}\frac{dV_{pv}}{dt} = i_{pv} - i_L \tag{4}$$

$$(1-D)\cdot V_{dc} = V_{pv} - L\frac{di_L}{dt} \tag{5}$$

$$(1-D)\cdot i_L = C_{out}\frac{dV_{dc}}{dt} - i_{dc} \tag{6}$$

Concerning the duty ratio state, it can be defined instantaneously using MPPT control technique. Many papers have implemented numerous MPPT control strategies. In this work, we used the Incremental Conductance method (INC) which is widely preferred due to its rapidity and accuracy response against sudden variations and step changes in solar radiation when compared for example, to its rival the Perturb and Observe method (P&O) [13]. As called, the INC MPPT method is based on the PV array's incremental conductance (dI_{pv}/dV_{pv}) to extract the (dP_{pv}/dV_{pv}) sign. In Fig. 5, an explanatory INC control algorithm is presented. Frugally, the algorithm searches for the point in which the dI_{pv}/dV_{pv} equals and in opposition with I_{pv}/V_{pv}, (dI_{pv}/dV_{pv} = - I_{pv}/V_{pv}), the algorithm detects this point that matches dP_{pv}/dV_{pv} = 0 and means that the maximum power value is reached [14].

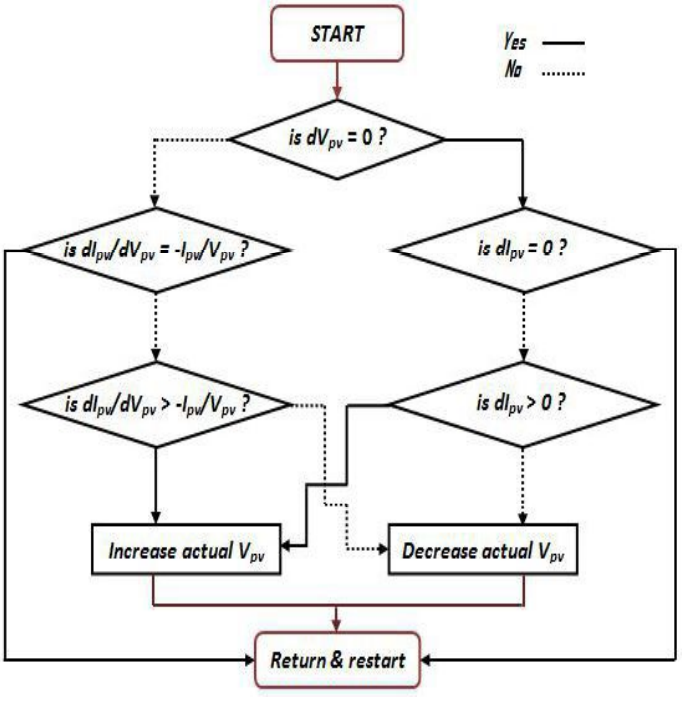

Fig. 5 Flow chart of Incremental Conductance control algorithm

ISSN 1737-9334

C. Grid side and AC part model

The grid side part of the proposed system shown by Fig. 6 consists a three-phase grid lines and a two-level three-phase DC-AC *PWM* inverter linked through *RL* filter for current filtering. Although, the galvanic isolation transformer have no effect from modeling standpoint.

The output voltages of the DC-AC inverter are modeled in function of the DC link voltage and upper switches states (S_1, S_2 and S_3) by the following equation system [15]:

$$\begin{cases} V_{1i} = 1/3\left(2\,V_N\,S_1 - V_N\,S_2 - V_N\,S_3\right) \\ V_{2i} = 1/3\left(-V_N\,S_1 + 2\,V_N\,S_2 - V_N\,S_3\right) \\ V_{3i} = 1/3\left(-V_N\,S_1 - V_N\,S_2 + 2\,V_N\,S_3\right) \end{cases} \quad (7)$$

Where V_N is the DC voltage relative to the fictitious midpoint of the inverter defined as $V_N = 1/2V_{dc}$. Whereas the switch states S_i values are considered either 1 or 0 for ON state and OFF state, respectively.

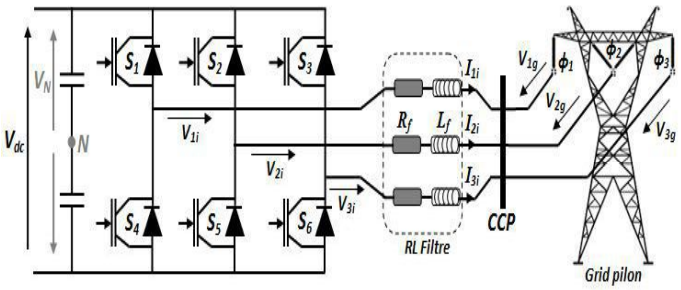

Fig. 6 Grid side and AC part diagram

Thus, the grid per phase voltages are denoted relatively to grid neutral point and are expressed by the following formula:

$$\begin{cases} V_{1g} = V_{mg}\,\cos\left(\omega_g\,t\right) \\ V_{2g} = V_{mg}\,\cos\left(\omega_g\,t - 2\pi/3\right) \\ V_{3g} = V_{mg}\,\cos\left(\omega_g\,t - 4\pi/3\right) \end{cases} \quad (8)$$

III. Control Systems Description

A. Phase and Frequency Control Loop Design

The grid coupling with photovoltaic sources via power electronics components, In particular, boost converter and inverters is often caused a phase and frequency imbalance in grid side between voltage and current signals. Here is reflected the inevitability of phase and frequency control loop (PFCL) in such installations. The main task of the PFCL in the proposed system is presented by Fig. 7, mainly, it's used to detect instantaneously the grid phase using grid voltage measurement, and therefore, the frequency is obtained inasmuch as: $\theta_g = \omega_g\,t = 2\,\pi\,f_g\,t$ [16].

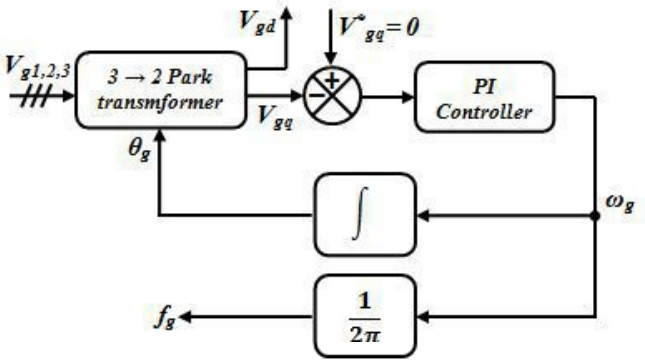

Fig. 7 PFCL schematic diagram

The operating principle of the PFCL is based on *dq* Park asynchronous reference frame transformation of the grid voltage. Thence, the quadrature component V_{gq} is forced at zero using proportional-integral (PI) controller. Then, the obtained output is an angular frequency ω_g which can be transformed either to natural frequency f_g or to phase angle θ_g to be used in *dq* Park transformation matrix defined by [17]:

$$[P] = \begin{bmatrix} \cos\theta_g & \cos\left(\theta_g - \frac{2\pi}{3}\right) & \cos\left(\theta_g + \frac{2\pi}{3}\right) \\ -\sin\theta_g & -\sin\left(\theta_g - \frac{2\pi}{3}\right) & -\sin\left(\theta_g + \frac{2\pi}{3}\right) \end{bmatrix}$$

B. Grid Voltage Control and Power Decoupling

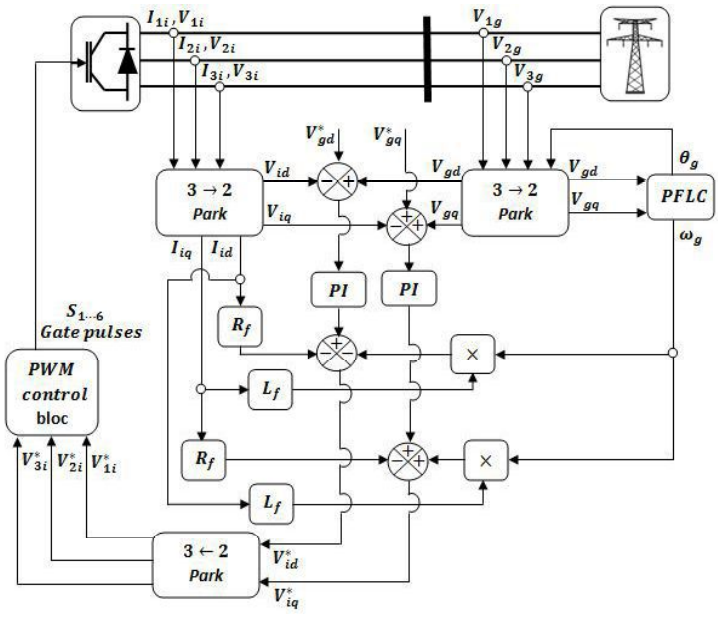

Fig. 8 Diagram of the grid side voltage control

ISSN 1737-9334

Regarding Kirchhoff principle laws applied on each grid phase branches of the system presented on Fig. 6, the grid voltage can be expressed in function of inverter's voltage and injected currents in the following forme:

$$\begin{cases} V_{1g} = V_{1i} - R_f\, I_{1i} - L_f \dfrac{dI_{1i}}{dt} \\ V_{2g} = V_{2i} - R_f\, I_{2i} - L_f \dfrac{dI_{2i}}{dt} \\ V_{3g} = V_{3i} - R_f\, I_{3i} - L_f \dfrac{dI_{3i}}{dt} \end{cases} \quad (9)$$

With reference to the *dq* Park transformation matrix defined previously, the mathematical model of the proposed system can be denoted in *dq* forme as follow:

$$\begin{cases} V_{gd} = L_f \dfrac{dI_{id}}{dt} + R_f\, I_{id} + \omega_g\, L_f\, I_{iq} - V_{id} \\ V_{gq} = L_f \dfrac{dI_{iq}}{dt} + R_f\, I_{iq} - \omega_g\, L_f\, I_{id} - V_{iq} \end{cases} \quad (10)$$

As can be seen in Fig. 8, the grid voltage control structure requires two PI controllers, while the first is intended for d-axis voltage control, the other controller is used to control the q-axis control. Likewise, the feed-forward and feed-back terms $+\omega_g\, L_f\, I_{iq}$ and $-\omega_g\, L_f\, I_{id}$ are introduced for grid current control. Therefore, the *d* and *q* voltage control components are decoupled. So, the new formulation of the *dq* grid voltage under PI control by:

$$\begin{cases} \left(Kp + \dfrac{Ki}{S}\right)\left(V_{gd} - V_{id}\right) = -L_f \dfrac{dI_{id}}{dt} - R_f\, I_{id} - \omega_g\, L_f\, I_{iq} \\ \left(Kp + \dfrac{Ki}{S}\right)\left(V_{gq} - V_{iq}\right) = \omega_g\, L_f\, I_{id} - L_f \dfrac{dI_{iq}}{dt} - R_f\, I_{iq} \end{cases} \quad (11)$$

whereupon, the PI output voltage signal is transferred to the inverter PWM control bloc.

on the other side, since the active and reactive powers are an important quantities in consumer delivered grid energy quality in which their coupling is often influence the power factor $cos\ \theta_g$, a simple PQ control is added to the system in order to ensure a separate relation in P and Q grid powers defined by [18]:

$$\begin{cases} P = V_{gd}\, I_{id} + V_{gq}\, I_{iq} \\ Q = V_{gq} I_{id} - V_{gd}\, I_{iq} \end{cases} \quad (12)$$

In this case, to get a decoupled powers, the *d* grid voltage is steadied at zero value and this ensures a semi-unscrewed PQ relation. Then for total powers dismantle, the *d* current is also forced at zero.

IV. Simulation Results and Discussion

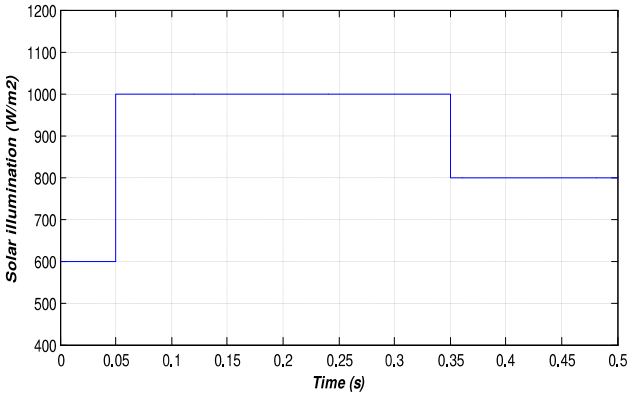

Fig. 9 Solar illumination level

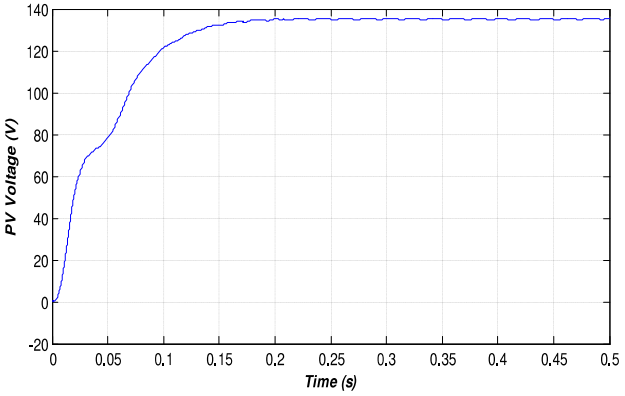

Fig. 10 Output PV voltage

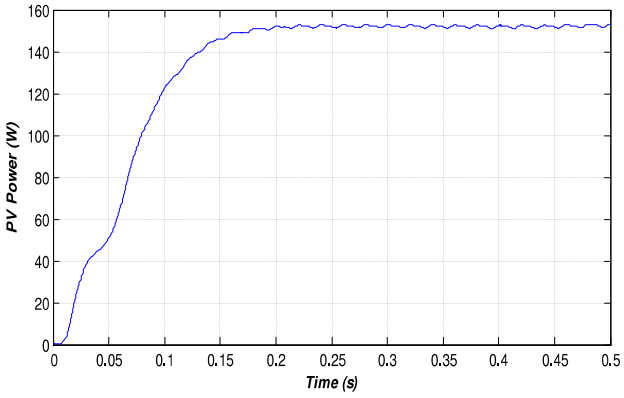

Fig. 11 PV delivered power

In order to test the dynamic response of the elaborated INC MPPT control, the system is simulated for three levels of solar illumination as depicted in Fig. 9. The system has initially started with 600 W/m^2 solar irradiance. Hence, the PV generation system starts instantaneously and quickly to

ISSN 1737-9334

deliver voltage and power as shown by Fig. 10 and Fig. 11, respectively. Then, for a considerable augmentation of solar irradiance in 0.05s (400W/m^2 added), the system has reacted rapidly with this augmentation and has provided an added power until its maximum possible delivery power estimated on 150 Watts approximately. Then, for more credibility of the used MPPT technique, another variation has been carried by the system where, in spite of a 200 W/m^2 decreased in solar illumination level at 0.35s, the PV generator kept delivering the maximum power except few limited oscillations.

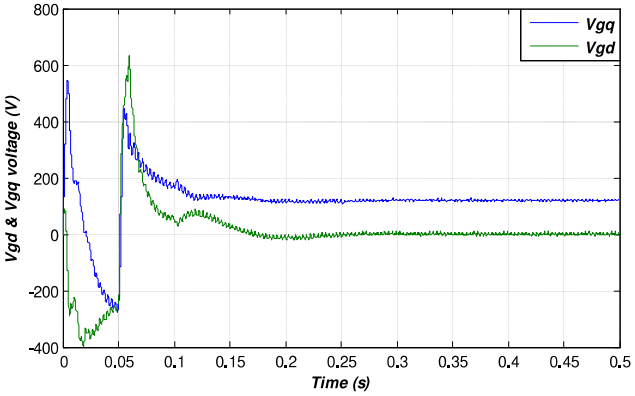

Fig. 12 Direct and quadratic grid control voltages

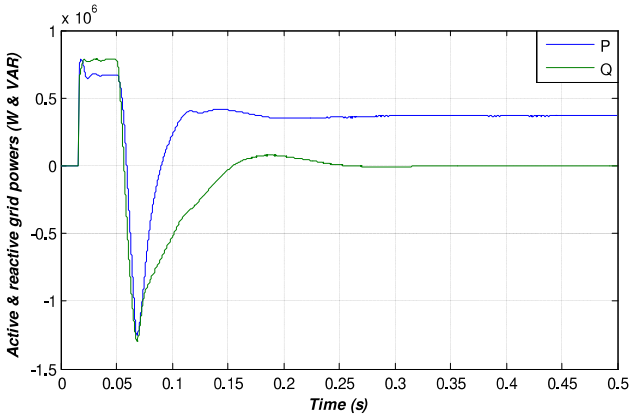

Fig. 13 Active and reactive power

Fig. 12 presents the direct and quadratic grid control voltage which have used to control grid power quality and synchronism between the different system signals. As seen in Fig. 13, the grid power quality has been affected by solar irradiance variation, a down sudden peak is appears, then, after a transient phase and after that the active power have been increased and tracks the quadratic control voltage V_{gq} however the reactive power have been over compensated as its control signal V_{gd} which have been quasi removed.

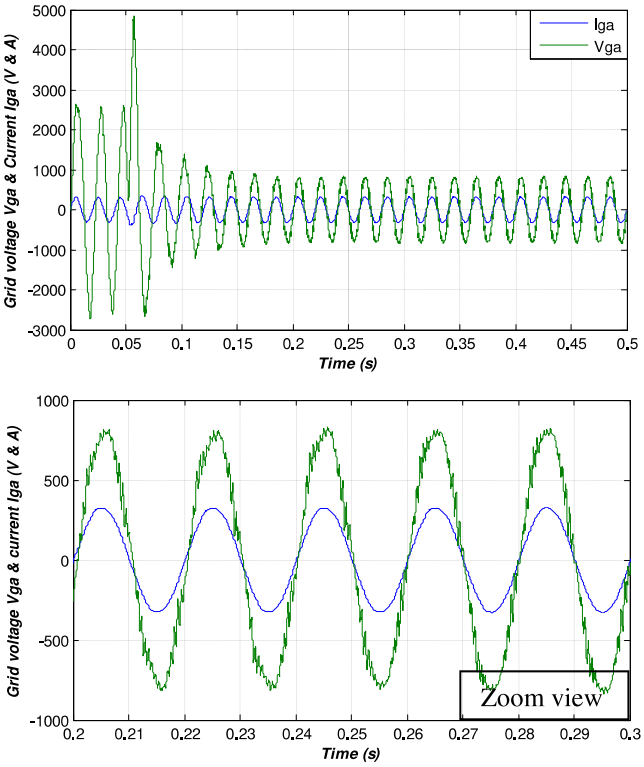

Fig. 14 Grid voltage and current signals

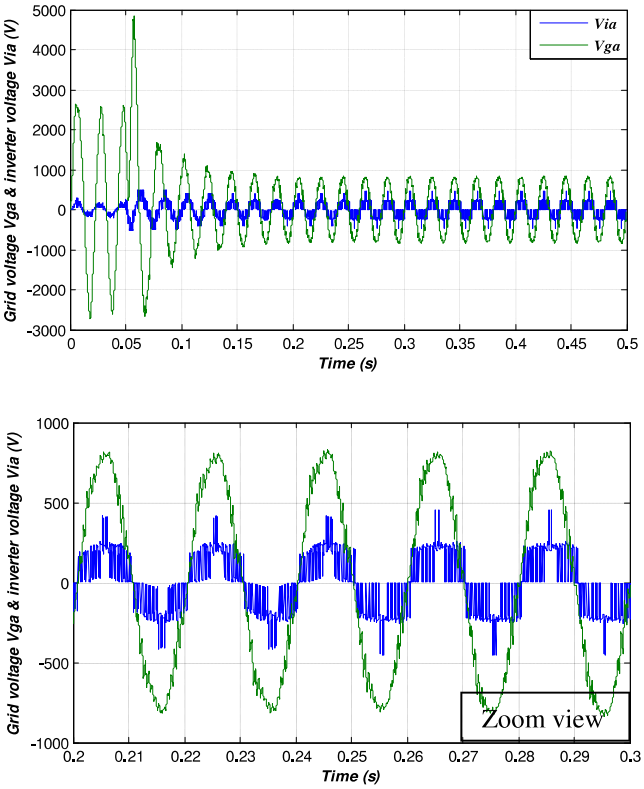

Fig. 15 Grid voltage and inverter voltage signals

ISSN 1737-9334

To investigate the credibility of the phase and frequency loop control (PFLC) in the proposed structure, the grid voltage and current have been superimposed in one pad in Fig. 14. As remarked, at the beginning of the system operating, the synchronisation is disturbed because of the PV injected power via electronic devices such as the boost converter and the inverter. But, during 0.2 seconds the grid has regained phase balance as presented in zoom view. Also, Fig. 15 presents the grid voltage and inverter voltage which have been also unbalanced at first time, then , they have been synchronised in 0.2 seconds too and this investigates the massive role of the phase and frequency control loop to keep synchronisation in such systems.

V. CONCLUSIONS

The presented work involved the necessity of maximum power point control strategy in grid connected systems to ensure max-power delivering where the incremental conductance strategy that we have used in this paper proven merit. Furthermore, the voltage control of a grid connected photovoltaic system that we have applied has verified its effectiveness for grid power enhancement in either decoupling powers or reactive power compensation. Also, the importance of phase and frequency control is proved since the PV grid power injection causes an unsteadiness in grid side and common coupling point (CCP).

REFERENCES

[1] N. Patel, N. Gupta, A. Kumar, A. Kumar Verma, "Multifunctional grid interactive solar photovoltaic systems: A comprehensive review," *International Journal of Renewable Energy Research*, vol. 8, no. 4, pp. 2116-2130, Dec. 2018.

[2] (November 2014) International Energy Agency. World Energy Outlook 2014 [online]. Available: http://www.iea.org/bookshop/477-World_Energy_Outlook_2014.

[3] Y. T. Tan, D. S. Kirschen, and N. Jenkins, "Impact of a large penetration of photovoltaics on the power system," *In Proc. of CIRED 17th International Conference on Electricity Distribution*, 2003.

[4] D. C. Martins, "Analysis of a three-phase grid-connected PV power system using a modified dual-stage inverter," *ISRN Renewable Energy,* vol. 2013, 2013.

[5] Q. N. Trinh, H. H. Lee, "An enhanced grid current compensator for grid-connected distributed generation under non linear loads and grid voltage distortion," *IEEE Transactions on Industrial Electronics*, vol.61, no. 12, pp. 6528-6537, Dec. 2014.

[6] Satyaranjan Jena; B.Chitti Babu; S.R.Samantaray and Mohamayee Mohapatra, "Comparative study between adaptive hysteresis and svpwm current control for grid-connected inverter system," *Proceedings Of IEEE Students' Technology Symposium*, pp. 310-315, Jan. 2011.

[7] M. A. Özçelik, A. S. Yilmaz, "Improving the incremental conductance algorithm for two-stage grid-connected photovoltaic systems," *Turkish Journal of Electrical Engineering & Computer Sciences*, vol. 26, no. 1, pp. 442-453, 2018.

[8] A. Zerga, F. Benyarou, B. Benyousef, "Optimisation du rendement d'une cellule solaire N+P au silicium monocristallin," *Revue des Energies Renouvelables*, pp. 95-100, 1998.

[9] G. K. SINGH, "Solar power generation by PV (photovoltaic) technology" A review. *Energy*, vol. 53, pp. 1-13, 2013.

[10] P. Ghosh, P. K. Kundu, "Modeling and simulation of solar cell using embedded matlab simulink tool," *International Journal of Electronics, Electrical and Computational System,* vol. 6, no. 7, pp. 101-114, Jul. 2017.

[11] R. Hegazy, "Performance of incremental resistance mppt based proton exchange membrane fuel cell power system," *Eighteenth International Middle East Power Systems Conference, IEEE*, pp. 199-205, 2016.

[12] G. Esmaili, "Application of advanced power electronics in renewable energy sources and Hybrid generating systems," *Doctoral dissertation*, Ohio State University, 2006.

[13] K. H. Hussein, I. Muta, T. Hoshino, M. Osakada, "Maximum photovoltaic power tracking: an algorithm for rapidly changing atmospheric conditions," *IEE Proceedings on Generation, Transmission and Distribution*, vol. 142, no. 1, pp. 59-64, Jan. 1995.

[14] A. Kumar, M. Kumar, D. H. Nagaraj, A. Singh, J. Prattapati, "Implementation of MPPT Algorithm for Grid Connected PV Module with IC and P&O Method," *International Journal of Electrical, Computer, Energetic, Electronic and Communication Engineering*, vol. 8, no. 7, pp. 1201-1208, 2014.

[15] A. Borni, T. Abdelkrim, N. Bouarroudj, A. Bouchakour, L. Zaghba, A. Lakhdari, L. Zarour," Optimized MPPT controllers using GA for grid connected photovoltaic systems, comparative study," *Energy Procedia*, vol. 119, pp. 278-296, 2017.

[16] S. Golestan, M. Monfared, F. D. Freijedo, J. M. Guerrero," Performance improvement of a prefiltered synchronous-reference-frame PLL by using a PID type loop filter," *IEEE Transactions on Industrial Electronics*, vol. 61, no. 7, pp. 3469-3479, Jul. 2014.

[17] C. Khomsi, M. Bouzid, K. Jelassi, "Power quality improvement in a three-phase grid tied photovoltaic system supplying unbalanced and nonlinear loads," *International Journal Of Renewable Energy Research*, Vol. 8, no. 2, Jun. 2018

[18] Z. CEN, "Modeling and simulation for an 8 kW three-phase grid-connected photo-voltaic power system," *Open Physics*, vol. 15, no 1, pp. 603-612, 2017.

ISSN 1737-9334

Pattern Reconfigurable Antenna with four Switchable Beams in Azimuth Plane

FAOUZI RAHMANI[#1], N. AMAR TOUHAMI[#1], A. BELBACHIR KCHAIRI[#2], NIHADE TAHER[#3]

[1]*Laboratory of Information Systems & Telecommunications, Faculty of Sciences of Tetouan, Abdelmalek Essaadi University, Tetouan, 93030, Morocco*

[2] *LEEA&TI, Faculty of Sciences and Techniques of Mohammedia, Hassan II University, Mohammedia, 28806, Morocco*

[3]*Laboratory Advanced Sciences and Technologies, National School of Applied Sciences, Abdelmalek Essaadi University, Tetouan, 93030, Morocco*

[1]mr.faouzi.rahmani@gmail.com

***Abstract*— This work presents a square planar antenna with reconfigurable radiation pattern using parasitic patches. The antenna achieves four-state pattern reconfigurability by controlling the on and off of four PIN diodes to change the direction. The mode change is made using the PIN diodes connected in the gap between the central square patch and the parasitic patches. A short circuit or an open circuit can be provided by this gap. The antenna has a bandwidth of 5.71-5.89 GHz and is capable of steering the beam in the direction 0°, 360° in the azimuthal plane. Meanwhile, the antenna works at four states with the same band. The goal is to provide wider coverage by redirecting the main lobe and controlling the main beam directions. Simulated results are also shown and discussed.**

***Keywords*— Reconfigurable antenna, Square planar antenna, PIN diode, Radiation pattern**

I. INTRODUCTION

With the rapid development of wireless communication systems, the design of reconfigurable antennas has gained a lot of attention due to its flexibility in frequency selection, pattern reconfiguration, and polarization selectivity. This makes it highly suitable for different wireless communication systems, such as intelligent transportation system (ITS) (e.g. [1]–[3]).

The radiation pattern reconfigurable antenna at the same operating frequency has received considerable attention in recent years. By different approaches this antenna concept can be obtained, such as, varactor diodes, radio-frequency micro-electromechanical systems (RF-MEMSs), field effect transistors (FETs) and PIN diodes (e.g. [3]–[8]). The PIN diodes are very reliable since there are no moving parts and are extremely low cost. Patch antenna can be integrated easily with PIN diode switches to form reconfigurable patch antennas (e.g. [9]–[13]). The effect of the PIN diode intrinsic resistance for antenna gain: The simulated gain variations depending on the PIN-diode intrinsic resistance (R) for the State 3 (e.g. Table II) are plotted in Fig.3. The antenna gains decreases when the resistance of the PIN-diode increases from 0 (ideal) to 3Ω.

In this paper, we propose a square planar antenna with reconfigurable radiation pattern using parasitic patches. The radiation pattern of the proposed antenna can be changed into four states using four micro-semi MPP4203 PIN diodes (e. g. [11]). The designed antenna operates at about 5.71GHz and 5.89 GHz frequencies. In this work, a new reconfigurable radiation pattern antenna using a central square patch and four parasitic patches is presented, studied and simulated.

II. ANTENNA DESIGN

A. *Geometry of the proposed antenna*

The proposed antenna consists of a central square patch and four parasitic patches graved on the Rogers RT5880 substrate (dielectric permittivity constant of 2.2, dielectric loss tangent of 0,0009). The first (red area) part is a square-shaped patch located at the center of the proposed antenna for connecting a 50Ω coaxial cable. The second (yellow area) parts are four fan-shaped radiation cells, which distribute around the antenna center symmetrically.

The size of the substrate which has the circular shape is (Ø×H) = (90mm×1.57mm). The parasitic patches are connected to the central square patch using four PIN diodes in the gap between them (with the width $W_a = 0.4mm$). After many series of optimization using the CST simulator, the final geometry of the proposed antenna is shown below in Fig.1.The final optimized values for the parameters of the proposed pattern reconfigurable antenna are given in Table I.

B. *Design parameters*

The geometrical parameters which affect the antenna performance will be analyzed to derive some design rules. The simulation results are obtained when the antenna operates in state 3 (e.g. Table II). This study gives the same results for the other operation states.

1) *The effect of the angle β*

The antenna reflection coefficient and gain are simulated with variations values of the angle (β) and keeping other dimensions fixed, except the parameter A, are plotted in Fig.2.

ISSN 1737-9334

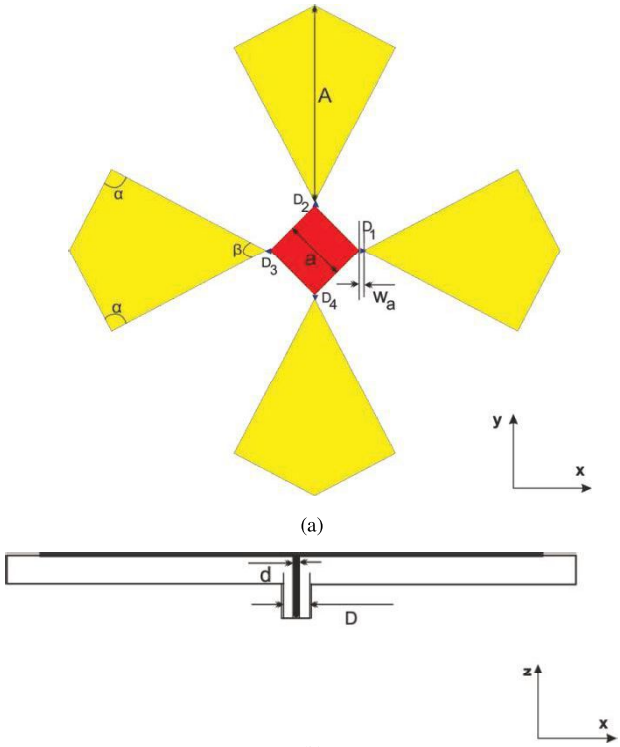

(a)

(b)

Fig. 1 Geometry of the proposed reconfigurable antenna: (a) Top view, (b) side view

TABLE I
DIMENSIONS OF THE PROPOSED ANTENNA

Parameter	Dimension
A	18.6 mm
a	6 mm
W_a	0.4 mm
α	90°
β	57.4°
D	4.1 mm
d	1.2 mm

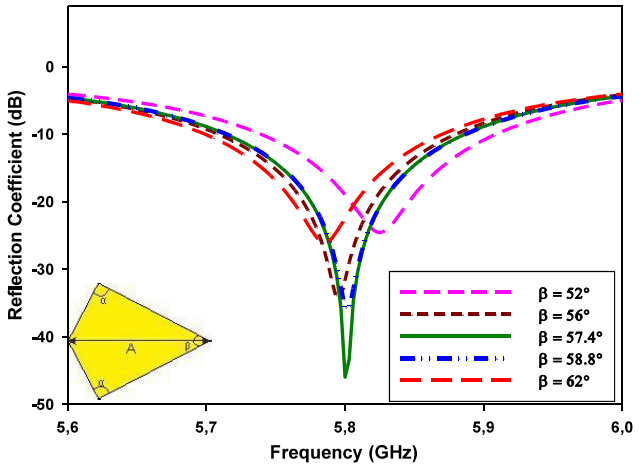

(a)

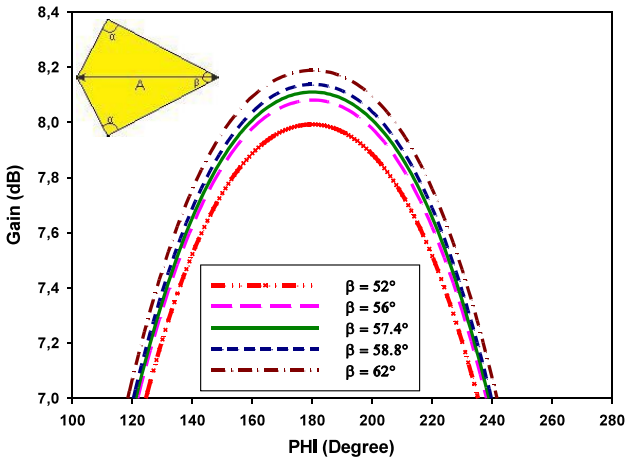

(b)

Fig. 2 Simulated Reflection coefficient and antenna gain versus angle β: (a) Reflection coefficient, (b) gain

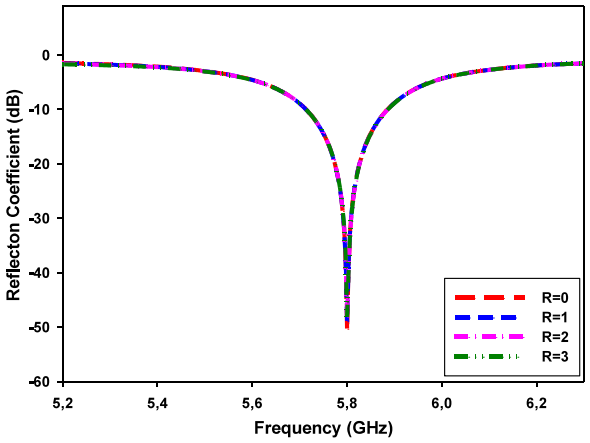

(a)

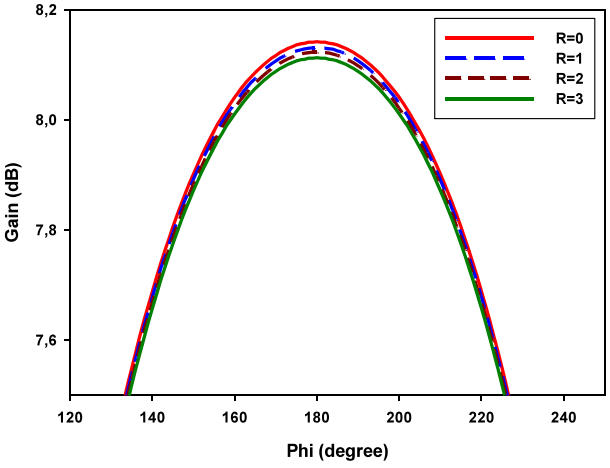

(b)

Fig. 3 Simulated Reflection coefficient and antenna gain depending on the PIN-diode intrinsic resistance: (a) Reflection coefficient, (b) gain

ISSN 1737-9334

It can be seen that the impedance bandwidth of the proposed antenna remains stable and that the frequency resonances are shifted. When β = 57.4°, the antenna becomes more adapted (e.g. Fig. 2-a). The antenna gain increases when the angle B value increases from 52° to 62° (e.g. Fig. 2-b).

2) The effect of the PIN diode intrinsic resistance

The antenna gain and reflection coefficient are also simulated with variations of the PIN-diode's resistance (R) in Fig. 3. The impedance bandwidth of the proposed antenna and the frequency resonances remain stable (e.g. Fig. 3-a). While the antenna gains decreases when the resistance of the PIN-diode increases from 0 (ideal) to 3Ω (e.g. Fig. 3-b).

III. OPERATION AND RESULTS

A. *Equivalent circuit model of PIN diodes*

Based on the PIN diode biasing, the different fan-shaped radiating elements of the antenna can be selectively powered by the square patch (e.g. Fig.1). Based on the equivalent circuit model shown in Fig.4, a series of simulations were performed (e.g. Table II).

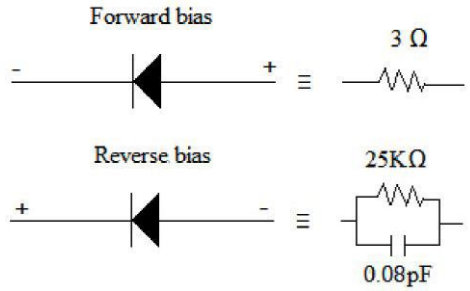

Fig. 4 Equivalent linear circuit for PIN diode in the ON state (forward bias) and OFF state (reverse bias) (e. g. [9]- [10])

The equivalent linear circuit of a PIN diode is shown in Figure 4. In this work, the states ON and OFF of the PIN diodes are replaced by a resistance of 3 Ω and a resistance of 25 KΩ in parallel with a capacitor of 0.08 pF, respectively (e. g. [11]).

B. *Radiation Pattern Reconfigurability*

In our study, the development of the proposed pattern reconfigurable antenna is achieved to find the optimized geometric parameters (e.g. Table I). With controlling the states of the PIN diodes, the distribution of the antenna surface current will be changed; this will deflect the direction of the antenna radiation. It shows that the proposed antenna has four operating states named as S1, S2, S3 and S4. Table II shows specific biasing requirement for these four states.

TABLE II
OPERATING STATES OF THE PROPOSED ANTENNA

Parameters		State 1	State 2	State 3	State 4
PIN diodes states	D_1	OF	ON	ON	ON
	D_2	ON	OF	ON	ON
	D_3	ON	ON	OF	ON
	D_4	ON	ON	ON	OF
Resonance frequency		5.8 GHz	5.8 GHz	5.8 GHz	5.8 GHz
Frequency band (GHz)		5.71-5.89	5.71-5.89	5.71-5.89	5.71-5.89
Beam Direction		0°	90°	180°	270°
Gain (dB)		8.11	8.11	8.11	8.11

The reflection coefficient S11 of the proposed reconfigurable antenna is displayed in the Fig. 5. The simulation results show that the antenna resonance frequencies are stable at ≈ 5.8GHz. The simulated -10 dB impedance bandwidth covers 5.71-5.89 GHz.

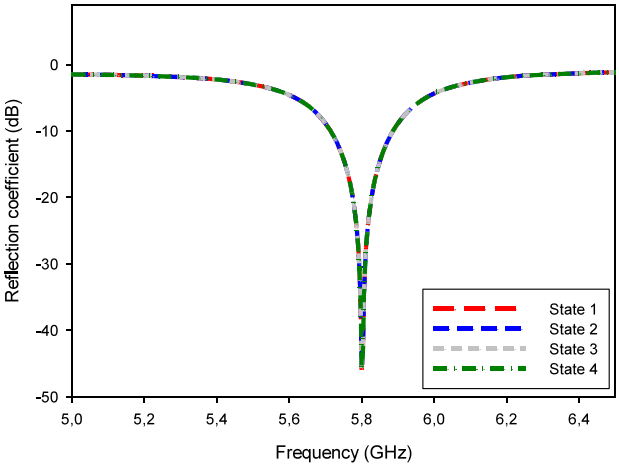

Fig. 5 Reflection Coefficient for different operating modes

When the operating states of the proposed reconfigurable radiation pattern antenna move sequentially, the direction of the main radiation beam can rotate from 0° (state 1) to 270° (state 4) in the azimuth plane (Fig. 6) with step increment of 90°.

- The direction of the main radiation beam of state 2 rotated by 90° compared to state 1.
- The direction of the main radiation beam of state 3 rotated by 180° compared to state 1.
- The direction of the main radiation beam of state 4 rotated by 270° compared to state 1.

The radiation beam directions in elevation plane of the proposed antenna for different operation states are stable at about 20° (e.g. Fig.7).

ISSN 1737-9334

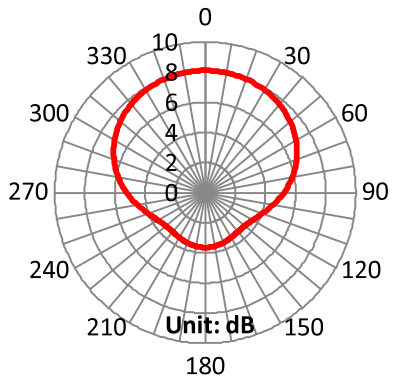

(a)

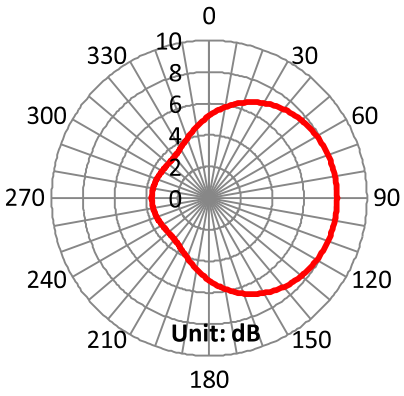

(b)

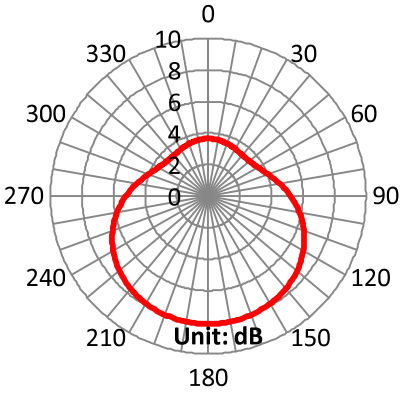

(c)

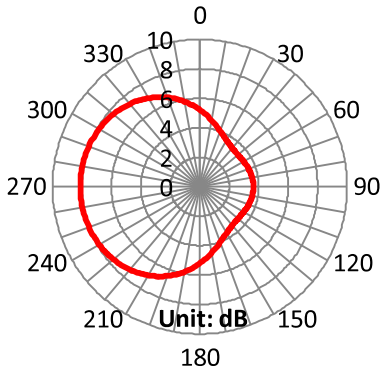

(d)

Fig. 6 Simulated radiation patterns for different operation states: (a) state 1, (b) state 2, (c) state 3, (d) state 4

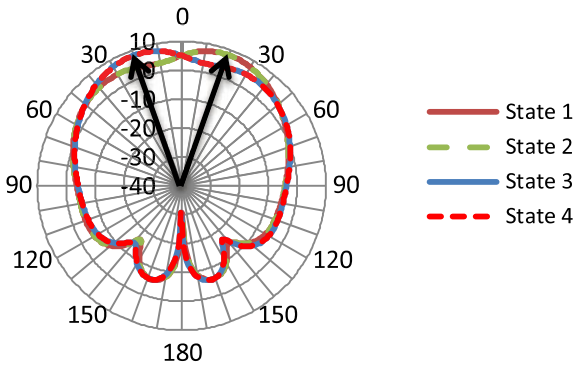

Fig. 7 Simulated 2-D radiation patterns in elevation plane

TABLE III
COMPARISON OF THE PROPOSED PATTERN RECONFIGURABLE ANTENNA AND THE PREVIOUSLY REPORTED DESIGNS

Parameters	**[12]**	**[13]**	**[14]**	**This work**
Antenna Size	$0.48\lambda_0$ ×$0.64\lambda_0$ ×$0.01\lambda_0$	$0{,}55\ \lambda_0$ ×$0{,}55\ \lambda_0$ ×$0{,}04\ \lambda_0$	$1{,}31\ \lambda_0$ ×$1{,}31\ \lambda_0$ ×$0.05\lambda_0$	$1{,}02\ \lambda_0$ ×$1{,}02\ \lambda_0$ ×$0{,}03\ \lambda_0$
No. of States	4	12	4	4
No. of Diodes	4	6	4	4
BW	34%	3%	6,6%	3,1%
Gain (dB)	4	5,1~5,7	2,8~6	8,11
Resonance Frequency (GHz)	2-2,4	4	2,4	5,8
Azimuth plane beam-scanning	180°	360°	360°	360°

λ_0: The free-space wavelength at the center frequency of pass-band.

A comprehensive comparison between the proposed pattern reconfigurable antenna and the previously reported designs is tabulated in Table III. According to the table, the antennas in [12], [14] have wide bandwidth but they have a small gain than this design, and the antenna in [12] covers only 180° in azimuth plane. A reconfigurable radiation pattern microstrip antenna was realized in [13]; nevertheless, its impedance bandwidth was as narrow as about 3%. In this work, the proposed square planar antenna with reconfigurable radiation pattern using parasitic patches covers the whole azimuth plane (360°). The simulated antenna gain across the band (5.71GHz - 5.89 GHz) is stable at 8.11 dB.

IV. Conclusions

In this paper, a square planar antenna with reconfigurable radiation pattern using parasitic patches is simulated and investigated. Based on the PIN diode switches biasing, the proposed reconfigurable antenna can operate at 4 basic different states and achieve radiation pattern reconfigurable characteristic. When the operation state of the proposed planar antenna steer sequentially, the main radiation beam direction can rotate 90 °, from 0° to 270° in azimuth plane. It indicates that this novel antenna can cover the whole azimuth plane.

ISSN 1737-9334

The designed antenna is almost centered on the 5.8GHz frequency with a bandwidth of 180MHz. The proposed reconfigurable antenna operates for IEEE 802.11ac and ETSI EN 300 674 applications.

REFERENCES

[1] Constantine A. Balanis, *Antenna Theory: Analysis and Design*, 3rd ed., Hoboken, New Jersey: John Wiley & Sons, 2005.

[2] Claudia Campolo, Antonella Molinaro, Riccardo Scopigno, Vehicular ad hoc Networks: Standards, Solutions, and Research, Springer, 2015.

[3] Khan, M. S., Iftikhar, A., Capobianco, A.-D., Shubair, R. M., & Ijaz, B. Pattern and frequency reconfiguration of patch antenna using PIN diodes. Microwave and Optical Technology Letters, Vol 59, no 9 2180–2185, Feb. 2017.

[4] Mehta, A., Gautam, S., Goonesinghe, H., Pal, A., Lewis, R., &Clow, N., Planar pattern reconfigurable antenna integrated with a WiFi system for multipath mitigation and sustained high definition video networking in a complex EM environment, IEEE International Symposium on Antennas and Propagation & USNC/URSI National Radio Science Meeting, pp. 2229-2230, Jul. 2015.

[5] Jung, C., Lee, M., Li, G. P., & De Flaviis, F., Reconfigurable Scan-Beam Single-Arm Spiral Antenna Integrated With RF-MEMS Switches, IEEE Transactions on Antennas and Propagation, Vol 54, No 2, pp.455-463, Feb. 2006.

[6] Huff, G. H., & Bernhard, J. T., Integration of Packaged RF MEMS Switches With Radiation Pattern Reconfigurable Square Spiral Microstrip Antennas, IEEE Transactions on Antennas and Propagation, Vol 54, No 2, pp. 464–469, Feb. 2006.

[7] Xiao-Lin Yang, Jian-Cheng Lin, Gang Chen, Fangling Kong. Frequency reconfigurable antenna for wireless communications using GaAs FET switches. IEEE Antennas and Wireless propagation Letters, vol. 14, pp. 807–810, 2015.

[8] Wang, B.Z., S. Xiao, and J. Wang, Reconfigurable patch-antenna design for wideband wireless communication systems, IET Microwaves, Antennas & Propagation, vol. 1, No 2, pp. 414-419, Apr. 2007.

[9] Jong-Hyuk Lim, Gyu-Tae Back, Young-Il Ko, Chang-Wook Song, & Tae-Yeoul Yun. A Reconfigurable PIFA Using a Switchable PIN-Diode and a Fine-Tuning Varactor for USPCS/WCDMA/m-WiMAX/WLAN, IEEE Transactions on Antennas and Propagation, Vol.58, no. 7, pp. 2404–2411, Jul. 2010.

[10] Woong Kang, Seokjae Lee, and Kangwook Kim. A pattern-reconfigurable antenna using PIN diodes, Microwave and Optical Technology Letters. Vol. 53, no 8, pp.1883-1887, Aug. 2011.

[11] Datasheet of MPP4203 PIN Diodes, Microsemi, Application Note [Online]. Available: http://www.microsemi.com.

[12] M.S. Alam, and A.M. Abbosh. Wideband Pattern Reconfigurable Antenna Using Pair of Radial Radiators on Truncated Ground with Switchable Director and Reflector, IEEE Antennas and Wireless Propagation Letters, Vol. 16,pp. 24-28, Dec. 2016.

[13] Wei-Dong MA, Guang-Ming WANG, Ya-Wei WANG, Bin-Feng ZONG. Compact Microstrip Antenna with Pattern-Reconfigurable Characteristic. Radioengineering Lett., Vol. 26, NO. 3, pp. ,662-667, Sep. 2017.

[14] M. S. Alam and A. M. Abbosh, "Beam-steerable planar antenna using circular disc and four PIN-controlled tapered stubs for WiMAX and WLAN applications," *IEEE Antennas Wireless Propag. Lett.,* vol. 15, pp. 980-983, 2016.

ISSN 1737-9334

The accelerometer characteristics improvement

Zine Ghemari
Electrical Engineering Department
University Mohamed Boudiaf, M'sila
BP 166 M'sila 28000, Algeria
ghemari-zine@live.fr

***Abstract*— In this work, The modeling of the vibration sensor is done through the application of Newton's law of motion and the developed model is an equation related to the motion of the seismic mass with the measurement error. This model is validated by simulation and experimental tests.**
The object of developing this model is to improve the characteristics of this sensor and to propose a new design.

***Index Terms*—model, vibration, Sensor, development, simulation, frequency**

I. INTRODUCTION

The maintenance plays a very important role in the industrial sector, most industries applying maintenance policy to reduce or eliminate the unnecessary repairs, to prevent the system failure and to reduce negative impact of maintenance operation on business performance.

Among the maintenance methods, the conditional preventive maintenance is the most used in the various industry organizations for their monitoring and do not require downtime.

Usually the rotating machines in operation generate efforts, caused by the failure of the machine components. To make a correct diagnosis, it is necessary to choose a tool of conditional preventive maintenance (the vibration analysis, the oil analysis, the thermograph ....).

For early detection of machines defects, some measurements and techniques must be performed on the machines in operation (vibration analysis). The individual faults sensed by the vibration analysis technique are: the imbalance shafts, the bad lineage coupled machines, the degradation couplings, the games, the bearing wear and even electrical faults can be detected early to plan an intervention before the failure.

These vibrations are detected using sensor called accelerometer or vibration sensor. Its function is to transform the level of vibration into a time electric signal. The rest of measuring equipments (amplifier, FFT analyzer) convert the time electric signal to a frequency electric signal by signal processing operations using software [1-3] and vibration sensors. These operations are signal generation, signal decomposition and signal spectrum calculation. The purpose of signal conversion from time to frequency domain is to identify the frequencies of vibration [4] and [5].

Several searches were carried out on development of accelerometer and the improvement of its performances [7-10].

The objectives of this work are:

- Proposal for a new model that connects the relative movement according to the measurement error of the vibration sensor.
- Validation of the developed model by simulation and experimental tests.
- Improvement of measurement precision of vibration sensor.

These objectives enable vibration sensor performances improvement of and making it more accurate and reliable.

II. VIBRATION SENSOR

A vibration sensor is a sensor that measures the physical acceleration experienced by an object due to inertial forces or due to mechanical excitation. In aerospace applications accelerometers are used along with gyroscopes for navigation guidance and flight control. Conceptually, an accelerometer behaves as a damped mass on a spring. When the accelerometer experiences acceleration, the mass is displaced and the displacement is then measured to give the acceleration [11-16].

In these devices, piezoelectric, piezoresistive and capacitive techniques are commonly used to convert the mechanical motion into an electrical signal. Piezoelectric accelerometers rely on piezoceramics (e.g. lead zirconate titanate) or single crystals (e.g. quartz, tourmaline) (see figure 1). They are unmatched in terms of their upper frequency range, low packaged weight and high temperature range. Piezoresistive accelerometers are preferred in high shock applications. Capacitive accelerometers performance is superior in low frequency range and they can be operated in servo mode to achieve high stability and linearity. Modern accelerometers are often small micro electro-mechanical systems (MEMS), consisting of little more than a cantilever beam with a proof-mass (also known as seismic-mass) realized in single crystal silicon using surface micromachining or bulk micromachining processes.

ISSN 1737-9334

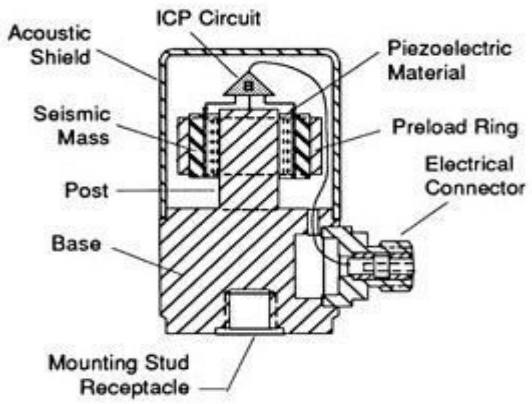

Fig.1. Structure of sensor vibration (accelerometer)

There are several types of sensors to appreciate vibratory movements. The sensitivity of the sensors represents the proportionality of the exploitable electrical output (voltage, load, current) with respect to the vibration parameter (acceleration, speed, displacement). It is expressed in terms of: electrical output / vibration parameter.

III. MODELING THE RELATIVE MOVEMENT ACCORDING TO THE MEASUREMENT ERROR

The modeling is the mathematical presentation of a physical object. In the mathematical model, the inputs and outputs of the process are linked by a sum of mathematical laws. This sum can be represented by algebraic equations, differential equations and recurrent relationships [11].

The development of accelerometer mathematical model is explained in details in ref [11].

The accelerometer is a system composed from a mass, a spring and a damper, defined by m, K and C, respectively Fig. 2.

Where:

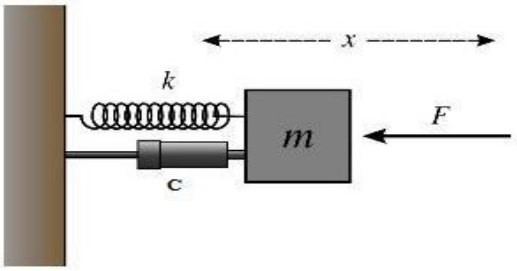

Fig.2. Modeling an accelerometer

The developed model in Ref [11] is validated through a series of simulation and experiments, and is presented in the following two equations.

$$Z = y\,\omega^2 / \omega_n^2\,[(1-(\omega/\omega_n)^2)^2 + (2\zeta\omega/\omega_n)^2]^{1/2} \quad (1)$$

$$E = (\ddot{z}/\ddot{Y}) - 1 = [1/(1-(\omega/\omega_n)^2)^2 + (2\zeta\omega/\omega_n)^2]^{1/2} - 1 \quad (2)$$

Z: sensor relative movement

E: measurement error

Y: amplitude of movement,

ξ: damping rate,

ω_n: sensor natural frequency

ω: relative frequency,

From equations (1) and (2), the following equation is obtained:

$$Z = y\,(E+1).\,\omega^2 / \omega_n^2 \quad (3)$$

This equation shows the new model which links the relative movement as a function of the measurement error of the vibration sensor, in the following; we will validate this model by simulation and experiment tests.

A. Simulation of the relative movement

To simulate the relative movement of equation (1), we take the sensor parameters presented in Table (I):

TABLE I
THE VALUES OF THE SIMULATION PARAMETERS

Input Parameters	Values
Movement amplitude (mm)	0. 15
Damping rate	0.67
Natural frequency (Hz)	100
Relative frequency (Hz)	0, 5, 10, 15, 20, 25, 30

Computer simulations were performed by programs working under Matlab. The obtained results are summarized and illustrated in Fig.3.

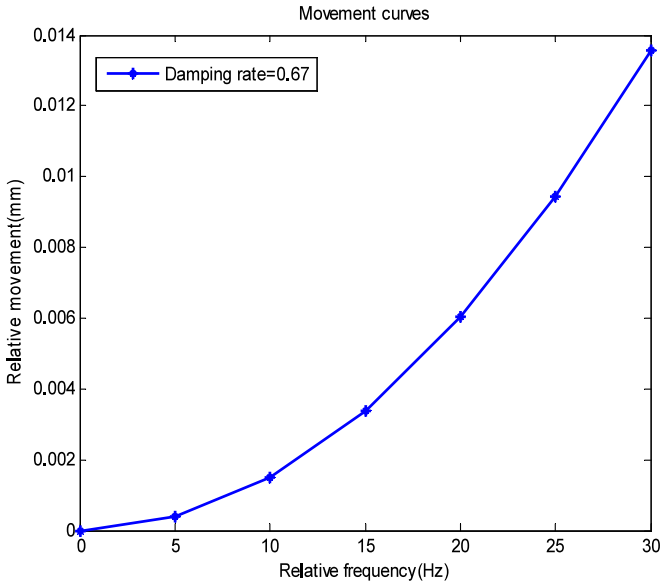

Fig.3. Relative movement modulus of vibration sensor

From the curves shown in Fig. 3, it can be observed that the relative movement Z is increasing and decreasing according to relative frequency ω.

B. Simulation of the measurement error

Measurement error of equation (2) is shown on the curve of Fig.4. The parameters values used for accelerometer measurement error determination are presented in table 1.

ISSN 1737-9334

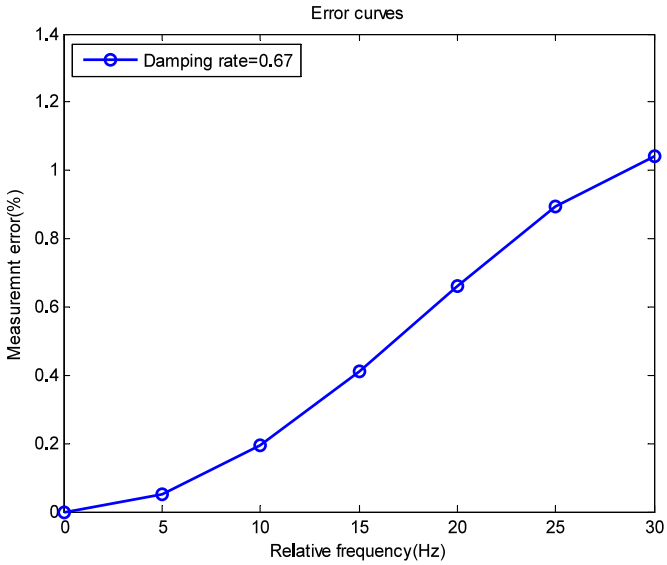

Fig.4. Measurement error of vibration sensor

From the figure (4), we note that the value of the depreciation rate which equals 0.67 minimizes the measurement error and limits it to 1%.

C. Relative movement modulus according to measurement error

The simulation of the relative motion as a function of the measurement error of the vibration sensor is performed by the use of equation (3).

The computer simulation is carried out with data shown in table 1. The obtained results are summarized in Fig.5.

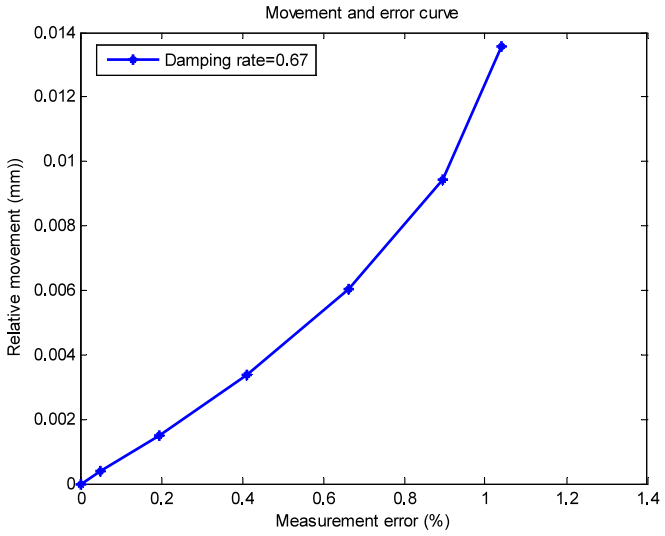

Fig.5. Relative movement according to measurement error

The Fig.5 shows a curve of relative movement as a function of measurement error.

The table 2 shows the simulation results of equations (1) and (2).

TABLE 2
SIMULATION RESULTS OF EQUATIONS (2) AND (3)

Relative freqeancy (Hz)	Z (mm)	Measurement error (E)
0	0	0
5	0.0004	0.0005
10	0.0015	0.0019
15	0.0034	0.0041
20	0.006	0.0066
25	0.0094	0.0089
30	0.0136	0.0104

Figure.5 and Table3 show that the damping rate choice of 0.67 limits the sensor measurement error to a value of 1%, which increases the measurement accuracy and the vibration sensor performances.

IV. EXPERIMENTAL VALIDATION OF NEW MODEL OF RELATIVE MOVEMENT (EQ.3)

The experimental work is carried out using experiment set up represented in blocks as shown in Fig.6. The different values of vibration movement frequency are generated by vibration generator and the values are detected by vibration sensor (accelerometer).

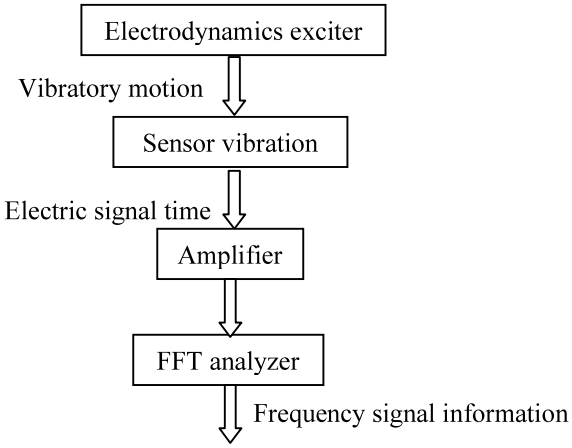

Fig.6. Measurement setup

Vibration is produced by an electrodynamics exciter which has the advantage of maintaining the perturbation, but requires the design of a structure of fixation which may produce incorrect results if it vibrates. In addition, an electrodynamics exciter is often limited to frequencies ranging from 3 to 2000 Hz.

The current (I) flow through an inductance placed in a magnetic field creates a force proportional to the induction. The electrodynamics exciter can generate forces of 10 000 N in a frequency range of 3 to 2000 Hz.

The vibration sensor measures vibration movements generated by a vibrating structure. The vibration sensor used in the

ISSN 1737-9334

experiment is piezoresistive accelerometer and its parameters are: natural frequency is 100 Hz, damping rate is 0.60, mechanical sensitivity is 100 mV /g and finally movement amplitude is 0.015m.

The electrodynamics exciter is adjusted to generate the following relative frequencies: 0, 5, 10, 15, 20, 25, and 30 Hz. The relative movement amplitude (vibration level) is estimated for each frequency value.

The results obtained by experiments and simulation are summarized and presented below (Table 3):

TABLE 3
RESULTS OBTAINED BY EXPERIMENTS

Relative frequency (Hz)	Relative movement Z (mm)	
	Experimental results	Simulation of eq.3
0	0	0
5	0.0004	0.0004
10	0.0012	0.0015
15	0.0036	0.0034
20	0.0056	0.0061
25	0.01	0.0095
30	0.013	0.0138

From the results obtained by experiment tests and simulation (see table.3), it can be concluded that the new model of relative movement is validated experimentally. Since the experimental values of relative movement is closest to the values calculated by the new model.

According to the obtained results, it is found that the developed model makes it possible to optimize the vibration sensor performance by the appropriate choice of the damping rate. The damping rate chosen in our work is 0.67 reduces the measurement error to a value not exceeding 1% and improving the accuracy to a value of 99 %.

VI. CONCLUSION

In this paper, we have developed a new model that relates the relative movement modulus according to the measurement error, which improves some parameters of the vibration sensor.

Simulation and experimental work are carried out in order to determine and validate the new model respectively.

The aim of this work is to improve the performances of vibration sensor by improving its accuracy, sensitivity and loyalty.

The simulation allows presenting graphically the relative movement modulus according to the measurement error and finding the new model.

The results of the experimental work show that the developed model is acceptable and can be used to improve the vibration sensor performances.

Finally, a vibration sensor is developed by finding a new model of relative movement modulus.

In the future work, it is important to investigate the accelerometer reliability to determine vibration level with a great accuracy.

Acknowledgments

The authors like to thank the Algerian general direction of research for their financial support.

REFERENCES

[1] Xinliang . Z, Yonghong. T, Miyong. S ”Modeling of hysteresis in piezoelectric actuators using neural networks” Vol. 23, N. 8, November 2009, PP: 2699 – 2711.

[2] El Hafidi. A, Martin. B, Loredo. A and Jego. E “vibration reduction on city buses; determination of optimal position of engine mounts” Mechanical systems and signal processing, Vol. 24, N. 7, October 2010, PP: 2198 -2209.

[3] Diaz. IM and Reynolds .P “On-Off nonlinear active control of floor vibrations” Mechanical Systems and Signal Processing, Vol. 24, N. 6, August 2010, PP: 1711-1726.

[4] Ghemari. Z and Saad. S, “Development of measurement precision of sensor vibration” Journal of Vibration and Control, Vol.19, No. 10, PP: 1480-1486.

[5] Ghemari. Z and Saad. S “Development of model and enhancement of measurement precision of sensor vibration” IEEE Sensors; Vol. 12, No. 12, Dec 2012, PP: 3454 - 3459.

[6] Peng LI. « Formalisme pour la Supervision des Systèmes Hybrides Multi-Sources de Générateurs d’Energie Répartie : Application à la Gestion d’un Micro Réseau » Thèse de doctorat, Soutenue le 19 juin 2009, Ecole Centrale de Lille, France.

[7] R. Yan , X. Li , Z. Chen, Q. Xu, X. Chen “Improving calibration accuracy of a vibration sensor through a closed loop measurement system” IEEE Instrumentation & Measurement Magazine, Vol.19, No. 1, February 2016, **PP:** 42 – 46.

[8] C. Ma et all “A Continuous Wavelet Transform Based Time Delay Estimation Method for Long Range Fiber Interferometric Vibration Sensor” Journal of Lightwave Technology, Vol.34, No.16, Aug 2016, PP:3785-3789.

[9] T. Li, C. Shi, Y. Tan, R. Li, Z. Zhou, H. Ren“A Diaphragm Type Fiber Bragg Grating Vibration Sensor Based on Transverse Property of Optical Fiber With Temperature Compensation” IEEE Sensors Journal, Vol.17, No.4, Feb 2017, **PP:** 1021 – 1029

[10] R. Ajith et all “Low-Cost Vibration Sensor for Condition-Based Monitoring Manufactured From Polyurethane Foam” IEEE Sensors Letters, Vol.1, No. 6, Dec. 2017.

[11] Z. Ghemari and S. Saad “Piezoresistive Accelerometer Mathematical Model Development with Experimental Validation” IEEE Sensors Journal, 2018, Vol.18, No.7, Pages: 2690-2696.

[12] Zine Ghemari, Salah Saad: Enhancement of capacitive accelerometer operation by parameters improvement. International Journal of Numerical Modelling Electronic Networks Devices and Fields 02/2019; 32(22):e2568. DOI:10.1002/jnm.2568

ISSN 1737-9334

[13] Zine Ghemari, Salah Saad: The use of mechanical sensitivity model to enhance capacitive sensor characteristics. Analog Integrated Circuits and Signal Processing 01/2019;, DOI:10.1007/s10470-018-01383-w

[14] Salima Khaoula Reguieg, Zine Ghemari, Tarak Benslimane, Salah Saad: Modeling and Enhancement of Piezoelectric Accelerometer Relative Sensitivity. Sensing and Imaging An International Journal 12/2019; 20(1)., DOI:10.1007/s11220-018-0222-y

[15] Zine Ghemari: Progression of the vibratory analysis technique by improving the piezoelectric sensor measurement accuracy. Microwave and Optical Technology Letters 10/2018;, DOI:10.1002/mop.31436

[16] Zine Ghemari and Salah Saad "Resonance effect decrease and accuracy increase of piezoelectric accelerometer measurement by appropriate choice of frequency" Journal of shock and vibration, Accepted 9 May 2018.

ISSN 1737-9334

Comparative Study of Solar-Based Cooling Systems

I. Amlal[#], A. El Fadar*
Laboratory of Innovating Technologies, National School of Applied Sciences, Tangier, Abdelmalek Essaadi University, Morocco
iamlal@uae.ac.ma
*aelfadar@ensat.ac.ma

***Abstract*— In recent decades, the solar cooling technology has attracted much attention due to the environmental and energy benefits of solar energy and since cooling needs often coincide with the solar radiation availability. The objective of this work is to investigate the main solar cooling systems, namely photovoltaic (PV) and thermal sorption (absorption and adsorption) systems, in order to identify the most cost-effective technology according to operating and climatic conditions. A technical-economic and environmental comparison has been carried out through a case study.**

The results revealed that the conventional system powered by photovoltaic panels represents the most appropriate choice in terms of annual cold production with a relatively low power consumption, as well as the levelized cost of energy (LCOE) which is found to be lower when compared with the adsorption and absorption systems, but in term of environmental aspect the choice of these latter systems is more profitable.

***Keywords*— Solar cooling; Absorption; Adsorption; Conventional cycle; Photovoltaic; LCOE; GHG**

I. INTRODUCTION

The intensive use of fossil fuels (oil, gas, coal, etc.) for nearly 150 years placed humans today in a dual context: the increase in the greenhouse effect with catastrophic climatic consequences, and the predictable exhaustion of these sources of energy from the underground. Indeed, global reserves of oil, natural gas and coal are estimated at about 40, 61 and 227 years respectively [1]. The importance of improving thermal comfort in buildings has led to the large-scale implementation of HVAC (heating, ventilation and air-conditioning) systems, which has resulted in an increase in the building's energy consumption. It is therefore crucial to improve the energy performance of HVAC systems in order to reduce building energy consumption and carbon emissions.

In the field of refrigeration, cooling systems are currently numerous and varied and their operating principle remains however the same; it is based on extracting a quantity of heat from a cold source and injecting a quantity of heat to a hot source at another higher temperature level [2].

Besides, the use of solar energy is one of the promising solutions, especially in non-electrified regions where there is abundant sunlight, since the need for air conditioning and refrigeration generally matched with the availability of solar resources [3,4]. In this regard, there are two basic approaches to produce cold with solar energy. The first approach is based on photovoltaic effect by using PV cells, a direct conversion of solar energy into electricity that can be used to operate a conventional compression cycle. The second one is to convert solar rays into heat at a relatively high temperature, then use it to increase the temperature of the refrigerant that allows it to be pressurized. This approach, called sorption refrigeration, is based on well-established thermodynamic principles.

The refrigerant undergoes four thermodynamic transformations (compression, condensation, expansion, evaporation), the main difference between them is the way in which the refrigerant is compressed, see Fig. 1. During condensation and evaporation, the refrigerant changes its phase liquid/ vapor.

ISSN 1737-9334

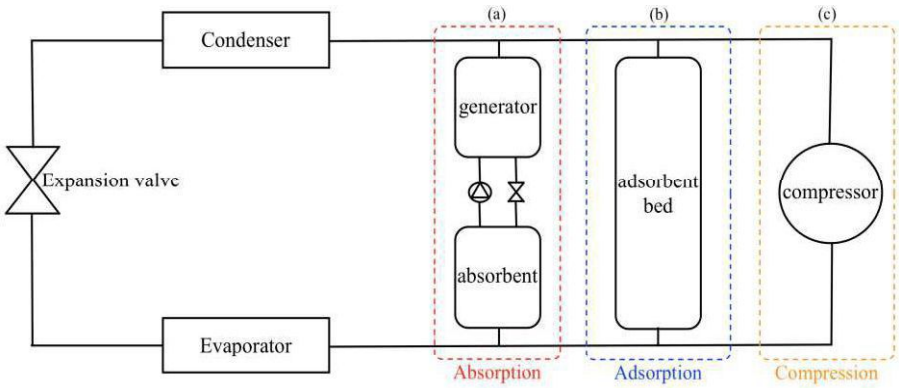

Fig. 1. Schematic diagram of the main cooling systems with different compressors.

II. CASE STUDY

The objective of this section is to carry out a comparative study of three cooling systems in order to identify, for the same annual cold needs and operating conditions, the most appropriate cooling technology, (i) economically in terms of levelized cost of energy (produced cold), and (ii) technically in terms of coefficient of performance and overall efficiency as well as (iii) environmentally by estimating the greenhouse gas (GHG) emissions.

For this aim, we chose a building located in the city of Tangier with a latitude of 35.76°N and a longitude of 5.79°W.

The cooling needs can be calculated based on the dimensions, location of the house and the characteristics of the building materials. Thus, the building has an area of 137.75 m^2 and a roof height of 2.5 m facing north. Table. I show the detailed data of building dimensions. The chosen comfort temperature is 22°C for the summer and the global thermal resistance of the system including lateral walls and windows is 0.38 $m^2.K.W^{-1}$.

Table I
Characteristics of the proposed building.

	Length (m)	**Width (m)**	**Height (m)**	**Surface (m^2)**	**Heat losses (W/m^3)**
Room 1	5	4	2.5	20	2.63
Room 2	5	4	2.5	20	2.63
Kitchen	9.5	5.5	2.5	38.25	5.54
Living room	9.5	5	2.5	47.5	3.18
Bathroom	4	3	2.5	12	2.98
				137.75	16.97

The annual heating and cooling energy requirements are calculated using the following formula:

$$E = 24 \times G \times Dj \times V$$

where G is the total heat losses per volume unit ($W/m^3.°C$) with a temperature difference of 1°C, Dj is the annual number of degree-days (°C/year) and V is total volume of building (m^3).

The GHG evaluation is corresponding to the CO2 emitted during the electricity production necessary for the operation of cooling equipment during its lifetime [5], it is given by the following formula:

$$GHG = annual\ leakage\ rate \times refrigeration\ charge \times GWP\ (Refrigerant)$$

where GWP is the global warming potential measured by units of carbon dioxide equivalents (CO_{2e}) [6]. For the absorption / adsorption systems using H_2O/LiBr and silica-gel/H_2O pairs respectively, the compression process of refrigerant is based on the heat where there is no electricity use; in these systems the CO_2 emitted is only related to GWP (global warming potential) of the refrigerant, which is often negligible due to the thermodynamic properties of the refrigerants used in these systems.

In the conventional cycle driven by PV panel, the refrigerant mass is evaluated from the amount of cold-generated under the operating conditions.

ISSN 1737-9334

III. RESULTS AND DISCUSSION

The results obtained from the three compared systems are summarized in Table. II, with consideration of the cooling capacity required to satisfy the building's climate needs.

Table II

Results from technical-economic and environmental study.

Refrigerating machine	PV-Compression	Absorption	Adsorption
Life time system (year)	20	20	20
COP	3.5	0.79	0.45
Refrigeration energy demand (kWh/year)	45 749	45 749	45 749
Consumption (kWh/year)	95 310.41	89 703.92	101 664.44
Initial investment (€)	17 525	65 765	110 257
TRI (year)	5.25	13.18	16.50
LCOE (€/kWh)	0.073	0.109	0.146
Total surface area (m^2)	$44_{PV\ panels}$	$140_{Vacuum\ tube}$	$210_{Vacuum\ tube}$
GHG emissions of the system (Tonne/year)	0.412 (R134a)	0 (Water)	0 (Water)

According to Table II, the system that represents the high coefficient of performance is the conventional system powered by photovoltaic panels with a surface area occupied by the PV-panels much smaller than that of the vacuum collectors feeding the absorption and adsorption systems, which are larger than the total surface area of the building. For an annual cold production achieved using the three studied machines, the COP obtained by the conventional compression system is 7 times greater than that of adsorption system and 4 times greater than that of absorption system.

From Fig. 2, the lowest LCOE of 0.073 €/kWh is obtained for conventional system driven by PV panels that is lower than that of absorption system by 33% and that of adsorption system by 50%. Moreover, the conventional system driven by PV panels has a low payback period of 5.25 years versus 7.93 and 10.25 years for absorption and adsorption system respectively. This drawback, makes their choice unprofitable in the short term because of their higher investment cost and LCOE.

In terms of the environmental aspect, Table II shows that the two sorption systems are found to be better with a negligible GHG emissions compared to the conventional system which represent an annual emission of 0.412 tonnes equivalent to the global warming caused by the R134a used as refrigerant fluid, given that photovoltaic panels' emissions are negligible.

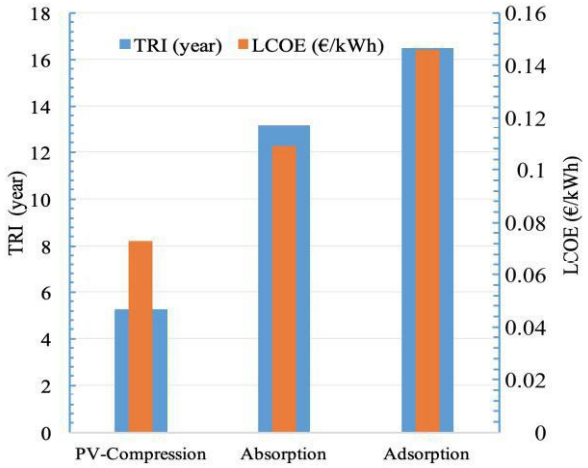

Fig. 2. Economic indicators found for each system.

IV. CONCLUSION

In this work, a comparative study was thoroughly carried out for three types of solar cooling systems for a building located in Tangier city. The main findings from this study were drawn as follows:

- The lower LCOE was found for the conventional compression refrigeration system driven by PV panels because of the lower investment cost and high coefficient of performance compared to the two other systems.
- In terms of environmental impact, the ad/absorption refrigeration systems are more environmentally friendly due to the absence of greenhouse gas emissions. Furthermore, they are silent; contrary to the compression refrigeration system that generates a noise since it uses a rotating device (compressor).
- Refrigerants used in conventional cycle represent the major disadvantage of being unsafe because most of them are flammable and toxic.

ISSN 1737-9334

REFERENCES

[1] La vérité sur les réserves mondiales », Yves Mathieu, Editions Technip (2011) Travaux de Roland Vially, géologue à IFPEN.
[2] Chekirou Wassila. Etude et analyse d'une machine frigorifique solaire à adsorption (2008) 40–4.
[3] A. El Fadar. Novel process for performance enhancement of a solar continuous adsorption cooling system. Energy 114 (2016) 10–23.
[4] A. El Fadar. Thermal behaviour and performance assessment of a solar adsorption cooling system with finned adsorber. Energy 83 (2015) 674–684.
[5] Ahmed Hamza H. Ali. Performance-cost and global warming assessments of two residential scale solar cooling systems versus a conventional one in hot arid areas. Sustainable Energy Technologies and Assessments 20 (2017) 1–8.
[6] Nicholas J Santero, Arpad Horvath. Global warming potential of pavements. Environmental Research Letters. 23 September 2009.

ISSN 1737-9334

Complex Shannon Wavelets Method for Modeling the Arbitrary Bent Thin Wires antenna

Mohamed Bayjja[#1], Gamil Alsharahi[#2], Naima Amar Touhami[#3], Doae El Hadri*[4], Mohamed Aghoutane[#5]

[#]*Faculty of Science, University Abdelmalek Essaâdi, Tetouan, Morocco.*

[1]m.bayjja@gmail.com

[2]alsharahigamil@gmail.com

[3]nai_amar@yahoo.fr

[5]aghoutane@gmail.com

[*] *National School of Applied Sciences, University Abdelmalek Essaâdi, Tetouan, Morocco.*

[4]doae93@gmail.com

Abstract— **The aim of this paper is to highlight the Complex Shannon wavelets in electromagnetic, modeling the arbitrary bent thin wire antenna. The first set the Electric field integral equation for the arbitrary bent thin wire antenna is solved with moment's method and Complex Shannon wavelet. The current distribution, computational time, percentage sparsity achieved in the impedance matrix and the radiation pattern of an arbitrary bent thin wire antenna is presented using Complex Shannon wavelet-MoM. Numerical results are in good agreement with those in previous publications.**

Keywords— **Complex Shannon wavelet, Methods of Moment, Antenna, Sparsity, and CPU Time**

I. Introduction

Wavelets are mathematical functions that cut up data into different frequency components, and then study each component with a resolution matched to its scale. Wavelets were developed independently in the fields of mathematics, quantum physics, electrical engineering, and seismic geology [1].

Conventional method of moments (MoM), when applied directly to integral equations (IE), leads to a dense matrix which often becomes computationally intractable due to the large memory requirement and high computation time necessary to invert a dense matrix. To overcome these difficulties, the Complex Shannon wavelet bases have been used, primarily because of their local supports and vanishing moment properties, lead to a sparse matrix. We apply this technique to modeling the arbitrary bent thin wires antenna [2,4].

Complex Shannon wavelets are the real part of the so-called harmonic wavelets [9]. They have a slow decay in the time domain but a very sharp compact support in the frequency (Fourier) domain. This fact, together with the Parseval's identity is used to easily compute the inner product and the expansion coefficients of the Shannon wavelets [9].

In this paper, Complex Shannon Shannon wavelets are used in solving, by the method of moments (MoM), an arbitrary bent thin wires electric field integral equation (EFIE), in frequency domain. The solution, with the MoM, can be found in the applied literature for straight thin wires, Balanis [5]. For arbitrary shaped wires is necessary another integral equation formulation, starting with Mei's analysis and successors, [3,4].

II. The Electric Field Integral Equation

The Electric field integral equation (EFIE) can be derived from Maxwell's equations. Mathematically:

$$E^t(r) = -\frac{j\eta}{k}\int_{s'} J(r')[K^2 + \nabla^2]\frac{e^{-jk|r-r'|}}{4\pi|r-r'|}ds' \qquad (1)$$

$E^t(r)$ is the total electric field vector measured at the observation point, $J(r')$ is the current distribution located at source point r', $k = \omega\sqrt{\mu_0\varepsilon_0}$, and η is the intrinsic impedance for free given by; $\eta = \sqrt{\mu_0/\varepsilon_0}$.

Considering figure 1, arbitrary bent thin wires, and the current is located over the wire's surface [2,4,8].

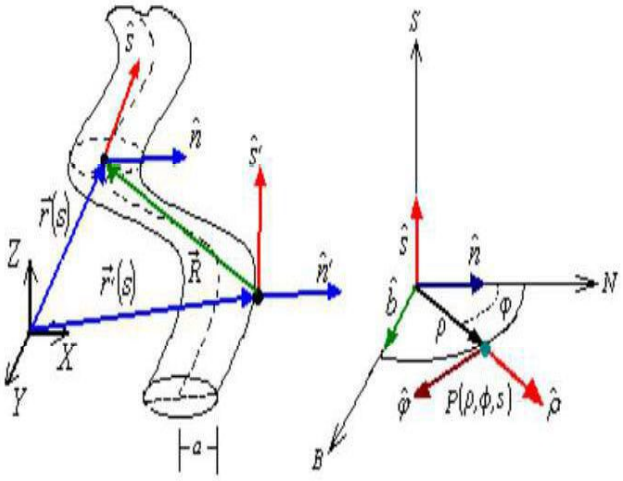

Figure 1: Relations among the vectors of the arbitrary shape wire.

The electric field boundary condition over the structure of the arbitrary shaped thin wire is giving:

$$E^t(r) = E^i(r) + E^s(r) = 0 \quad (2)$$

$E^i(r)$ and $E^s(r)$ are the impressed and scattered electric fields, respectively.

Pocklington's IE is derived from eqn (1), applying the electric field boundary condition over the structure of the arbitrary shaped thin wire is giving:

$$E^i(r) = -\frac{j}{\omega\varepsilon}\int_{s'} I_S(s')[k^2 s * s' + \frac{\partial^2}{\partial s \partial s'}]\frac{e^{-jk|r-r'|}}{4\pi|r-r'|}ds' \quad (3)$$

Where, E_S^I is the tangential impressed electric field.

Equation (3) is the general Pocklington's equation applicable to wires of any possible geometry.

III. Solving the EFIE Bay Shannon Wavelet and MoM.

We consider a Complex Shannon wavelet basis adapted to L2, with compactly supported wavelets that are Cq with q vanishing moments [6]:

$$B = \left[\{\varphi_{j,n}\}_{0\le n\le 2^{-j}}, \{\psi_{j,n}\}_{-\infty\le j\le J\ ,0\le n\le 2^{-j}}\right] \quad (4)$$

To simplify notation,we write $\varphi_{j,n} = \psi_{j+1,n}$.

If the analog signal f ∈ L2 is approximated at the scale 2L with N=2-L samples $\{\langle f, \varphi_{l,n}\rangle\}_{0\le n\le 2^{-L}}$, then the corresponding N wavelet coefficients $\{\langle f, \psi_{J,n}\rangle\}_{n,j>L}$, are computed with O(N) operations with the fast wavelet transform algorithm of reference [6].

The complex Shannon wavelet is obtained from the frequency B-spline wavelets by setting m to 1. A complex Shannon wavelet is defined by [11]

$$\psi(x) = \sqrt{f_b}\,\sin(f_b x)\, e^{2i\pi f_c x} \quad (5)$$

Depending on two parameters:

- fb is a bandwidth parameter.
- fc is a wavelet center frequency

The Complex Shannon wavelet of order L = 4 and resolution level j0 are employed to expand the unknown current distribution Is in Eq.5 in the form

$$I_s(x) = \sum_n a_n \emptyset_{j,n}(x) + \sum_{m=j}^{2^j-1}\sum_n C_{m,n}\psi_{m,n}(x) \quad (6)$$

$\varphi_{j,n}$ *and* $\psi_{j,n}$ are Complex Shannon scaling and Complex Shannon wavelet, respectively.

In the Galerkin procedure the testing functions are the same as the basis functions. After testing the integral equation (3) with the same wavelet $\{\psi_{m,n}(x)\}$, we obtain [4,11]:

$$< \sum_{n\in Z} \emptyset_{j,n}(s) + \sum_{m=j}^{2^j-1}\sum_l \psi_{m,l}(s)\ , E_s^I > = -\frac{j}{\omega\varepsilon} < \sum_{n\in Z} \emptyset_{j,n}(s) + \sum_{m=j}^{2^j-1}\sum_l \psi_{m,l}(s)\ , \int_{s'}\left[\sum_{n\in Z} a_n \emptyset_{j,n}(s') + \sum_{m=j}^{2^j-1}\sum_l C_{m,l}\psi_{m,l}(s')\right]\left[k^2 s.s' + \frac{\partial^2}{\partial s \partial s'}\right]\frac{e^{-jk|r-r'|}}{4\pi|r-r'|}ds' > \quad (7)$$

S' and S are, respectively, the supports of the expansion and testing functions. This set of equations can be written in matrix form:

$$\begin{bmatrix}[Z_{\emptyset,\emptyset}] & [Z_{\emptyset,\psi}]\\ [Z_{\psi,\emptyset}] & [Z_{\psi,\psi}]\end{bmatrix}\begin{bmatrix} a_{nx,ny} \\ c_{m,nx,ny}\end{bmatrix} = \begin{bmatrix} < V, \emptyset_{j,n} > \\ < V, \psi_{m,n} >\end{bmatrix} \quad (8)$$

IV. Numerical Results and Discussions

In this section, we compute certain important results developed in the preceding sections. All the programs for the solutions have been solved using MATLAB software. To evaluate the performance of Complex Shannon wavelet base, the current distributions and radiated far-field of an arbitrary bent thin wire has been evaluated using the method of moments and Complex Shannon wavelets. Consider an arbitrary bent thin wire with the following parameters:

Table1: Parameters of arbitrary bent thin wire.

Parameters	Frequency	Radius	Length	Number of segments	Excitation Type
Values	f=0.4 Ghz	a=0.005λ	L=λ and1.5λ	101	Delta-gap source

Figure 2 illustrate current distributions for arbitrary bent thin wire antenna, for two selected wire lengths so that they

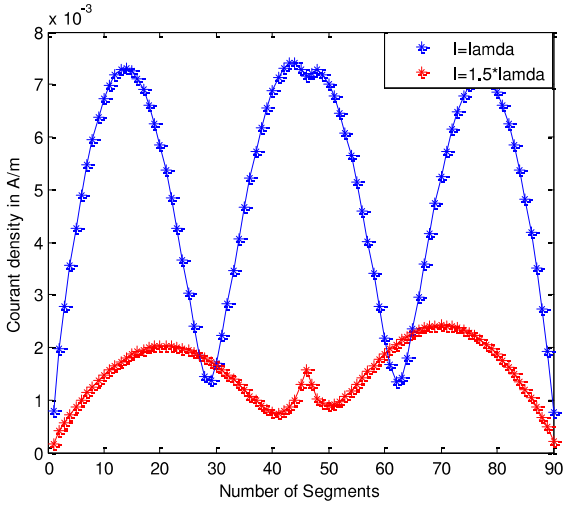

Figure 2: Current distributions for arbitrary bent thin wire antenna, for l=1*λ and l=1.5*λ

ISSN 1737-9334

include special cases of practical interest, e.g for l=1*λ and l=1.5*λ, by conventional moment method. The results show good agreement with ref.[2].

Figure 3 and figure 4 shows the current distributions and radiated far-field for the arbitrary bent thin wire antenna by the classical pulse basis as well as Complex Shannon bases, in function of the electric lengths for antenna and scattering angles, respectively.

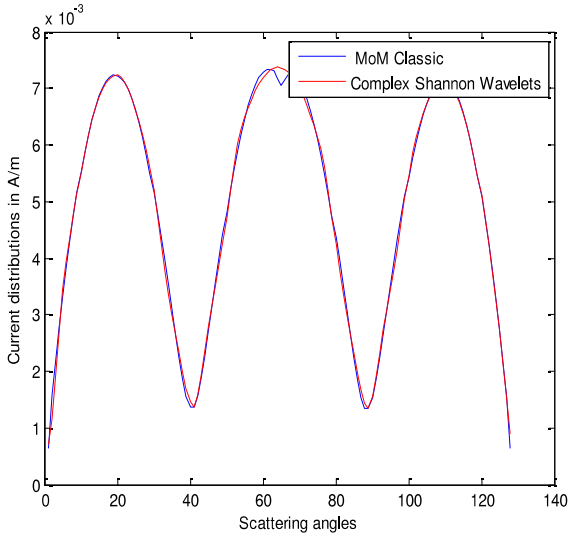

Figure 3: Current distributions for arbitrary bent thin wire antenna

Results are presented with comparison of traditional Moment Method Complex Shannon wavelet, and we see a good agreement between the two methods. Results are Compared with previous work published [2] and [3].

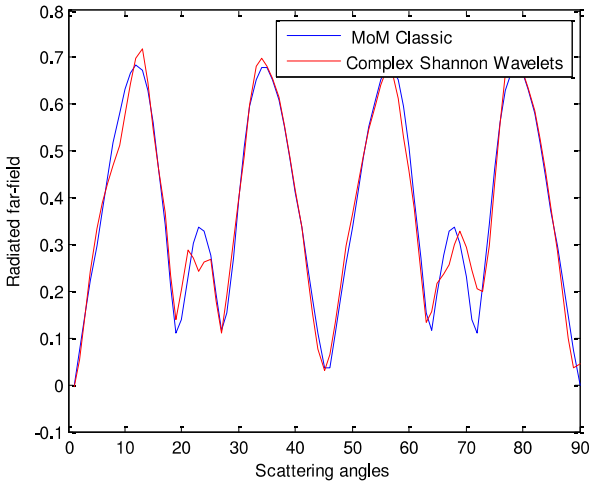

Figure 4: radiated far-field for the arbitrary bent thin wire antenna

Table 2 compares the performance of Complex Shannon wavelet bases in terms of the computational time, percentage sparsity achieved in the IM and Relative error. As seen in the Table 2, the Complex Shannon wavelet expansion extracts the variation of current distributions more rapidly than the MoM classic.

Table 2: Sparsity, CPU Time to reverse an impedance matrix and Relative error for Complex Shannon wavelet

	MoM	Complex Shannon Wavelets
Sparsity %		88.9706
CPU Time to reverse IM (ms)	0.024143	0.017330
CPU Time reduction %		28.21
Relative error		0.0078

Figure 5 shows the sparsity pattern of impedance matrix for all aforementioned Complex Shannon wavelet base after threshold process.

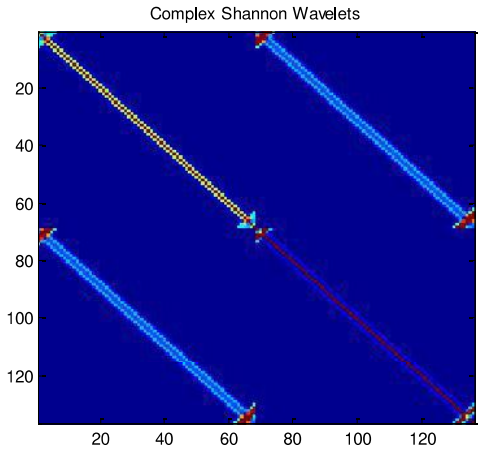

Figure 5: Sparsified wavelet matrix of the thin wire antenna

V. CONCLUSION

The analysis of an arbitrary bent thin wire antenna by the moment method with Complex Shannon wavelet expansions has been presented. By using the Complex Shannon wavelet as the weighting and expansion functions, the sparse generalized impedance matrix is obtained and the reconstructing current distributions and radiated far-field agree well with the results of the conventional MoM. With the threshold processing for the matrix, the Complex Shannon wavelet-MoM exhibits the advantages of shorter computation time and less storage compared with the conventional MOM. Thus the Complex Shannon wavelet-MoM is more suitable for the analysis of a large sized model.

REFERENCES:

[1] George W. Pan, *Wavelets in Electromagnetics and Device Modeling*, 1st ed., by John Wiley & Sons, Hoboken, 2008

[2] V. Barrera-Figueroa, J. Sosa-Pedroza and J. López-Bonilla, "Simplification of Pocklington's integral equation for arbitrary bent thin wires", *WIT Transactions on Modelling and Simulation*, Vol 39, pp. 563-574, 2005.

[3] Walton C.Gibson, *The method of Moments in Electromagnetics*, 2nd ed., by Taylor and Francis Group, London. 2015.

ISSN 1737-9334

[4] Mohamed Bayjja, A.K. Belbachir, M. Boussouis, and Naima Amar Touhami, ''Orthogonal and biorthogonal compactly supported wavelets in modeling the circular loop antenna'', *International Journal of Microwave and Optical Technology*,VOL. 12, NO. 5, September 2017.

[5] Constantine A. Balanis, Antenna, *Theory Analysis and Design*, 4th ed., by John Wiley, 2016.

[6] Stéphane Mallat, *A Wavelet Tour of Signal Processing The Sparse Wa*y, Elsevier Inc, 2009.

[7] Tian-Xiao He, "Biorthogonal Spline Type Wavelets", *Computers and Mathematics with Applications*, Vol. 48, Issue 9, pp. 1319-1334, November 2004.

[8] Akshay Joshi, S. K. Behera," Method of Moments Analysis of Circular Loop Linear Array and Circular Loop Circular Array", 2016 IEEE Students' Conference on Electrical, Electronics and Computer Science, 978-1-4673-7918-2/16/$31.00 ©2016 IEEE.

[9] R. Danesfahani and S. Hatamzadeh-Varmazyar, APPLYING SHANNON WAVELET BASIS FUNCTIONS TO THE METHOD OF MOMENTS FOR EVALUATING THE RADAR CROSS SECTION OF THE CONDUCTING AND RESISTIVE SURFACES, *Progress In Electromagnetics Research B*, Vol. 8, 257–292, 2008.

[10] Bayjja, M., Moubadir, M., Alsharahi, G., Aghoutane, M., & Amar Touhami, N. (2019). Modeling a Planar Coupled Microstrip Lines using various Wavelets and Method of Moments. *Advanced Electromagnetics*,8(1),51-58. https://doi.org/10.7716/aem.v8i1.771.

[11] Michel Misiti, Yves Misiti, Georges Oppenheim, Jean-Michel Poggi, *Wavelet Toolbox*™ User's Guide, by The MathWorks, Inc. 1997–2015.

[12] Jaideva C. Goswami, Andrew K. Chan, *Fundamentals Wavelets Theory, Algorithms, and Applications*, 2nd ed., by John Wiley & Sons, Hoboken, 2010

ISSN 1737-9334

Hybrid artificial neural network- Backstepping MPPT controller PV systems

Boudia assam
LGE laboratory, department of electrical engineering,
Faculty of technology, university of Msila
M'sila, Algeria, assam.boudia@univ-msila.dz

Messalti sabir
Department of electrical engineering, Faculty of technology,
university of Msila,Algeria
sabir.messalti@univ-msila.dz

Harrag abdelghani
CCNS Laboratory, Electronics Department, Faculty of Technology
University of Ferhat Abbas Setif 1
Setif, Algeria
abdelghani.harrag@gmail.com

***Abstract*— In this paper, new maximum power point tracking (MPPT) using artificial neural network and backstepping techniques has been proposed and investigated. In which the voltage reference is calculated by artificial neural network, then the optimal duty cycle is obtained by backstepping controller. In addition proposed method has been compared to P&O method. The proposed MPPT controller has been validated using BP SX 150 solar panel connected to DC-DC boost converter. Simulation results have been demonstrated for different atmospheric conditions.**

Keywords- combined backstepping-neural network MPPT, PV systems , P&O method.

I. INTRODUCTION

Sun power is one of the most significant sustainable vitality sources. Rather than regular unrenewable assets, for example, fuel, coal. Sun power is clean, boundless and free. The primary utilizations of photovoltaic (PV) system are in either stand-alone (water siphoning, local and road lighting, electric vehicles, military and space applications) or system associated setups (power plants) .

PV generation system has two major problems, first, the electric power produced by photovoltaic cell changes constantly with climate conditions, secondly, the change effectiveness of electric power generation is low (9÷17%), particularly under low insolation conditions. Moreover, the PV characteristics P-V and I-V are nonlinear and affected directly by the change of the irradiation and temperature

Maximum power point (MPP) is unique point in the P-V curve, in which the PV system works with maximum efficiency and provide its maximum output power, this point in not known but it can be calculated using maximum power point tracking (MPPT) technique.

Lot of MPPT methods have been present, such as Perturb and observe [1-3], incremental Conductance (IC) [4-6], artificial Neural Network [7-8], fuzzy logic method [9-11], etc..., the difference between those techniques depends on several factors: response time, cost, stability and simplicity.

In this paper, two MPPT techniques are compared under the climates changes, P&O and Backstepping combined with artificial neural network. P&O is classical method using classic algorithm to generate the duty cycles, backstepping is robust method use mathematical calculation to control the system and calculate the duty cycles and use artificial neural network to calculate the reference voltage.

An artificial neural network is a mathematical model that tries to simulate the structure and functionalities of biological neural networks. A neural network is an information processing system. It consists of a number of simple highly interconnected processors (units) known as neurons similar to biological cells of the brain. These neurons are interconnected by a large number of weighted links, over which signals can pass. Each neuron receives many signals over its incoming connections, and produces a single outgoing response. Such networks have exceptional pattern recognition and learning capabilities. Recent applications of ANN have shown that they have considerable potential in overcoming the difficult tasks of data processing and interpretation. Four major steps are necessary in ANN applications [7-8,12-15]:

II. PV MODULE

For the most part, PV module involves various PV cells associated in series or parallel in this paper we chose PV module type BSX 150 which contains 72 series cells, the mathematical of PV cell can be expressed as:

$$I = N_p I_{ph} - N_p I_{rs}\left[e^{\left(\frac{q(v+R_S I)}{A.k.T.N_S}\right)} - 1\right] - N_p\left(\frac{q(v+R_S I)}{N_S.R_{Sh}}\right) \quad (1)$$

Where I is the PV array output current, Iph is the cell photocurrent that is proportional to solar irradiation, V is the PV output voltage, Iph is the cell photocurrent that is proportional to solar irradiation, Irs is the cell reverse saturation current, ns and np are the numbers of series strings and parallel strings.

ISSN 1737-9334

TABLE I. PV CELL SPECIFICATIONS BP SX 150.

Parameter	*Value*
Maximum power (P_{max})	150W
Voltage at maximum power (V_{mp})	34.5 V
Current at maximum power (I_{mp})	4.35 A
Open circuit voltage (V_{oc})	43.5 V
Short circuit voltage (I_{sc})	4.75 A
Temperature coefficient of I_{sc}(a)	0.065±0.015% /C°

III. PERTURB AND OBSERVE

Perturb and Observe is the most commonly used method in practice for its simplicity and ease of implementation. In this method, the output voltage of the solar panel is perturbed periodically, and then the output power is compared to the previous cycle. Next, corrective action is taken to enforce the voltage to move toward the maximum operation output voltage. The comparison can determine the position of the operation point and the direction of perturbation [16-19].

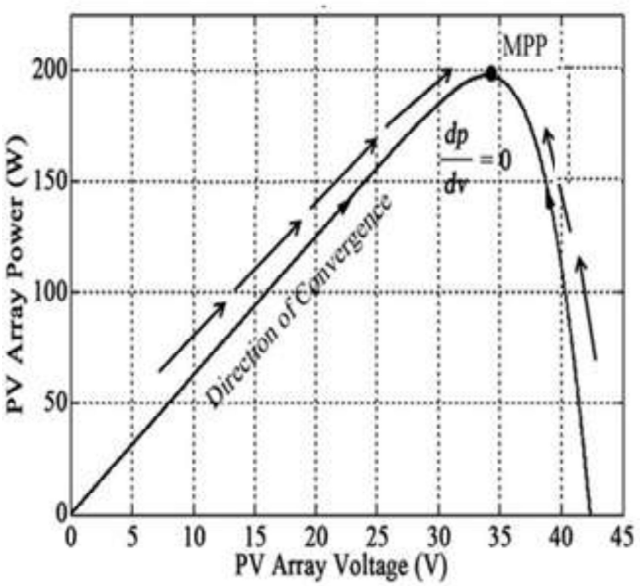

Figure 1. the algorithm of perturb and observe method.

IV. BOOST CONVERTER MODELING

Applying the fundamental laws that govern the functioning of the boost converter; the averaged model is achieved. Fig3. shows the scheme of the converter. The dynamic equations of this converter can be expressed by the following equation:

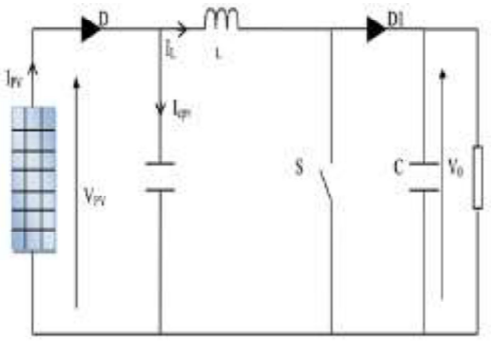

Figure 2.Boost DC-OC Converter.

$$\begin{cases} \dfrac{dx_1}{dt} = \dfrac{1}{C_{pv}} i_{pv} - \dfrac{1}{C_{pv}} x_2 \\ \dfrac{dx_2}{dt} = \dfrac{1}{L} x_1 - \dfrac{1}{L}(1-\alpha) V_0 \end{cases} \quad (2)$$

Where $x=[x_1\ x_2]^T=[V_{pv}\ I_L]^T$, and $\alpha \in [0-1]$ is a switching signal control and M is averaging value of (1- α)

$$M=1-\alpha \quad (3)$$

V. BACKSTEPPING CONTROLLER

The base idea of Backstepping approach is stabilized the system from the first sub system by stabilizing function known via a Lyapunov function selected, and then add to its input integrator. The same procedure for the next under increased system and so on for the successive subsystems to finally reach a global Lyapunov function giving overall control law that stabilizes the system.

The Backstepping technique is relatively a new control method. It allows sequentially and systematically, by choosing a Lyapunov function to determine the system control law [20, 22].

The purpose of the order is to achieve convergence towards zero errors thus achieving the stability and balance of the system which allows the output to follow a reference.Fig3

ISSN 1737-9334

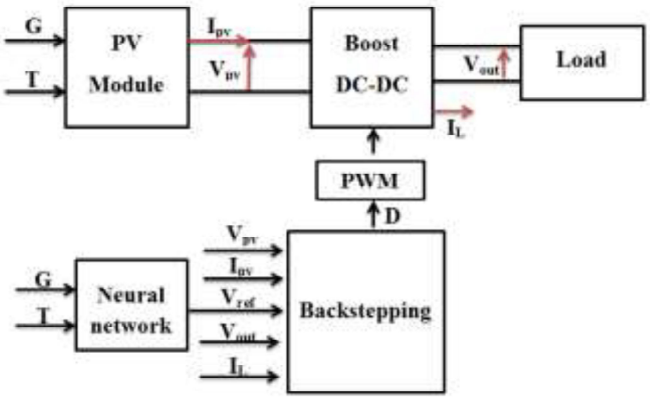

Figure 3. Backstepping MPPT combined with neural network

Step1:

The equations modeling the boost converter required for synthesis of backsteppingcontrol are shown in (2)

The first tracking error variable is:

$$e_1 = x_1 - v_{ref} (4)$$

The tracking error derivative is written as follows:

$$\dot{e_1} = (\dot{x_1} - \dot{v_{pref}}) = \frac{1}{c_{pv}}(i_{pv} - x_2) - \dot{v_{pref}} (5)$$

The following lyaponov function is considered:

$$V_1(e_1) = V_1 = \frac{1}{2}e_1^2 (6)$$

The derivative versus time using equation (5)

$$\dot{v_1} = e_1\dot{e_1} = e_1\left(\frac{1}{C_{pv}}(i_{pv} - x_2) - \ddot{v_{pvref}}\right) \quad (7)$$

Judicious choice of $\dot{e_1} = -k_1e_1$ permits writing $\dot{v_1} = -ke_1^2$ where k_1 is positive constant that represents a design parameter of backstepping controller.

In (3), x_2 behaves as a virtual control input, for i $x_2 = x_{ref}$ we can find the stabilizing function:

$$x_{ref} = k_1c_{pv}e_1 + i_{pv} - c_{pv}\dot{v_{pref}} (8)$$

Step 2:

The second error variable that represents the difference between the x_2 state variable and its desired value xref is defined by:

$$e_2 = x_2 - x_{ref} (9)$$

Then the system equations in the errors space ($\dot{e_2}$) are deduced:

$$\dot{x_{ref}} = k_1c_1\dot{e_1} + \dot{i_{pv}} - c_{pv}\ddot{v_{pref}} (10)$$

$$\dot{e_2} = \dot{x_2} - \dot{x_{ref}} = \frac{1}{L}(x_1 - Mv_0) - k_1c_1\dot{e_1} - \dot{\iota_{pv}} + c_{pv}\ddot{v_{pref}} (11)$$

The new Lyapunov function:

$$v_2 = v_1 + \frac{1}{2}e_2^2 (12)$$

The derivative can be expressed by:

$$\dot{v_2} = \dot{v_1} + e_2\dot{e_2} (13)$$

$$\dot{v_2} = -k_1e_1^2 + e_2(\frac{1}{L}(x_1 - Mv_0) - k_1c_1\dot{e_1} + \dot{\iota_{pv}} + c_{pv}\ddot{v_{pref}}) (14)$$

Inthis step command M is chosen so as to obtain the following expression:

$$\dot{e_2} = -k_2e_2 = \frac{1}{L}(x_1 - Mv_0) - k_1c_1\dot{e_1} - \dot{i_{pv}} + c_{pv}\ddot{v_{pref}} (15)$$

Hence the expression of command M to be produced by the backstepping controller:

$$M = \frac{L}{v_0}[\frac{x_1}{L} - \frac{e_1}{C_{pv}} + k_2e_2 - k_1c_1\dot{e_1} - \dot{i_{pv}} - c_{pv}\ddot{v_{pref}} (16)$$

With k_2>0 leads to negative derivative of the Lyapunov function:

$$\dot{v_2} = k_1e_1^2 - k_2e_2^2 < 0 \quad (17)$$

Which ensures that the error variables (e_1, e_2) converge asymptotically to the origin, implying that X_1converges asymptotically to the origin V_{pvref}thus extracting the maximum power from the PV array is performed.

VI. SIMULTAION RESULT

The simulation results is carried out using PV module type BSX 150 which generates 150 w at its maximum power point, Dc-Dc boost converter and resistive load, obtained results are given by the following figures:

ISSN 1737-9334

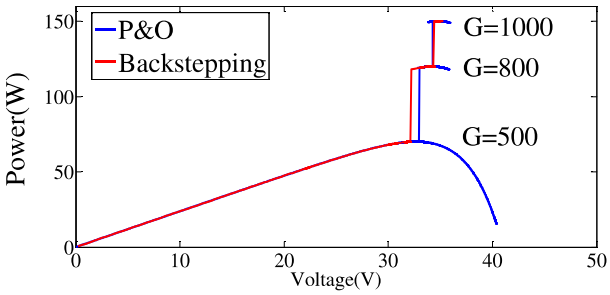

Figure 4. P-V curve with ANN - backstepping and P&O under different irradiation.

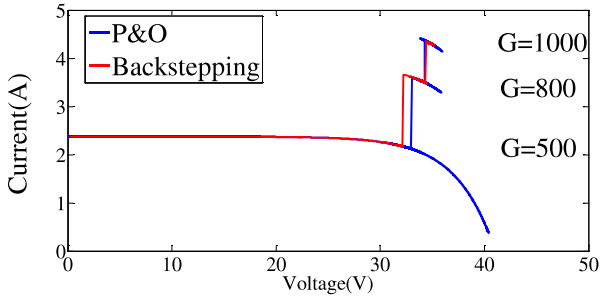

Figure 5.I-V curve with ANN - backstepping and P&O under different irradiations.

Fig 4 to 8 show respectively the P-V curve, the I-V curve the PV output power. Its clear that both mthods provides a good performances, but we can observe that the ANN - backstepping performances (response time, ripple, accuracy) are better than P&O method.

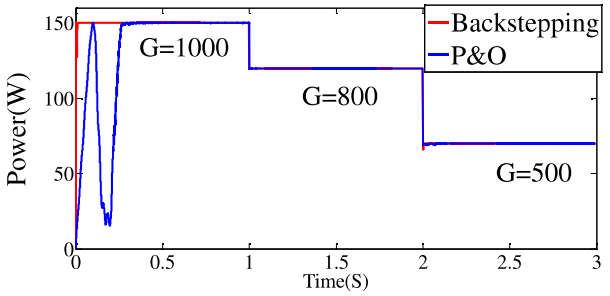

Figure 6. PV output power with ANN -backstepping and P&O under different irradiation.

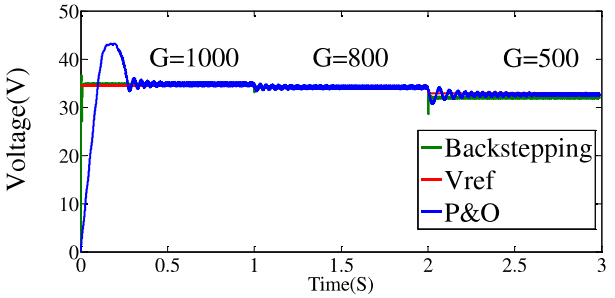

Figure 7. PV output voltage with ANN -backstepping and P&O under different irradiation.

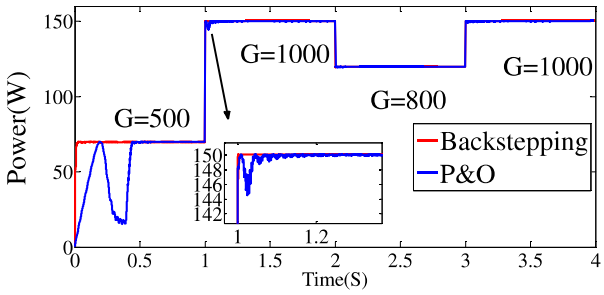

Figure 8. PV output power with ANN -backstepping and P&O under different irradiation.

VII. CONCLUSION

In this paper, new combined Maximum power point tracking employing ANN - backstepping has been presented, the proposed method has been compared to classical P&O method, the efficiency of developed ANN – backstepping has been studied for several conditions. Simulation results confirm the superiority of ANN– backstepping compared to conventional P&O method. The present method can be extended by successfully implementing the proposed algorithm in experimental prototype and embedded to PV-grid systems.

REFERENCES

[1] Harrag, A., & Messalti, S. " Variable step size modified P&O MPPT algorithm using GA-based hybrid offline/online PID controller". Renewable and Sustainable Energy Reviews, 49, 1247-1260.2015

[2] Femia, N., Petrone, G., Spagnuolo, G., & Vitelli, M. "Optimizing duty-cycle perturbation of P&O MPPT technique". In 2004 IEEE 35th Annual Power Electronics Specialists Conference (IEEE Cat. No. 04CH37551) (Vol. 3, pp. 1939-1944). IEEE.

[3] Liu, F., Kang, Y., Zhang, Y., & Duan, S. " Comparison of P&O and hill climbing MPPT methods for grid-connected PV converter". In 2008 3rd IEEE Conference on Industrial Electronics and Applications (pp. 804-807). IEEE.2008

[4] Loukriz, Messalti, S. Harrag, A., Design, simulation, and hardware implementation of novel optimum operating point tracker of PV system using adaptive step size, The International Journal of Advanced Manufacturing Technology,2019, Vol 101,(5), pp 1671–1680

[5] Sera, D., Mathe, L., Kerekes, T., Spataru, S. V., & Teodorescu, R. " On the perturb-and-observe and incremental conductance MPPT methods for PV systems". IEEE journal of photovoltaics, 3(3), 1070-1078.2013

[6] Loukriz, A., Haddadi, M., & Messalti, S. " Simulation and experimental design of a new advanced variable step size Incremental Conductance MPPT algorithm for PV systems". ISA transactions, 62, 30-38.2016

[7] Messalti, S.,Harrag, A. G., & Loukriz, A. E. ". A new neural networks MPPT controller for PV systems". In IREC2015 The Sixth International Renewable Energy Congress(pp. 1-6). IEEE.2015

[8] Messalti, S., Harrag, A., & Loukriz, A. " A new variable step size neural networks MPPT controller". Review, simulation and hardware implementation. Renewable and Sustainable Energy Reviews, 68, 221-233.2017

[9] Algazar, M. M., El-Halim, H. A., & Salem, M. E. E. K. " Maximum power point tracking using fuzzy logic control". International Journal of Electrical Power & Energy Systems, 39(1), 21-28.2012

[10] Cheikh, M. A., Larbes, C., Kebir, G. T., & Zerguerras, "A.Maximum power point tracking using a fuzzy logic control scheme". Revue des energies Renouvelables, 10(3), 387-395.2007

[11] Chekired, F., Larbes, C., Rekioua, D., & Haddad, F. " Implementation of a MPPT fuzzy controller for photovoltaic systems on FPGA circuit". Energy Procedia, 6, 541-549.2011.

ISSN 1737-9334

[12] Ibrahim M. El-Amin, Abdul-Aziz M. Al-Shams, " Transient Stability Assessment Using Artificial Neural Networks ", Electrical Power systems, Elsevier Science, Electric Power Systems Research 40 (1997), pp. 7-16.

[13] Loi Lei Lai," Intelligent System Application in Power Engineering Evolutionary Programming and Neural Network", Ed. John Wiley & sons Canada, 1999.

[14] S Krishna S., Padiyar K.R. " Transient Stability Assessment Using Artificial Neural Networks ", IEEE Transactions on Power Systems, 2000, p. 627-632.

[15] D. Bonkoungou, Z. Koalaga, D. Njomo,"Modelling and simulation of photovoltaic module considering single diode equivalent circuit model in MATLAB"- International Journal of Emerging Technology and Advanced Engineering (IJETAE), Iss.3, Vol. 3, 2013 .

[16] Villalva, M. G., & Ruppert, E. " Analysis and simulation of the P&O MPPT algorithm using a linearized PV array model". In 2009 35th Annual Conference of IEEE Industrial Electronics (pp. 231-236). IEEE.2009

[17] Kollimalla, S. K., & Mishra, M. K. " A novel adaptive P&O MPPT algorithm considering sudden changes in the irradiance". IEEE Transactions on Energy conversion, 29(3), 602-610.2014

[18] Amrouche, B., Belhamel, M., & Guessoum, A. " Artificial intelligence based P&O MPPT method for photovoltaic systems". Revue des Energies Renouvelables ICRESD-07 Tlemcen, 11-16.2007

[19] Mamarelis, E., Petrone, G., & Spagnuolo, G. " A two-steps algorithm improving the P&O steady state MPPT efficiency". Applied Energy, 113, 414-421.2014

[20] Martin, A. D., & Vazquez, J. R. " MPPT algorithms comparison in PV systems: P&O, PI, neuro-fuzzy and backstepping controls". In 2015 IEEE International Conference on Industrial Technology (ICIT) (pp. 2841-2847). IEEE.2015

[21] Khemiri, N., Khedher, A., & Mimouni, M. F. " A backstepping control strategy applied to the connected hybrid renewable energy system operated in MPPT". In 2013 Eighth International Conference and Exhibition on Ecological Vehicles and Renewable Energies (EVER) (pp. 1-10). IEEE.2013

[22] Armghan, H., Ahmad, I., Armghan, A., Khan, S., & Arsalan, M. " Backstepping based non-linear control for maximum power point tracking in photovoltaic system". Solar Energy, 159, 134-141.2018

ISSN 1737-9334

Design of a compact 5G MIMO antenna with low mutual coupling at 28 GHz band

Aziz Dkiouak[#1], Alia Zakriti[*#2], Mohsinne El Ouahabi[#3], Aicha Mchbal[*4]

[#] *Department of Civil and Industrial Science and Technology*
Abdelmalek Essaâdi University, National School
of applied Sciences. Tetuan, Morocco
[1] dkiouakaziz@hotmail.fr
[2] aazakriti@hotmail.fr
[3] elouahabi87@gmail.com

[*] *Department of physics*
Abdelmalek Essaâdi University, Faculty of
Sciences Tetuan, Morocco
[4] aicha.mchbal8@gmail.com

***Abstract*—In this letter a two-port multi-input-multi-output (MIMO) antenna resonating at 28 GHz with high isolation and compact size for 5G mobile applications is proposed. The proposed antenna consists of two identical monopole antenna elements and placed parallel to each other on 11x31 mm2 Rogers substrat. The impedance bandwidth from 3.21 % (27.12 – 28.92 GHz) is enriched by using a symmetrical slot in the radiating patch. We separate the two antenna elements by a distance of 6.5 mm in order to achieve a low mutual coupling at the desired band. The simulations results show that the MIMO antenna has a return loss less than 10 dB and high isolation that is more than 24 dB at 28 GHz. As a result, an envelope correlation coefficient lower than 0.0008 and a diversity gain higher than 9.98 dB are obtained at 28 GHz band enabling 5G cellular communications.**

***Keywords*—MIMO antenna, 5G, mutual coupling, envelope correlation coefficient, diversity gain**

I. INTRODUCTION

The introduction of 5G wireless communication system pioneers a new level of mobile performance with ultra-high speeds and low latencies. The 28 GHz frequency band has emerged as potential candidates for next generation communication. The mmWave MIMO technique is going to be the promising candidate to deliver high data rates required for streaming 8K video content and virtual reality services [1].

Multiple-Input-Multiple-Output (MIMO) antenna systems are widely used in modern wireless communication system.The use of multiple antennas at both the transmitter and the receiver can increase the data rate without extra need of bandwidth and power levels. However, in practical mobile terminal design, closely spaced antennas can cause strong electromagnetic coupling between them. The mutual coupling between the antennas plays an important role in determining the performance of the MIMO communication network. Neutralization line is proposed to reduce the coupling between antennas in [2-3]. In [4], a low mutual coupling antenna array with gain enhancement using metamaterial loading and neutralization line structure is employed to suppress the coupling between two monopole antennas. The authors in [5-8] have enhanced the isolation between two monopole antennas using electromagnetic band-gap (EBG) structure. In the reported works [9-11], the isolation between ports and the smaller size can be improved by using using metamaterial structures.

Various MIMO antennas for 5G applications have been reported in the literature. Ikram, M have designed in [12], a multiband dual-standard MIMO antenna system based on monopoles (4G) and connected slots (5G) for future smart phones. Complementary split ring resonator for isolation enhancement in 5G communication antenna array and Dielectric resonator based MIMO antenna system enabling millimetre-wave mobile devices has been presented in [13-14].

In this letter, an mmWave MIMO antenna with high isolation and compact size is designed. The antenna consist of two equal monopoles and operates at 28 GHz frequency that is suitable for 5G applications. A low mutual coupling is achieved by

ISSN 1737-9334

separating the two antenna elements by a distance of 6.5 mm. The antenna has a compact size of 0.787mm × 11mm × 31mm and is adapted for mmWave MIMO applications. Furthermore, it has a simple structure and is easy in fabrication.

II. Antenna Configurations

The proposed MIMO antenna is designed on a Rogers RT-5880 substrate with a permittivity of 2.2, a loss tangent of 0.0009, and a thickness of the copper layer on the Substrate is 0.787 mm. One symmetrical slot of 0.8 mm width and 2 mm length is loaded at the rectangular patch. The radiating element is fed by a 50 Ohm microstrip line and a complet ground plane is used. The detailed dimensions of the top view are shown in Figure 1 and the optimum dimensions of the proposed MIMO antenna are given in Table 1.

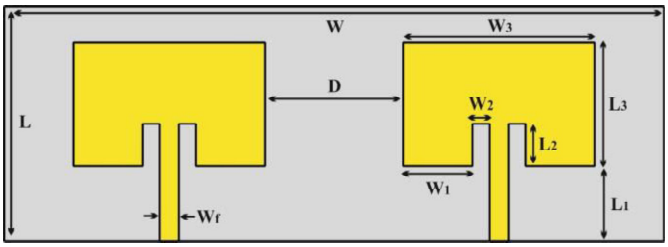

Fig. 1 Geometry of the proposed MIMO antenna.

TABLE I
DIMENSIONAL PARAMETERS OF THE DESIGNED MIMO ANTENNA ARRAY

Parameters	Values (mm)
W	31
L	11
Wf	0.9
D	6.5
W1	3.25
W2	0.8
W3	9
L1	3.5
L2	2
L3	5.85

III. Simulated Results and Discussions

The proposed two port antenna for MIMO applications at 28 GHz frequency band is simulated by using Computer Simulation Technology (CST) Microwave Studio Software. As the two radiators are identical (S11 = S22 and S21= S12), we present only S11 and S21. Figure 2 shows the simulated S parameters of the proposed MIMO antenna array. As can be seen from this figure, the reflection coefficient is less than - 10 dB over the frequency range of (27.12 – 28.92 GHz) and the transmission coefficient between the two port antennas is less than -24 dB at 28 GHz mm-wave frequency.

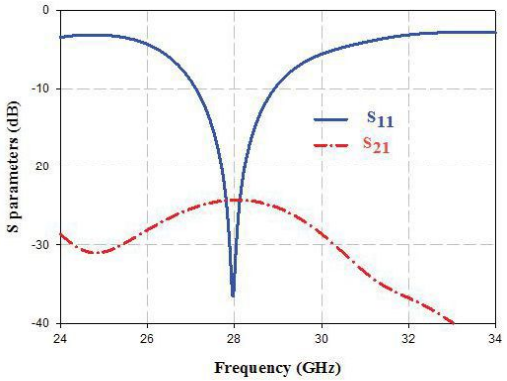

Fig. 2 Simulated S-parameters.

A. Envelope Correlation Coefficient and Diversity Gain

The envelope correlation (ECC) between the ith and jth antenna elements using far-field patterns [15] can be calculated from (1):

$$ECC(i,j)=\frac{\left|\oint\left(X_{PR}E_{\theta i}(\Omega)E^{*}_{\theta j}(\Omega)P_{\theta}(\Omega)+E_{\varphi i}(\Omega)E^{*}_{\varphi j}(\Omega)P_{\varphi}(\Omega)\right)d(\Omega)\right|^{2}}{\oint\left(X_{PR}G_{\theta i}(\Omega)P_{\theta}(\Omega)+G_{\varphi i}(\Omega)P_{\varphi}(\Omega)\right)d(\Omega)\cdot\oint\left(X_{PR}G_{\theta j}(\Omega)P_{\theta}(\Omega)+G_{\varphi j}(\Omega)P_{\varphi}(\Omega)\right)d(\Omega)} \quad (1)$$

Where, X_{PR} denotes cross-polarization power ratio of the propagation environment. In the formula above, $G_{\theta}(\Omega)=E_{\theta}(\Omega)E^{*}{}_{\theta}(\Omega)$ and $G_{\varphi}(\Omega)=E_{\varphi}(\Omega)E^{*}{}_{\varphi}(\Omega)$ are the power patterns of θ and φ polarizations, respectively. $P_{\theta}(\Omega)$ and $P_{\varphi}(\Omega)$ denote the angular density functions of the θ and φ polarizations, respectively. $E_{\theta i}(\Omega)$ and $E_{\theta j}(\Omega)$ are the electric field patterns of the ith and jth antenna elements in the θ polarization, respectively. $E_{\varphi i}(\Omega)$ and $E_{\varphi j}(\Omega)$ are the electric field patterns of the ith and jth antenna elements in the φ polarization, respectively.

In the case of uniform multipath environment, $X_{PR}=1$ and $P_{\theta}(\Omega)=P_{\varphi}(\Omega)=\frac{1}{4\pi}$

The envelope correlation coefficient ECC for two antennas can be approximated as follow:

ISSN 1737-9334

$$ECC = \frac{\left|\oint\left(E_{\theta 1}(\Omega)E^{*}{}_{\theta 2}(\Omega)+E_{\varphi 1}(\Omega)E^{*}{}_{\varphi 2}(\Omega)\right)d(\Omega)\right|^{2}}{\oint\left(G_{\theta 1}(\Omega)+G_{\varphi 1}(\Omega)\right)d(\Omega)\oint\left(G_{\theta 2}(\Omega)+G_{\varphi 2}(\Omega)\right)d(\Omega)} \quad (2)$$

Where, E1 and E2 are the far-field radiation patterns, generated from ports 1 and 2 respectively.

The diversity gain (DG) is dependent on the correlation coefficient and can be given by the following approximate expression [16, 17].

$$DG = 10\sqrt{1-|\rho|^{2}} \quad (3)$$

Where ρ is the complex cross correlation coefficient, and $|\rho|^{2} = ECC$

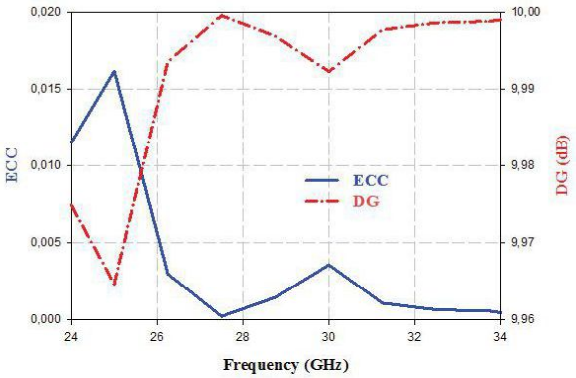

Fig. 3 The envelope correlation coefficient and diversity gain curve.

Figure 3 represents the simulated result of the envelope correlation coefficient and the diversity gain of the presented antenna from far-field patterns. The simulated ECC is below 0.0008 within specified bands. The diversity gain (DG) is mathematically related to ECC and attains the highest value of 9.98 dB at 28 GHz

B. Efficiency

The simulated radiation efficiency of the presented MIMO antenna is very high, maintaining at least a value above 83.58% in the desired frequency band as shown in Figure 4.

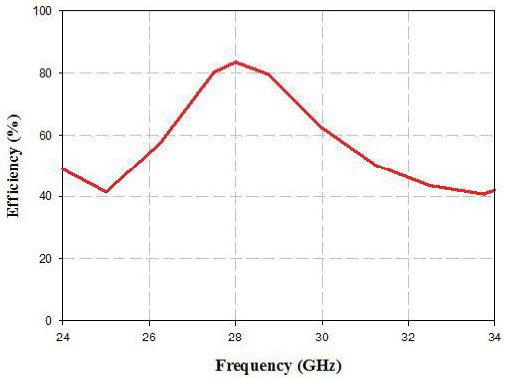

Fig. 4 The efficiency curve

IV. Performance Comparison

Table 2 summarized the comparison of the proposed 5G MIMO antenna and other planar mm-wave antennas intended for future 5G applications published in literature. The proposed structure (P.S) offers a reasonable combination of the most popular preferred antenna traits such as size, isolation, ECC, bandwidth and efficiency. All these traits are expected in modern portable devices targeting the futuristic mm-wave 5G wireless communication.

TABLE II
Performance Comparison between the proposed structure and other recent MIMO antenna

Ref. N°	P.S	[1]	[18]	[19]
Size (mm3)	11×31	48 × 31	55×110	34.8×34.8
Isolation (dB)	24	21	26	18
ECC	0.0008	0.0015	0.01	–
Bandwidth (GHz)	27.12 – 28.92	26 – 31	28.044 & 38.04	25.5–29.5 & 35.5–39.9 & 45–49
Efficiency (%)	>83.58	–	>88.25	>79
Thickness	0.787	0.254	0.508	0.508
Substrate	Rogers RT5880	Neltec	Rogers RT5880	Rogers RT5880

V. Conclusions

A compact mono-band MIMO antenna with high isolation has been proposed and studied for the next generations in this paper. The MIMO antenna is characterized by two simple antennas symmetrically placed on a Rogers RT5880 substrate with a size of 31mm × 11mm × 0, 787mm. We achieve a good impedance bandwidth of 1.8 GHz and high isolation at 28 GHz (under −24 dB) by using a symmetrical slot in the radiating patch

ISSN 1737-9334

and increasing the distance D, respectively. Moreover, a low envelope correlation of less than 8.10−4 and a high diversity gain of more than 9.98 dB are obtained. Furthermore, it has a simple structure, compact in size, is easy in fabrication and suitable for applications such as mobile phone terminals for the fifth generation of mobile communications.

REFERENCES

[1] Z. Wani, M. P. Abegaonkar, and S. K. Koul, "A 28-GHz Antenna for 5G MIMO Applications," vol. 78, no. August, pp. 73–79, 2018.

[2] Kayabasi, A., Toktas, A., Yigit, E., & Sabanci, K. , "Triangular quad-port multi-polarized UWB MIMO antenna with enhanced isolation using neutralization ring", AEU - International Journal of Electronics and Communications, 2017

[3] Zhang, S. and Pedersen, G. F, "Mutual Coupling Reduction for UWB MIMO Antennas With a Wideband Neutralization Line", IEEE Antennas and Wireless Propagation Letters, 15, 166–169, 2016

[4] S. Luo, Y. Li, Y. Xia, and L. Zhang, "A Low Mutual Coupling Antenna Array with Gain Enhancement Using Metamaterial Loading and Neutralization Line Structure," ACES JOURNAL, vol. 34, no. 3, pp. 411–418, 2019

[5] N. Jaglan, S. D. Gupta, B. K. Kanaujia, S. Srivastava, and E. Thakur "Triple Band Notched DG-CEBG Structure Based UWB MIMO/Diversity Antenna", Progress In Electromagnetics Research C, Vol. 80, 21-37, 2018

[6] N. Kumar, and U. K. Kommuri, "MIMO Antenna Mutual Coupling Reduction for WLAN Using Spiro Meander Line UC-EBG", Progress In Electromagnetics Research C, Vol. 80, 65-77, 2018

[7] Dabas, T., Gangwar, D., Kanaujia, B. K., and Gautam, A. K, " Mutual coupling reduction between elements of UWB MIMO antenna using small size uniplanar EBG exhibiting multiple stop bands", AEU - International Journal of Electronics and Communications, Vol. 93, 32-38, 2018

[8] T. Jiang, T. Jiao, and Y. Li, "A Low Mutual Coupling MIMO Antenna Using Periodic Multi-Layered Electromagnetic Band Gap Structures," ACES JOURNAL, vol. 33, no. 3, pp. 305–311, 2018.

[9] Amjad Iqbal , Omar A Saraereh, Amal Bouazizi and Abdul Basir, "Metamaterial-Based Highly Isolated MIMO Antenna for Portable Wireless Applications", electronics, Vol. 7(10), 267, 22 October 2018

[10] S. Luo, Y. Li, Y. Xia, G. Yang, and L. Sun, "Mutual Coupling Reduction of a Dual-Band Antenna Array Using Dual-Frequency Metamaterial Structure," ACES JOURNAL, vol. 34, no. 3, pp. 403–410, 2019

[11] Y. Torabi, A. Bahri, and A. R. Sharifi, "A Novel Metamaterial MIMO Antenna with Improved Isolation and Compact Size Based on LSRR Resonator," IETE J. Res., vol. 62, no. 1, pp. 106–112, 2016.

[12] Ikram, M., M. S. Sharawi, A. Shamim, and A. Sebak, "A multiband dual-standard MIMO antenna system based on monopoles (4G) and connected slots (5G) for future smart phones," Microw. Opt.Technol. Lett., Vol. 60, No. 6, 1468–1476, Jun. 2018.

[13] Selvaraju, R., M. H. Jamaluddin, M. R. Kamarudin, J. Nasir, and M. H. Dahri, "Complementary split ring resonator for isolation enhancement in 5G communication antenna array," Progress In Electromagnetics Research C, Vol. 83, 217–228, 2018.

[14] Sharawi, M. S., S. K. Podilchak, M. T. Hussain, and Y. M. M. Antar, "Dielectric resonator based MIMO antenna system enabling millimetre-wave mobile devices," Antennas Propag. IET Microw.,Vol. 11, No. 2, 287–293, 2017.

[15] Jian Zhang, Jun OuYang, Kai Zhi Zhang, and Feng Yang, "A Novel Dual-BandMIMO Antenna with Lower Correlation Coefficient," International Journal of Antennas and Propagation, Vol. 1-7, 2012

[16] Pierce, J. N. and S. Stein, "Multiple diversity with non independent fading," Proceedings of the IRE, Vol. 48, 89–104, Jan, 1960

[17] Schwartz, M., W. R. Bennett, and S. Stein, " Communication System and Techniques", McGraw-Hill, New York, 470–474, 1965

[18] Hala M. Marzouk, Mohamed I. Ahmed, and Abdelhamed A. Shaalan, "Novel Dual-Band 28/38 GHz MIMO Antennas for 5G Mobile Applications", Progress In Electromagnetics Research C, Vol. 93, 103–117, 2019

[19] Mahmoud, K. R., & Montaser, A. M. , " Performance of Tri-Band Multi-Polarized Array Antenna for 5G Mobile Base Station Adopting Polarization and Directivity Control", IEEE Access, 6, 8682–869, 2018

ISSN 1737-9334

Novel fuzzy logic FLC MPPT controller driving Wind Energy Conversion Systems Based on DFIG controlled by artificial neural network

Azzouz said [a,]*,
Electrical Engineering Department, Faculty of Technology,MsilaUniversity, Algeria.LGE laboratory
azzouzibrahim1985@yahoo.com

Messalti sabir
Department of electrical engineering, Faculty of technology, university of m'sila
M'sila, Algeria
sabir.messalti@univ-msila.dz

Harrag abdelghani
CCNS Laboratory, Electronics Department, Faculty of Technology
University of Ferhat Abbas Setif 1, Setif, Algeria
abdelghani.harrag@gmail.com

Abstract— **In this paper, two intelligent control techniques applied on Wind Energy Conversion Systems (WECS) have proposed and tested, the first uses a novel FLC MPPT (fuzzy logic maximum power point tracking) Fuzzy Logic MPPT Controller extracting the highest power of wind turbine .The second controller is an artificial neural network controller applied to doubly-fed induction generator(DFIG) to improve their control performances, the neural network controller is proposed as an alternative of the conventional proportional and integral (PI) controller to overcome any disturbance, such as fast wind speed variation, short grid voltage fault, parameter variations. The proposed system is designed and evaluated in MATLAB/SIMULINK. Simulation results show the good dynamic performances of the proposed system, in which the effectiveness of the proposed controllers for both wind turbine and DFIG has been demonstrated under variable wind speed.**

Keywords- ***ANN controller, Novel fuzzy logic FLC MPPT controller, active and reactive power control.***

I. INTRODUCTION

The global warming effect together with the diminishing reserves of fossil fuels has contributed to increasing attention given to renewable clean energies [1-8].These renewable clean energy include solar energy, hydro energy and wind energy. There has been an enormous interest in many countries on renewable energy for power generation. This is a feasible power level to be interfaced to the power grid. Wind and solar power are the fastest growth among all renewable energy sources [9-13]. The wind power resources are massive among the world. It has been evaluated that only ten percent of raw wind potential are able to satisfy all the world requirements in electricity if it could be put to use. In light of this, improving the performance of wind turbines and wind energy conversion systems (WECS) is progressively increasing attention as a topic research.[14] [16].This type of energy depends mainly on geographical conditions and weather conditions. Therefore, it is necessary to design a system capable of generating maximum power under these constraints [14-15]. So Maximum Power Point Tracking, (MPPT) technique is required to extract the maximum power from WECS. In wind turbine, the rotor speed continuously changes with changing the wind speed to get maximum power [17-19]. Many researchers have proposed various control schemes in order to extract the optimal accessible power given by the WECS [14]. The simplest techniques for searching the maximum power point are based on PI controller and Perturb and Observe algorithm, but these methods are still classical and lack of performance.

Intelligent control techniques can be considered one of the most important dimensions for the wind turbine efficiency and hence the control techniques enhancement has direct contribution to the better performance of wind turbines. In this paper, in order to overcome the drawbacks of the conventional MPPT algorithms, a novel FLC MPPT (fuzzy logic maximum power point tracking) is presented. This technique gives a very good tracking of reference and then the increase of efficiency of the wind turbine generator system,,,and offers independence to the variation of the parameters [20] [21].

The proposed MPPT strategy has been applied to a wind energy conversion system based on doubly-fed induction generator, that has several advantages [22-24]. It reduces the stresses of the mechanical structure and the acoustic noise, and regulates both active and reactive power. Its backto-back PWM converters, connected between the grid and the rotor circuit are sized only for 30% of the full power of the generator[16,22,25].The topology of PWM rectifier-inverter that integrates PWM converters in the machine side and the grid side is investigated to offer the possibility of the bidirectional power flow.

Intelligent methods, as Genetic algorithms and artificial neural networks are being adopted applications for the control of the double-feed induction generator, because of their flexibility, and explanation capabilities that are useful to deal with strong nonlinearities. [28]

The control algorithm is developed to use the artificial neural network, due to its ability of separately controlling the active

ISSN 1737-9334

and reactive power of the generator efficiently [28], as well as they are independent to parametric variation, in which the quadrature voltage component controls the active power while the direct voltage component controls the reactive power.
The paper is organized as follows. Section 2 presents the dynamics models of both DFIG and wind turbine system. Section 3detailed the proposed MPPT strategy based on fuzzy logic techniques. Section 4 presents the control of the DFIG based on artificial neural network, the proposed control scheme is investigated according to wind speed variations. Section 6 is reserved to present numerical simulations that illustrate the effectiveness of the proposed control topology. Finally, conclusions about the effectiveness and the performance of the proposed FLC MPPT and ANN DFIG control algorithms are outlined.

1. WIND ENERGY CONVERSION SYSTEM MODELLING.

The conversion chain consists of a fixed-pitch turbine that captures the wind energy coupled with a DFIG which permits the transformation of the captured mechanical power to electrical power. Power electronic converters are employed with DFIG in order to maintain the power at its optimum with various wind speed. A schematic overview of the WECS is shown in Fig.1.

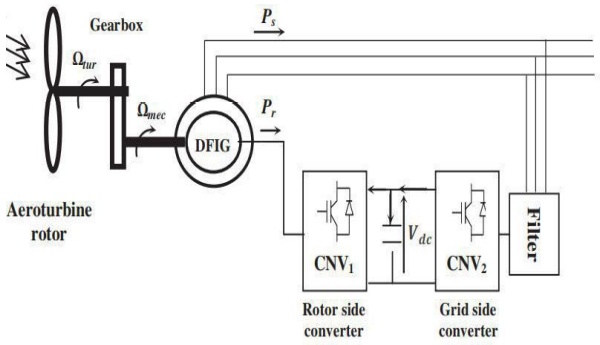

Figure 1 Wind turbine system based on DFIG.

2.1Wind turbine model

A total scheme of a wind energy conversion system is shown in Fig1. P_t is the mechanical power captured by the wind turbine blades, which are functions of the air density ρ , the radius R and the wind speed v , given as.

$$P_t = \frac{1}{2}\rho\pi R^2 C_p(\lambda,\beta)v^3 \quad (1)$$

The efficiency coefficient $C_p(\lambda,\beta)$, which depends on tip speed ratio λ and blade pitch angle β , determines the amount of wind kinetic energy that can be captured by the wind turbine system.A generic equation is used to model $C_p(\lambda,\beta)$. This equation, based on the modeling turbine characteristics, is shown as follows:

$$C_p(\lambda,\beta) = (0.5-0.0167(\beta-2))\sin\left[\frac{\pi.(\lambda+0.1)}{18.5-0.3.(\beta-2)}\right] - (2)$$
$$0.00184.(\lambda-3).(\beta-2)$$

The equation of the TSR (λ) can be explained as follows,

$$\lambda = \frac{\Omega_t . R_t}{v} \quad (3)$$

Where, Ω_t is the rotor speed of a wind turbine.

2.2 DFIG Model

The mathematical model of the DFIG is derived from the PARK theory in order to simplify the differential equations as shown in fig.2. The DFIG model is described in the d-q Park reference frame, through the following equations [33-35].

$$\begin{cases} V_{sd} = -R_s . I_{sd} + \dfrac{d\phi_{sd}}{dt} - \omega_s \phi_{sq} \\ V_{sq} = -R_s . I_{sq} + \dfrac{d\phi_{sq}}{dt} + \omega_s \phi_{sd} \\ V_{rd} = R_r . I_{rd} + \dfrac{d\phi_{rd}}{dt} - \omega \phi_{rq} \\ V_{rq} = R_r . I_{rq} + \dfrac{d\phi_{rq}}{dt} + \omega \phi_{rd} \end{cases} \quad (4)$$

Where R_s and R_r are respectively the resistance of the stator and rotor windings, ω_s is the rotational speed of the synchronous reference frame, and ω the rotor reference frame rotating. The flux linkages are given by.

$$\begin{cases} \phi_{sd} = -L_s I_{sd} + M I_{rd} \\ \phi_{sq} = -L_s I_{sq} + M I_{rq} \\ \phi_{rd} = L_r I_{rd} - M I_{sd} \\ \phi_{rq} = L_r I_{rq} - M I_{sq} \end{cases} \quad (5)$$

Where L_s and L_r are respectively the inductances of the.
The electromagnetic torque of the DFIG is expressed by:.

$$T_{em} = p.M_{sr}.\left(I_{sq}.I_{rd} - I_{sd}.I_{rq}\right) \quad (7)$$

Where p is the number of pole pairs.
By neglecting the power losses associated with the stator resistances, the active and reactive power stator powers for the DFIG can be expressed as:

$$\begin{cases} P_s = -V_{sd}.I_{sd} - V_{sq}.I_{sq} \\ Q_s = -V_{sq}.I_{sd} + V_{sd}.I_{sq} \end{cases} \quad (8)$$

2. DFIG wind turbine control

The control schemes for a wind turbine include the maximum power point tracking control, and the DFIG control.

3.1Wind turbine control

The generator can be directly controlled by the generator side controller to track the maximum power available from the wind turbine. To extract maximum power at variable wind speed, the turbine should always operate at λ_{opt} . This occurs by controlling the rotational speed. So, it always operates at

ISSN 1737-9334

the optimum rotational speed, ω_{opt} , for different wind speed.

The fuzzy logic controller is used to search the optimum rotational speed which tracks the maximum power point at variable wind speeds [36].

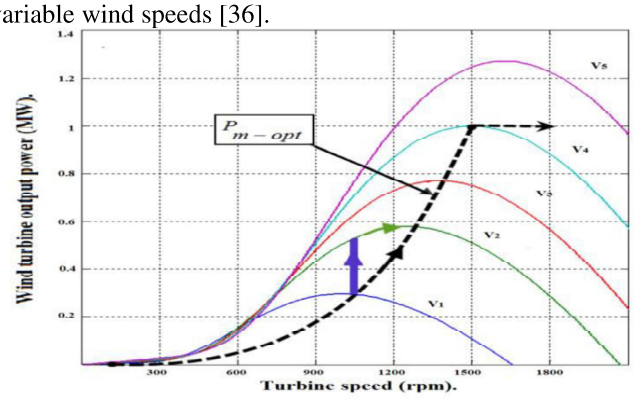

Fig.3. The characteristic of power-speed for a wind power conversion system with a fixed pitch.

3.1.1Fuzzy logic MPPT controller

A fuzzy control system is a logical mathematical system that analyzes analog input values in terms of logical variables that take on continuous values between 0 and 1, in contrast to classical or digital logic, which operates on discrete values of either 1 or 0.This type of control, approaching the human reasoning, making use of tolerance, uncertainty, imprecision and fuzziness in the decision-making process, managed to offer a very satisfactory performance, with no need of a detailed mathematical model of the system, but just incorporating the expert knowledge into fuzzy rules. In addition, FLC has inherent abilities to deal with noisy or imprecise data; thus, it is able to extend its control capability even to operating conditions where linear control techniques fail, as in the case of system control with parameter variation [37-39]. The FLC system consists of three components. They are fuzzification, the rule base, and defuzzification. Fuzzification, the first component of the FLC, converts the exact inputs to fuzzy value [40]. These fuzzy values are sent to the rule-base unit and processed with fuzzy rules, and then these derived fuzzy values are sent to the defuzzification unit. In this unit, the fuzzy results are converted to exact values using centre of area method [36,41].

At first, the various terms are selected to form the fuzzy rules. Based on these terms, the different rules are formed.The linguistic error terms are: Very Negative VN, Negative N, Small Negative SN, Zero Z, Small Positive SP, Positive P, Very Positive VP.and for derivative of error are Negative, Zero, Positive.

The seven various terms of error and three terms of change in error are shown in figure 4 and figure 5 respectively.

In the proposed fuzzy controller, totally 21 rules are formed and it shown in table 2.

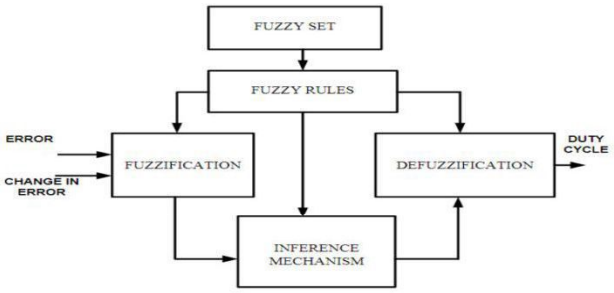

Fig. 4. Basic structure of FLC.

Table 2: Various fuzzy rules for MPPT

FLC Set of rules		**Derivative of error**		
		Negative	Zero	Positive
Error	VN	VP	VP	VP
	N	SN	SN	VN
	SN	N	SN	VN
	Z	Z	Z	Z
	SP	SP	SP	P
	P	P	VP	VP
	VP	VP	VP	VP

.

The fuzzy logic controller is present to track the maximum power from the wind by using the rotor speed of the wind T. In our MPPT controller, we use the error between reference speed and the real rotor speed and the change of this error as inputs. Output of the fuzzy controller is the duty cycle of the boost converter. By adjusting the duty cycle of the boost converter the maximum power will be achieved.

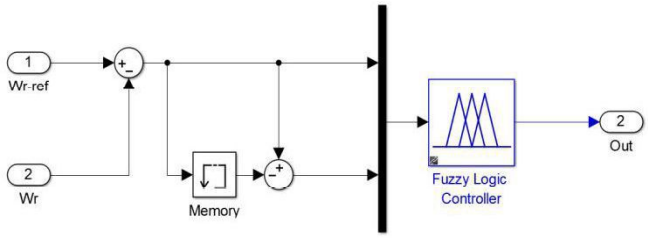

Figure5: Model of the Proposed Fuzzy Logic Controller.

3.2. DFIG control using NEURAL NETWORK

Neural networks are a computational method that uses an enormous group of artificial neurons [28] [42]. These neurons are inexactly equivalent to axon in a biological brain [43-44]. Neural networks are used in various fields such as speech recognition, language translation, image processing, machine learning, and computer science, controlling power electronics converters that interface the WECS systems [28,4548].

ISSN 1737-9334

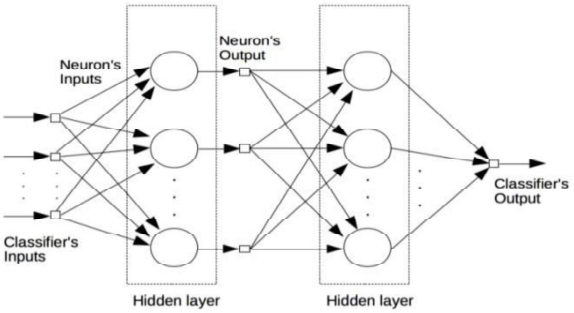

Fig. 6. The structure of the feed-forward neural network.

3.4. Design of the Neuronal Network Controller.

The objective of this section is to design a new controller in order to assure a robust control of the DFIG facing the parametric changes, we presented the design of the proposed neuronal network controller.

Active power and reactive power are the inputs to the ANN, and the object is the direct and quadrature rotor references voltages. The direct component of the rotor voltage is related to the reactive power at the stator, and the quadrature component of the rotor voltage is related to the real power at the stator.The training data of inputs and objectives come from the look up table with PI controller operation which is acquired with different points of wind speed (different values of optimal reference active power) during simulation processes.

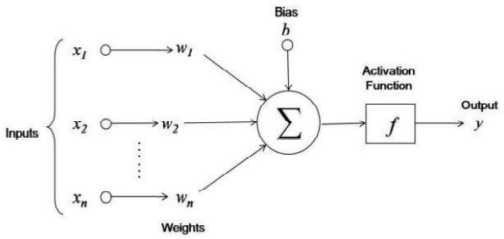

Fig.7 Developed ANN Controller for WECS

Feed forward or multi-layer perceptron consist of three parts: neurons, activation functions, and bias. The neurons can be either input neurons, output neurons, or hidden neurons[28] +[45] [48].The determination of the combinations of hidden layers and the number of neurons in each layer which can give the best performance for a given problem has no general guidelines. In our case, the number of hidden layers and the number of neurons in each hidden layer were chosen heuristically on a trial and error basis. After several attempts, we opted for two hidden layers containing 06 neurons where the first hidden layer has 04 neurons and the second has 02 neurons. The linear transfer function "purelin" are used in the final layer of multilayer networks that are used as function approximators. The sigmoid activation function "tansig" is commonly used in the hidden layers of multilayer Networks.

3. SIMULATION RESULTS

The proposed work is implemented in MATLAB/SIMULINK and its simulation diagram is shown in figure 5. The numerical illustration considers the wind conversion system with the parameter values given by the table2

The proposed strategy of control is tested for different wind velocity variations. The wind speed signal variation is presented in Fig.8.

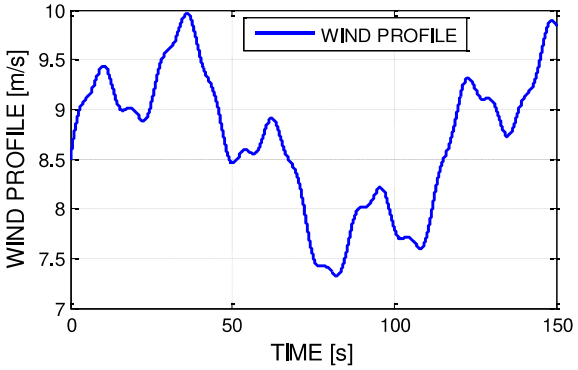

Fig. 8 Wind speed variation

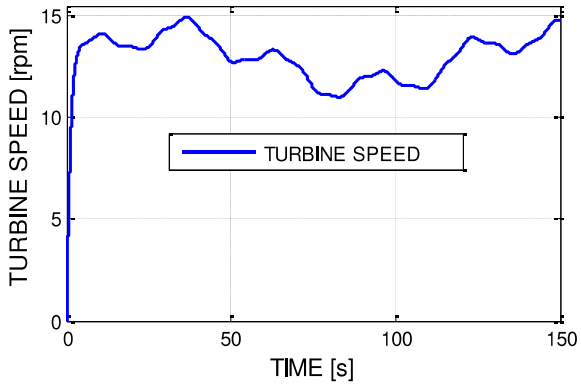

Fig. 9 Turbine rotational speed.

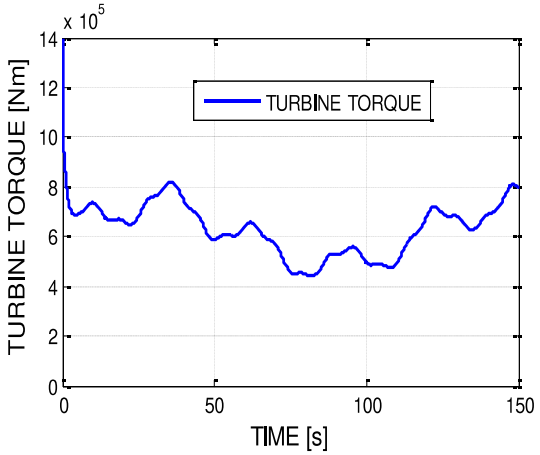

Fig. 10 Turbine torque

.

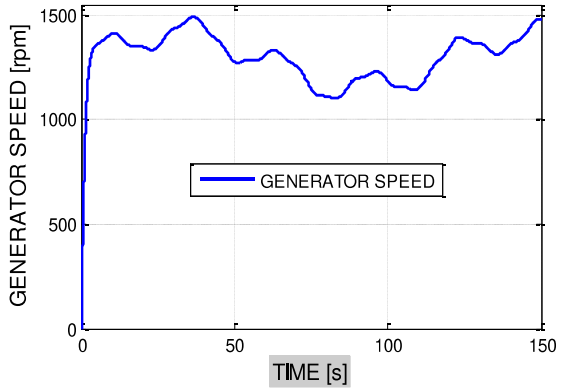

Fig.11generator rotational speed.

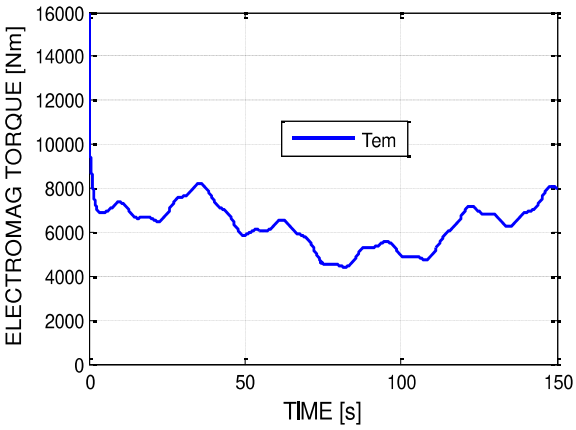

Fig.11. Electromagnetic torque.

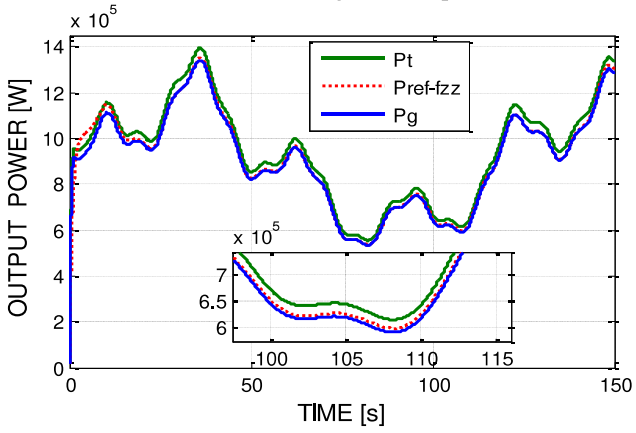

Fig. 12 Output power

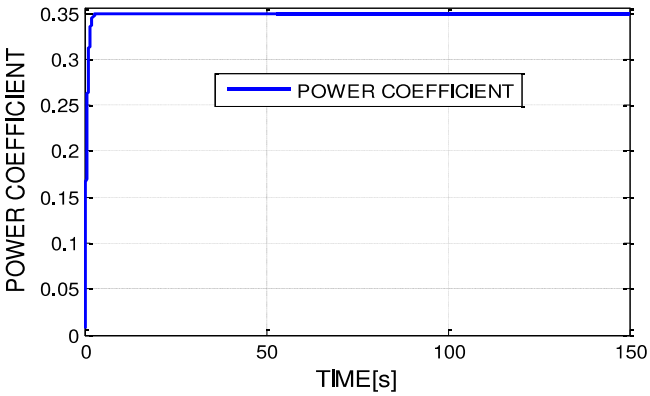

Fig. 13 Coefficient of power.

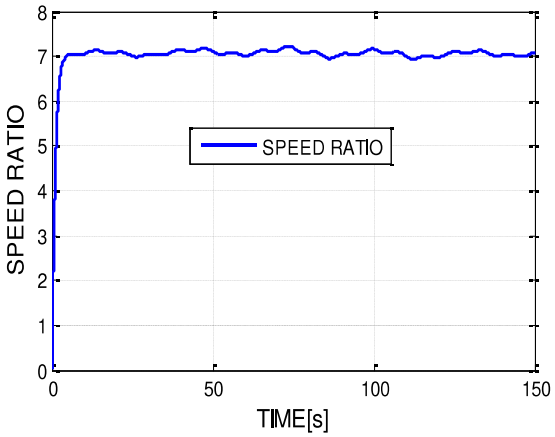

Fig.14tip speed ratioλ of WECS.

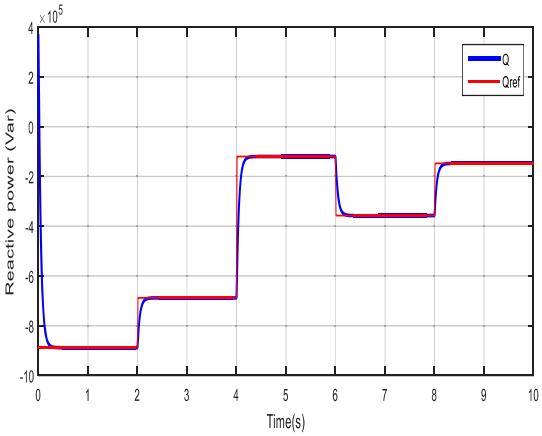

Fig.15 Active power control using ANN controller

ISSN 1737-9334

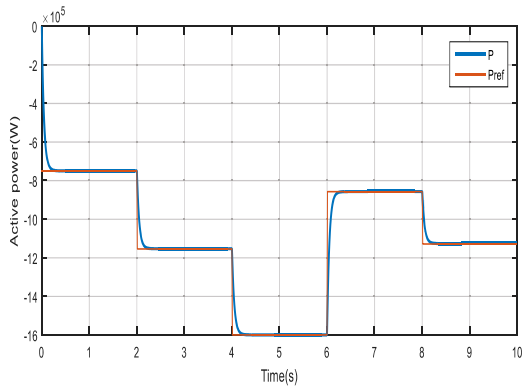

Fig.16 Reactive power control using ANN controller

4. Conclusion.

This paper focuses on control strategy dedicated for a wind conversion system to ensure maximum peak power tracking (MPPT) and control of active and reactive powers generated by DFIG by two intelligent techniques. In the first step, a Fuzzy Logic Controller for MPPT was designed and developed. It was shown that the designed controller is able to track reference maximum power for the WECS with good accuracy for fluctuating wind speeds. In second step, the ANN algorithm for independent control of powers has been proposed and implemented. It can be noticed the better result with the ANN-based controllers: transient regimes present small peaks, or absence of them in some cases; faster system responses, reaching the steady state condition in shorter time. Thus, it was demonstrated that the DFIG rotor-side converter control voltages can be obtained using ANN-based controllers; Artificial intelligence techniques are a strong alternative to linear controllers and can substitute them with the referred advantages.

5. Reference

[1] WenchaoMeng, Qinmin Yang, You Ying, Yong Sun, Zaiyue Yang, Youxian Sun. "Adaptive Power Capture Control of Variable-Speed Wind Energy Conversion Systems With Guaranteed Transient and Steady-State Performance"IEEE Transactions on Energy Conversion (Volume: 28, Issue: 3, Sept. 2013) Page(s): 716 - 725

[2] Muhammad Shahzad Nazir, Qinghua Wu, Mengshi Li,Symmetrical Short-Circuit Parameters Comparison of DFIG–WT, International Journal of Electrical and Computer Engineering Systems,Vol 8, No 2, 77-83 (2017)

[3] A. K. Rathore, A. K. S. Bhat, R. Oruganti, "Analysis design and experimental results of wide range ZVS active-clamped L–L type current-fed DC/DC converter for fuel cells to utility interface", IEEE Trans. Ind. Electron., vol. 59, no. 1, pp. 473-485, Jan. 2012.

[4] Danijel Topić, Damir Šljivac, Mirko Gagro Influence of Distributed Power Generation from Renewable Energy Sources on Reliability of Distribution Networks, International Journal of Electrical and Computer Engineering Systems,Vol 6, No 2, 51-56 (2015)

B. Bose, "Global warming: Energy environmental pollution and the impact of power electronics", *IEEE Ind. Electron. Mag.*, vol. 4, no. 1, pp. 6-17, Mar. 2010.

[5] N. Denniston, A. M. Massoud, S. Ahmed, P. N. Enjeti, "Multiple-module high-gain high-voltage DC–DC transformers for offshore wind energy systems", IEEE Trans. Ind. Electron., vol. 58, no. 5, pp. 1877-1886, May 2011.

[6] C. T. Pan, C. M. Lai, "A high-efficiency high step-up converter with low switch voltage stress for fuel-cell system applications", *IEEE Trans. Ind. Electron.*, vol. 57, no. 6, pp. 1998-2006, Jun. 2010.

[7] A. I. Bratcu, I. Munteanu, S. Bacha, D. Picault, B. Raison, "Cascaded DC–DC converter photovoltaic systems: Power optimization issues", *IEEE Trans. Ind. Electron.*, vol. 58, no. 2, pp. 403-411, Feb. 2011.

[8] D. Kumar, K. Chattrejee, "A review of conventional and advanced MPPT algorithms for wind energy systems", *Renewable and sustainable energy reviews*, vol. 55, pp. 957-970, 2016.

[9] G. Todeschini, A. E. Emanuel, "Transient response of a wind energy conversion system used as active filter", *IEEE Trans. Energy Convers.*, vol. 26, no. 2, pp. 522-531, Jun. 2011.

[10] F. A. Ramirez, "Development of a Grid-Connected Wind GenerationSystem with a Modified PLL Structure" "" IEEE transactions on sustainable energy, vol. 3, no. 3, July 2012.

[11] Mukhtiar Singh "Grid Interconnection of Renewable Energy Sources at the Distribution Level with Power-Quality Improvement Features," IEEE transactions on power delivery, vol. 26, no. 1, January 2011.

[12] G. M. Joselin Herbert, S. Iniyan, E. Sreevalsan, S. Rajapandian, "A review of wind energy technologies", *Renewable Sustainable Energy Rev.*, vol. 11, no. 6, pp. 1117-1145, Aug. 2007.

[13] Hoang Thinh Do ; Tri Dung Dang ; Hoai Vu Anh Truong ; Kyoung Kwan Ahn ."Maximum Power Point Tracking and Output Power Control on Pressure Coupling Wind Energy Conversion System" IEEE Transactions on Industrial Electronics (Volume: 65, Issue: 2, Feb. 2018)Page(s): 1316 - 1324

[14] Cheng-ShionShieh "Fuzzy control for maximum power extraction"2018 IEEE International Conference on Applied System Invention (ICASI) Chiba, Japan

[15] Donghai Zhu, ZouXudong, Lu Deng, Qingjun Huang, Shiying Zhou, Yong Kang, "Inductance-Emulating Control for DFIG-Based Wind Turbine to Ride-Through Grid Faults", *IEEE Transactions on Power Electronics*, vol. 32, no. 11, pp. 8514-8525, 2017.

[16] Abdullah M.A., Yatim A.H.M., Tan C.W., Saidur R., "A Review of Maximum power point tracking algorithms for wind energy systems", Elsevier, Renewable and Sustainable Energy Reviews, vol. 16, no. 5, pp. 3220-3227, June 2012.

ISSN 1737-9334

Molecular Docking Studies of Human COX-2 with Lignins

TAIDI Loubna[#1], MAURADY Amal[*2], BRITEL Mohammed Reda [#3]

Laboratory of innovative technology
University Abdelmalek Essaadi

Taidiloubna_91@hotmail.fr
amal-maurady@hotmail.com

***Abstract*— Natural products present in medicinal plants play an important role in several biological processes, and many have been involved in the alleviation and control of inflammation-related diseases. These actions have been linked to an action involving a direct inhibitory binding especially on COX-2 protein and not for COX-1 protein. The present study reports the molecular docking study of lignins for COX-2 and COX-1 inhibitory and anti-inflammatory activities utilizing Pymol/Autodockvina Plugin as docking protocols. Our aim is to well understand the structural and conformational features of lignins for the inhibitory capability and illustrate their binding mode COX-2 and COX-1 active site using the structural difference between them and the binding mode of the co-crystallized COX-2 with the rofecoxib. In this paper, six lignins namely pinoresinol, syringaresinol,1-Acetoxypinoresinol, berchemol, 8-Hydroxypinoresinol and (-)-Olivil were analysed through molecular docking study and compared to refecoxib and their drug like proprieties on the basis of ADME and Lipinski rules of five. The described docking score, the interaction profile and the obtained conformations suggested berchemol as the best inhibitor for COX-2 protein. In silico lipinski rule of five and ADME study were also performed to assess drug likeness and toxicity profiles of the selected molecules and show that berchemol is a best candidate to inhibit COX-2 enzyme. This study opens up a new platform for the development of lignins as a based on natural drugs for treating. In this study berchemol was found to be the best among all the six lignins analyzed, followed with syringaresinol.**

***Keywords*— Cyclooxygenase-2; inhibition; selectivity; terpenoids; lignins; molecular docking study; Lipinski rule of five, ADMET prediction.**

I. INTRODUCTION

Inflammation is the immune system's response to infection and injury and has been implicated in the pathogeneses of diseases such as arthritis, cancer, atherosclerosis, stroke and epilepsy, as well as neurodegenerative diseases (for example, multiple sclerosis, Alzheimer's and Parkinson's diseases) (1). Prostaglandins, that sustain homeostaticfunctions and mediate pathogenic mechanisms, including the inflammatory response, are generated from arachidonate by the action of cyclooxygenase (COX) isoenzymes (2). The two isoforms of cyclooxygenase, COX-1 and COX-2, have been identified. Whereas COX-1 is referred to as a 'constitutive isoform', and is considered to be expressed in most tissues under basal conditions (3). In contrast, COX-2 expression was found to be induced in response to various pro-inflammatory factors, hormones, growth factors and oncogenes, and inhibited by glucocorticoids (4, 5).

Nonsteroidal anti-inflammatory drug (NSAIDs) blocks the COX enzymes and reduces prostaglandins throughout the body. As a consequence, ongoing inflammation, pain, and fever are reduced (6). NSAIDs vary in their potency, duration of action, how they are eliminated from the body, how strongly they inhibit COX-1 versus COX-2 (7). Since the prostaglandins that protect the stomach and support platelets and blood clotting also are reduced in inhibiting COX-1 protein, NSAIDs can cause ulcers in the stomach and promote bleeding (8). Alternatively, a large number of natural compounds have been consumed in medicinal plants, and their anti-inflammatory activities have been reported.

Many studies on natural compounds have already been explored and proven to show anti-inflammatory activity. Anthocyanins and cyanidins were showed a good inhibitory activity against COX-2 enzyme (9-11). Else, the docking analyses of 10 selected terpenoids revealed that all of the terpenoids present a potential inhibition against COX-1 rather than COX-2 with the oleanolic acid as the most potent inhibitor of COX-2 with the binding energy of [−18.68 Kcal/mol and −18.25 Kcal/mol] (12). Whereas, lignins such as syringaldehyde present in fruiting bodies of Elaphomyces granulates shows cyclooxygenase-2 (COX-2) inhibitory activity and demonstrated moderately inhibits COX-2 activity, with an IC 50 of 3.5 μg/ml (13). On the other hand, sinapyl alcohol, a lignin precursor, exhibits anti-inflammatory and antinociceptive properties. It also performs the inhibition of lipopolysaccharide-induced nitric oxide, PGE2 (prostaglandin) and TNF-α production by macrophages; and reduces the expression of inducible NO synthase and cyclooxygenase (COX)-2 in a concentration-dependent manner (14). In many cases, the effects of lignins could be explained by their antioxidant capacity (15).

As with other biological macromolecules, the interest in lignin has increased due to its potential applications. Some aspects related to the applications of lignin have been summarized, including some pharmacological applications, such as anti-tumor, anti-virus, antioxidant and antimicrobial activities (16). They are bioactive compounds exhibiting

ISSN 1737-9334

various biological properties, including anti-inflammatory, antioxidant and antitumor activities (17). The present review attempts to describe the potential beneficial effects of six lignans intake on human COX-2 inhibition. Our aim is to study the inhibition activity of selective lignins against COX-2 enzyme in the view of the role that they play in anti-inflammatory process, of their important three-cyclic and flexible structure which resemble to the selective drugs. In this work pinoresinol, syringaresinol, 1-Acetoxypinoresinol, berchemol, 8-Hydroxypinoresinol, (-)-Olivil, that are lignins identified using hyphenated LC-SPE-NMR technique using postcolumn solid-phase extraction to the direct analysis of phenolic compounds in the polar part of olive oil (18), will be tested with in silico study for COX-2 activity inhibition.

II. MATERIAL AND METHODS

A. *Molecular docking protocol*

Molecular docking protocols are widely used for predicting the binding affinities for a number of natural compounds. In current work, our aim was to examine the binding affinity and the chemical properties of lignans under the docking scores. The docking studies of the selected structures into the COX-2 active site were performed using *PyMol molecular visualization platform* with *AutoDock/Vina PyMol plugin*. Human COX-2 and COX-1 were used as the target protein for the docking studies. Crystal structure of COX-2 (PDB ID; 5KIR) was obtained from the protein data bank (PDB). Since there is no crystallographic structure of human COX-1, the model of human COX-1 was calculated. Primary sequences of human COX-1 (ID: P23219) was used to obtain COX-1 model. *SWISS- MODEL* was performed to build the 3D structures of human COX-1 according to the homology modeling method using ovine prostaglandin H2 synthase-1(PDB ID: 1EQG) as template. Steriochemical validations of the models were done using *PROCHECK tool* (http://nihserver.mbi.ucla.edu/SAVES/). Proteins were refined by removal of water molecules and adding hydrogen with *Pymol* software. Compounds stucrtures have been shown in table 1, they were obtained from *PubChem* datanase (https://pubchem.ncbi.nlm.nih.gov/), and converted into pdb files using *Openbabel* software (*http://openbabel.org/wiki/Category:Installation*). Energy minimized conformations of ligands were subjected to calculation of amber force field (GAFF). The number of runs for each docking analysis was set to 100. Grids were generated using the information on the crystal structure and docking information on the synthetic COX-1 and COX-2 inhibitors previously reported in the literature. Thus the active site comprised of His-90 Arg-120, Tyr-355, Tyr-385, Arg 513, Val-523 and Ser-530 (19). It was centered with the x,y,z coordinates for COX-2 receptor with 23.21 1.32 34.26 and 251,47 107,43 0,92 for COX-1 receptor . The boxes size were 60, 60, 60. Autodock tools (ADT) package was employed to produce both grids and docking parameter files gpf and dpf. A 2.0 Å clustering tolerance was applied to construct clusters of the closest compounds, and the initial coordinates of the ligand were used as the reference structure. At the end of docking, the structures were ranked by energy.

TABLE I: The selected lignins and rofecoxib chemical structures

NO	Compound name	2D structure
1	Pinoresinol	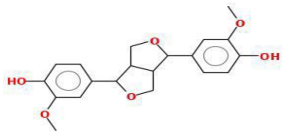
2	Syringaresinol	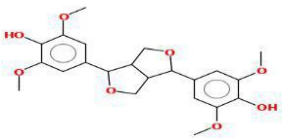
3	1-Acetoxypinoresinol	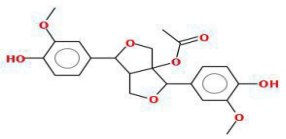
4	Berchemol	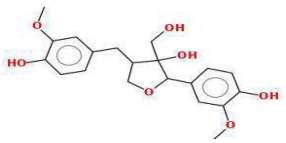
5	8-Hydroxypinoresinol	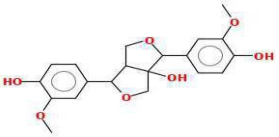
6	(-)-Olivil	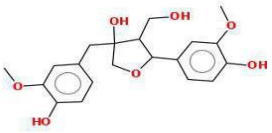
7	Rofexocib	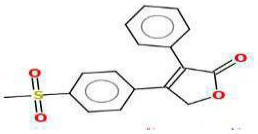

B. *Lipinski's rule of five parameters*

Lipinski's Rule of Five describes molecular properties important for a drug's pharmacokinetics in the human body, including their absorption, distribution, metabolism, and excretion (20). Based on a series of physicochemical requirements, not more than one of which should be violated. Molecules violating any of

ISSN 1737-9334

these rules may have problems with bioavailability (21). The analysis was carried out to find whether the newly proposed compounds obeyed this rule using *Molinspiration* server (https://www.molinspiration.com/).

C. ADME properties

Efficacy and safety of a drug compound is a determinant factor in bringing it into the market and these factors can be considered through the absorption, distribution, metabolism, excretion and toxicity (ADME) profiling (22). Commonly, compounds with inappropriate properties enhance the development costs and put a considerable burden on patients (23). Consequently, it is significant to predict ADME properties during hit identification and optimization. ADME properties of the natural compounds were estimated by *preADMET* online database (https://preadmet.bmdrc.kr/).

III. Results and Discussion

Many drugs fail to enter into clinical markets due to poor pharmacokinetics. In the present study, we explored the pharmacokinetics of the selected compounds using *Molinspiration* and *preADMET* online database.

A. Lipinski's rule of 5 results

Lipinski'sThe traditional method to evaluate drug-likeness is to check compliance to Lipinski's Ro5, which includes the numbers of hydrophilic groups, molecular weight and hydrophobicity (Lipinski, 2000). Selected lignins under study showed good results when analyzed using Lipinski's Ro5. Results showed in table 2 revealed that Ro5 parameters are qualified by all lignin's, therefore we can conclude that they can increase its chances of becoming a drug. rule of 5 results

TABLE II: Summary of drug like properties of the six selected lignins and the refecoxib on the basis of Lipinski Rule of Five

NO	ligand	LogP	H-acc	H-don	MW	NOV
1	Pinoresinol	2.59	6	2	358.39	0
2	Syringaresinol	2.62	8	2	418.44	0
3	1-Acetoxypinoresinol	2.35	8	2	416.43	0
4	Berchemol	1.39	7	4	376.40	0
5	8-Hydroxypinoresinol	1.64	7	3	374.39	0
6	(-)-Olivil	1.39	7	4	376.40	0
7	Rofexocib	2.79	4	0	314.36	0

B. ADMET properties results

Blood brain barrier: range between 0.094 and 0.07. Table 3 shows that all compounds are having values less than 1 which means low absorption to CNS. We conclude that the predicated BBB filter indicated low for all lignins, so we suggest that they may not permeate to the brain and thus not causing damage to the central nervous system.

Caco2 cell permeability: Values less than 4 are poorly permeable, 4-70 are moderately permeable and more than 70 are considered as highly permeable. In the present study, preADMET has determined that all compounds are in the range of 20-39 which means all compounds are moderately permeable to Caco 2 cell lines. For rofecoxib, is in the range lees than 4 (2.72), which means that it poorly permeable.

Human intestinal absorption: preADMET assess the intestinal absorption capacity of the tested compounds. Values ranging 0-20 % found to be poorly absorbed and 20-70 % moderately absorbed, values ranging 70-100 % are found to be compounds with greater absorption. From table 3, all the selected compounds are above % HIA values. Hence all these molecules are found to be efficiently absorbed by human intestine.

MDCK cell permeability: Oral bioavailability was predicated by using Madin-Darby canine kidney (MDCK) cell permeability, the recommended range for MDCK is <25 poor and >500 great. Results indicated that all lignins and rofecoxib were indicated to have poor oral bioavailability.

TABLE III: preADMET prediction of selected lignins and rofecoxib

NO	Ligand	BBB	Caco2 nm/sec	HIA %	MDCK nm/se
1	Pinoresinol	0.07	35.13	93.47	2.61
2	Syringaresinol	0.02	39.30	94.14	0.20
3	1-Acetoxypinoresinol	0.02	27.75	93.96	4.47
4	Berchemol	0.14	20.75	83.20	5.17
5	8-Hydroxypinoresinol	0.09	22.79	89.61	4.33
6	(-)-Olivil	0.13	20.75	83.20	4.35
7	Rofecoxib	0.01	2.72	98,22	11,27

The obtained results improve the efficacy and safety of the selected compound as drugs.

C. Pymol/Autodockvina Plugin results

The active site of COX-2 is divided into three important regions, the first being a hydrophobic pocket defined by Tyr-385, Trp-387, Phe5-18, Ala-201, Tyr-248 and Leu-352; the second region being the entrance of the active site lined with the hydrophilic residues Arg-120, Glu524, Tyr355 and the third is a side pocket lined by His-90, Arg-513 and Val-523 (24) . In case of the selective COX-2 inhibitors such as rofecoxib, the phenyl ring was in the close vicinity of the hydrophobic pocket and the phenyl sulphonamide group occupied the side pocket and showed binding with an important residues in the binding of selective COX-2 inhibitors Gln-192 and Ile-517 (Figure 7). The results are in accordance with the literature reports of docking of the selective COX-2 inhibitors (25). One of the keys to developing COX-2 selective drugs is the larger active site of COX-2, which makes it possible to make molecules able to fit the COX-2 (26).

Based on the binding energy parameter showing in table 5, berchemol was found to be the best among all the six lignins analysed, followed with 1-Acetoxypinoresinol, (-)-Olivil, 8-Hedroxypinoresinol, pinoresinol and syringaresinol.

ISSN 1737-9334

The superimposition of these molecules with rofecoxib in COX-2 active site showed that berchemol have the highest recognition at the COX-2 binding site. It flexible structure allows to create conformation to embed properly within the active site, such as rofecoxib and to interact with the selectivity residues Gln-192 and Val-349 (Figure 4). Followed with pinoresinol, with the binding energy of -8.38 Kcal/mol, it structure allows to to interact with the fixation residue such as Arg-120, selectivity residue Gln-192 and hydrophobic pocket residues Phe-518 and Ile-517 (Figure 1), but without embedding properly in the three regions of COX-2 active site such as rofecoxib and berchemol. In contrary of pinoresinol, 1-Acetoxypinoresinol, (-)-Olivil and 8-Hydroxypinoresinol, with the binding energy of -9.02, -8.63 and -8.46 successively, take the same pose in COX-2 active site (Figure 7), and did not embed the lateral pocket for to interact with the selectivity residues such as berchemol, pinoresinol and rofecoxib. Their structures allows to create hydrogen bound only with the entrance of the active site, specially with Arg-120, and hydrophobic pocket amino acid Ser-530 and Tyr-385 (Figure 3, 5 and 6). Whereas, syringaresinol lets to interact only with a fixation residue Arg-120 and Met-522 from the hydrophobic pocket.

TABLE IV: preADMET prediction of selected lignins and rofecoxib

NO	Ligqnds	COX-2		COX-1	
		Binding energy (Kcal/ mol)	Hydrogen bound	Binding energy (Kcal/ mol)	Hydrogen bound
1	Pinoresinol	-8.38	Arg-120 Gln-192 Phe-518 Ile-517	-7.45	-
2	Syringaresinol	-8.23	Arg-120 Met-522	-8.29	Ser-530
3	1-Acetoxypinoresinol	-9.02	Arg-120 Tyr-385 Ser-530	-7.48	-
4	Berchemol	-9.71	Gln-192 Val-349	-8.48	Arg-120
5	8-Hydroxypinoresinol	-8.46	Arg-120 Tyr-385	-8.5	Arg-120 Tyr-355 Met-522
6	(-)-Olivil	-8.63	Arg-120 Tyr-385 Val-349	-7.85	Ala-527
7	Rofexocib	-10.3	Gln-192 Ile-517 Phe-518	-8.52	Arg-120 Gly-526

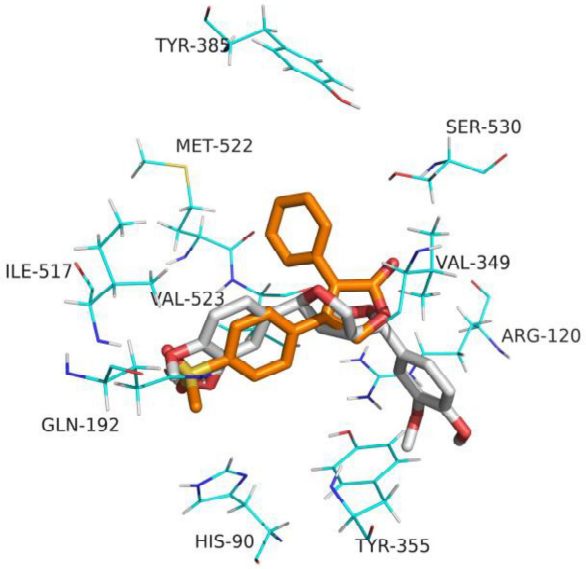

Fig. 1 Superimposition of rofecoxib in oragne and pinoresinol in gery in COX-2 active site

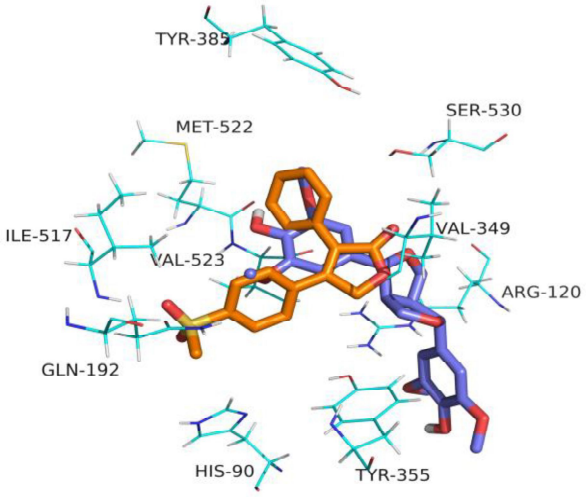

Fig. 2 Superimposition of rofecoxib in orange and syringaresinol in blue in COX-2 active site

ISSN 1737-9334

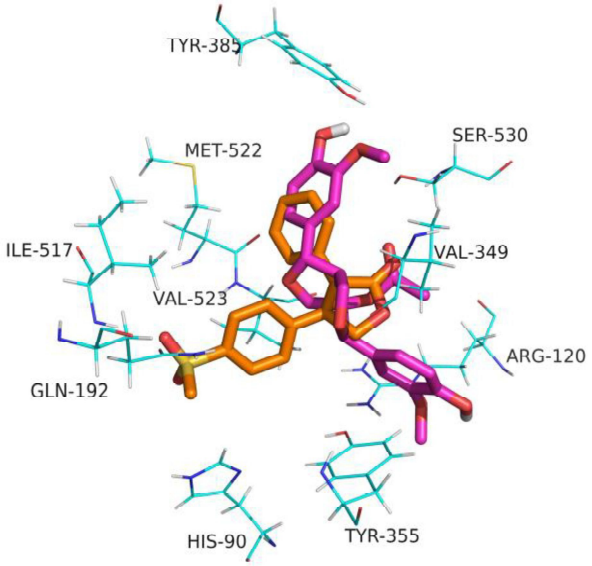

Fig. 3 Superimposition of rofecoxib in orange and 1-Acetoxypinoresinol in purple in COX-2 active site

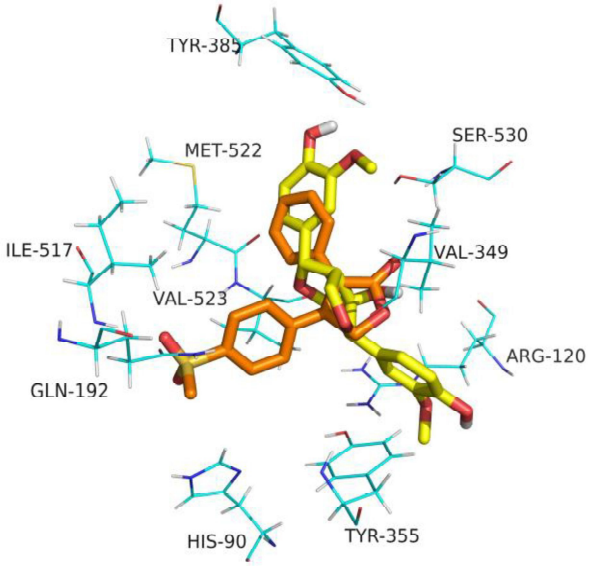

Fig. 5 Superimposition of rofecoxib in orange and 8-Hydroxypinoresinol in yellow in COX-2 active site

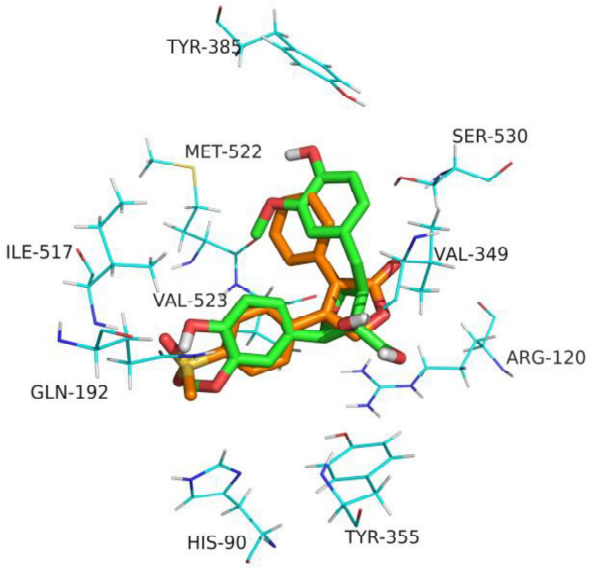

Fig. 4 Superimposition of rofecoxib in orange and berchemol in green in COX-2 active site

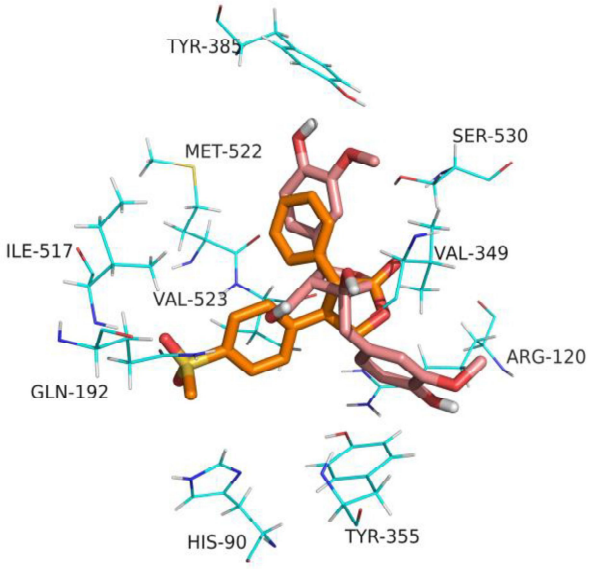

Fig. 6 Superimposition of rofecoxib in orange and (-)-Olivil in pink in COX-2 active site

ISSN 1737-9334

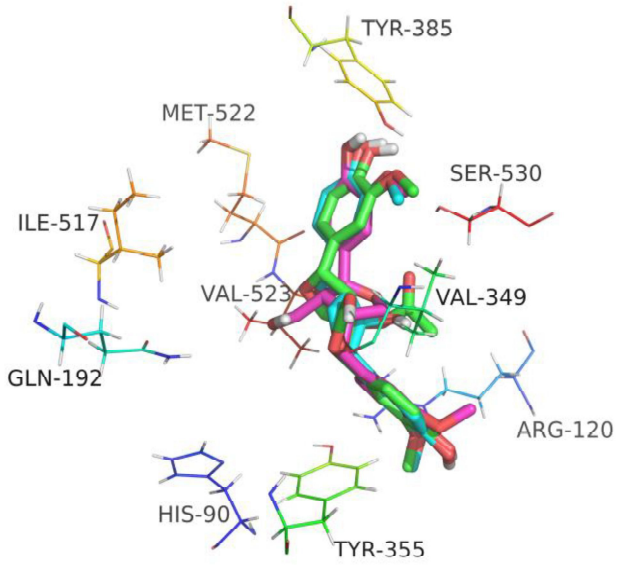

Fig. 7 Superimposition of (-)-Olivil in pink, 8-Hydroxypinoresinol in blue and 1-Acetoxypinoresinol in green in COX-2 active site

IV. Conclusions

The present study demonstrates that berchemol, a natural product isolated from olive oil, is a competitive and selective inhibitor of COX-2 with binding energy of -9.71 kcal/mol. The docking results show that the carboxylate moiety of berchemol interact with the amino acids at the selectivity pocket of COX-2 active site of the hydrophobic active site channel, such as rofecoxib, mainly with Gln-192 and Val-349. Being a smaller size natural product and a selective inhibitor of COX-2, berchemol would form an ideal compound for lead optimization and for developing a potent anti-inflammatory drug candidate.

References

[1] COX-2's new role in inflammation, nature chemical biology | VOL 6 | JUNE 2010 |

[2] Emanuela Ricciotti, PhD and Garret A. FitzGerald, MD. Prostaglandins and Inflammation. Arterioscler Thromb Vasc Biol. 2011 May ; 31(5): 986–1000. doi:10.1161/ATVBAHA.110.207449.

[3] Nina Zidar a, *, Katarina Odar a , Damjan Glavač a , Maja Jerše a , Tomaž Zupanc b , Dušan Štajer c. Cyclooxygenase in normal human tissues is COX-1 really a constitutive isoform, and COX-2 an inducible isoform?. J. Cell. Mol. Med. Vol 13, No 9B, 2009 pp. 3753-3763.

[4] Seibert K, Masferrer JL. Role of inducible cyclooxygenase (COX-2) in inflammation. Receptor. 1994; 4: 17–23.

[5] Vane JR, Bakhle YS, Botting RM. Cyclooxygenases 1 and 2. Annu Rev Pharmacol Toxicol. 1998; 38: 97–120.

[6] Joo-Heon Yoon 1,2 and Seung Joon Baek 3. Molecular Targets of Dietary Polyphenols with anti-inflammatory Properties. Yonsei Med J Vol. 46, No. 5, 2005.

[7] Afshin Zarghi* and Sara Arfaei. Selective COX-2 Inhibitors: A Review of Their Structure-Activity Relationships. Iran J Pharm Res. 2011 Autumn; 10(4): 655–683.

[8] https://www.rxlist.com/cox-2_inhibitors/drugs-condition.htm.

[9] V ANISREE M ULABAGAL , † S TEVEN V AN N OCKER , ‡ D AVID L. D EWITT , § M URALEEDHARAN G. N AIR * ,†. Cultivars of Apple Fruits That Are Not Marketed with Potential for Anthocyanin Production. Article in Journal of Agricultural and Food Chemistry · October 2007.

[10] Urszula Szymanowska * and Barbara Baraniak. Antioxidant and Potentially Anti-Inflammatory Activity of Anthocyanin Fractions from Pomace Obtained from Enzymatically Treated Raspberries. Antioxidants 2019, 8, 299; doi:10.3390/antiox8080299.

[11] N. P. Seeram 1 , R. A. Momin 1 , M. G. Nair 1 and L. D. Bourquin 2. Cyclooxygenase inhibitory and antioxidant cyanidin glycosides in cherries and berries. Phytomedicine, Vol. 8(5), pp. 362–369.

[12] Swati Singh, Veda P Pandey, Huma Naaz, Priyanka Singh, Upendra N. Dwivedi, Structural modeling and simulation studies of human cyclooxygenase (COX) isozymes with selected terpenes: Implications in drug designing and development, Computers in Biology and Medicine 43 (2013) 744–750.

[13] Stanikunaite, R, Khan, S. I, Trappe, J.M . and Ross, S. A. (2009) cyclooxygenase-2 inhibitory and antioxidant compounds from the truffleelaphomyces granulatus. Phytother. Res.23, 575-578.

[14] J. Choi, K. M. Shin, H. J. Park, H. J. Jung et al., Planta Med., 70, 1027 (2004).

[15] Maria Pilar Vinardell * and Montserrat Mitjans. Lignins and Their Derivatives with Beneficial Effects on Human Health. Int. J. Mol. Sci. 2017, 18, 1219; doi:10.3390/ijms18061219.

[16] IULIANA SPIRIDON. BIOLOGICAL AND PHARMACEUTICAL APPLICATIONS OF LIGNIN AND ITS DERIVATIVES: A MINI-REVIEW. Cellulose Chem. Technol., 52 (7-8), 543-550 (2018)

[17] Magoulas, G.E.; Papaioannou, D. Bioinspired syntheses of dimeric hydroxycinnamic acids (lignans), hybrids, using phenol oxidative coupling as key reaction, medicinal significance thereof. Molecules 2014, 19, 19769–19835.

[18] S TELLA C HRISTOPHORIDOU , † P HOTIS D AIS ,* ,† L I -H ONG T SENG , ‡ M ANFRED S PRAUL ‡. Separation and Identification of Phenolic Compounds in Olive Oil by Coupling High-Performance Liquid Chromatography with Postcolumn Solid-Phase Extraction to Nuclear Magnetic Resonance Spectroscopy (LC-SPE-NMR). J. Agric. Food Chem. 2005, 53, 4667–4679.

[19] Reshma N Tendulkar*Supriya S Mahajan. Molecular Docking studies of Novel Flavones as Cyclooxygenase-2 (Cox 2) Inhibitors. ournal of Advanced Pharmacy Education & ResearchJul-Sep 2014, Vol 4, Issue 3.

[20] Veber DF, Johnson SR, Cheng HY, Smith BR, Ward KW, et al. (2002), Molecular properties that influence the oral bioavailability of drug candidates. J Med Chem 45: 2615-2623.

ISSN 1737-9334

[21] SARATH SASI KUMAR1*, ANJALI T. IN SILICO DESIGN AND MOLECULAR DOCKING STUDIES OF SOME 1, 2-BENZISOXAZOLE DERIVATIVES FOR THEIR ANALGESIC AND ANTI-INFLAMMATORY ACTIVITY. nt J Curr Pharm Res, Vol 9, Issue 2, 133-136.

[22] C.M. Nisha, A. Kumar, A. Vimal, B.M. Bai, D. Pal, A. Kumar, Docking and ADMET prediction of few GSK-3 inhibitors divulges 6-bromoindirubin-3-oxime as a potential inhibitor, J. Mol. Graph. Model. 65 (2016) 100e107.

[23] Price MLP., Jorgensen WL. Rationale for the observed COX-2/COX-1 selectivity of celecoxib from Monte Carlo simulations. Bioorg. Med. Chem. Lett. 2001; 11:1541–1544.

[24] Price MLP., Jorgensen WL. Rationale for the observed COX-2/COX-1 selectivity of celecoxib from Monte Carlo simulations. Bioorg. Med. Chem. Lett. 2001; 11:1541–1544.

[25] Llorens O., Perez J., Palomer A., Mauleon D. Differential binding mode of diverse cyclooxygenase inhibitors. Journal of Molecular Graphics and Modelling. 2002; 20:359–371.

[26] Xin Feng Zhang., Tran Manh Hung., Phuong Thien Phuong.: Anti-inflammatory activity of flavonoids from Populus davidiana. Arch Pharm Res. 2006; 29(12):1102–1108.

ISSN 1737-9334

Characterization of 2.4 GHz Antenna for Wi-Fi Application with Modal Method

Doae El Hadri[#1], Asmaa Zugari[*2], Alia Zakriti[#3], Mohamed Bayjja[*4]

[#] *National School of Applied Sciences, Abdelmalek Essaadi University, Tetuan, Morocco.*

[1]doae93@gmail.com

[3]aazakriti@hotmail.fr

[*]*Faculty of Sciences, Abdelmalek Essaadi University, Tetuan, Morocco.*

[2]asmaa.zugari@gmail.com

[4]m.bayjja@gmail.com

Abstract— **A patch antenna for Wi-Fi application is presented in this paper. The main intention of this research is to analyse the proposed antenna using the Wave Concept Iterative Procedure method, which is characterized by a faster computation time .The iterative process consists in establishing a recurrence relationship between the incident waves and those reflected in the spatial and modal domains. The passage of waves between these two domains is ensured by the FMT (Fast Modal Transform) and its inverse FMT^{-1}. The results obtained are validated by comparison with those of the CST software.**

Keywords— **Patch Antenna; Wi-Fi application; WCIP Method; Return loss; FMT**

I. Introduction

In recent years, research activity has focused enormously on the study of planar structures in the field of microwaves. The patch antenna concept appeared in the 1950s, but the real development did not take place until the 1970s [1].

Microstrip antennas, and particularly patch antennas, have the advantage of being easily integrated into surfaces, low production cost and good resonance performance, they are the most widely used as they meet many of the constraints imposed by the transmission system. Their dimensions facilitate their integration on many mobiles.

The printed antenna, also known as the patch antenna, is a recent type of antenna whose development and use are becoming more and more frequent. It consists of a dielectric, with a metallic ground plane on one side. On the other side, a metal engraving supports surface currents that create electromagnetic radiation. The patch is generally made of a conductive material such as copper or gold …, and it can take any shape possible.

Several analysis methods have been used to study patch antennas, we could classify them into two main categories: Analytical Methods and Numerical Methods. A description of the different Numerical Methods such as (Moments Method (MoM), Finite-Difierence Time-Domain (FDTD) and Finite Element Method (FEM)) and their advantages and disadvantages are detailed in [2].

The iterative method was introduced by Professor Baudrand in 1995 for the study of two-dimensional electromagnetic problems. Then, it was developed and improved by Professor Baudrand and Professor Raveu to study the couplings between antennas placed on a cylinder [3].

The advantage of this method remains in its ease of use due to the absence of test functions, it is not limited by the shape of the metal, its fast computation time, mainly due to the systematic use of Fast Mode Transform (FMT), and a gridded mesh use, and the convergence was insured independently of the circuit complexity [4].

In this paper, the WCIP method is used to analyse a patch antenna. The proposed antenna operate at 2.4 GHz, band allocated for Wi-Fi application.

The results obtained were satisfactory since they were compared with those of CST software and presented a good agreement. In addition the computation time of iterative method is smaller than the CST Microwave Studio.

II. WCIP Method

The analytical expression of the iterative process involves a system of two equations: one written in the spatial domain (1), the other expressed in the modal domain (2). The iterative process is defined by:

$$\begin{cases} \vec{A} = \hat{S}\,\vec{B} + \vec{A}_0 & Spatial\ domain \quad (1) \\ \vec{B} = \hat{\Gamma}\,\vec{A} & Spectral\ domain \quad (2) \end{cases}$$

Where:

A_0 incident wave generated by the source

$\vec{A} = FMT(\vec{A})$, $\vec{B} = FMT^{-1}(\vec{B})$

$\vec{A}$ incident waves, $\vec{B}$ reflected waves seen from the interface.

The equations of the tangential electric field $\vec{E}_{Ti}$ and current density $\vec{J}_{Ti}$ are derived from the following equations [5]:

$$\begin{cases} \vec{A}_i = \dfrac{1}{2\sqrt{Z_{0i}}}\left(\vec{E}_{Ti} + Z_{0i}\,\vec{J}_{Ti}\right) & (3) \\ \vec{B}_i = \dfrac{1}{2\sqrt{Z_{0i}}}\left(\vec{E}_{Ti} - Z_{0i}\,\vec{J}_{Ti}\right) & (4) \end{cases}$$

Z_{0i} is the characteristic impedance of the medium i (i=1, 2)

A. Scattering Operator

The Scattering Operator takes into account the boundary conditions in the spatial domain [6]:

- Metal: $E_1 = E_2 = 0$
- Dielectric: $J_1 + J_2 = 0$, $E_1 = E_2 \neq 0$

ISSN 1737-9334

- Source: $E_1 = E_2 = E_0 - Z_0(J_1 + J_2)$

The scattering matrix of the general structure is:

$$[\hat{S}] = \begin{bmatrix} -H_m - \frac{n^2-1}{n^2+1} H_d + \frac{-1+n_1-n_2}{1+n_1+n_2} H_S & \frac{2n}{n^2+1} H_d + \frac{n_3}{1+n_1+n_2} H_S \\ \frac{2n}{n^2+1} H_d + \frac{n_3}{1+n_1+n_2} H_S & -H_m + \frac{n^2-1}{n^2+1} H_d + \frac{-1-n_1+n_2}{1+n_1+n_2} H_S \end{bmatrix} \quad (5)$$

H_i :Is Heaviside unit step defined as:

$$H_i = \begin{cases} 1 & on\ the\ i\ domain \\ 0 & other\ domain \end{cases} \quad \text{(i= Metal, Dielectric, Source)}$$

$$n = \sqrt{\frac{Z_{01}}{Z_{02}}}\ , n_1 = \frac{Z_0}{Z_{01}}\ , n_2 = \frac{Z_0}{Z_{02}}\ , n_3 = \frac{2\,Z_0}{\sqrt{Z_{01}}\sqrt{Z_{02}}}$$

$$and \begin{bmatrix} A_{01} \\ A_{02} \end{bmatrix} = \frac{1}{1+n_1+n_2} \begin{bmatrix} \frac{E_0}{\sqrt{Z_{01}}} H_S \\ \frac{E_0}{\sqrt{Z_{02}}} H_S \end{bmatrix}$$

B. *Reflection Operator*

The expression of the reflection coefficient in the spectral domain is given by [7]:

$$\Gamma_{mn}^{\alpha} = \frac{1 - Z_{0i} Y_{mn}^{\alpha}}{1 + Z_{0i} Y_{mn}^{\alpha}} \quad (6)$$

Y_{mn}^{α}: is the admittance of the mn mode at the medium i

α : represents the TE or TM modes.

$$Y_{mn}^{TE}(\varepsilon_r) = \frac{\gamma_{mn}}{j\omega\mu_0}\ ,\quad Y_{mn}^{TM}(\varepsilon_r) = \frac{j\omega\varepsilon_0\varepsilon_r}{\gamma_{mn}}$$

γ_{mn} is the propagation constant, obtained by the equation:

$$(\gamma_{mn}^2) = \left(\frac{m\pi}{a}\right)^2 + \left(\frac{n\pi}{b}\right)^2 - K_0^2(\varepsilon_r)_i$$

C. *Fast Modal Transform*

The Fast Mode Transformation (FMT) and its inverse (FMT^{-1}) are used to transform waves from spatial to spectral domain and vice versa. It is summarized in the following two equations [8]:

$$\begin{bmatrix} A_{mn}^{TE} \\ A_{mn}^{TM} \end{bmatrix} = C_{mn} \begin{bmatrix} -\frac{m}{a} & \frac{n}{b} \\ \frac{n}{b} & \frac{m}{a} \end{bmatrix} FFT \begin{bmatrix} A_x \\ A_y \end{bmatrix} \quad (7)$$

$$\begin{bmatrix} B_x \\ B_y \end{bmatrix} = IFFT \left\{ \left[C_{mn} \begin{bmatrix} -\frac{m}{a} & \frac{n}{b} \\ \frac{n}{b} & \frac{m}{a} \end{bmatrix} \right]^{-1} \begin{bmatrix} B_{mn}^{TE} \\ B_{mn}^{TM} \end{bmatrix} \right\} \quad (8)$$

Where: $C_{mn} = \sqrt{\frac{ab}{2\,\sigma_{mn}}}\ \frac{1}{\sqrt{\left(\frac{m}{a}\right)^2 + \left(\frac{n}{b}\right)^2}}$

and $\sigma_{mn} = \begin{cases} 2 & mn \neq 0 \\ 1 & mn = 0 \end{cases}$

III. Antenna Design

The configuration of the proposed 2.4 GHz antenna is shown in Fig.1. The patch is printed on a FR4 substrate with a dielectric constant of 4.4 and thickness of 1.6 *mm*. The ground plane is composed of Copper material with 0.035 mm of thickness, 30 mm in length and 26.5 mm in width. The feed line has a characteristic impedance (Z_c) of 50 Ω.

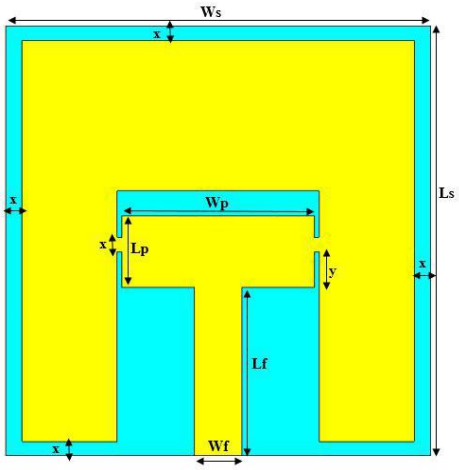

Fig. 1 Structure of the proposed antenna

The values of proposed design parameters are specified in table 1:

TABLE I
Dimensions of the 2.4 GHz Antenna Parameters

Parameters	Value (mm)
Ws	26.5
Ls	30
Wp	12
Lp	5
Wf	3
Lf	11.75
X	1
Y	2.5

The circuit plan of the antenna is meshed into 64x64 pixels in Fig.2:

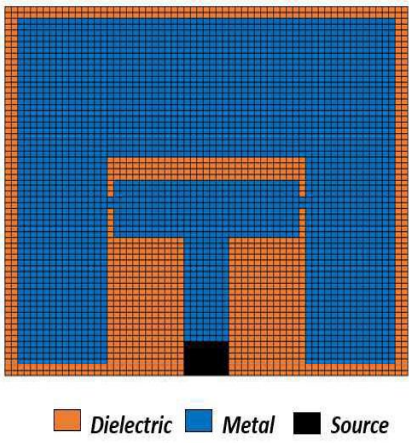

Fig. 2 Discretization of Wi-Fi antenna in the WCIP interface

IV. Numerical Results and Discussions

A. *Study of WCIP Convergence*

The simulation frequency is fixed at 2.5 GHz and the variations of the reflection coefficient module S11 are plotted according to the number of iterations as shown in the Fig.3. Convergence is achieved after 1000 iterations and the iterative

ISSN 1737-9334

process is stopped. Electromagnetic simulations were performed using MATLAB code program [9].

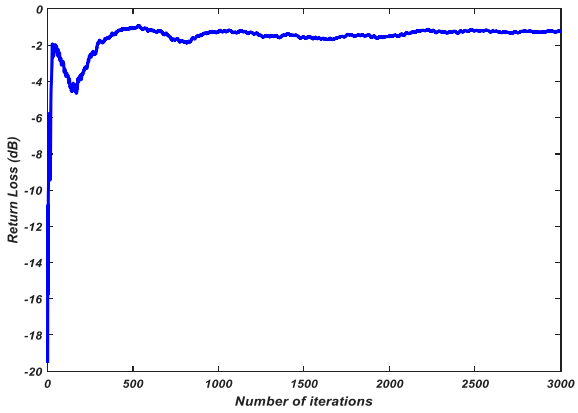

Fig. 3 convergence of the reflection coefficient according to the number of iterations

The distribution of the current density J and electric field E obtained on the two axes Ox and Oy is shown in Fig.4 and Fig.5, respectively.

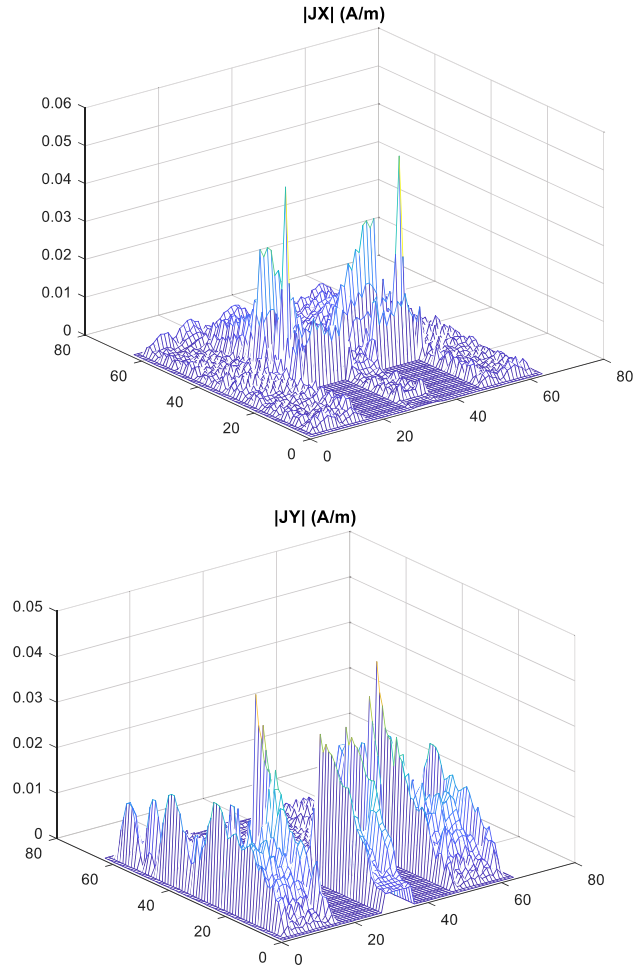

Fig. 4 Distribution of the current density

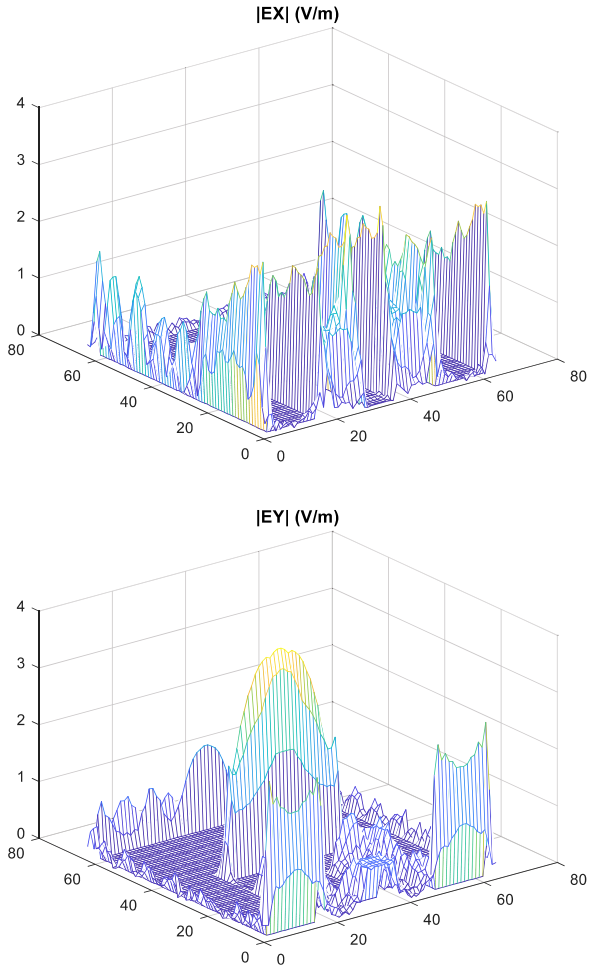

Fig. 5 Distribution of the electric field

Figures 4 and 5 show that the boundary and continuity conditions introduced in the diffraction operator calculation are in accordance with the results of the simulations.

B. Reflection Coefficient

Figure 6 represent the results for the reflection coefficient S11 as a function of frequency.

To validate our approach, a comparison of the numerical results obtained by the iterative method WCIP with the simulation data achieved by CST microwave studio is reported in fig 6 and show a good agreement. The resonance frequency is around 2.4 GHz.

ISSN 1737-9334

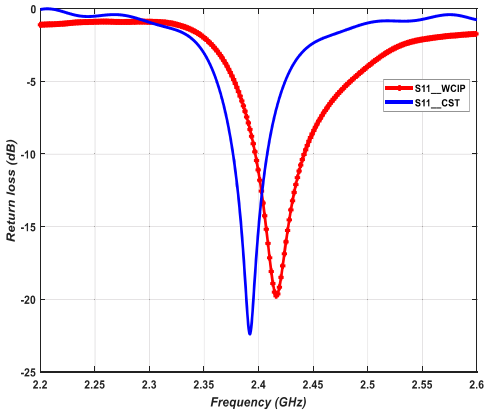

Fig. 6 The reflection coefficient S11 for proposed antenna

Table II present a comparison of computation time with two numerical techniques. The simulations are done in a computer of a 2 GHz CPU and 4G memory.

TABLE III
COMPUTATION TIME WITH DIFFERENT NUMERICAL METHODS

	Computation time (s)
WCIP	354
CST	622

It is clear from Table II that the computation time of the iterative method is less than that of the CST software.

V. CONCLUSIONS

In this paper the iterative method is presented to analyze a patch antenna. It has a small size of 26.5x30 mm^2, printed on a FR4 substrate. The proposed antenna operate at 2.4 GHz for Wi-Fi application. A convergence study is carried out and the distribution of the electric field and current density are presented. The numerical results show a good agreement compared with the CST simulation data. A comparison of the calculation time between two different methods shows that the iterative method is faster than the CST software.

ACKNOWLEDGMENT

The work is carried out with the support of the CNRST within the framework of the Research Excellence Scholarship Programme.

REFERENCES

[1] S. Berhab, M. Abri, and R. GHARBI, “Slotted Microstrip Patch Antenna Analysis Based on the Wave Concept Approach,” in ICOSIP 2015, At Tlemcen, Algeria.

[2] S. BERHAB, “Modélisation Rigoureuse par une Méthode Itérative des Structures Imprimées de Type DGS pour les Applications sans Fil,” Thèse Dr. Univ. _Tlemcen_, 2017.

[3] M. Hicham, “Contribution à l’étude des de s circuits planaires à éléments localisés à l’aide de la WCIP,” Thèse Dr. Univ. _Tlemcen_, 2018.

[4] D. Awatef, “Contribution à l’étude des structures planaires à plusieurs niveaux de métallisation et à substrats multicouches homogènes et inhomogènes par une formulation en ondes transverses,” Thèse Dr. Univ. Batna -2-, 2017.

[5] D. EL HADRI, A. ZUGARI, and A. ZAKRITI, “Analysis of a 38 GHz Band Antenna for 5G wireless communication using Wave Concept Iterative Procedure (WCIP) method,” in EAI, ICCWCS ,April 24-25, 2019,Kénitra,Morocco, 2019.

[6] Makrem YEDDES, “Modélisation et caractérisation des circuits micro-ondes par une méthode itérative,” THESE Dr. TUNIS, 2008.

[7] Z. Harouni, “Conception et caractérisation d’une Rectenna à double polarisation circulaire à 2 . 45 GHz,” Thése Dr. Paris-Est, 2011.

[8] M. Titaouine, A. G. Neto, H. Baudrand, and F. Djahli, “Analysis of Frequency Selective Surface on Isotropic / Anisotropic Layers Using WCIP Method,” ETRI J., vol. 29, no. 1, pp. 36–44, 2007.

[9] D. EL HADRI, A. ZUGARI, and A. ZAKRITI, “The study of a 5G antenna with encoche and Defected Ground Structure (DGS) using the Iterative Method,” in IEEE,WITS, 3-4 April 2019,FEZ,Morocco.

ISSN 1737-9334

Convolutional Neural Networks for Malware Detection

Hoda EL MERABET[1], Abderrahmane HAJRAOUI[2]

Faculty of Science, Abdelmalek Essaadi University
B.P. 2117 Quartier M'hanech II, Av. Palestine, Tetouan, Morocco
[1]helmerabet@uae.ac.ma
[2]hajraouiabder@gmail.com

Abstract— **Machine learning lives its golden age; it has been employed in various fields. Malware detection is one of these fields. In order to determine if a file is malicious or not, different features are extracted to be utilized as inputs, and numerous machine learning techniques are adopted in different combinations for classification. These techniques are, among others, Support Vector Machines SVMs, random forests, logistic regression and deep learning algorithms or deep artificial neural networks ANNs. Convolutional Neural Networks CNNs are a kind of ANNs that take in an image input. They have been used in diverse malware detection researches, by representing the whole file as an image. In this study we are using CNNs in a distinct way to classify malicious from benign files. Instead of representing all the byte sequences of a file as an image, we decided to choose just the PE header fields values, then convert them to byte values, and subsequently feed them to our CNN model as greyscale images. The obtained results were reasonably satisfying.**

Keywords— **Convolutional Neural Networks; Deep Learning; Machine Learning; Malware Classification; Cyber Security**

I. INTRODUCTION

The number of malwares is on an extended elevation every day. With the revolution of machine learning techniques, malware detection field got more attraction to invest on it. Traditional commercial anti-malware programs rely basically on the signature-based static technique, the technique that would never detect new malwares as they use novel signatures. The ability of machine learning models to learn from training data, and subsequently to generalize to previously unseen data is a major reason to have an expanding number of researches interested in this area. There are a lot of factors that influence the success of a model, namely the types of extracted features, the feature selection techniques used in order to get rid of irrelevant features, and the employed machine learning algorithms [1]. In this paper, we are using the PE features as input features, and a succession of convolutional layers for the training of our model.

II. RELATED WORK ON MALWARE DETECTION

There are three approaches for identifying malicious from benign files. The first one is the static approach. It relies on the extraction of signatures, which are constant attributes observed in the files or values that should be calculated using a hash function for example. The second approach is the dynamic approach. This one requires the execution of the files on a virtual environment or a sandbox in order to capture dynamic behaviour and detect doubtful activities in each file. The third one is the heuristic approach based on machine learning, which has been frequently successful the last two decades. It can utilize static features, or dynamic features, or both of them.

Dynamic features are strong features that represent the dynamic behaviour of an executable file. In [2], all the training set samples were executed on a virtual environment in order to extract dynamic features. They chose to gather nine activity metrics from each file. These metrics are: CPU user use, CPU system use, RAM use, SWAP use, received packets, received bytes, sent packets, sent bytes, and number of processes running. By saving these metrics each second in a time-window of 5 minutes, the researchers collected 300 vectors to represent each file. These vectors were subsequently converted to 300 vectors of x-y coordinates using Self Organizing Feature Map SOFM. The dataset was constituted of 1188 PE files; half the files is malicious and the other half is benign. One half constituted the training set and the other half represented the test set. Using logistic regression for classification, they obtained an accuracy of 86.70%.

API calls and operating system resource instances were utilized to identify API call graphs in [3]. These graphs represented the input features for the deep learning model. The researchers opted for a feature selection approach in order to reduce the size of the original extracted features. For this

ISSN 1737-9334

purpose, various layers of Sparse Auto Encoders SAEs were employed, followed by a Decision Tree classifier. The training dataset was constituted of equal numbers of malicious and benign files, with a total number of 1760 of samples. The researchers didn't use new unseen dataset specially for testing, nevertheless they used 10-fold cross-validation technique for training and testing. The achieved detection precision was 98.6%.

The features used in [7] were n-gram system call sequences. Two models were utilized in combination. The first model was the Long-Short-Term Memory LSTM. The information gain was used in order to remove redundant subsequences, then the LSTM model was fed, followed by a Max-Pooling layer then by a logistic regression classifier.

The second model was the Random Forest model. Here the input features were API statistical features, which are got from the association of two API calls based on the comparison of the two API call sequences hashes. By combining the two models they got a better accuracy than using each model separately. The obtained accuracy was 95.7%.

Since CNNs demonstrated high performances in image recognition, numerous malware detection researches took advantage of this type of algorithms. The work of [4] relied on a dynamic approach. The samples were executed on virtual machines, then process performance metrics were extracted. Each sample was represented as an image, the rows contained the executed processes, and the columns contained the 28 extracted features per process like the process status, the CPU usage percent, and the number of written bytes. CNNs were employed to classify the samples. An accuracy of 90% was obtained on the testing dataset.

The researchers in [5] converted the raw bytes of each file using an embedding layer, then they used them as input features. They built their model from CNNs and Recurrent Neural Networks RNNs followed by a fully connected layer of an ANN. A dataset of 400,000 files split evenly between benign and malicious files was used for training. A distinct testing dataset constituted of 77,349 files was used for the final test phase. They obtained an accuracy of 90.90%.

III. Convolutional Neural Networks

A. Strengthening Vision with CNNs

By looking at an image, several wasted space can be observed. Each image is constituted of a fixed number of pixels; hence it will be interesting to find a manner to condense it to just the important features that make the difference between one class of images and another. That is the importance of convolutions. That implies introducing a number of filters to pass them through the image like in image processing, and subsequently attain new images called feature maps. Each convolution, or the application of each filter in other words, will change the image in such a way that particular features get emphasized.

Together with convolutions, pooling can be used in CNNs. Pooling is a way of compressing an image; it reduces the size of a feature map almost always by a factor of 2. It takes a region of a fixed number of pixels; typically 2×2, and reduces it into one pixel in the next layer.

B. CNNs for Malware Detection

The ability of convolutional neural networks to learn the existence of a feature regardless of its position, made from them a widely used technique in image processing. Since the different parts of a PE executable file can be placed anywhere within the file, as observed for instance by Barker et al. in [5], CNNs have been introduced to malware detection field in plentiful researches. An image is a matrix of pixel values. By representing the extracted features from a PE file as a matrix, each file can be seen as an image to feed a CNN model.

IV. Implementation and Experiment Results

A. *Dataset Used*

The dataset used in this study is the EMBER dataset [6]. It consists of 900K training samples (300K malicious, 300K benign, and 300K unlabeled) where only the benign and the malicious ones were utilized in our experiments. Besides, it contains 200K test samples (100K malicious and 100K benign). The training of our model was done on 80% of the 600K training samples, the remaining 20% of the data was used for validation at the end of each epoch. The 200K test samples were kept totally to the end of the training in order to evaluate the performance of the model on unseen data. The utilized features are PE header fields values. As shown in [1], this kind of features has been largely adopted for malware

ISSN 1737-9334

detection obtaining high accuracy rates. Fig. 1 shows an example of the extracted features from an executable as given by [6].

B. Methodology

Motivated by the success of CNNs in image classification primarily, then in malware detection especially, we were convinced that new approaches of them can give favourable results in the classification of benign and malicious files. Our implementation of a model based on CNNs is different from the previous implementations.

The EMBER authors [6] provided the vectorizing of raw features with their open dataset. Each file is represented as a feature vector of dimension 2351. A CNN model needs images as input. To implement our malware detection model, we chose to represent each sample as a greyscale image of 50×50. Thus, we padded each vector by 149 zeros, then we reshaped it to an array of 50×50 to feed the model.

Various implementations were tested in our experiments. After comparison, we retained the implementation described below.

As a first step, a Gaussian noise layer was added to the input layer. This layer has a regularizing effect and helps to reduce overfitting. Afterwards, a 2D convolutional layer was added with 64 filters. Next, a Batch Normalization layer was introduced. As explained by [9], a batch normalization performs the normalization for each training mini-batch. This procedure accelerates the training of deep neural networks. Rectified Linear Unit ReLU was used as activation function. It is the more prevalent activation function nowadays. Later, a max pooling layer was added. This layer takes an area of a fixed size of the feature map, then selects the maximum value of the different pixels constituting it. Subsequently, 4 convolutional layers with batch normalization and a ReLU activation function were added. Finally, since binary decisions are involved, either benign or malicious class, then binary cross-entropy was utilized as loss function.

C. Experiments and Evaluation Results

All the experiments in this paper were done on a laptop computer with Intel® Core (TM) i7-6500U @ 2.50 GHz, 2.59 GHz, and 16GB of RAM.

"**sha256**": "000185977be72c8b007ac347b73ceb1ba3e5e4dae4fe98d4f2ea92250f7f580e",
"**appeared**": "2017-01",
"**label**": -1,
"**general**": {
"**file_size**": 33334,
"**vsize**": 45056,
"**has_debug**": 0,
"**exports**": 0,
"**imports**": 41,
"**has_relocations**": 1,
"**has_resources**": 0,
"**has_signature**": 0,
"**has_tls**": 0,
"**symbols**": 0
},
"**header**": {
"**coff**": {
"**timestamp**": 1365446976,
"**machine**": "I386",
"**characteristics**": ["LARGE_ADDRESS_AWARE", ..., "EXECUTABLE_IMAGE"]
},
"**optional**": {
"**subsystem**": "WINDOWS_CUI",
"**dll_characteristics**": ["DYNAMIC_BASE", ..., "TERMINAL_SERVER_AWARE"],
"**magic**": "PE32",
"**major_image_version**": 1,
"**minor_image_version**": 2,
"**major_linker_version**": 11,
"**minor_linker_version**": 0,
"**major_operating_system_version**": 6,
"**minor_operating_system_version**": 0,
"**major_subsystem_version**": 6,
"**minor_subsystem_version**": 0,
"**sizeof_code**": 3584,
"**sizeof_headers**": 1024,
"**sizeof_heap_commit**": 4096
}
},
"**imports**": {
"KERNEL32.dll": ["GetTickCount"],
...
},
"**exports**": []
"**section**": {
"**entry**": ".text",
"**sections**": [
{
"**name**": ".text",
"**size**": 3584,
"**entropy**": 6.368472139761825,
"**vsize**": 3270,
"**props**": ["CNT_CODE", "MEM_EXECUTE", "MEM_READ"]
},
...
]
},
"**histogram**": [3818, 155, ..., 377],
"**byteentropy**": [0, 0, ... 2943],
"**strings**": {
"**numstrings**": 170,
"**avlength**": 8.170588235294117,
"**printabledist**": [15, ... 6],
"**printables**": 1389,
"**entropy**": 6.259255409240723,
"**paths**": 0,
"**urls**": 0,
"**registry**": 0,
"**MZ**": 1
},
}

Fig. 1 Raw features extracted from a PE file [6]

Based on the dataset described in Section IV.A, we evaluate the experiments in two perspectives; a CNN model without dropout regularization and another model with dropout regularization. After several trials of parameter tuning, for both of our models, the best results were got using a learning rate of 0.00007, a batch size of 256, and 64 filters for the different convolutional layers.

Fig. 2 represents the train and validation loss and accuracy obtained with the CNN model without dropout regularization. Fig. 3 represents the same metrics obtained with the CNN model with dropout regularization. After a remarkable epoch, the model continues to learn particularities of the training samples and it is no more able to generalize to unseen data. Therefore, we had to go for an early stopping to get the best test accuracy. The epoch to stop at is different from a model to another.

For the CNN model without dropout regularization, the best validation accuracy was obtained at epoch 14, namely 91.36%. Consequently, the model saved at this epoch was retained. However, as explained by [1], the accuracy drops down after testing on previously unseen data. The test accuracy on the test dataset was 80.84%. The accuracy decreased by 10.52% from validation to testing data.

ISSN 1737-9334

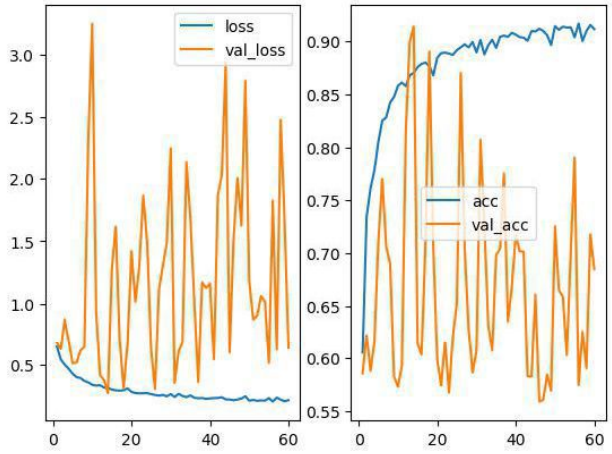

Fig. 2 Train and validation accuracy and loss obtained with our CNN model without dropout regularization

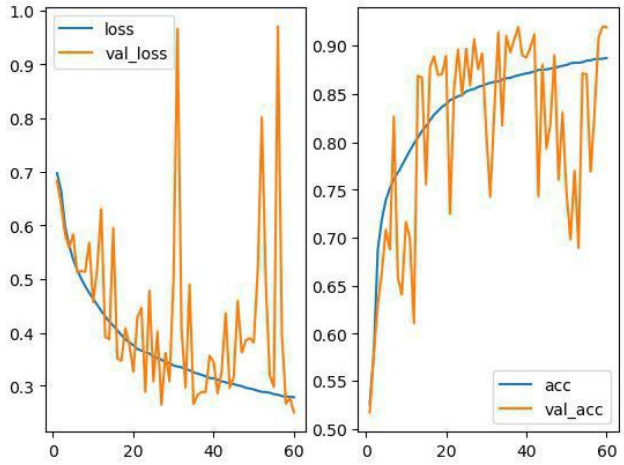

Fig. 3 Train and validation loss obtained with our CNN model with dropout regularization

For our CNN model with dropout regularization, the best validation accuracy was obtained at epoch 59, namely 92%, therefore we retained the model saved at this epoch. The test of this saved model on the previously unseen test dataset gave a test accuracy of 90.25%, which represents a decrease of 1.75%.

The results of both models are shown in Table1.

TABLE I
TEST ACCURACIES ON EMBER TEST DATASET FOR THE 4 STUDIED MODELS

	Our CNN Model
Without Dropout	80.84%
With Dropout	90.25%

We see clearly that the CNN model with dropout regularization performs better giving us an accuracy of 90.25%. This accuracy is even better than some other previous researches as shown in Table 2.

TABLE II
COMPARISON OF OUR MODEL WITH SOME OTHER RESEARCHES

	Accuracy
Reference [2]	86.70%
Reference [4]	90%
Our CNN model	**90.25%**

V. CONCLUSIONS

CNNs have been employed in malware detection field in several approaches. The new model built in this paper is based as well on CNNs. It has given satisfying results as shown. That can be much more improved in the future by choosing other types of features like machine activity metrics, by more hyper-parameters tuning, by the use of feature selection techniques, or by implementing deeper CNNs with greater number of hidden layers. Nevertheless, the training of deeper networks can be painfully slow and needs more puissant machines with GPUs and larger sizes of memory.

REFERENCES

[1] H. El Merabet and A. Hajraoui, "A survey of malware detection techniques based on machine learning," *International Journal of Advanced Computer Science and Applications (IJACSA),* vol. 10, pp. 366–373, Jan. 2019.

[2] P. Burnap, R. French, F.Turner and K. Jones. "Malware classification using self-organizing feature maps and machine activity data," *Journal Computers and Security,* vol. 73, pp. 399–410, 2018.

[3] F. Xiao, Z. Lin, Y. Sun and Y. Ma. "Malware detection based on deep learning behavior graphs," *Mathematical Problems in Engineering,* vol. 2019, Feb 2019.

[4] M. Abdelsalam, R. Krishnan, Y. Huang and R. Sandhu. "Malware detection in cloud infrastructures using convolutional neural networks," in *Proc. 11th IEEE Conference on Cloud Computing (CLOUD)*, San Francisco, CA, Jul 2-7 2018.

[5] E. Raff, J. Barker, J. Sylvester, R. Brandon, B. Catanzaro and C. Nicholas. "Malware detection by eating a whole exe," *AAAI Workshop on Artificial Intelligence for Cyber Security*, 2018.

[6] H. Anderson and P. Roth. "EMBER: An open dataset for training static PE malware machine learning models," in *ArXiv e-prints*. Apr 2018.

[7] L. Xiaofeng, Z. Xiao, J. FangshuoY. Shengwei and S. Jing. "ASSCA: API based sequence and statistics features combined malware detection architecture" in *Procedia Computer Science 129,* Jan 2018, pp 248-256.

[8] A. Krizhevsky. "Learning multiple layers of features from tiny images," *Tech Report*, 2009.

[9] S. Ioffe and C. Szegedy. "Batch normalization: Accelerating deep network training by reducing internal covariate shift," in *CoRR*, vol. 1502.03167, 2015.

ISSN 1737-9334

Nonlinear Control of a PV System Connected the single-phase Grid using a Three-level Boost

Fadwa El Otmani[#1], Abdelmajid Abouloifa [#2], Meriem Aourir[#3], Ibtissam Lachkar[*4], Fatima Zahra Assad[#5]

[#]*LTI Lab, Faculty of Sciences Ben M'sik, University Hasan II of Casablanca, BP 7955 Casablanca, Morocco*

[1]fadwa.elotmani@gmail.com

[2]abouloifa@yahoo.fr

[3]meriem.aourir@gmail.com

[5]fatimazahraa.assad@gmail.com

[*] *LRI Lab, ENSEM Casablanca, University Hasan II of Casablanca, BP 7955 Casablanca, Morocco*

[4]lachkaribtissam@gmail.com

***Abstract*—This paper focuses on the modelling and the control of a photovoltaic panel connected to the single phase-grid; through a three-level boost converter, a half bridge inventor and an LCL filter. This work seeks to achieve four control objectives, firstly the maximum energy generated by the PV panel must be ensured and exploited by regulating the input voltage to pursuit the reference provided by the MPPT block, then guarantee a satisfying power factor correction (PFC) respecting the power supply net, the DC-link voltage must be regulated to an accurate convenient reference and finally ensure the balance of the two voltages through the capacitors of the three-level boost. To meet those objectives a nonlinear controller that includes three blocks is synthesized based on the system model. The simulation results are performed through Matlab/SimPowerSystems environment and show that the designed controller meet the main objectives.**

***Keywords*—PV system; DC-DC controller; three-level boost; Nonlinear control; MPPT algorithm; PFC; Backstepping approach; Grid connected system; Lyapunov stability; inverters; LCL filter**

I. INTRODUCTION

Renewable energies have attracted growing attention thanks to many advantages as safety, inexhaustibility, simplicity of allocation and low cost of maintenance making research groups focus their efforts on improving operation and yield of the alternative sources.

The photovoltaic energy has multiples benefits [1] that make it a great deal of interest and many applications have been studied in the literature as [2] where the PV system is connected to three-phase grid and the system is controlled by using the backstepping approach and Lyapunov techniques, in [3] the author proposes two photovoltaic panels connected to the electrical network and a multi-loop controller is designed based on nonlinear approach and [4] intends to design a multi-input converter where the photovoltaic (PV) panel and energy storage system (ESS) are the input sources for the proposed converter. The photovoltaic panel voltage power depends on the climatic conditions, hence using a tracking algorithm was essential to ensure that the PV operates at the maximum power point regardless of climatic conditions changes such as temperature and irradiation. Various MPPT control methods have been proposed, such as perturb and observe algorithm [5], modified incremental conductance algorithm that responds accurately when the solar irradiation level increases presented in [6] and Fuzzy Logic MPPT method which is applied photovoltaic panel sourced boost converter in [7].

This paper deals with a PV system connected to a three-level dc-dc boost converter and a half bridge inverter connected to an electrical grid via LCL filter, as in Fig.1. This work seeks to achieve four control objectives: i. the maximum energy generated by the PV panel, must be ensured and exploited, ii. the DC-link voltage must be regulated to an accurate convenient reference, iii. Ensure the balance of the two voltages through the capacitors of the three-level boost and iv. Guarantee a satisfying power factor correction (PFC) respecting the power supply net. To meet those objectives a nonlinear controller [9] [10] is synthesized based on the accurate mathematical model and using Backstepping approach and Lyapunov stability tools [13] [14].

this work starts by introducing the PV system description and model in Section 2, the section 3 is devoted to designing the backstepping nonlinear controller based on the previous model, the controller includes three blocks whose performances and effectiveness are illustrated in section 6. This paper is summarized in Section 7 and conclusions are drawn with a reference list that end the paper.

II. PROBLEM FORMULATION

The Fig.1 illustrates the proposed system, where the photovoltaic generator is connected to the single-phase grid through an adaptation stage, this stage comprises: a three-level boost shopper that allows a step-up function of the PV voltage and maintain a constant voltage regardless of the solar cell module; then a half bridge inverter used to regulate the dc voltage supplied by the three-level boost and convert it to an ac voltage; the last part is the LCL filter which is vital to reduce the ripple cutting. The control inputs as appear on the system topology are defined as $[\mu, \mu_1, \mu_2]$:

ISSN 1737-9334

$$\mu_{(j=1,2)} = \begin{cases} 1 & \text{if } T_j \text{ is ON and } D_j \text{ is OFF} \\ 0 & \text{if } T_j \text{ is OFF and } D_j \text{ is ON} \end{cases}$$

$$\mu = \begin{cases} 1 & \text{if } s_1 \text{ is ON and } s_2 \text{ is OFF} \\ -1 & \text{if } s_1 \text{ is OFF and } s_2 \text{ is ON} \end{cases}$$

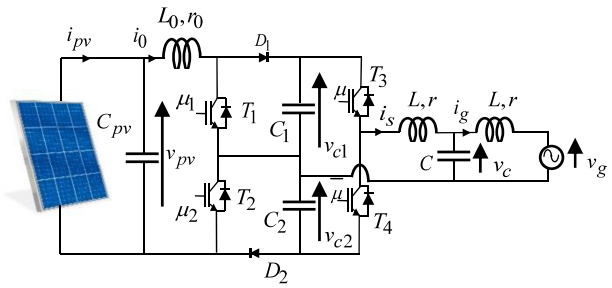

Fig.1 Photovoltaic system tied to the single-phase grid through a three-level boost converter

Where:

- i_{pv} and v_{pv} are respectively the current and the voltage generated by the PV array;
- i_0 is input current;
- v_{c1} and v_{c2} are denoted the DC link voltages;
- i_s , v_c are respectively the current in L and the voltage across C ;
- i_g and v_g present respectively the current and the voltage of the grid;
- μ_1, μ_2 and μ are denoted the control inputs:

$$\mu_j\,(j=1,2) = \begin{cases} 1 & \text{if } T_j \text{ is ON and } D_j \text{ is OFF} \\ 0 & \text{if } T_j \text{ is OFF and } D_j \text{ is ON} \end{cases}$$

$$\mu = \begin{cases} 1 & \text{if } T_3 \text{ is ON and } T_4 \text{ is OFF} \\ -1 & \text{if } T_3 \text{ is OFF and } T_4 \text{ is ON} \end{cases}$$

A. Average Model

The system is described using the average model. which is obtained by applying standard Kirchhoff Laws to the circuit using the average values of the state variables:

$$L\frac{dx_1}{dt} = -rx_1 + x_2 - v_g \quad (1a)$$

$$C\frac{dx_2}{dt} = x_3 - x_1 \quad (1b)$$

$$L\frac{dx_3}{dt} = \frac{u}{2}w_1 + \frac{w_2}{2} - x_2 - rx_3 \quad (1c)$$

$$C_{pv}\frac{dz_1}{dt} = -z_2 + \langle i_{pv} \rangle \quad (2a)$$

$$L_0\frac{dz_2}{dt} = z_1 - r_0 z_2 - w_1 + \frac{u_s}{2}w_1 - \frac{u_d}{2}w_2 \quad (2b)$$

$$C_1\frac{dw_1}{dt} = (2-u_s)z_2 - ux_3 \quad (3a)$$

$$C_2\frac{dw_2}{dt} = u_d z_2 - x_3 \quad (3b)$$

x_1 , x_2 , x_3 , z_1 , z_2 , w_1 , w_2 , u , u_s and u_d denote the average values over cutting periods, of the signals i_g , v_c , i_s , v_{pv} , i_0 , $(v_{c1}+v_{c2})$, $(v_{c1}-v_{c2})$, μ , $(\mu_1+\mu_2)$ and $(\mu_2-\mu_1)$ respectively. Noting that this model is non-linear as it involves products between the control signals and state variables.

III. Controller Design

This section is dedicated to design the adopted control strategy for the signal phase grid-connected to the PV system by using a nonlinear controller techniques based on the backstepping approach, as shown in Fig.2 the nonlinear regulator is composed of two blocs: the first one is the PV Controller which has an additional role looks for the voltage balance, and a second block constituted of wo nested loops: the inner loop looks for getting satisfying PFC, where the outer loop seeks to regulate the DC link voltage.

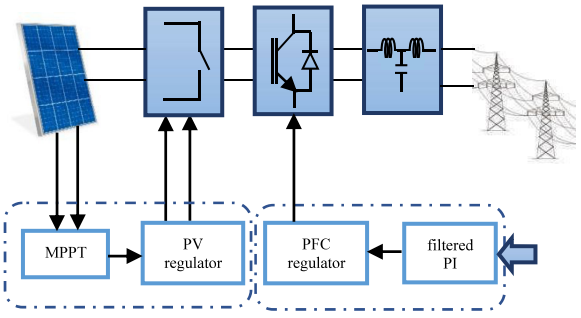

Figure 2: controlled system

A. Control Objectives

This work seeks to achieve four control objectives:

- the maximum power energy generated by the PV panel must be ensured.
- ensure the balance of the two voltages through the capacitor divider of the three-level boost.
- guarantee a satisfying power factor correction (PFC) respecting the power supply net.

ISSN 1737-9334

- regulating the DC link voltage to pursuit an appropriate reference.

B. PV Controller

The MPPT controller is a vital part to ensure that the PV array generates its maximum energy, this bloc is designed through two steps as shown follow, where the PV voltage must track the reference (z_1^*) provided by the MPPT block.

Step 1: stabilizing of subsystem (2a)

let's began by introducing the voltage error:

$$e_{z1} = C_{pv}(z_1 - z_1^*) \tag{4}$$

where z_1^* denotes, the reference signal provided by the MPPT controller block. Using (2b), the time derivation of e_{z1} yields to the following equation:

$$\dot{e}_{z1} = \langle i_{pv} \rangle - z_2 - C_{pv}\frac{dz_1^*}{dt} \tag{5}$$

z_2 will be chosen as the virtual control input, then a stabilizing function will guarantee the global stability of the subsystem (5), with respect to candidate Lyapunov function:

$$V_{z1} = 0.5e_{z1}^2 \tag{6}$$

Its time derivative is given as:

$$\dot{V}_{z1} = e_{z1}\dot{e}_{z1} = -k_{z1}e_{z1}^2 \tag{7}$$

k_{z1} is a positive design parameter. Then; using (5) and (7); one gets the virtual control z_2^*

$$z_2^* = k_{z1}e_{z1} + \langle i_{pv} \rangle - C_{pv}\frac{dz_1^*}{dt} \tag{8}$$

As z_2^* is not the actual control input, it is necessary to define a new error e_{z2} between the virtual control and its desired value z_2^*.

$$e_{z2} = L_0(z_2 - z_2^*) \tag{9}$$

Using (5), (8) and (9) the dynamic's $\dot{e}_{z1}$ error and Lyapunov function $\dot{V}_{z1}$ became:

$$\dot{e}_{z1} = -\frac{e_{z2}}{L_0} - k_{z1}e_{z1} \tag{10}$$

$$\dot{V}_{z1} = -\frac{e_{z1}e_{z2}}{L_0} - k_{z1}e_{z1}^2 \tag{11}$$

-Step 2: stabilizing of subsystem(2b)

Using (2b) and (9), time derivative of $\dot{e}_{z1}$ is given by:

$$\dot{e}_{z2} = z_1 - r_0 z_2 - w_1 + \frac{u_s}{2}w_1 - \frac{u_d}{2}w_2 - L_0\frac{dz_2^*}{dt} \tag{12}$$

Consider the augmented Lyapunov function:

$$V_{z2} = V_{z1} + \frac{e_{z2}^2}{2} \tag{13}$$

Where its time derivation yield to:

$$\dot{V}_{z2} = e_{z2}\left(\dot{e}_{z2} - \frac{e_{z1}}{L_0}\right) - k_{z1}e_{z1}^2 \tag{14}$$

To keep all during the negativity of the Lyapunov function, the following equality will be considered

$$\dot{e}_{z2} = \frac{e_{z1}}{L_0} - k_{z2}e_{z2} \tag{15}$$

Then the Lyapunov function's derivative became:

$$\dot{V}_{z2} = -k_{z2}e_{z2}^2 - k_{z1}e_{z1}^2 \tag{16}$$

Using (16) and (9), once get the control law u_s:

$$u_s = \frac{2}{w_1}\left(-k_{z2}e_{z2} + \frac{e_{z1}}{L_0} + \frac{u_d}{2}w_2 + L_0\frac{dz_2^*}{dt} - z_1 + r_0 z_2 + w_1\right) \tag{17}$$

C. v_{c1} and v_{c2} Balance

To complete the control law, it was necessary to ensure the balance between the capacitor divider voltages, to this end the difference between the two voltages must vanish. Let's began by introducing the following error:

$$e_{w2} = C_2(w_2 - w_2^*) \tag{18}$$

w_2^* denotes a null reference signal. Using (3b), the time derivation of e_{w2} yields to the following equation:

$$\dot{e}_{w2} = u_d z_2 - x_3 - C_2\frac{dw_2^*}{dt} \tag{19}$$

Consider the Lyapunov function:

$$V_{w2} = 0.5e_{w2}^2 \tag{20}$$

Its time derivative is given as:

$$\dot{V}_{w2} = e_{w2}\dot{e}_{w2} = -k_{w2}e_{w2}^2 \tag{21}$$

Using (19) and (21) once get the control law u_d:

$$u_d = \frac{1}{z_2}\left(x_3 + C_2\frac{dw_2^*}{dt} - k_{w2}e_{w2}\right) \tag{22}$$

Then using (11) and (22), once get the final control laws:

$$u_1 = \frac{u_s - u_d}{2} \tag{23}$$

$$u_2 = \frac{u_s + u_d}{2} \tag{24}$$

D. PFC regulator

To ensure the unity power factor correction a PFC regulator is designed with two nested loops where the inner loop guarantees that the grid current pursuit his reference, and the outer loop ensure the DC link voltage regulation.

1.inner loop

ISSN 1737-9334

Step1: stabilizing of subsystem (1a)

let's define the error in question:

$$e_{x1} = L(x_1 - x_1^*) \quad (25)$$

where x_1^* denotes the concerned reference. Using (1a), the time derivation of e_{x1} yields to the following equation:

$$\dot{e}_{x1} = -rx_1 + x_2 - v_g - L\frac{dx_1^*}{dt} \quad (26)$$

x_2 will be chosen as the virtual control input, then a stabilizing function will guarantee the global stability of the subsystem (26), with respect to candidate Lyapunov function:

$$V_{x1} = 0.5e_{x1}^2 \quad (27)$$

Its time derivative is given as:

$$\dot{V}_{x1} = \dot{e}_{x1}e_{x1} = -k_{x1}e_{x1}^2 \quad (28)$$

where, k_{x1} is a positive design parameter. Then using (26) and (28), one gets the virtual control x_2^*

$$x_2^* = rx_1 + v_g + L\frac{dx_1^*}{dt} - k_{x1}e_{x1} \quad (29)$$

As x_2^* is not the actual control input, it is necessary to define a new error e_{x2} between the virtual control and its desired value x_2^*.

$$e_{x2} = C(x_2 - x_2^*) \quad (30)$$

Using (29) and (30) in (26) and (28) the dynamic's $\dot{e}_{x1}$ error and Lyapunov function $\dot{V}_{x1}$ became:

$$\dot{e}_{x1} = \frac{e_{x2}}{C} - k_{x1}e_{x1} \quad (31)$$

$$\dot{V}_{x1} = \frac{e_{x1}e_{x2}}{C} - k_{x1}e_{x1}^2 \quad (32)$$

Step2: stabilizing of subsystem (1b)

Using (1b) and (30), time derivative of $\dot{e}_{x2}$ is given by:

$$\dot{e}_{x2} = \dot{x}_3 - \dot{x}_1 - C\frac{dx_2^*}{dt} \quad (33)$$

Now a new virtual control input x_3 appears, then a stabilizing function will guarantee the global stability of the subsystem (33), with respect to the augmented Lyapunov function:

$$V_{x2} = V_{x1} + 0,5e_{x2}^2 \quad (34)$$

Where its time derivation yield to:

$$\dot{V}_{x2} = e_{x2}\left(\frac{e_{x1}}{C} + \dot{e}_{x2}\right) - k_{x1}e_{x1}^2 \quad (35)$$

To keep all during the negativity of the Lyapunov function, the following equality will be considered

$$\dot{e}_{x2} = -\frac{e_{x1}}{C} - k_{x2}e_{x2} \quad (36)$$

Then the Lyapunov function's derivative became:

$$\dot{V}_{x2} = -k_{x2}e_{x2}^2 - k_{x1}e_{x1}^2 \quad (37)$$

where, k_{x2} is a positive design parameter. Then using (33) and (35), one gets the virtual control x_3^*

$$x_3^* = x_1 + C\frac{dx_2^*}{dt} - k_{x2}e_{x2} - \frac{e_{x1}}{C} \quad (38)$$

x_3^* is not the actual control input, a new error e_{x3} as well, will be defined between the virtual control and its desired value x_3^*.

$$e_{x3} = L(x_3 - x_3^*) \quad (39)$$

Using (38) and (39) in (33) and (35) the dynamic's $\dot{e}_{x2}$ error and Lyapunov function $\dot{V}_{x2}$ became:

$$\dot{e}_{x2} = \frac{e_{x3}}{L} - k_{x2}e_{x2} - \frac{e_{x1}}{C} \quad (40)$$

$$\dot{V}_{x2} = e_{x2}\left(\frac{e_{x3}}{L} - \frac{e_{x1}}{C}\right) - k_{x1}e_{x1}^2 - k_{x2}e_{x2}^2 \quad (41)$$

Step3: stabilizing of subsystem (1c)

Using (1c) and (38), time derivative of $\dot{e}_{x3}$ is given by:

$$\dot{e}_{x3} = \frac{u}{2}w_1 + \frac{w_2}{2} - x_2 - rx_3 - L\frac{dx_3^*}{dt} \quad (42)$$

Consider the augmented Lyapunov function:

$$V_{x3} = V_{x2} + \frac{e_{x3}^2}{2} \quad (43)$$

Where its time derivation yield to:

$$\dot{V}_{x3} = e_{x3}\left(\dot{e}_{x3} + \frac{e_{x2}}{L}\right) - k_{x2}e_{x2}^2 - k_{x1}e_{x1}^2 \quad (44)$$

To keep all during the negativity of the Lyapunov function, the following equality will be considered

$$\left(\dot{e}_{x3} + \frac{e_{x2}}{L}\right) = -k_{x3}e_{x3} \quad (45)$$

Then the Lyapunov function's derivative became:

$$\dot{V}_{x3} = -k_{x3}e_{x3}^2 - k_{x2}e_{x2}^2 - k_{x1}e_{x1}^2 \quad (46)$$

where, k_{x3} is a positive design parameter. Using (42) and (45), once get the final control law u:

$$u = \frac{2}{w_1}\left(L\frac{dx_3^*}{dt} + x_2 + rx_3 - \frac{w_2}{2} - k_{x3}e_{x3} - \frac{e_{x2}}{L}\right) \quad (47)$$

2. the outer loop: (PI regulator)

Based on the model (47) and considering the fact that β and its derivatives up to order 3 must be available, the following third order filtered PI is considered:

$$\beta = \left(\frac{a}{a+s}\right)^3\left(k_{y1}e_{y1} + k_{y2}e_{y2}\right) \quad (48)$$

ISSN 1737-9334

With $e_{y1} = y - y^*$ and $e_{y2} = \int e_{y1} de$

s denotes the Laplace variable and (a, k_{y1}, k_{y2}) are positive real design parameters.

Theorem1: (main result). Consider the closed-loop single-phase grid-connected PV system, represented by the average model (1a-c), (2a-b) and (3a-b) and comprising the control laws (23), (24) and (47). Leads to the following crucial results:

- the closed-loop system is globally asymptotically stable
- the tracking error e_{z1} vanish involving the MPPT reaching.
- the dc bus voltage is regulated and the balance of v_{c1} and v_{c2} is assured thanks to the convergence of e_{y1} and e_{w2} to zero.
- the error e_3 vanished and the real variable β converges to a constant implying the PF correction

IV. NUMERICAL SIMULATION

In this section, the simulation results of the model composed by the power and control subsystems described by Fig.1, is investigated by using SIMPOWER of MATLAB Simulink to verify the theoretical results using the parameters value shown in table 1and 2.

TABLE I
PV CONNECTED GRID SYSTEM CHARACTERISTICS

Parameters	Symbol	Value
Boost	C_{pv}	$2mF$
	L_0	$45mH$
	r_0	0.3Ω
Network	E	$220\sqrt{2}\ V$
	f	$50Hz$
LCL-Filter	L	$1mH$
	C	$0.15mF$
	r	$50m\Omega$
	r_g	$50m\Omega$
PWM switching frequency	f_{pwm}	$10Khz$
DC capacitance	C_1	$8mF$
	C_2	$8mF$

TABLE IIIII
CONTROLLER PARAMETERS

Parameters	Symbol	Value
Current regulator (PFC)	k_{x1}	5000
	k_{x2}	5000
	k_{x3}	5000
Voltage regulator	k_{z1}	10000
	k_{z2}	10000
DC Link regulator	k_p	$8e-7$
	k_i	$6e-5$
	a	$1e-4$
The voltage balance	k_{w2}	10000

Fig.3 shown that in standard climatic conditions the PV generator provides his maximal power, which is 400 V, after a response time that lasts 0.1 second thanks to the MPPT tracker. Fig.4 presents the regulated DC-link voltage $w_1 = v_{c1} + v_{c2}$, as shown in the figure, the voltage is maintained at a constant level (800 V), Consequently, the real power extracted from the PV generator can be totally transferred to the grid, as well the balance between v_{c1} and v_{c2} is insured as shown in fig.6. Fig.5 illustrate the injected current in the grid pursuit its reference and in phase with the grid voltage, where the grid current error vanishes in less than 0.1 second. The last figure shows the variation of the tuning ratio β which takes by mean a constant value.

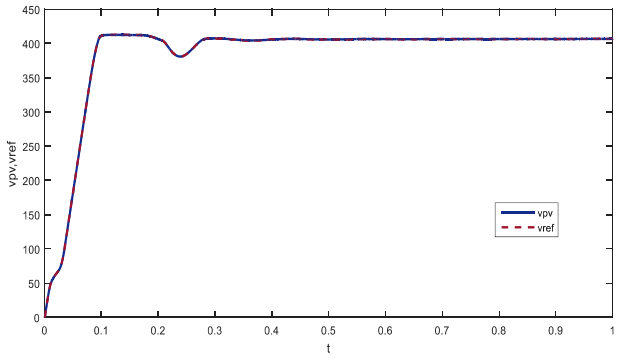

Fig.3 PV voltage & its reference

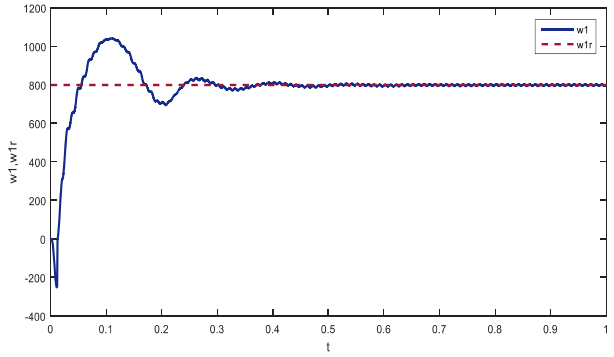

Fig.4 DC bus voltage

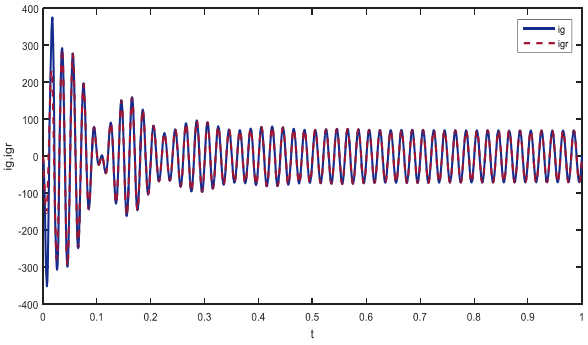

Fig.5 injected current and its reference

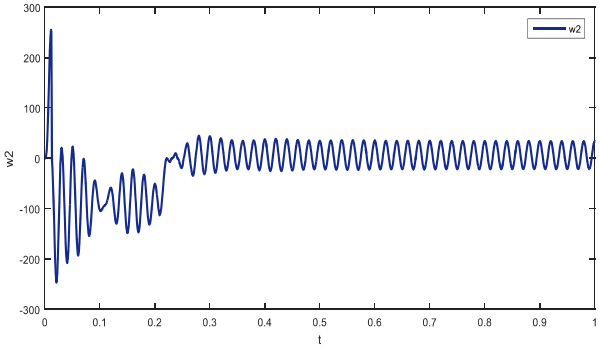

Fig.6: the balance between v_{c1} and v_{c2} ($w_2 = v_{c1} - v_{c2}$)

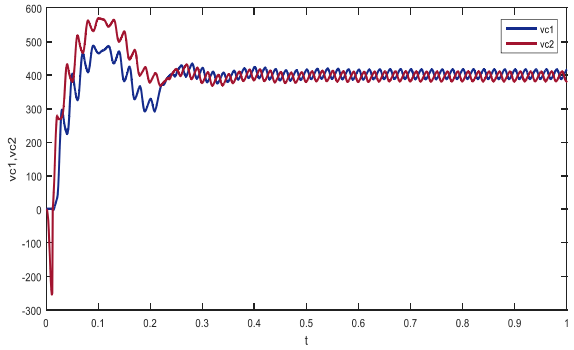

Fig7: the voltage balancing

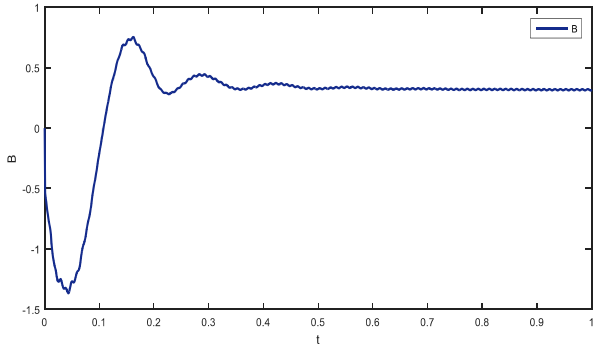

Fig8: the control signal β

V. Conclusions

This study considered the problem of controlling a single stage PV system connected to the single-phase grid through a three-level boost converter, the system dynamics have been described by the averaged 7th nonlinear state space model. The solution involves a cascade nonlinear controller based on the Backstepping approach. The simulation results confirmed that all control objectives are successfully accomplished and prove the effectiveness and robustness of this controller.

References

[1] S. M. Metev and V. P. Veiko, *Laser Assisted Microtechnology*, 2nd ed., R. M. Osgood, Jr., Ed. Berlin, Germany: Springer-Verlag, 1998.

[2] J. Breckling, Ed., *The Analysis of Directional Time Series: Applications to Wind Speed and Direction*, ser. Lecture Notes in Statistics. Berlin, Germany: Springer, 1989, vol. 61.

[3] S. Zhang, C. Zhu, J. K. O. Sin, and P. K. T. Mok, "A novel ultrathin elevated channel low-temperature poly-Si TFT," *IEEE Electron Device Lett.*, vol. 20, pp. 569–571, Nov. 1999.

[4] M. Wegmuller, J. P. von der Weid, P. Oberson, and N. Gisin, "High resolution fiber distributed measurements with coherent OFDR," in *Proc. ECOC'00*, 2000, paper 11.3.4, p. 109.

[5] R. E. Sorace, V. S. Reinhardt, and S. A. Vaughn, "High-speed digital-to-RF converter," U.S. Patent 5 668 842, Sept. 16, 1997.

[6] (2002) The IEEE website. [Online]. Available: http://www.ieee.org/

[7] M. Shell. (2002) IEEEtran homepage on CTAN. [Online]. Available: http://www.ctan.org/tex-archive/macros/latex/contrib/supported/IEEEtran/

[8] *FLEXChip Signal Processor (MC68175/D)*, Motorola, 1996.

[9] "PDCA12-70 data sheet," Opto Speed SA, Mezzovico, Switzerland.

[10] A. Karnik, "Performance of TCP congestion control with rate feedback: TCP/ABR and rate adaptive TCP/IP," M. Eng. thesis, Indian Institute of Science, Bangalore, India, Jan. 1999.

[11] J. Padhye, V. Firoiu, and D. Towsley, "A stochastic model of TCP Reno congestion avoidance and control," Univ. of Massachusetts, Amherst, MA, CMPSCI Tech. Rep. 99-02, 1999.

[12] *Wireless LAN Medium Access Control (MAC) and Physical Layer (PHY) Specification*, IEEE Std. 802.11, 1997.

[13] F. EL Otmani, A. Abouloifa, M. Aourir, A. Hamdoun, and I. Lachkar, 'Comparative study of two sliding surfaces to control a double boost converter', p. 11, 2017.

[14] F. E. Otmani, A. Abouloifa, M. Aourir, I. Lachkar, F. Z. Assad, and A. Hamdoun, 'A passivity-based control applied to a double cascade DC/DC converter using a fuel cell', in 2018 Renewable Energies, Power Systems Green Inclusive Economy (REPSGIE), 2018, pp. 1–6

ISSN 1737-9334

Epidemiological Researches Approach Using Data Mining Technics

Mohammed Sabri[*1], Menaouer Brahami[*2], Sidi Ahmed Rahal[#3]

[*]*Systems Engineering Department,*
National Polytechnic School of Oran, Algeria
[1]mohamed.sabri@enp-oran.dz
[2]menaouer.brahami@enp-oran.dz
[#] *Systems Engineering Department*
University of Sciences and Technology-Mohamed Boudiaf, Oran, Algeria
[3]rahalsa2001@yahoo.fr

Abstract— **Knowledge management is to acquire and represent knowledge relevant to a domain, a task or a specific organization in order to facilitate access, reuse and evolution. This usually means build, maintain and evolve an explicit representation of knowledge. Knowledge mapping is graphical techniques which allows of preserving and visualizing the patrimony strategic and trades of the knowledge domains acquired over the years. Moreover, Data Warehouse is the centralized store of detailed data from all relevant source systems, allowing for ad hoc discovery and drill-down analysis by multiple user groups. It provides an infrastructure that enables businesses to extract, cleanse, and store vast amounts of data. That is, the basic purpose of a data warehouse is to empower the knowledge workers (doctors, nurses, paramedics, etc...) with information that allows them to make decisions based on a solid foundation of fact. In this paper we propose a new medical knowledge mapping approach based, on the one hand, on integration technique of heterogeneous data in the medical field by creating a data warehouse and, on the other hand, on a technique of extracting epidemiological prediction rules from medical data by choosing a technique of service-oriented data mining of APESS platform whose objective to exploit these predictive rules to automatically improve the Boolean model of the medical knowledge mapping through CARTOCEL system. The proposed approach of epidemiological Knowledge Mapping would be new direction towards as a decision support tool, whether individual or collective in the public health for management and monitoring of some pathology (chronic diseases).**

Keywords — **Knowledge Management, Data Warehouse, Data mining, Services Web, APESS Platform, Decision Support System.**

I. INTRODUCTION

The approach of knowledge management, business intelligence and service-oriented data mining was used as theoretical technologies in order to build an intelligence enterprise framework. Knowledge management (KM) implementations in the healthcare sector depend on the methods and techniques to manage acquiring, structuring, transfer, and utilizing tacit and explicit knowledge. The continuous improvement to the epidemiological services and to the chronic diseases services requires adequate implementations to overcome the obstacles occurring in this service. Based on the interactions between those various public health services, the amount of knowledge is massive while all of knowledge details created by any of those services are necessary for a successful healthcare service delivery. Based on the interactions between those various public health services, the amount of knowledge is massive while all knowledge details created by any of those services are necessary for a successful healthcare service delivery. Since the business intelligence process can create additional customer value (Health Departments) through knowledge creation with integrating heterogeneous data, business intelligence can provide users (doctors) with reliable, accurate information and help them make decisions. In this sense, effective Business Intelligence system allows data collection from all departments within the company, their analysis, preparation the necessary reports through data mining and addressing those users who are most needed.

The doctor and these collaborators need to know its epidemiological data, which implies a strong collaboration between health trades actors and interoperability between the systems being used in the epidemiological services. Given the complexity of the epidemiological and chronic diseases field, we encounter several problems such as:

- The diversity of the distributed data sources and their heterogeneous in the different services.
- The difficulties of accessing to relevant information for the disease monitoring are related to the dispersion of epidemiological information on different hospital information systems (HIS) which are often autonomous and heterogeneous.
- The difficulty to understand the mechanisms of acquisition and interpretation of the medical experiences and epidemiologic diagnostic reasoning.
- The modelling of the information does not allow facilitate access to distributed mining in order to Increase data reliability, dissemination and use of medical knowledge.

Subsequently, we present case studies which illustrate good practices ‖ in either managing knowledge for, from and about a large healthcare organization. Likewise, the subsequent section presents the case of Business Intelligence development at large companies, followed by discussion and conclusions for understanding Business Intelligence (BI) systems

ISSN 1737-9334

evolution in practice and research. Thereafter, we utilized a service-oriented data mining platform (APESS) for business intelligence whose objective is to integrate of many services which coordinate and communicate to one another for their respective goals, thus enabling simplified data delivery and low-latency analytics. In addition, this APESS platform is composed of two main components, on the one hand, web services, which implement data mining algorithms and on the other hand a user web interface, which can be used for modelling applications that use the services of the platform.

II. Related Work

In order to understand the existing state of knowledge management and the knowledge extracted from the heterogeneous data using the different techniques of Business Intelligence (BI) and the service-oriented data mining platforms in healthcare organizations, it is essential to review similar efforts made by other researchers.

A. Knowledge Management: Concepts and Case Studies

Since KM is a relatively new discipline, and object of study of many researches, this research focuses the attention in the different approaches and models given to the topic. To be considered appropriate and relevant by the author of this research, initially will be taken the contribution of [7], who introduce the topic of the importance of knowledge management for organizational performance has been widely recognized and acknowledged in management literature. In this context, knowledge management is assumed to create value for organizations by applying their accumulated knowledge to their products and services outputs. Knowledge management is the formal decision-making process; the decision is made to grasp and make use of the new knowledge, and then to ensure that useful value is created for staff [10]. For Jennex [16] KM is the practice of selectively applying knowledge from previous experiences of decision making to current and future decision making activities with the express purpose of improving the organization's effectiveness. He also considers a Knowledge Management System (KMS) as that system which is created to facilitate the capture, storage, retrieval and reuse of knowledge. KM and KMS holistically combine organizational and technical solutions to achieve the goals of knowledge retention and reuse to ultimately improve organizational and individual decision making [16]. Plessis [18] considers knowledge management as a structured and planned approach to manage the creation, sharing, harvesting and how to use leverage as a result of organizational knowledge, capacity, speed and efficiency in the provision and delivery of goods and services to customers. According to Zack [24], knowledge management involves the process through which knowledge is acquired and edited, shared among the members of the organization and implemented to innovate and improve the functioning of the organization. For Montoro [19], it is the "discipline that is required to examine the design and implementation of systems whose main goal is that all the tacit, explicit, individual, internal and external knowledge involved in the organization can transform and become organizational knowledge.

However, practicing successful KM strategies within the organization can lead to achieve the following advantages [28]: (1) enhance customer services; (2) apply various quality methods to gain faster innovation processes; (3) improve communication and collaboration between all stakeholders; and finally (5) achieve financial goals. In this research, the conceptual definition of KM practices contains three dimensions; that is ―knowledge creation, knowledge storage and knowledge sharing. Therefore, Wulantika [9] argues that (1) knowledge Management (KM) is the organization's activities in managing knowledge so in the end become an asset, (2) a lot of knowledge of the strategies used by people in a short time so that they can interact with each other, and (3) apply knowledge in a variety of everyday work in order to improve organizational performance. Various academics and business practitioners began to apply to grow and develop knowledge management through research and application in business practices. For Yaghoubi [25], KM promotes an integrated approach for identifying, capturing, retrieving, sharing and evaluating all enterprises' information assets.

These information assets may include databases, documents, policies, procedures, as well as the uncaptured tacit expertise and experience stored in individuals' heads. Another study by Perez-Soltero [1], analyzed the knowledge management in small and medium enterprises in the restaurant industry in northern Mexico, in order to identify areas for improvement in their production processes. They analyzed the stages of identification, storage, creation, distribution, use and measurement of knowledge, and concluded that the use or application of knowledge is found to be more developed because past experiences are used to make better decisions and improve tasks, processes and services.

To sum up, a number of studies by Abas & Jali [38] highlighted an organizing review of Knowledge Management and conceptual review and empirical evidence of the three main themes of Knowledge Management, namely knowledge creation, knowledge transfer and knowledge application. Based on the empirical analysis, this paper concludes that huge number of prior studies only focuses on the knowledge transfer theme. This is because knowledge transfer is said to be more visible and easier to observe as compared to creation and application. Specifically, this paper highlights that the emerging concept of innovation process is about the capability of managing knowledge; as well as also displays past contribution of Knowledge Management towards new technology development. Al-qarioti [20] examined the impact of specific KM dimensions on organizational performance of small size business owners and managers at a management-level in their firms from (86) enterprises in Isfahan. The study results showed that some knowledge resources are directly related to organizational performance, while others are not.

Finally, Christozov & Toleva-Stoimenova [3] delineate four forms of knowledge, which we will use in our later discussion:

ISSN 1737-9334

- Explicit-individual (concepts): Examples include engineering formula calculation and basic spreadsheet manipulation.
- Tacit-individual (skills): Examples include managing teams and troubleshooting unusual exceptions.
- Explicit-group (stores): Examples include formalized processes and patents.
- Tacit-group (genres): Examples include corporate culture and norms of communication.

The process model associated with knowledge management consists of well-defined activities which: 1) help to ensure the quality of the data and information used by knowledge workers (Trades actor's and Managers), 2) assist in the refinement of data and information into knowledge (knowledge map and knowledge engineering methods), 3) allow the efficient storage and retrieval of metadata and knowledge (knowledge map and knowledge engineering methods), 4) promote the timely dissemination and distribution of knowledge, and 5) support the tailored sharing of knowledge (e-learning, community of practice, and knowledge servers).

B. Business Intelligence: Concepts

The value of information increases with the number of users who can access that information, multiplied by the number of business areas in which the user works companies desperately need timely and relevant information and knowledge [17].

Since the literature and the operating people have different definitions of Business Intelligence, we are going to show the different experts definition of the concept. All of the experts agreed with each other that the definition of BI is a tool to make the right decisions in an organization. This by, collect data from different systems to create strategic, operational and tactical decisions [22]. Furthermore, one of the experts mean that definition of BI can be viewed in two different ways: (1) A system oriented way which collect, store and present data in different tools, and (2) a process oriented way, which he describes that the users need some type of knowledge as well. Processes are collected and the data are presented and the next thing is to do the data analysable for the end users.

In other words, the aim of BI is to provide the decision makers with analytical tools and information to make good decisions, so they can improve the correctness and quality of inputs in to the decision making process [22]. For Negash & Gray [29], an ideal BI system should provide the decision maker with data delivered in the right time, at the right location and in the right form. This would improve the timelines and value of the decision process. Curko [8] in the chapter has explored the problems of capturing different types of structured and unstructured data relate to, filtering, grouping, cleansing, and enhancement. Business Intelligence (BI) is used to represent the tools and systems that play a vital role in knowledge sharing and dissemination at organizations [34]. According to Nemati [5], Business intelligence tools are software tools which allow the retrieval, analysis and reporting of data.

Based on earlier literature, BI is a set of techniques of gathering, accessing and analysing a big amount of data, while KM is a set of practices for the creation, development and application of knowledge to create a better performance in the organization [22]. For Davenport [31], there are several differences in the concepts. KM is mainly about human subjective knowledge, thus no data or objective information. According to Khan and Quadri [27], companies need both KM and BI as an integrated system to get value from explicit and tacit knowledge. For his part, Panian [40] has discussed the characteristics and benefits of Service-oriented Architecture (SOA) and suggested to use BI solutions as Web services in an SOA environment. Furthermore, Nguyen [32] have presented a real-time Business Intelligence architecture called SARESA with the aim of providing continuous, real-time analytics in order to enable proactive responses to a business environment for effectively managing and controlling time sensitive business processes. The authors have introduced Sense & Respond loops and a service-oriented architecture that is able to detect situations and exceptions, perform complex analytical tasks and reflect on the gap between current situations and desired management goals.

In conclusion, an understanding BI system enables any organization to implement an analytical approach that transforms data into information, information into knowledge and then knowledge into decisions. Hence, KM is about Knowledge sharing, extraction, communication, application and innovation by captures, stores, organizes, and distributes knowledge, while BI converts data into knowledge for the need of the end user by identifying trends for new business strategies.

C. Service-Oriented Data Mining: Concepts and Platforms

Data mining is a complex process, which can be deployed by means of multiple approaches. Otherwise, health, Science, and pharmacy fields often need to analyze very large datasets maintained over geographically distributed sites by using the computational power of distributed and parallel systems. The grid can play a significant role in providing an effective computational support for distributed knowledge discovery applications. For this, Georgescu [33], was discusses how to design and implement data mining applications by using the Knowledge Grid tools starting from searching grid resources, composing software and data components, and executing the resulting data mining process on a grid. Some performance results are also discussed.

Nevertheless, several authors say that the distributed nature of data and the extension of information sharing make the SOA a suitable scenario in which data mining applications can be executed. For this and after a literature search, we can observe that there is an attempt to design architecture for performing data mining on the Grid, especially in the research work of [14]. The authors have presented the design of a Knowledge Grid architecture based on the non-OGSA-based version of the Globus Toolkit. This architecture extends the basic grid services with services of knowledge discovery on geographically distributed infrastructures. Furthermore, Brezany [26] have described the service oriented architecture

ISSN 1737-9334

and its components implemented in the GridMiner application. Several data mining and OLAP services have been already deployed and are ready to perform the knowledge discovery tasks. Moreover, it is essential that the system provides a powerful, flexible and simple to use graphical user interface (GUI) which hides the complexity of the Grid but still offering possibilities to interfere during the execution phase, control the task execution and visualize results. AlSairafi [30] have developed the Discovery Net architecture for building grid-based knowledge discovery applications. This architecture enables the creation of highlevel, re-usable and distributed application workflows that use a variety of distributed resources. It is built on top of standard protocols and standard infrastructures such as Globus but also defines its own protocols such as the Discovery Process Markup Language for data flow management. Perez and Pëna [23] have proposed both a novel architecture for Data Mining Grid, named DMGA, and the implementation of this architecture, named WekaG. The DMGA (Data Mining Grid Architecture) is a vertical and generic architecture which is based on the main data mining stages: pre-processing, data mining and post-processing and usage patterns for their composition in a real scenario. However, the implementation of WekaG architecture is based on Weka, a well-known tool form developing machine learning algorithms, which can be used for solving data mining problems. Finally, Beynona et al., [15] have described a middleware framework, called DataCutter that is designed to provide support for subletting and processing of datasets in a distributed and heterogeneous environment. In DataCutter, data intensive applications are represented as a set of filters. A filter is a user-defined object with methods to carry out application-specific processing on data. Both the filtering and indexing services use the data access service to read data and index information from files stored on archival storage systems. The indexing service manages the indices and indexing methods registered with DataCutter. The filtering service manages the filters for application-specific aggregation operations.

Similarly, Talia et al., [4] have presented Weka4WS, a framework that extends the Weka toolkit for supporting distributed data mining on Grid environments. Weka4WS adopts the emerging Web Services Resource Framework (WSRF) for accessing remote data mining algorithms and managing distributed computations. The Weka4WS user interface is a modified Weka Explorer environment that supports the execution of both local and remote data mining tasks. On every computing node, a WSRF-compliant Web Service is used to expose all the data mining algorithms provided by the Weka library. Wu et al., [37] have developed a support platform, called CGSP, is a grid middleware for the construction of the ChinaGrid. ChinaGrid aims at building a public service system for Chinese education and research. Function modules of CGSP for system running are Domain Manager, Information Center, Job Manager, Data Manager, Service Container and Security Manager. Furthermore, (Stankovski et al., 2008) have designed the DataMiningGrid system according to three principles: service-oriented architecture (SOA), standardization, and open technology. SOA promotes the sharing of geographically dispersed business functions in an "exible way". Its main features include high performance, scalability, "exibility, ease of use, conceptual simplicity, compliance with emerging grid and data mining standards, and the use of mainstream grid and open technology. Finally, Podpecan et al., [35] have proposed a novel Service-oriented Knowledge Discovery framework and its implementation in a service-oriented data mining environment Orange4WS (Orange for Web Services), based on the existing Orange data mining toolbox and its visual programming environment, which enables manual composition of data mining workflows. The new service-oriented data mining environment Orange4WS includes the following new features: simple use of web services as remote components that can be included into a data mining workflow; simple incorporation of relational data mining algorithms; a knowledge discovery ontology to describe workflow components (data, knowledge and data mining services) in an abstract and machine-interpretable way, and its use by a planner that enables automated composition of data mining workflows.

III. APPROACH

The objective of our approach, illustrated in Figure 1, is to propose a new medical knowledge mapping approach based, on the one hand, on integration technique of heterogeneous data in the medical field by creating a data warehouse and, on the other hand, on a technique of extracting epidemiological prediction rules from medical data by choosing a technique of service-oriented data mining of APESS platform [21] whose objective to exploit these predictive rules to automatically improve the Boolean model of the medical knowledge mapping through CARTOCEL system [11, 12]. The proposed approach of epidemiological Knowledge Mapping would be new direction towards as a decision support tool, whether individual or collective in the public health for management and monitoring of some pathology (chronic diseases).

ISSN 1737-9334

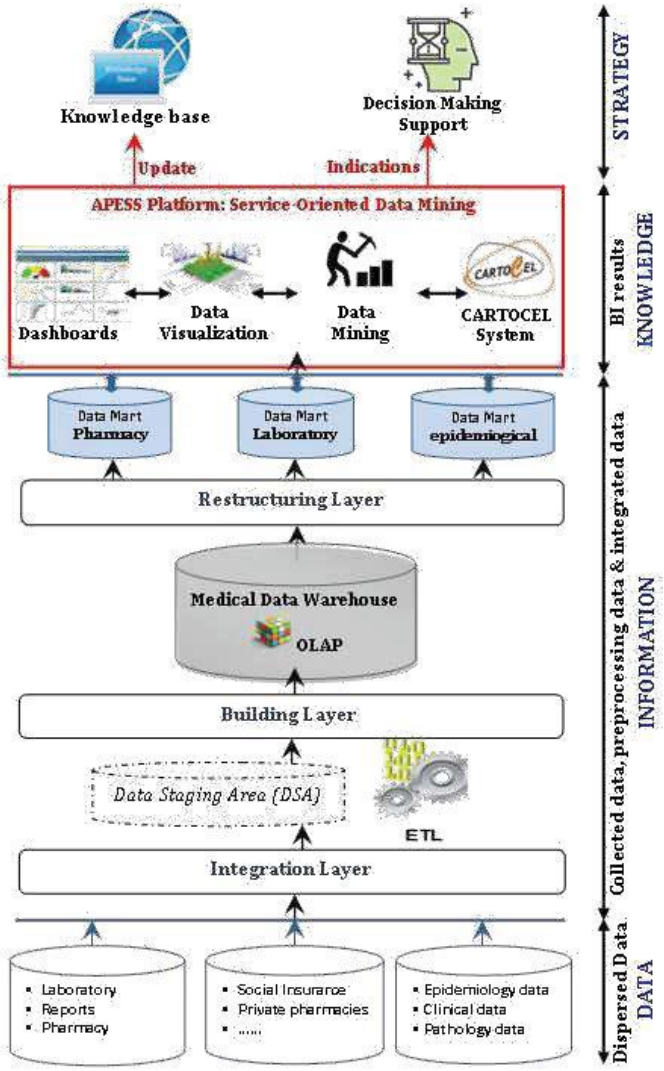

Fig. 1 Architecture of the approach proposed.

A. *Data Warehousing*

The first phase of our approach is the design of the data warehousing, with the objective of obtaining a unique source of data to carry out the data mining services web tasks.

Our data sources are the records of sales from the public and private pharmacies. To be usable, all data from distributed systems must be organized, coordinated, integrated, and finally stored to give the user an overview of information. The architecture of the steps processing of pharmaceutical data warehouse (see Figure 2), is articulated around three axes:

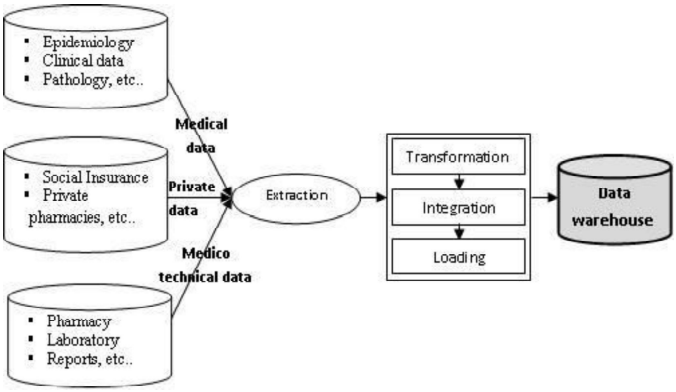

Fig. 2 Steps of processing building of medical data warehouse.

Integration: This first step consists of extracting and gathering the data coming from the various databases of public and private pharmacies and the external sources. These databases are supported by the same relational DBMS, they are identical from the point of view of their structures, and they are installed in different sites where no connection exists between these sites, neither the existence of a centralized system. The source recovered databases (files) are coded and stored in the file system.

Building: It consists of extracting the relevant data and copying it in the warehouse. Consequently, our data warehouse will constitute a centralized collection of materialized and historical data, available for data mining services web. The data related to the drug sales and the characteristics related to the sold products, are taken into account within the scope of this study, and the other data, such as the purchases, are neglected. During the transformation of data, we encountered several types of conflicts that are each treated separately: conflict of classification, descriptive conflict, structural conflict, and data conflicts.

Restructuring: This step consists of reorganizing the data, in data marts, to support the data mining services web; a specific data mart is created, in relation to the information concerning the chronic diseases selected out of all the retail sales and the characteristics of the patients belonging to the essential variables for the data mining services web.

Construction of the warehouse schema: according to Zerf Boudjettou [39], the result of processing of the data warehouse building is to define a global schema providing an integrated view of the sources the will be exploited later in the process of extracting knowledge from data. For this, our data warehouse is based on the star model (see Figure 3) and contains all the information about retail sales, products and places where the pharmacies are located. The source data available is commercial data (basic sales records) to carry out medical research (epidemiologic), and we chose a traditional multidimensional modeling for our data warehouse.

ISSN 1737-9334

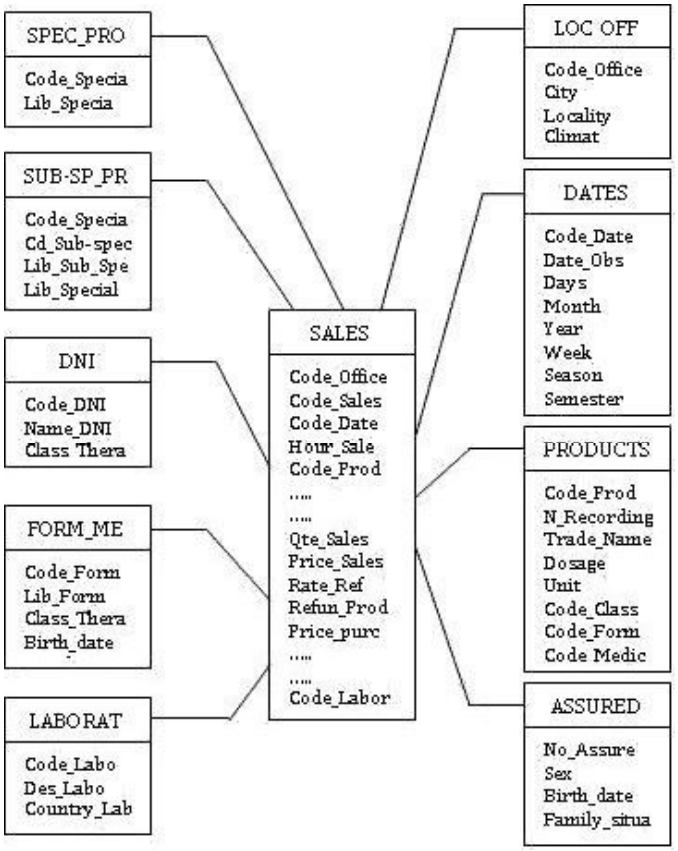

Fig. 3 Global schema of our data warehouse (dimensions and fact tables)

B. *Data Mart Epidemiological*

The data mart "MACHR" is focused and driven by the needs of our system. It has the same purpose as the medical data warehouse (provide architectural decisions), but it aims to solve our problems with a smaller number of users [39].

The data mart "MACHR" store is specialized for the epidemiological study of chronic disease: asthma, high blood pressure, and diabetes, where extractions are performed on the data warehouse, it is not taking that sale for these pathologies. From which extractions are made on our data warehouse it is taking sales for these pathologies. Recall that the data mart "MACHR" is part materialized on the data warehouse. MACHR is modeled as a star schema and implemented in the ORACLE database, and for launching data mining tasks on multiple views and depending on the selected dimensions. The MACHR data is as follows (see Figure 4):

- The fact table SALES; contains sold quantity (gross), selling price, etc.
- The dimension tables:
  - Localization of selected pharmacies : LOCALIZATIONS_OFFICINES.
  - Dimension date - DATES.
  - Table of the handled products : PRODUCTS; includes commercial name, etc.
  - Specialties of the various existing products in database : SPECIALITIES_PDT.
  - DNI (Denominations Nonproprietary International) and corresponding disease.
  - Laboratories manufacturers products : LABORATORIES.
  - Patients : ASSURED. Confidential details NOT downloaded in data warehouse.

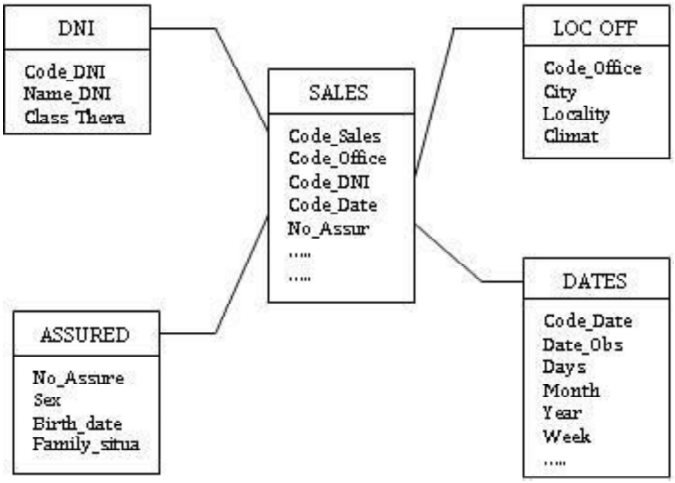

Fig. 4 The star model of MACHR (Data Mart epidemiological)

C. *Data Mart Epidemiological*

Before launching the process of extracting knowledge from data, we thought it useful to give a brief presentation on APESS (Assistance Platform for Epidemiological Searches and Surveillance) platform.

Let's remember that, The APESS platform's concept has been proposed on service-oriented architecture based on data mining and applied to Epidemiological Searches and Surveillance [21]. The Data mining tasks of the APESS Platform include several basic services. Each of these services is adapted to a specific usage context. The process of services selection and composition is based a priori on predefined rules. According to Sabri & Rahal [21], the APESS platform is a runtime environment that is designed and implemented according to a multilayer structure: Data Access Services Layer, Data Mining Services Layer and User Services Layer. (see figure 5).

In this part of the system, we'll create a process for extracting epidemiological knowledge from the data warehouse (data mart "MACHR") constructed in the previous section. The process we have used is divided into several phases of APESS platform [21]: data selection, data preparation, use of an intelligent data mining method applied to the processed data and finally the evaluation and validation of models.

ISSN 1737-9334

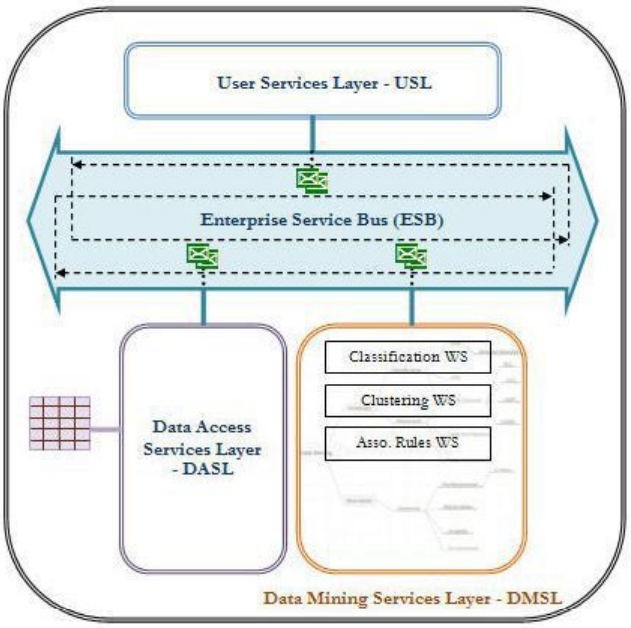

Fig. 5 Architecture of APESS platform for service-oriented data mining [21]

D. Pre-processing

Data from the warehouse is very varied and is not necessarily all exploitable by the data mining techniques. Most of the used techniques process only data tables in the traditional lines/columns. The objective is to prepare lines/columns tables; in other words, tables of individuals/variables, obtained by the following stages (see Table1).

TABLE I
EXAMPLE OF A LEARNING SAMPLE - DISEASES

	Locality	Season	Age	Sex	Diseases
ω_1	Oran	Winter	young	Male	Asthma
ω_2	Oran	Winter	young	Female	Asthma
ω_3	Tlemcen	Winter	young	Male	diabetes
ω_4	Témouchent	spring	young	Male	diabetes
ω_5	Témouchent	summer	old	Male	diabetes
ω_6	Témouchent	summer	old	Female	Asthma
ω_7	Tlemcen	summer	old	Female	diabetes
ω_8	Oran	spring	young	Male	Asthma
ω_9	Oran	summer	old	Male	diabetes
ω_{10}	Témouchent	spring	old	Male	diabetes
ω_{11}	Oran	spring	old	Female	diabetes
ω_{12}	Tlemcen	spring	young	Female	diabetes
ω_{13}	Tlemcen	Winter	old	Male	diabetes
ω_{14}	Témouchent	spring	young	Female	Asthma

Data selection: It is carried out on the data which already exist in the data warehouse and which are in tabular form. It is then a question of applying filters which will enable us to select a subset of lines or columns. Data selection is based on the following information:

- From the fact table SALES, we will take the sold quantity, taken first in its gross state and aggregated according to the selected dimensions.
- From table LOCALIZATIONS_OFFICINES, the attribute LOCALITY.
- The date dimension DATES in order to carry out the data mining on a time interval. In our case, we proceed by the period MONTH.
- From the table DNI, we take information about present diseases. A filter is then applied to keep the records related to the selected diseases only.
- Finally, the patients, present in the table ASSURED and from which we take the gender and age attributes (recommendations of the experts).

Cleaning and enrichment of the data: A stage of cleaning of the data is essential in order to process the missing data (suppression of records). Besides, enrichment by external sources was carried out during the creation of the data warehouse.

Transformation and reduction of dimension: This is about transforming an attribute (A) into another (A') which would be more relevant to match the objectives of the study. For example, patients' dates of birth have been transformed to obtain age within intervals.

E. Data Mining by Decision Tree

After data storage and pre-processing, the phase of data mining may start. To illustrate this step, consider the problem of Epidemiological study of chronic diseases.

In this case, the patient population affected by the problem of learning is a set of tuples consisting of the four predictor variables X1, X2, X3, X4 (Locality, Season, Age, and Gender) and their classes (Asthma and diabetes), from these examples, we construct a tree said decision.

For these reasons, suppose our learning sample is composed of 14 patients. s0 the initial partition has a single element denoted s0, which includes all the learning sample with nine (09) individuals (patients) belonging to the class « diabetes» and five (05) belonging to the class «asthma» (see Table 1).

For the construction of the decision tree, we used the algorithm of ID3 method in our ARESS platform [21]. ID3 (Iterative Dichotomiser 3) [6] is a heuristic tree to construct a decision tree. Its principal consists in generating a succession of partitions by splitting nodes of the tree. Its objective is to optimize a criterion of information gain. From the sample of learning method ID3 symbolic processing begins for the construction of the decision tree [6]. Thus, the decision tree can be then exploited to: extract the classification rules concerning our target attribute « Diseases ».

ISSN 1737-9334

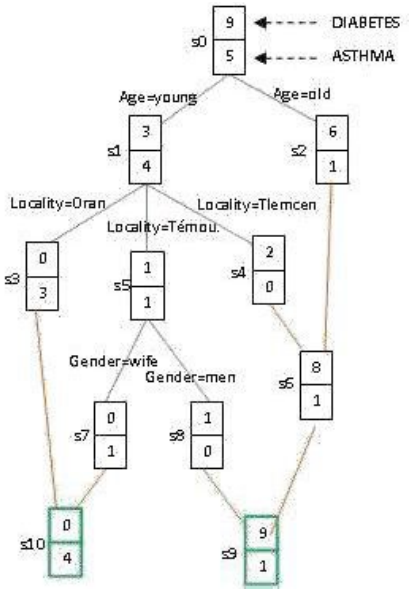

Fig. 6 The induction graph of the table xx sample realized by APESS platform

Finally, we exploited the tree before (see figure 6) to extract five rules R1, R2 … and R5 of inductions epidemiogical of some pathologies (chronic diseases) also on the target attribute « Diseases » useful and bearing knowledge critical have not been explicit in advance and which are of the form: If Condition then Conclusion. Where Condition is a logical expression composed summits which will be called Premise. And Conclusion would be the majority class in the summits described by the condition.

1. If (Locality = Oran and Age = young) then Asthma
2. If (Locality = Tlemcen and Age = young) then Diabetes
3. If (Locality = Temouchent and Age = young and gender = female) Alors Asthma
4. If (Locality = Temouchent Et Age = young and gender = male) then Diabetes
5. If (Age = old) then Diabetes

F. Exploitation of induction rules

For the experimentation phase, we used the CARTOCEL tool [11], [12], [13] that has been integrated into our APESS platform for extraction and the Boolean modeling the rules of epidemiogical prediction.

Furthermore, we launch the validation phase across the BV module (Boolean validation) on induction rules epidemiogical of some pathologies (chronic diseases) presented in the previous section, using the same Boolean basic principle from Boolean engine inference BIE, and the same transition functions δfact and δrule that exists in CARTOCEL Tool [11], [12], [13].

The figure 7 shows how the Boolean knowledge base extracted starting from the rules induction epidemiogical of some pathologies (chronic diseases) is modeled by layers CELFACT and CELRULE with the same principle CELSUMMIT and CELARC [11], [12], [13]. Note that in this step; the two incidence matrices of input (RE) and output (RS) are generated.

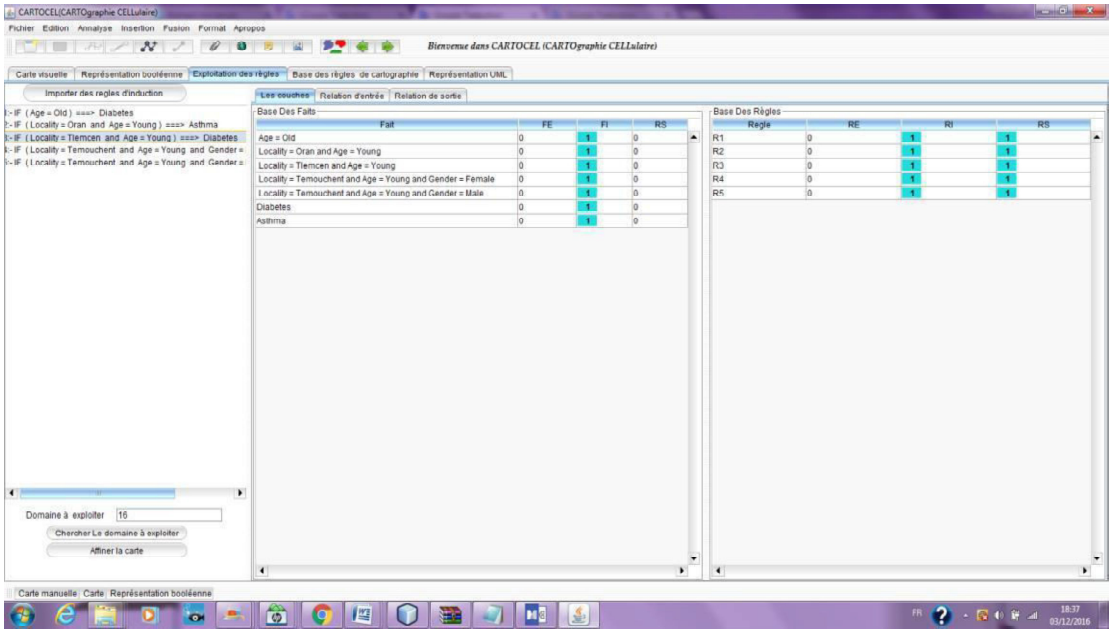

Fig. 7 The induction graph of the table xx sample realized by APESS platform

Nevertheless, we want to highlight the fact that the data warehousing has represented a major task in the implementation of the project, especially the data collection. We have nevertheless be able to put in APESS platform over thirty million data records of sales, spread out between January 2010 and April 2016, and related to 230 pharmacies distributed over 10 departments. Further, it should be noted

ISSN 1737-9334

that these records represent raw data of sales on which no form of aggregation was carried out, to finally obtain, after the pre-processing and the task of identification of the characteristics of the patients (Gender and Age), nearly 500,000 sales transactions for the selected diseases (Asthma and Diabete). Furthermore, our experiment action is related to a sample of 80,112 sales transactions.

Finally, the objective and the automatic improvement the knowledge mapping critical epidemiological of SEMEP [11], [12], [13] guided by integration technique of heterogeneous data and the oriented-services data mining (APESS platform) in order to use it as a decision support tool, whether individual or collective in the public health for management and monitoring of some pathologies (chronic diseases).

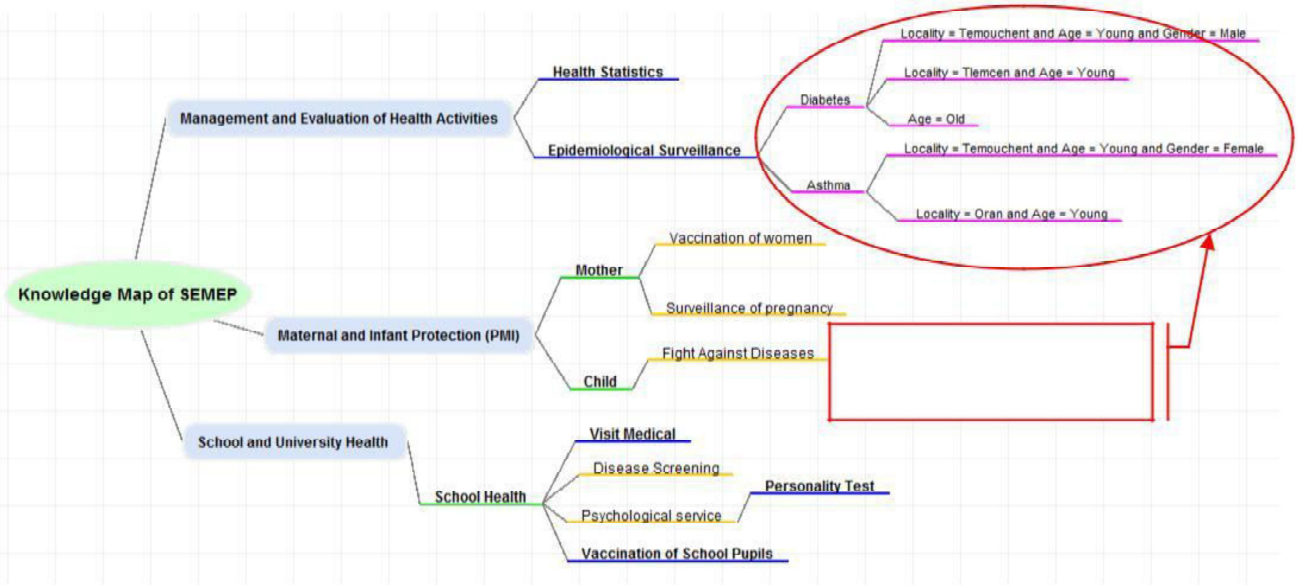

Fig. 8 The Knowledge map of SEMEP refined by a process of knowledge extraction by APESS platform

IV. Conclusions

Knowledge management has aimed at extraction of useful knowledge from such sources and its representation in several forms. Likewise, the health institutions have realized the importance of huge amount of data and information medicals that are collected to make enhanced decisions concerning chronic diseases. Moreover, we recorded and we are convinced of the interest of applying the techniques of data warehouse and oriented service data mining on several types of information stored in various media (Database, ERP, CRM, SCM, XLT, etc..) to improve the extraction process and knowledge management process and, in particular the knowledge mapping of the epidemiological services.

In this context, this paper aimed to propose a new medical knowledge mapping approach based, on the one hand, on integration technique of heterogeneous data in the medical field by creating a data warehouse and, on the other hand, on a technique of extracting epidemiological prediction rules from medical data by choosing a technique of service-oriented data mining of APESS platform whose objective to exploit these predictive rules to automatically improve the Boolean model of the medical knowledge mapping through CARTOCEL system. Finally, this approach of epidemiological knowledge mapping would be new direction towards as a decision support tool, whether individual or collective in the public health for management and monitoring of some pathology (chronic diseases).

References

[1] A. Perez-Soltero, V. Leal, Barceló, M. & J. León, “A diagnostic of knowledge management processes at the restaurant industry SMEs to identify improvements at their productive processes”, Intangible Capital (IC), 9 (1), 2013, p.153-183.

[2] D. Christozov, & S. Toleva-Stoimenova, The role of information brokers in knowledge management. Online Journal of Applied Knowledge Management, 2 (2), 2014, p.109-119.

[3] D. Christozov, & S. Toleva-Stoimenova, Knowledge diffusion via social networks: The 21st cen-tury challenge. International Journal of Digital Literacy and Digital Competence, 4(2), 2013, p.1-12.

[4] D. Talia, P. Trunfio, and O. Verta, “Weka4WS: a WSRFenabled Weka Toolkit for Distributed Data Mining on Grids”, Proceeding of the 9th European Conference on Principles and Practice of Knowledge Discovery in Databases (PKDD 2005.

[5] H. Nemati, D. Steiger, L. Iyer, & R. Herschel, Knowledge warehouse: an architectural integration of knowledge management ‖ , decision support, artificial intelligence and data warehousing. Decision Support Systems, 33(1), 2002, p.143-61.

[6] J.R Quinlan. Induction of decision trees Wadsworth Statistics/Probability,Berkeley, 1986.

[7] L. C. Cámpiz Mercado, “Influence of Critical Success Factors of Knowledge Management on the Innovation Performance of Colombian Organizations”, 8th LACCEI Latin American and Caribbean Conference for Engineering and Technology (LACCEI ’ 2010) - Innovation and Development for the Americas ‖ , June 1-4, 2010, Arequipa, Perú, p. 1-10.

[8] K. Curko, V. Vuksic, & A. Lovric, The Role of Business Process Management Systems and Business Intelligence Systems in Knowledge Management. International Journal of Computer and Communications, 3,(2), 2009, p.17-24.

[9] L.Wulantika, “Knowledge Management Dalam Meningkatkan Kreasi Dan Inovasi Perusahaan”, Majalah Ilmiah UNIKOM, Vol.10, No. 2. P. 263 -270.

ISSN 1737-9334

[10] M.B. Lloria, "A review of the main approaches to knowledge management", Knowledge Management Research and Practice, 6, p.77-89 (2008).
[11] M. Brahami, B. Atmani, & N. Matta, Using rules to enhance evolution of knowledge mapping: Application on healthcare ‖ . International Journal of Computer Science Issues (IJCSI), 10 (3), 2013, p.261-270.
[12] M. Brahami, Boolean Knowledge Mapping guided by Data Mining, PHD Thesis, Department of Computer Science, University of Oran, 2014.
[13] M. Brahami, B. Atmani, & N. Matta, "An Approach to Dynamic Fusion of the Knowledge Maps of an Activities Process: Application on Healthcare", International Journal of Information Systems in the Service Sector, 7(4), 2015, p.1-26.
[14] M. Cannataro, & D. Talia, The knowledge grid, Communication of the ACM 46 (1), 2003, p.89–93.
[15] M. D. Beynona, T. Kurcb, U. Catalyurekb, C. Changa, A. Sussmana, & J. Saltza, "Distributed processing of very large datasets with DataCutter", Clusters and computational grids for scientific computing, 27 (11), 2001, p. 1457–1478.
[16] M.E. Jennex, I. Zakharova, Knowledge Management Critical Success Factors.
[17] M. Gadu, & N. El-Khameesy, "A Knowledge Management Framework Using Business Intelligence Solutions", International Journal of Computer Science Issues, 11 (5), 2014, p.102-106.
[18] M. Plessis, "Knowledge management: what makes complex implementations successful? ", Journal of Knowledge Management, Vol. 11, 2, p.91 – 101.
[19] M. Montoro, "Gestión del conocimiento en las organizaciones: fundamentos, metodología y praxis", España: Ediciones Trea, S.L .
[20] M. Q. A. Al-qarioti, "The impact of knowledge management on organizational performance: an empirical study of kuwait university". Eurasian Journal of Business and Management, 3(4), 2015, p. 36-54.
[21] M. Sabri, and S. A. Rahal, APESS - A Service-Oriented Data Mining Platform: Application for Medical Sciences, International Journal of Information Technology and Computer Science, 2016, 7, 36-42.
[22] M. Sonesson, & R. Storgren, The relationship between Knowledge Management and Business Intelligence: How the concepts are affected by each other inside organizations. Master thesis, 2016, Department of Informatics, Lund University School of Economics and Management.
[23] M. S. Perez, A. Sanchez, V. Robles, P. Herrero, & J. M. Pëna, "Design and implementation of a data mining grid-aware architecture. Future Generation Computer Systems, 23 (2007), p.42–47.
[24] M. Zack, J. McKeen, and S. Singh, "Knowledge management and organizational performance: an exploratory survey", Journal of Knowledge Management, Vol. 13, (6), p. 392-409.
[25] N. M. Yaghoubi, J. Moloudi, and S. Ali Banihashemi, The relationship between knowledge management and agile supply chain management: Case study of Jihad-e-Agriculture Organization. African Journal of Agricultural Research, Vol. 8(17), 2013, p. 1700-1708.
[26] P. Brezany, I. Janciak, A. Wöhrer, & A. M. Tjoa, GridMiner: A Framework for Knowledge Discovery on the Grid - from a Vision to Design and Implementation. Proceedings of the Cracow Grid Workshop, December 2004, Cracow, Poland.
[27] R. A. Khan, and S.M. K. Quadri, Business Intelligence: AN Integrated Approach, Business Intelligence Journal - January, 2012 Vol.5 No.1, p. 64-70.
[28] S. Wamundila, and P. Ngulube, Enhancing knowledge retention in higher education: a case of the University of Zambia ‖ , South African Journal of Information Management, 13(1), p.439-448.
[29] S. Negash, & P. Gray, "Business intelligence", In F. Burstein, & C. W. Holsapple (Eds.), Decision support systems, 2008, p. 175-193, Berlin: Springer.
[30] S. Alsairafi, M. Ghanem, N. Giannadakis, Y. Guo, D. Kalaitzopoulos, M. Osmond, A. Rowe, J. Syed, P. Wendel, "The design of discovery net: Towards open grid services for knowledge discovery", International Journal of High Performance Computing Applications 17(3), 2003, p.297–315.
[31] T. H. Davenport. Competing on analytics. Harvard business review, 84(1), 2006, p.98.
[32] T. Nguyen Manh, J. Schiefer, and A.M. Tjoa, "Data warehouse design 2: sense & response service architecture (SARESA): an approach towards a real-time business intelligence solution and its use for a fraud detection application", Proceedings of the 8th ACM International Workshop on Data Warehousing and OLAP, DOLAP '05, ACM Press, New York, NY.
[33] V. Georgescu, WSRP-Enabled Distributed Data Mining Services Deliverable over a Knowledge-Driven Portal. 7th WSEAS International Conference on Applied Computer & Applied Computational Science (ACACOS '08), April 6-8, Hangzhou, China.
[34] V. Lomte, & S. Shah, "The Survey Paper on Importance of Integration of Knowledge Management and Business Intelligence", International Journal of Science and Research (IJSR), 3 (6), 2014, p.1789-1791.
[35] V. Podpecan, M. Zemenova, & N. Lavrac., "Orange4ws: environment for service-oriented data mining". The Computer Journal, 55 (1), 2011, p. 82-89.
[36] V. Stankovski, M. Swain, V. Kravtsov, T. Niessen, D. Wegener, J. Kindermann, & W. Dubitzky, Grid-enabling data mining applications with DataMiningGrid: An architectural perspective ‖ . Future Generation Computer Systems, 24(4), 2008, p.259 – 279.
[37] Y. Wu, S. Wu, H. Yu, & H. Hu, "Introduction to ChinaGrid Support Platform", Proceedings of 7th International Conference on Asian Digital Libraries, ICADL 2004, December 13-17, Shanghai, China.
[38] Z. Abas, and M. N. Jali., "Understanding Knowledge Management in Developing Emerging Concept of Innovation and Technology Into Business: Conceptual Review and Empirical Evidence", International Academic Research Journal of Business and Technology 1(2) 2015, p. 149-164.
[39] Z. N. Boudjettou, F. Nader, & R. Chalal, "Medical Knowledge Management since the Integration Heterogeneous Data until the Knowledge Exploitation in a Decision-making System," Recent Advances in Environmental Science and Biomedicine, Proceedings of the 3rd International Conference on Health Science and Biomedical Systems (HSBS '14), November 22-24, 2014, Florence, Italy.
[40] Z. Panian, "Business Intelligence inSupport of Business Strategy", Proceeding of the 7th WSEAS International Conference on Mathematics & Computer in Business Economics, Cavtat (Croatia), 13-15 June, 2006, p. 204-215.

ISSN 1737-9334

7th International Conference on Control Engineering & Information Technology (CEIT-2019)
Proceedings of Engineering and Technology PET

Physical Model Traffic Control System to Decreasing Density in Roundabout

Sidina Boudaakat
SSDIA Laboratory, ENSET
Mohammedia, Hassan II University of Casablanca
Mohammedia, Casablanca
Morocco
boudaakat.sidina@gmail.com

Ahmed Rebbani
SSDIA Laboratory, ENSET
Mohammedia, Hassan II University of Casablanca
Mohammedia, Casablanca
Morocco
a.rebbani@gmail.com

Omar Bouattane
SSDIA Laboratory, ENSET
Mohammedia, Hassan II University of Casablanca
Mohammedia, Casablanca
Morocco
o.bouattane@gmail.com

***Abstract*—The roundabout is a very old shape of junction which have been used, but when there are more than two lanes create a congestion problem. This paper deals with a physical model, simulation and analysis traffic congestion occur at roundabout, the concept is collecting traffic data from inputs and outputs sources of a specific roundabout to avoid congestion. Our model is controlling the traffic light on roundabout before the occurrence of congestion based on fluid mechanics methods.**

***Index Terms*—road traffic control, traffic flow, roundabout, density, fluid mechanics.**

I. Introduction

Road traffic - especially urban - is at the heart of many issues and has become an essential aspect of everyday life.

It is the source of many problems that cost daily time, money, health and environmental quality, whether through traffic congestions, accidents or offenses. The roundabout congestion which follow the rule of the left priority is one of the most common problems on the roads mega cities [1], which occur in most roundabouts during the day at peak hours. There is a large amount of research concerned on roundabouts. [2] Roundabouts are more efficient for travelers throughout nonpeak hours. Akelik [3] during the heavy demand conditions they installed metering signals on selected roundabout. In [4] the authors proposed an optimization model based on a signal timing strategy for metering signals by minimizing the total entry delay of a roundabout and constraints on cycle length, the degree of saturation, and queues. Hawi et.al. presented the design and implementation of a smart traffic light using wireless sensor network (WSN) and fuzzy logic [5], Ashraff Mohd et.al considered dynamic traffic light system by presenting smart traffic light for congestion monitoring using LoRaWAN [6]. In [7] it has been developed an adaptive traffic light system through traffic density calculation on road pattern by controlling traffic light timing.

In this paper, we are interested in the microscopic model which describe the individual behavior of each vehicle and driver on the road network by focusing on the technologies of information and communication to improve the flow of road traffic in an urban environment. The modeling of the traffic flow is an expensive and difficult task given the variability of the flow and the number of data to be processed. Several models have been designed to simulate and control the flow of traffic. This paper is organized as follows Section 2,discuss the design and methodology and in Section 3, we give conclusion.

II. Design And Methodology

In this model, which is inspired by fluid mechanics, we consider our system as a tank with a well-defined surface as shown in the figure 1. This tank represents an roundabout that contains several entries and exits of vehicles flow.

The idea is each roundabout can support a maximum number of vehicles, this number is density L as shown in the figure 2 the colored surface at the roundabout.

We used the fundamental equation (1) of fluid statics for the incompressible fluids to calculate density.

$$dP = -\rho.g.dz \tag{1}$$

where dP pressure variation between z and $(z + dz)$. With ρ and g are constant.

we have:

$$L = \frac{\sum \alpha_i x_i}{C_{Total}} \tag{2}$$

$$L = \frac{\sum \alpha_i x_i(t) - \sum \alpha_i x_i(t + \delta_i)}{C_{Total}} \tag{3}$$

Where:

x_i : An individual vehicle.

α_i: Vehicle Dimension.

δ_i: The duration of x_i in the roundabout.

ISSN 1737-9334

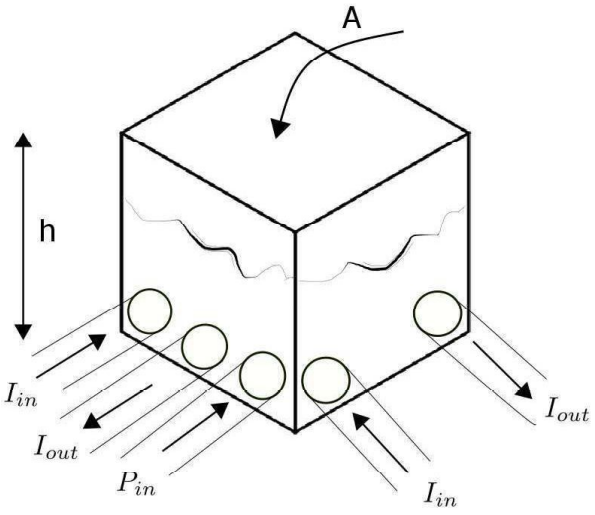

Fig. 1. represents the output and the input of a fluid mechanics on a tank.

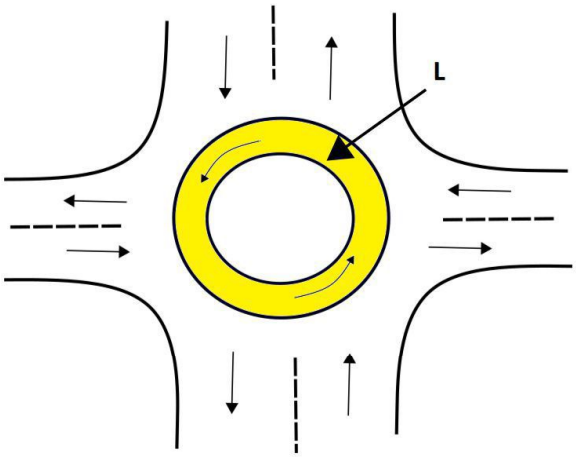

Fig. 2. roundabout with four edges two lanes, the colored surface is the area's density which we should calculate.

C_{total}: Total capacity of roundabout.

The variety of a tank filling during time equals to the variety of the density L.

$$A.dh = dL \tag{4}$$

$$A.\frac{dh}{dt} = \frac{dL}{dt} \tag{5}$$

Where:
A: The base of the tank.
h: A level of the liquid in the tank.

Therefore:

$$\frac{dL}{dt} = F_{in} - F_{out} \tag{6}$$

Where:
F_{in}: Incoming flow.
F_{out}: Outgoing flow.
Then:

$$A.\frac{dh}{dt} = F_{in} - F_{out} \tag{7}$$

With:

$$k_{p1}.F_{in} = P_{in} - \rho.g.h \tag{8}$$

Where P_{in} is the pressure at the input "i" measurable grumbler matches set of vehicles waiting in the input "i".

$$k_{p2}.F_{out} = \rho.g.h \tag{9}$$

where :
k_{p1} and k_{p2} designate the coefficients associated with the input and output rates respectively.
ρ: Density.
g: Gravity equal to 9.8 m/s^2
h: Altitude in m.

$$A.\frac{dh}{dt} = \frac{P_{in} - \rho.g.h}{k_{p1}} - \frac{\rho.g.h}{k_{p2}} \tag{10}$$

$$\frac{dL}{dt} = \frac{P_{in} - \rho.g.h}{k_{p1}} - \frac{\rho.g.h}{k_{p2}} \tag{11}$$

1) Standard Model: In this model, we consider all vehicles at the same sizes. We take the variable $k_1 = \rho.g.$ where k_1 designates the coefficient associated with incoming and outgoing vehicles.

$$\rho.g.h = k_i.L \tag{12}$$

Then equation (6) become:

$$\frac{dL}{dt} = \frac{P_{in} - k_i.L}{k_{p1}} - \frac{k_i.L}{k_{p2}} \tag{13}$$

Each roundabout has a number of entries and exits that depend on the nature of each junction.
To treat all the sources we take the sum of the entries and the exits.
We have:

$$k_{p1}.F_{in} = P_{in} - k_1.L \tag{14}$$

$$k_{p2}.F_{out} = k_1.L \tag{15}$$

ISSN 1737-9334

The sum become:

$$F_{in_i} = \begin{cases} F_{in_1} = \frac{P_{in_1} - k_1.L}{k_{p1}} \\ F_{in_2} = \frac{P_{in_2} - k_1.L}{k_{p1}} \\ F_{in_3} = \frac{P_{in_3} - k_1.L}{k_{p1}} \\ . \\ . \\ . \\ F_{in_n} = \frac{P_{in_n} - k_1.L}{k_{p1}} \end{cases} \quad (16)$$

$$F_{out_i} = \begin{cases} F_{out_1} = \frac{k_1.L}{k_{p2}} \\ F_{out_2} = \frac{k_1.L}{k_{p2}} \\ F_{out_3} = \frac{k_1.L}{k_{p2}} \\ . \\ . \\ . \\ F_{out_n} = \frac{k_1.L}{k_{p2}} \end{cases} \quad (17)$$

Then :

$$\begin{aligned} \frac{dL}{dt} &= \sum_{i=1}^{n} \frac{P_{in_i} - k_1.L}{k_{p1_i}} - \sum_{i=1}^{n} \frac{k_1.L}{k_{p2_i}} \\ &= \sum_{i=1}^{n} (\frac{P_{in_i}}{k_{p1_i}} - \frac{k_1.L}{k_{p1_i}}) - \sum_{i=1}^{n} \frac{k_1.L}{k_{p2_i}} \\ &= \sum_{i=1}^{n} (\frac{P_{in_i}}{k_{p1_i}}) - k_1.L \sum_{i=1}^{n} (\frac{1}{k_{p1_i}} + \frac{1}{k_{p2_i}}), \end{aligned} \quad (18)$$

$$\frac{dL}{dt} + k_1.L \sum_{i=1}^{n} (\frac{1}{k_{p1_i}} + \frac{1}{k_{p2_i}}) = \sum_{i=1}^{n} (\frac{P_{in_i}}{k_{p1_i}}) \quad (19)$$

Taking : $\alpha_i = \frac{1}{k_{p1_i}}; \beta_i = \frac{1}{k_{p2_i}}$

$$\frac{dL}{dt} + k_1.L \sum_{i=1}^{n} (\alpha_i + \beta_i) = \sum_{i=1}^{n} (\alpha_i P_{in_i}) \quad (20)$$

The equation (20) shows that all vehicles have the same size k_1 .

2) Heterogeneous model: This model shows that vehicles as a collection of different sizes.

$$\frac{dL}{dt} = \frac{P_{in} - K.L}{k_{p1}} - \frac{H.L}{k_{p2}} \quad (21)$$

Where:
K, H are the coefficients associated with incoming and outgoing vehicles respectively.

$$F_{in_i} = \begin{cases} F_{in_1} = \frac{P_{in_1} - k_1.L}{k_{p1}} \\ F_{in_2} = \frac{P_{in_2} - k_2.L}{k_{p1}} \\ F_{in_3} = \frac{P_{in_3} - k_3.L}{k_{p1}} \\ . \\ . \\ . \\ F_{in_n} = \frac{P_{in_n} - k_n.L}{k_{p1}} \end{cases} \quad (22)$$

$$F_{out_i} = \begin{cases} F_{out_1} = \frac{h_1.L}{k_{p2}} \\ F_{out_2} = \frac{h_2.L}{k_{p2}} \\ F_{out_3} = \frac{h_3.L}{k_{p2}} \\ . \\ . \\ . \\ F_{out_n} = \frac{h_n.L}{k_{p2}} \end{cases} \quad (23)$$

k_i and h_i denote the coefficients associated with the incoming and outgoing vehicles respectively, they are equivalent to the densities of vehicles.
The size of vehicle k_i and h_i varies between 1 and T = 10 as shown in the table I.
The figure 3 shows an example of the type of vehicles entering and leaving an roundabout.

TABLE I
TABLE REPRESENT THE UNITS CORRESPONDENT OF TYPE OF VEHICLES

Type of vehicle	Unit matches (k_i, h_i)
bike	1
motorcycle	1
automotive	2
ambulance	3
pickup	3
road tractor	3
Tractor	3
camping car	4
truck	5
minibus	5
bus	6
because	6
Tractor semi-trailer	7
Liquid tank tractor	8
Car transporter trailer truck	10

$$\begin{aligned} \frac{dL}{dt} &= \sum_{i=1}^{n} \frac{P_{in_i} - k_i.L}{k_{p1_i}} - \sum_{i=1}^{n} \frac{h_i.L}{k_{p2_i}} \\ &= \sum_{i=1}^{n} (\frac{P_{in_i}}{k_{p1_i}}) - L \sum_{i=1}^{n} (\frac{k_i}{k_{p1_i}} + \frac{h_i}{k_{p2_i}}), \end{aligned} \quad (24)$$

$$\frac{dL}{dt} + L \sum_{i=1}^{n} (\frac{k_i}{k_{p1_i}} + \frac{h_i}{k_{p2_i}}) = \sum_{i=1}^{n} (\frac{P_{in_i}}{k_{p1_i}}) \quad (25)$$

ISSN 1737-9334

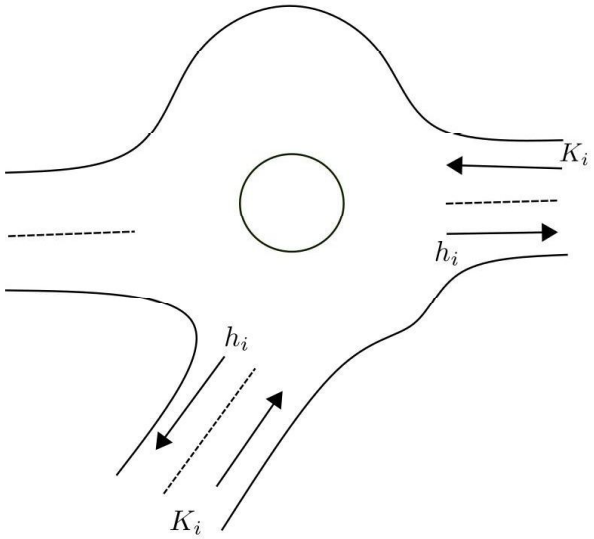

Fig. 3. An example of the type of vehicles entering and leaving a roundabout.

Taking : $\alpha_i' = \frac{k_i}{k_{p1_i}}; \beta_i' = \frac{h_i}{k_{p2_i}}$

$$\frac{dL}{dt} + L\sum_{i=1}^{n}(\alpha_i' + \beta_i') = \sum_{i=1}^{n}(\alpha_i P_{in_i}) \tag{26}$$

the equation (26) shows that vehicles are a different size. In order to simplify the calculations the equation (26) become:

$$\frac{dL}{dt} + L * H = Q \tag{27}$$

With:

$$H = \sum_{i=1}^{n}(\frac{k_i}{k_{p1_i}} + \frac{h_i}{k_{p2_i}}) \tag{28}$$

$$Q = \sum_{i=1}^{n}(\frac{P_{in_i}}{k_{p1_i}}) \tag{29}$$

are constants.

By solving the differential equation (27) we get three scenarios possible shown in the figure 4, the value of the density L depending on the values of H and Q:

- $H > Q$;
- $H = Q$;
- $H < Q$.

In figure 4 the three scenarios possible of the density L, graph (a) is an example of $H < Q$ with $H = 1.359$ and $Q = 2.728$, and graph (b) represents $H > Q$ with $Q = 1.359$ and $H = 2.728$, graph (c) an example of $H = Q$.

The graph (a) shows that the roundabout has the value of $L > 1$, which means that the roundabout is saturated, (b) and (c) shows the roundabout unsaturated.

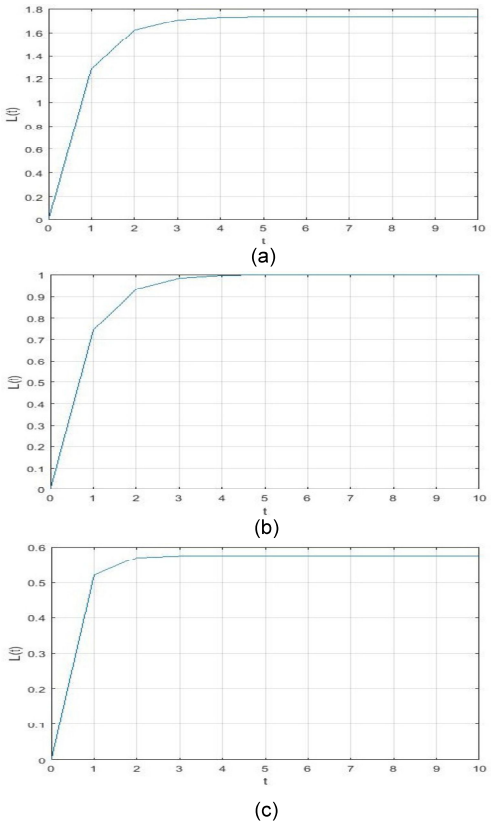

Fig. 4. represents the graphs with maximum value of density L.

III. Conclusion

In this paper, a physical model traffic control system proposed to measuring the density with the purpose of decreasing traffic congestion, the traffic density has been calculated to release traffic light system.

References

[1] A. Kanungo, A. Sharma, and C. Singla, "Smart traffic lights switching and traffic density calculation using video processing," in *2014 Recent Advances in Engineering and Computational Sciences (RAECS)*. Chandigarh, India: IEEE, Mar. 2014, pp. 1–6. [Online]. Available: http://ieeexplore.ieee.org/document/6799542/

[2] J. E. Hummer, J. S. Milazzo, B. Schroeder, and K. Salamati, "Potential for Metering to Help Roundabouts Manage Peak Period Demands in the United States," *Transportation Research Record: Journal of the Transportation Research Board*, vol. 2402, no. 1, pp. 56–66, Jan. 2014. [Online]. Available: http://journals.sagepub.com/doi/10.3141/2402-07

[3] R. Akelik, "Roundabout Metering Signals: Capacity, Performance and Timing," *Procedia - Social and Behavioral Sciences*, vol. 16, pp. 686–696, 2011. [Online]. Available: https://linkinghub.elsevier.com/retrieve/pii/S1877042811010342

ISSN 1737-9334

[4] Y. Duan, X. Qu, S. Easa, and Y. Yan, "Optimising total entry delay at roundabouts with unbalanced flow: a dynamic strategy for smart metering," *IET Intelligent Transport Systems*, vol. 13, no. 3, pp. 485–494, Mar. 2019. [Online]. Available: https://digital-library.theiet.org/content/journals/10.1049/iet-its.2018.5180

[5] R. Hawi, G. Okeyo, and M. Kimwele, "Smart traffic light control using fuzzy logic and wireless sensor network," in *2017 Computing Conference*. London: IEEE, Jul. 2017, pp. 450–460. [Online]. Available: http://ieeexplore.ieee.org/document/8252137/

[6] R. F. A. M. Nor, F. H. K. Zaman, and S. Mubdi, "Smart traffic light for congestion monitoring using LoRaWAN," in *2017 IEEE 8th Control and System Graduate Research Colloquium (ICSGRC)*. SHAH ALAM, Malaysia: IEEE, Aug. 2017, pp. 132–137. [Online]. Available: http://ieeexplore.ieee.org/document/8070582/

[7] B. Pratama, J. Christanto, M. T. Hadyantama, and A. Muis, "Adaptive Traffic Lights through Traffic Density Calculation on Road Pattern," in *2018 International Conference on Applied Science and Technology (iCAST)*. Manado, Indonesia: IEEE, Oct. 2018, pp. 82–86. [Online]. Available: https://ieeexplore.ieee.org/document/8751540/

ISSN 1737-9334

Contribution of CWDM multiplexing in bidirectional Passive Optical Network at 4×2.5 Gbps.

Cheikh Kherici [#1], Malika Kandouci [#2]

[#] *Laboratory of Electronic, Photonic and Optronic (LEPO)*
University of Djillali Liabes
Sidi Bel-Abbes, Algeria

[1]khericic@yahoo.fr
[2]maikand04@gmail.com

***Abstract* - In this article, the authors proposed a CWDM-PON system for implementation in the PON network. The results will prove that the CWDM-PON system provides broadband services to subscribers. Passive Optical Network (PON) solves the problem of bandwidth as it extends the optical network to individuals and businesses [1]. The second work in this paper is a comparative study was made between the CWDM-PON system and the PON WDM system using two different architectures, one for the CWDM-PON and the other for the WDM-PON, to illustrate the appropriate technique for the PON network by increasing the Q factor and minimizing the bit error rate (BER <10^{-9}). Both systems are simulated at 10 Gbps and the link has been designed for fiber lengths ranging from 20 km up to 60 km, as well as for powers of -10, -8, -5, 0, 5, 8, and 10 dBm.**

The use of the EDFA amplifier in the WDM-PON system is required in this document to minimize degradation caused by attenuation.

Keywords – CWDM, PON, eye diagram, EDFA, BER, Q factor, WDM, OSNR, comparison.

I. INTRODUCTION

Migration to WDM PON wavelength division multiplexing becomes essential since the time division multiplexing (TDM) used in current PON solutions can't exploit the enormous bandwidth of optical fibers and not be able to respond to the demands of ever-increasing bandwidth growth by future network applications. To meet the requirements of the PON network, we offer two solutions, the Coarse WDM-PON (CWDM-PON) and the WDM-PON technology, both systems provide a satisfactory bandwidth solution as well as high data rates can be across the network.

The purpose of this article is to study the performance of the CWDM-PON system and illustrate the performance by comparing with the WDM-PON system, taking into account the profitability of both systems, including component costs.

The figure 1 shows a standard architecture for the Passive Optical Network (PON). The PON network is a point-to-multipoint optical network, consisting of an Optical Line Terminal (OLT) located in the central office and an Optical Network Unit (ONU) located on remote nodes in the network. The connection between the OLT and the ONUs is made by a single bidirectional fiber and the use of one or more splitters. Between the OLT and the ONU, the network is passive, which means it does not require any power. The presence of passive elements in the network makes it relatively more fault-tolerant and reduces its operating and maintenance costs once the infrastructure is in place [2].

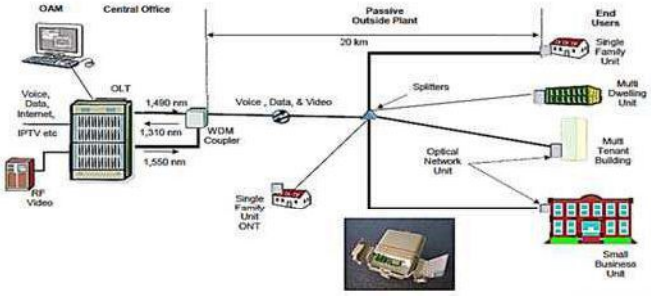

Fig. 1 Standard architecture of PON network [2].

II. THE CWDM PON

Coarse Wavelength Division Multiplexing (CWDM) is a multiplexing scheme whose wavelengths are combined into a single optical fiber cable without interference, it is a good solution for adding more services on a single exit without interrupting other services to customers. CWDM operates at a higher bandwidth than WDM, where the operating wavelength extends from 1271 nm to 1611 nm and covers 18 CWDM channels with a channel spacing of 20 nm. This system is used in local and wide area networks. [3]

The CWDM-PON operates downstream from the OLT to the ONU using a wavelength of 1490 nm for voice and data and upstream from the ONU to the OLT using a wavelength of 1310 nm for voice and data. The video is sent downstream at a wavelength of 1550 nm and there is no video service upstream.

III. THE WDM PON

The WDM-PON (Wavelength Division Multiplex Passive Optical Network) offer higher bandwidth in access networks. It is a candidate solution for next-generation PON systems [4].

The WDM-PON architecture has various advantages than the traditional PON-TDM systems. First, the WDM-PON allows each user to be dedicated with one or more wavelengths (λ_1, λ_2, λ_3, ..., λ_N), allowing each subscriber to access the entire bandwidth adapted to the wavelengths. This architecture generally offers

ISSN 1737-9334

increased security and scalability because each subscriber receives only its own wavelength.

The WDM PON allows point-to-point (P2P) connections between the OLT and the ONU and does not require point-to-multipoint (P2MP) access controllers in other PON networks.

IV. Simulations and Results

A. System Parameters:

Tables I and II, show the parameters for both systems.

TABLE I. CWDM PON SYSTEM PARAMETERS.

Bite rate		2.5 Gbps/channel Downstream, 2.5 Gbps/channel Upstream.
Power		-10 dBm, -8 dBm, -5 dBm, 0 dBm, 5 dBm, 8 dBm, 10 dBm.
Pulse generators		NRZ.
SMF	**L**	20 km, 30 km, 40 km, 50 km, 60 km.
	DC	17 ps/nm/km.
Number of input ports		4.
Down-stream wavelength		1490 nm, 1510 nm, 1530 nm, 1550 nm.
Up-stream wavelength		1290 nm, 1310 nm, 1330 nm, 1350 nm.
Video Down-stream		1550 nm.

TABLE II. WDM PON SYSTEM PARAMETERS.

Bite rate		2.5 Gbps/channel Downstream, 2.5 Gbps/channel Upstream.
Power		-10 dBm, -8 dBm, -5 dBm, 0 dBm, 5 dBm, 8 dBm, 10 dBm.
Pulse generators		NRZ.
SMF	**L**	20 km, 30 km, 40 km, 50 km, 60 km.
	DC	17 ps/nm/km.
Gain EDFA		17 dB.
Number of input ports		4.
Down-stream wavelength		1550 nm (Individual per channel).
Up-stream wavelength		1550 nm (Individual per channel).
Video		1550 nm.
Wavelength Spacing		0.8 nm.

B. The CWDM PON system:

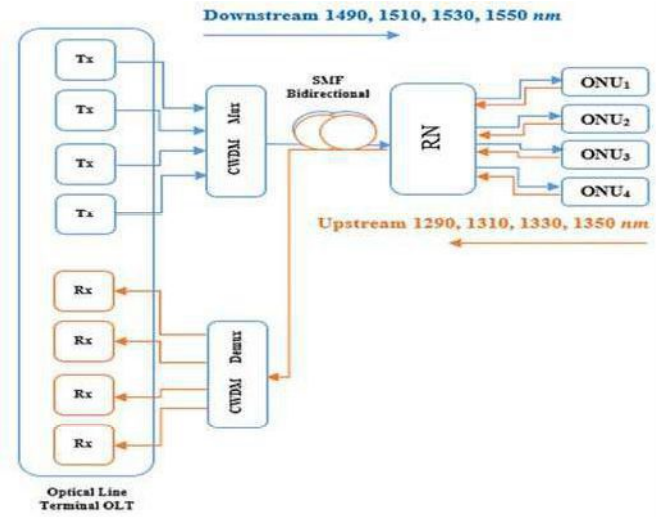

Fig. 2 Block diagram of the CWDM PON system.

1) Q factor versus length and power:

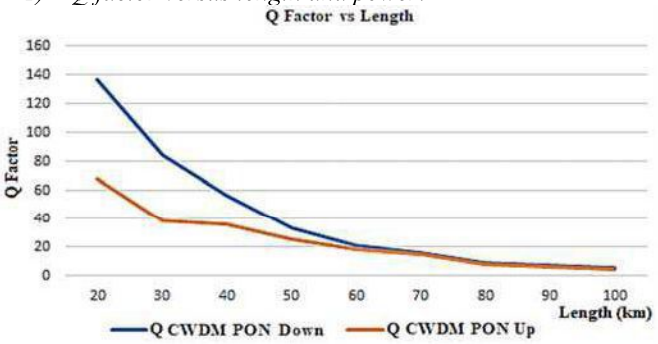

Fig.3 Q Factor vs. Length.

The figure 3 shows that the maximum length that limits the performance of the CWDM PON system is 100 km ($Q_{Downstream}$ = 5.768 and $Q_{Upstream}$ = 4.412). Same for figure 4, for power of -12 dBm and length = 20 km, we obtain low results ($Q_{Downstream}$ = 11.331 and $Q_{Upstream}$ = 6.671).

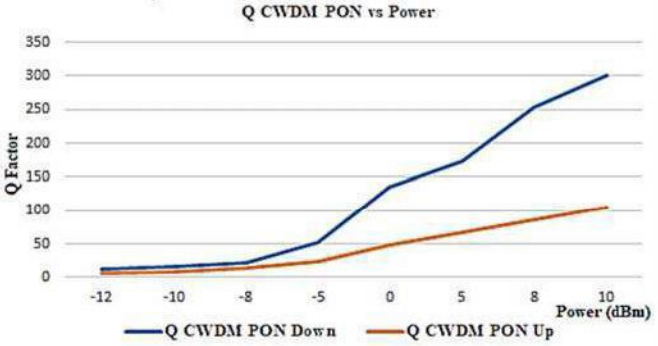

Fig.4 Q Factor vs. Power.

It should be noted that for L = 20 km, the eye is completely open, but for L = 100 km, the eye diagram begins to degrade (see figure 5). It can be seen that the system is limited to the distance of 100 km.

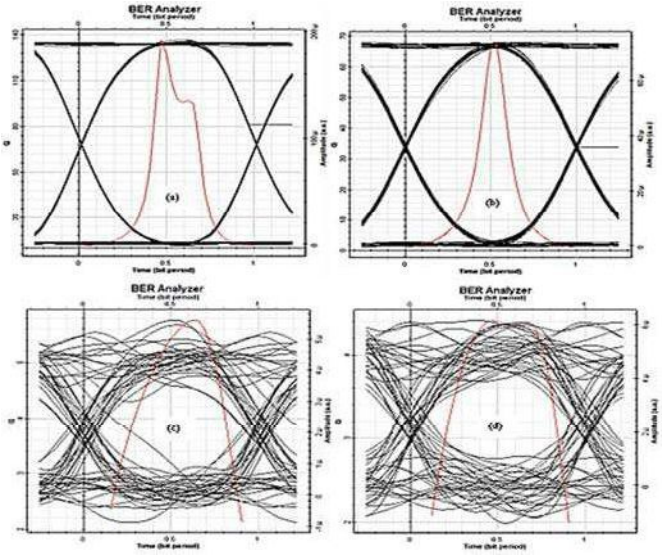

Fig. 5 Eye diagram downstream at 20 km (a), Eye diagram upstream at 20 km (b), Eye diagram downstream at 100 km (c), Eye diagram upstream at 100 km (d).

ISSN 1737-9334

C. *The WDM PON system:*

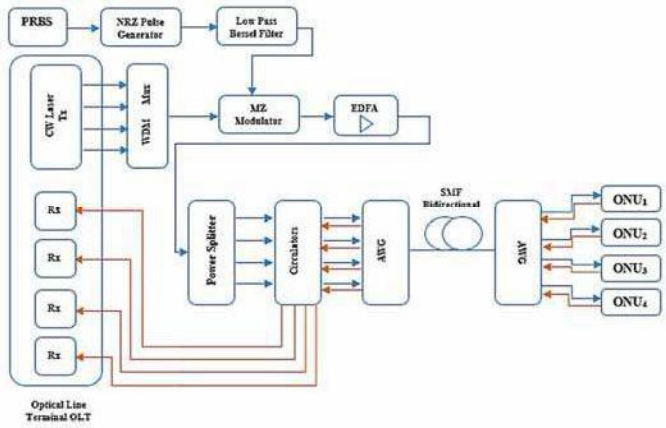

Fig. 6 Block diagram of the WDM PON system.

1) *Q factor versus length and power:*

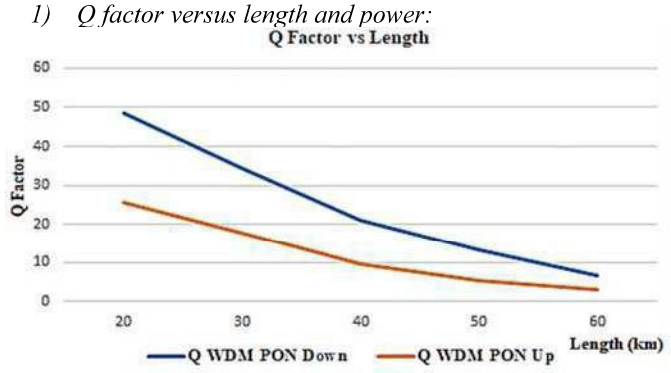

Fig. 7 Q Factor vs. Length.

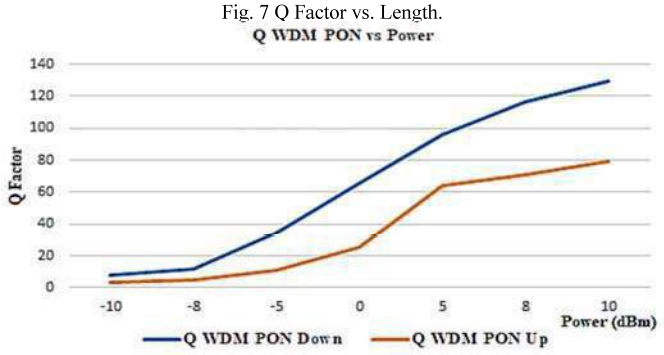

Fig. 8 Q Factor vs. Power.

The figure 7 shows that as the link length increases, the Q factor decreases. Beyond 60 km, the performance of the WDM PON system is beginning to deteriorate ($Q_{Downstream}$ = 6.721 and $Q_{Upstream}$ = 3.108). From the figure 8, for the power = -10 dBm and the length = 20 km, we get weak results ($Q_{Downstream}$ = 7.851 and $Q_{Upstream}$ = 3.212). This means that the fiber length and the power laser of the WDM PON system are important factors.

It should be noted that for L = 20 km, the eye is fully open, i.e. $BER_{Downstream}$ and $BER_{Upstream} \approx 0$, but for L = 60 km, the $BER_{Downstream} = 8.991\ 10^{-12}$ and the $BER_{Upstream} = 4.417\ 10^{-5}$ (see figure 9). So, the performance of the WDM PON system starts to deteriorate beyond 60 km.

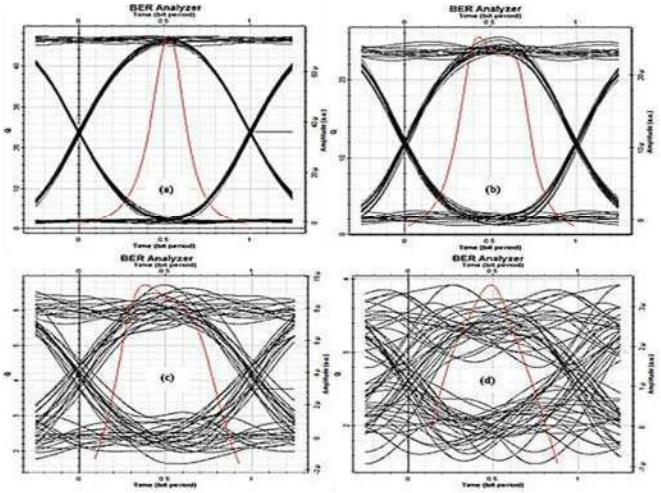

Fig. 9 Eye diagram downstream at 20 km (a), Eye diagram upstream at 20 km (b), Eye diagram downstream at 60 km (c), Eye diagram upstream at 60 km (d).

D. *Comparison between the CWDM PON system and the WDM PON system:*

1) *Q factor versus length and power:*

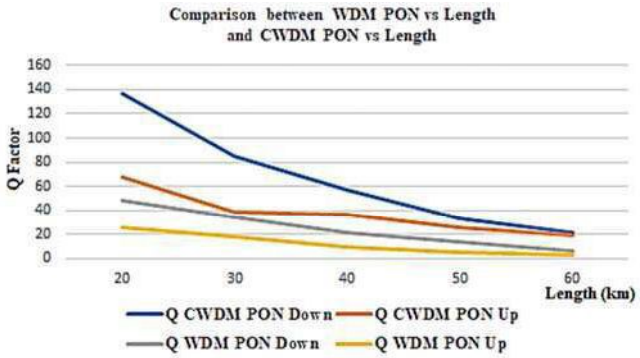

Fig. 10 Q Factor vs. Length.

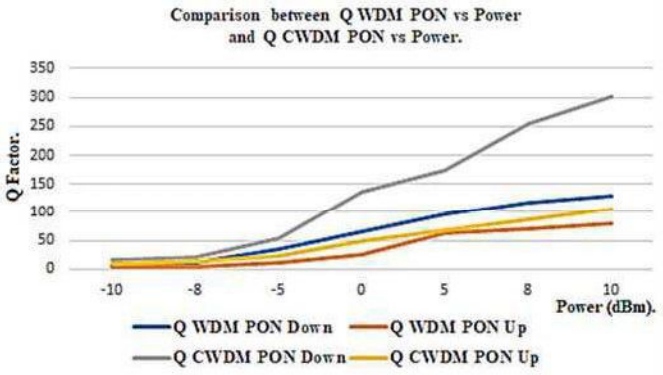

Fig. 11 Q Factor vs. Power at 20 km.

ISSN 1737-9334

2) BER versus length:

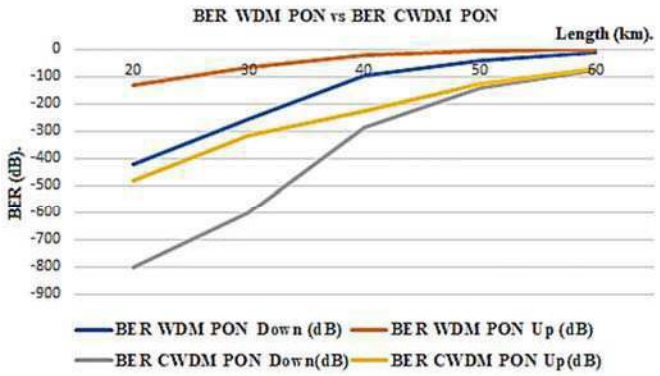

Fig. 12 BER vs. Length.

The figures 10, 11 and 12 show that the CWDM PON system has been successfully evaluated against the WDM PON system. The CWDM PON works well over a distance of 20 km to 100 km and a power of -12 dBm with a better quality factor and BER compared to the WDM PON system. However, the performance of the WDM PON system has deteriorated beyond a distance of 60 km and for a power of less than -10 dBm.

V. Conclusion

The performance of the WDM PON system seems better with a distance of 20 km to 60 km and a minimum power of -10 dBm with NRZ modulation format, but this system remains unusable for distances greater than 60 km, because Beyond this distance, the WDM PON is affected by the non-linear effects, like the Four Wave Mixing FWM and the cross-phase modulation XPM due to the channel spacing (less than 0.8 nm) which causes interference between the adjacent channels [5]. The WDM PON requires an EDFA type amplification device which is expensive. The results obtained in this paper make it possible to assert that the CWDM PON system was the most appropriate technique for optical transmission in PON access network, because it does not require expensive elements that require control (laser, amplifiers, filters, ...) as the WDM PON system. The main disadvantage of CWDM is that the number of channels is limited compared to WDM. [6]

Acknowledgment

The research described in this paper was supported by Mr. Ashok Suryawanshi, Deputy Director and Professor at the Center for Excellence in Technology and Management (CETTM) -MTNL in Mumbai-India for his assistance in practice sessions and PON courses (in November, 24th, 2018).

References

[1] Radim SIFTA, Petr MUNSTER, Ondrej KRAJSA, Miloslav FILKA, “Simulation of bidirectional traffic in WDM-PON networks”, Brno University of Technology, ISSN 0033-2097, R. 90 NR 1/2014.

[2] CETTM-MTNL, “ITEC Training Programme on Optical Fibre Cables, Systems and Modern Telecom Transport Technologies Volume III”, Centre for Excellence in Telecom Technology and Management Technology, Powai, Mumbai-India, November, 24th, 2018.

[3] Amitabha Banerjee, Youngil Park, Frederick Clarke and Huan Song, “Wavelength-division-multiplexed passive optical network (WDM-PON) technologies for broadband access”, Vol. 4, No. 11/JOURNAL OF OPTICAL NETWORKING, USA, November 2005.

[4] Bostjan Batagelj, Vesna Erzen, Jurij Tratnik, Luka Naglic “Optical Access Network Migration from GPON to XG-PON”, The Third International Conference on Access Networks, Slovenia-2012.

[5] C. Kherici, M. Kandouci, “Comparative Study Between the WDM System and the DWDM in an Optical Transmission Link at 40 Gb/s”, Advanced Control Engineering Methods in Electrical Engineering Systems pp 488-98 - Springer 2019.

[6] J. George, “Designing passive optical networks for cost effective triple play support,” in Proceedings of FTTH conference, Orlando, Florida, 4-6 October 2004.

ISSN 1737-9334

Comparative analysis of transfer efficiency of down-conversion glass and glass ceramic layers based on $70SiO_2$-$30HfO_2$ doped Tb^{3+}/Yb^{3+}

L. Oulmaati[1,2], K. Bouziane[1], A. Bouajaj[2], S. Belmokhtar[2], M.R. Britel[2] , A. Harrandou[2], F. Enrichi[5], L.Zur[3], A.Lukowiak[6], M.Ferrari[3,4]

1 International University of Rabat, LERMA, Parc Technopolis, 11100 – Sala Al Jadida, Morocco

2 Laboratory of Innovative Technologies, LTI, ENSA–Tangier, University Abdelmalek Essaâdi, Tangier, Morocco.

3 CNR-IFN, Istituto di Fotonica e Nanotecnologie, CSMFO Lab and FBK Photonics Unit, Via alla Cascata 56/C, 38123 Povo (Trento), Italy.

4 Museo Storico della Fisica e Centro Studi e Ricerche Enrico Fermi, Piazza del Viminale 1, 00184 Roma, Italy

5 Dipartimento di Scienze Molecolari e Nanosistemi, Universit_a Ca' Foscari Venezia, via Torino 155/b, 30172 Mestre, Venezia, Italy.

6 Institute of Low Temperature and Structure Research, PAS, Wroclaw, Poland

Abstract— **The main losses in solar cells result from the incomplete utilization of the solar spectrum. By the addition of a down-converting (DC) layer on the front side of a silicon solar cell, the generation more than one low-energy photon for energy incident can be utilized.**

In this paper we demonstrate the possibility to improve the efficiency of solar cells by using down-conversion glass and glass ceramic layers based on $70SiO_2$-$30HfO_2$ doped Tb^{3+}/Yb^{3+}.

The down-conversion process is based on a cooperative energy transfer mechanism between one Tb^{3+} and two Yb^{3+} ions. Yb^{3+} has only one excited level $^2F_{5/2}$. The relaxation $^2F_{5/2} \rightarrow {}^2F_{7/2}$ between the excited state and the fundamental level produces a near infra-red (NIR) photon at 980 nm wavelength, which is close to the edge of silicon band gap. On the other hand Tb^{3+} is used as sensitizer, with absorption in the blue at 488 nm through the $^7F_6 \rightarrow {}^5D_4$ energy levels and cooperative transfer to Yb^{3+} ions.

Keywords— **Quantum cutting; Down-conversion; Rare earths; Glass-ceramic; Energy transfer; photovoltaic solar cells**

I. INTRODUCTION

The low conversion efficiency of silicon solar cells is mainly due to the mismatch between the incident solar spectrum and the spectral absorption properties of cell's material (Fig. 1). Photons with energies smaller than the silicon band gap are not absorbed, and their energy is totally wasted. Photons with energies larger than twice the silicon band gap are absorbed, but the excess energy is lost to heating [1]. Before generating a significant fraction of energy demand with PV cells, increasing the conversion efficiency of these cells is essential. Different approaches have been proposed in recent years to improve the conversion efficiency of a solar cell semiconductor [1-2]. The best result is obtained with PV solar cells having a multijunction structure. The gap junctions narrows from top to bottom, which allows efficient use of solar energy in different spectral ranges. However, this technique is very complicated and expensive to be competitive economically. A more simple and interesting approach is the modification of the spectrum solar by engineering of luminescence. The down-conversion and up-conversion mechanisms are usually exploited to modify the incident solar spectrum [3] (see Fig. 1). In down-conversion, multiple low-energy photons are generated to exploit the energy of one incident high-energy photon. In up-conversion, two or more incoming photons generate at least one photon with a higher energy than the incoming photons [4].

In this paper we focus on a down-conversion mechanism which can reduce thermal losses. The down conversion, also called quantum cutting, permits to generate more than one low energy photon exploiting the energy of one incident high energy photon [2]. The advantage of this approach is best exploited by deposing a "down-conversion" layer on the cell (Fig. 2). Therefore we can convert UV / blue light inefficiently used by cells in near-infrared light very efficiently absorbed, increasing significantly the cell efficiency. Trupke et al. suggested that the performance can be improved by a layer of "down-conversion" to the cells. According to their calculations, a layer of "down-conversion" ideal that intersects each solar high-energy photon (UV / blue) into two photons in the near infrared can increase the limit of the cell efficiency from 30% to 36.6% [5].

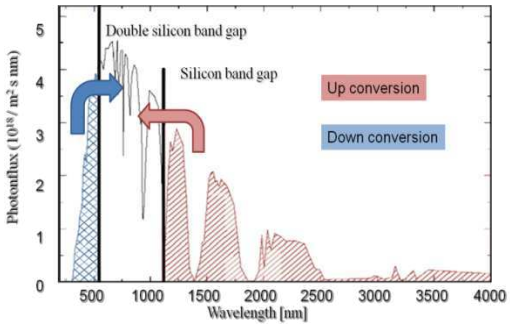

Fig.1 Solar spectrum with the indication of the band gap and twice the band gap of silicon [1]. The down-conversion converts photons from a high energy band (in blue) to the maximum absorption band of the silicon (in white). The up-conversion converts photons from a low energy band (in red) to the maximum absorption band of the silicon (in white)

Different mechanisms based on energy transfer between a RE^{3+} (absorbing ion) and Yb^{3+} (emitting ion) were investigated recently: Pr^{3+}/Yb^{3+}; Er^{3+}/Yb^{3+}, Tb^{3+}/Yb^{3+}; Tm^{3+}/Yb^{3+} [6-7-8]. With the rich energy levels of RE^{3+} ions, it is possible to dividing the energy absorbed into several parts

ISSN 1737-9334

and transfers the energy to Yb^{3+} ions. And Yb^{3+} only emits light around 980nm used very effectively by Si solar cells.

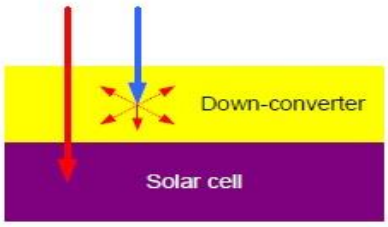

Fig.2 Down-conversion for photovoltaic solar cells, layer placed over a solar cell converting violet–blue photons into red-NIR ones.

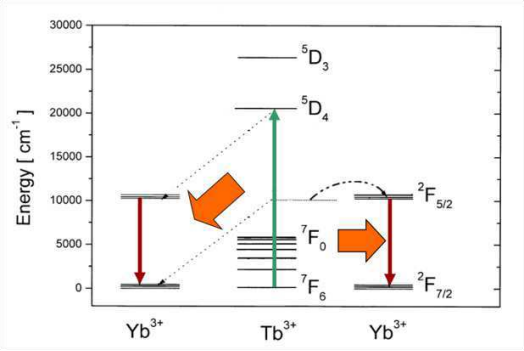

Fig. 3 Schematic energy level diagram of Tb^{3+}+ and Yb^{3+} showing the cooperative energy transfer process between the doped ions [10].

In this work on the down-conversion process, we used cooperative energy transfer between Tb^{3+} ion and two Yb^{3+} ions [4]. Fig. 3 shows the schematic diagram for the Tb^{3+}→Yb^{3+}cooperative energy transfer process. The Tb^{3+}: $^5D_4$ energy level corresponds at about twice the energy of the Yb^{3+}: $2^2F_{5/2}$ energy level. The Yb3+ ions don't present an energy level above the $2^2F_{5/2}$ level up to the UV region. The cooperative energy transfer between a Tb^{3+} ion and two Yb^{3+} ions can be the main relaxation route to achieve the NIR luminescence of the Yb^{3+}. Therefore two NIR photons are emitted by Yb^{3+} ions after the absorption of a single photon by a Tb^{3+} ion. We used decay curve analysis to evaluate the transfer efficiency.

Most studies of down conversion have been performed on single crystals characterized by a low phonon cut-off energy to minimize non-radiative transitions from the RE ions to the host matrix. Recent studies, however, have demonstrated that some glasses (G) and transparent glass ceramics (GC) could be alternative systems for supporting an effective quantum cutting process. [10].

Sol gel-derived silica-hafnia is a reliable and flexible system that has proved to be suitable for rare earth doping and fabrication of glass-ceramic planar waveguides [11]. Moreover, we demonstrated that sol-gel derived Er^{3+} activated silica-hafnia planar glass ceramic exhibits good optical and spectroscopic properties for photonic applications [12-13]. In silica-hafnia glass-ceramic the rare earth ions are embedded in hafnia nanocrystals which have a cut-off frequency of about 700 cm^{-1} [14]. So the presence of hafnia nanocrystal produces a strong reduction of the non-radiative transition process reflected by a lengthening of the measured emission lifetime. For these reasons the silica hafnia glass ceramic seems a suitable matrix to produce rare-earth activated films suitable for down conversion process. However, different parameters remain to be determined before synthesizing a layer potentially useable in a photovoltaic system. A critical parameter is the active ions content necessary to get the best conversion efficiency.

In this work, the process of "down-conversion" is studied in a $70SiO_2$-$30HfO_2$glass ceramic planar waveguides co-activated by Tb^{3+}/Yb^{3+}fabricated by sol gel route. The energy transfer from Tb^{3+} to Yb^{3+} ions was investigated as a function of the Tb^{3+}/Yb^{3+}concentration.

II. EXPERIMENTAL

A series of glass ceramic $70SiO_2$-$30HfO_2$planar waveguides samples co-doped by fixed 0.5 mol% $Tb^{3+}$and different mol% Yb^{3+} were prepared by sol–gel route using the dip-coating technique.

The starting solution, obtained by mixing tetraethylorthosilicate (TEOS), ethanol, deionized water and hydrochloric acid as a catalyst, was pre-hydrolyzed for 1 h at 65 °C. The molar ratio of TEOS:HCl: H_2O was 1:0.01:2. An ethanolic colloidal suspension was prepared using as a precursor $HfOCl_2$ and then added to the TEOS solutions, with a Si/Hf molar ratio of 70/30. The quantity of ethanol was adjusted for each solution in order to obtain a final total [Si+Hf] concentration of 0.448 mol/l. Terbium and ytterbium were added as Tb(NO3)3;5H2O and Yb(NO3)3;5H2O. The final mixture was left at room temperature under stirring for 16 h. The obtained sol was filtered with a 0.2 µm Millipore filter. Silica–hafnia films were deposited on cleaned pure SiO2 substrates by dip-coating, with a dipping rate of 40 mm/min. Before further coating, each layer was annealed in air for 50 s at 900 °C. After a 10 dipping cycle, the film was heated for 2 min at 900 °C. Final films, obtained after 30 dips, were stabilized by a treatment for 5 min in air at 900 °C. As a result of the procedure, transparent and crack-free films were obtained. An additional heat treatment was performed in air at a temperature of 1000 °C for 30 min in order to nucleate nanocrystals inside the film $70SiO_2$-$30HfO_2$glass ceramic planar waveguides doped with rare earth ions were thus produced. Table 1 gives the compositional and optical parameters of the obtained silica-hafnia planar waveguides.

The thickness of the waveguides and the refractive index at 632.8 and 543.5 nm were obtained by a m-lines apparatus (Metricon, mod2010) based on the prism coupling technique, using a Gadolinium Gallium Garnet (GGG) prism, with the setup reported in [15].

XRD measurements were carried out at room temperature an X'Pert PRO diffractometer (Panalytical). A Cu anode (with Kα1,2 lines) was used as a radiation source. Owing to the small thickness of the investigated waveguides, the grazing incidence x-ray diffraction (GIXRD) geometry was employed. XRD

ISSN 1737-9334

spectra were collected in continuous scan mode in the 2θ range 10◦–100◦, with a scanning step of 0.1◦ and counting time of 60 s. The transmittance spectra were recorded in an UV near-infrared spectrophotometer Photoluminescence spectroscopy was performed by far-field excitation using the 476 nm line of an Ar+ ion laser as excitation source. The luminescence spectrum in the region of the transition $^2F_{5/2} \rightarrow {}^{11}F_{7/2}$ of Yb^{3+} ion was analyzed by a single grating monochromator with a resolution of 2 nm and detected using a Si/InGaAs two-color photodiode and standard lock-in technique. Luminescence decay measurements of the 5D4 state of Tb^{3+} ion were performed after excitation with the third harmonic of a pulsed Nd-YAG laser. The visible emission was collected by a double monochromator with a resolution of 5 cm^{-1} and the signal was analyzed by a photon-counting system. Decay curves were obtained recording the signal by a multichannel analyzer Stanford SR430. More information about the experimental setups can be found in [16].

TABLE I
RARE EARTH CONCENTRATION, RELATIVE INDEX AND LAYER TICKNESS OF THE SAMPLE

Sample label	Terbium concentration in mol%	Ytterbium concentration in mol%	n@543.5 nm TE [± 0.001]	n@632.8 nm TE [± 0.001]	Layer thickness [±0.2µm]
AR1	0,5	0	1,621	1,616	1,0
A1	0,5	1	1,626	1,621	1,0
A2	0,5	2	1,631	1,626	1,0
A3	0,5	3	1,633	1,628	1,1

III. RESULTS AND DISCUSSION

The structural properties of the waveguides are obtained by the XRD measurements. Fig 4 shows the XRD patterns of $70SiO_2$-$30HfO_2$ waveguides doped O,5% Tb^{3+} treatment at 900 °C (glass) and 1000 °C (ceramic glass) and the 70SiO2–30HfO2 waveguides doped O,5% Tb^{3+} : 3%Yb^{3+} treated at 1000 °C. All XRD spectra contain contributions from amorphous structures. In particular, the hump centred at 2θ ≈ 21◦ is a typical feature of a- SiO_2, originating from the silica substrate and from the SiO2 component of the waveguides (70 mol %). According to XRD, the waveguides treated at 900 °C are fully amorphous. As clearly shown in fig. 4(a), crystallization in the $70SiO_2$-$30HfO_2$ waveguide starts after heat treatment at about 1000 °C for 30 min as documented by the presence of Bragg reflection peaks. As shown in fig. 4 the effect of the crystallization increases by increasing the concentration of rare earth showing that in silica–hafnia glass ceramic, the RE ions are embedded in hafnia nanocrystals. Similar result has founded by Roca and all in Er^{3+} doped 70SiO2–30HfO2 planar waveguides [17]. From the comparison between XRD data and the ICSD database, we attribute the crystalline phase in waveguides to the metastable tetragonal hafnium oxide (t-HfO2),The diffraction peaks calculated from the matched ICSD card (No 85322) are shown (vertical lines). The ICSD card belongs to the isostructural metastable t-HfO_2 phase [17].

Fig. 5 shows the optical transmission spectra of the investigation $70SiO_2$-$30HfO_2$ waveguides doped 0,5% Tb^{3+} treated at 900 °C (glass) and that treated at 1000 °C (glass ceramic). The spectra reveals that, despite the difference in refractive index between the v-SiO slabs (n= 1.46 at 632 .8 nm) as substrates and the layer glass ceramic (∼1.612 at 632 .8 nm) the transmittance of the glass ceramic reaches as high as 90% in the visible infrared range, which is due to the much smaller size of the precipitated crystals than the wavelength of the visible light [18].

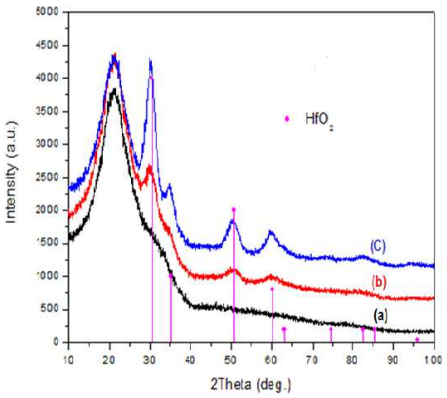

Fig. 4 Observed XRD patterns of $70SiO_2$-$30HfO_2$ waveguides: (a) 0,5mol% Tb^{3+}: 0 mol% Yb^{3+} treated at 900 °C. (b) AR1, (c) A3

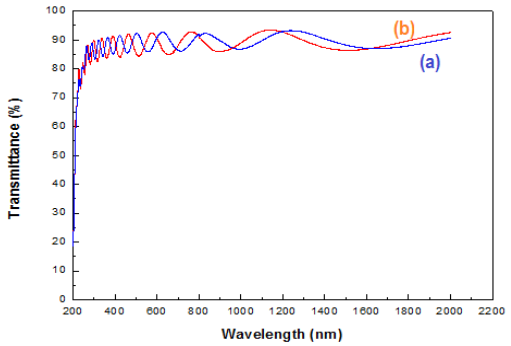

Fig. 5 Optical transmission spectra for (a) $70SiO_2$-$30HfO_2$ waveguides with 0,5mol% Tb^{3+}: 0 mol% Yb^{3+} treated at 900 °C. (b) AR1

Fig 6 shows the photoluminescence spectra recorded between 960 and 1060 nm of the Tb^{3+}-Yb^{3+} co-doped samples. The intense emission band centered at 977 nm, with a shoulder at 1027 nm, is attributed to the $^2F_{5/2} \rightarrow {}^2F_{7/2}$ transition of Yb^{3+} ions. The emission of the Yb^{3+} ions after excitation in the blue region is an indication of the presence of an efficient energy transfer from Tb^{3+} to Yb^{3+} and so of an effective down-conversion. For application of Tb^{3+} and Yb^{3+} co-doped $70SiO_2$ - $30HfO_2$ glass ceramic layer as down converter, high external quantum efficiency is required. However, it is not possible to evaluate the conversion efficiency only on the base of the photoluminescence spectra. Assessment of the conversion

ISSN 1737-9334

efficiency is obtained from the estimation of the energy transfer efficiency between terbium and ytterbium. The evaluation of the energy transfer efficiency between Tb^{3+} and Yb^{3+} can be obtained by comparing the luminescence decay of terbium with and without ytterbium co-doping ions.

In fig. 7, the decay curves of the Tb^{3+} $^5D_4 \rightarrow {}^7F_5$ emission at 543.5 nm are plotted for the different samples. Nearly single exponential luminescence decay is observed for the sample without Yb^{3+}. The fast luminescence decay observed for the co-doped samples is attributed to the energy transfer from the Tb^{3+}: $^5D_4$ to the Yb^{3+}: $^2F_{5/2}$ [19].

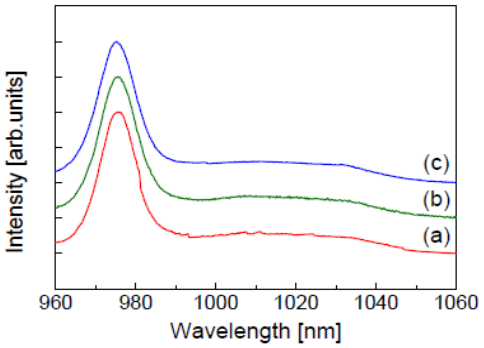

Fig.6 Room temperature photoluminescence spectra of the $^2F_{5/2} \rightarrow {}^2F_{7/2}$ transition of Yb^{3+} ions after excitation at 476 nm for the three samples: (a) A1; (b) A2; (c) A3. Each spectrum was normalized to the maximum of the luminescence intensity

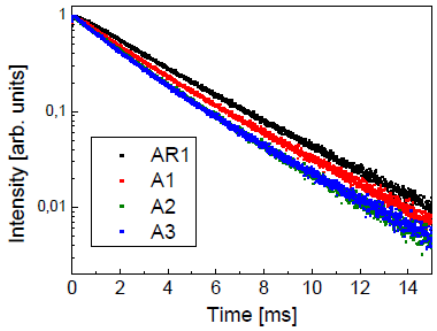

Fig. 7 Decay curves of the luminescence from the $^5D_4$ metastable state of Tb^{3+}ions for the second samples series under excitation at 355 nm.

The not exponential behavior of the decay can be explained by different distributions of Yb^{3+} ions around the Tb^{3+} ions, which lead to different energy transfer rates for the different Tb^{3+} ions [20]. The energy transfer efficiency $\eta_{Tb\text{-}Yb}$ can be obtained experimentally by dividing the integrated intensity of the decay curves of the $Tb^{3+} \rightarrow Yb^{3+}$ co-doped glass ceramics by the integrated intensity of the Tb^{3+} single doped curve [19]:

$$\eta_{Tb-Yb} = 1 - \frac{\int I_{Tb-Yb}\,dt}{\int I_{Tb}\,dt} \qquad (1)$$

The effective quantum efficiency can be defined by the ratio between the number of emitted photons and the number of photons absorbed by the material. In our case, a perfect down-conversion system would have an effective quantum efficiency value of 200%, corresponding to the emission of two photons for one absorbed. The relation between the transfer efficiency and the effective quantum efficiency is linear [19] and is defined as:

$$\eta_{EQE} = \eta_{Tb-r}(1 - \eta_{Tb-Yb}) + 2\eta_{Tb-Yb} \qquad (2)$$

Where, the quantum efficiency for Tb^{3+} ions $\eta_{Tb\text{-}r}$ is set equal to 1. The evaluated values of energy transfer efficiency and effective quantum efficiency for the different samples are reported in Table 2.

.

TABLE II
TRANSFER EFFICIENCY AND EFFECTIVE QUANTUM EFFICIENCY AS A FUNCTION OF Yb^{3+}MOLAR CONCENTRATION FOR 70SIO2–30HFO2 GLASS CERAMIC WAVEGUIDES WHERE Tb^{3+} CONTENT IS FIXED AT 0.5 MOL%.

Composition (Yb concentration in mol%)	1%	2%	3%
Transfer efficiency	14%	24%	25%
Effective quantum efficiency	114%	124%	125%

IV. CONCLUSIONS

$70SiO_2$-$30HfO_2$ glass ceramics co-doped $Tb^{3+}/Yb^{3+}$with Tb^{3+} content kept constant at 0.5 mol% and increasing Yb^{3+} molar concentration were prepared by sol-gel method and dip coating processing. The XRD measurements show that the crystallization of the waveguide starts after heat treatment at about 1000 °C, the effect of the crystallization increase by increasing the concentration of the rare earth. Near-infrared emission at 980nm assigned to the $^2F_{5/2} \rightarrow {}^2F_{7/2}$ transition of the Yb^{3+} ions was observed upon excitation at 476 nm. The energy transfer efficiencies were estimated from the decay curves of the $^5D_4$ metastable state of the Tb^{3+} ion. The Tb-Yb energy transfer efficiency increases with the increase of the molar ratio Yb/Tb but don't exceed 24-25%. For this reason another series of sample has been fabrication with higher content of rare earth ions [Tb^{3+} +Yb^{3+}] for the future work.

This work is an progress to explore the possibility of enhancement silicon based solar cell efficiency using down conversion layer by electrical characterization. The photovoltaic efficiency of cells with and without down-converting (DC) layer will be evaluated according to photovoltaic current density-voltage (I-V).

ACKNOWLEDGMENT

The research activity was performed in the framework of the CNR-CNRST joint project (2014-2015).

REFERENCES

ISSN 1737-9334

[1] C. Strumpel, M. McCann, G. Beaucarne, V. Arkhipov,A. Slaoui, V. ek, C. Cañizo, I. Tobias., *Modifying the solar spectrum to enhance silicon solar cell efficiency - An overview of available materials*, Solar Energy Material & Solar Cells, vol. 91, pp. 238-249, (2007).

[2] B.S Richards, *Luminescent layers for enhanced silicon solar cell performance: Down-conversion*, Solar Energy Material & Solar Cells, vol. 90, pp. 1189-1207 (2006).[2bis] V.D. Rodrı´guez a,n, V.K.Tikhomirov b, J.Me´ndez-Ramos a, A.C.Yanes c, V.V.Moshchalkov b *Towards broad range and highly efficient down-conversion of solar spectrum by Er^{3+}–Yb^{3+} co-doped nano-structured glass-ceramics* Solar Energy Materials & Solar Cells 94 (2010) 1612–1617.

[3] Xiaomin Li, Fan Zhang, Dongyuan Zhao. Nano Today (2013) 8, 643—676

[4] A. Boccolini, J. Marques-Huesoa, D. Chenb, Y. Wang, B.S. Richards. Solar Energy Materials & Solar Cells 122 (2014) 8–14.

[5] T. Trupke, M. A. Green, and P. Wurfel*, Improving solar cell efficiencies by down-conversion of high-energy photons*. Journal of Applied Physics, 92 (2002): 1668-1674.

[6] S. Ye et al., *Enhanced cooperative quantum cutting in Tm^{3+}-Yb^{3+} codoped glass ceramics containing LaF3 nanocrystals*, Opt. Lett., vol. 16, pp. 8989-8994 (2008).

[7] G Lakshminarayana, et al., *Co-operative downconversion luminescence in Tm^{3+}/Yb^{3+}: SiO_2-Al_2O_3-$LiFGdF_3$glasses* , J. Phys. D: Appl. Phys. vol. 41, pp. 175111-1/6 (2008)

[8] Q. Zhang et al., *Quantum Cutting in Tm^{3+}/Yb^{3+}-Codoped Lanthanum Aluminum Germanate Glasses* ,J. Am. Ceram. Soc., vol. 93, pp. 654-657 (2010).

[9] V.D. Rodrıguez, et al., *Towards broad range and highly efficient down-conversion of solar spectrum byEr^{3+}–Yb^{3+} co-doped nano-structured glass-ceramics* , Solar Energy Material & Solar Cells, vol. 94,pp.1612-1617 (2010).

[10] G. Alombert-Goget, C. Armellini, A. Chiappini, A. Chiasera, M. Ferrari, S. Berneschi, M. Brenci, S. Pelli, G. C. Righini, M. Bregoli, A. Maglione, G. Pucker, and G. Speranza, *Frequency converter layers based on terbium and ytterbium activated HfO_2 glass-ceramics*, Proc. SPIE 7598, pp. 75980P–1/9, 2010. doi: 10.1117/12.841907.

[11] Y. Jestin, N. Afify, C. Armellini, S. Berneschi, S. N. B. Bhaktha, B. Boulard, A. Chiappini, A. Chiasera, G. Dalba, C. Duverger, M. Ferrari, C. E. Goyes Lopez, M. Mattarelli, M. Montagna, E. Moser, G. Nunzi Conti, S. Pelli, G. C. Righini, F. Rocca, *Er^{3+} activated silica-hafnia glass-ceramics planar waveguides*, SPIE 6183, 438-445 (2006).

[12] Y. Jestin, C. Armellini, A. Chiasera, A. Chiappini, M. Ferrari, E. Moser, R. Retoux, G. C. Righini, *Low-loss optical Er^{3+}-activated glass-ceramics planar waveguides fabricated by bottom-up approach*, Appl. Phys. Lett. 91, 071909-1 – 071909-3 (2007)

[13] Y. Jestin, C. Armellini, A. Chiappini, A. Chiasera, M. Ferrari, C. Goyes, M. Mattarelli, M. Montagna, E. Moser, G.Nunzi Conti, S. Pelli, G.C. Righini, and G. Speranza, *Erbium activated HfO2-based glass-ceramics waveguides for photonics,* J. Non-Cryst. Solids 353, 494-497 (2007).

[14] D. A. Neumayer and E. Cartier, *Materials characterization of ZrO_2-SiO_2 and HfO_2-SiO_2 binary oxides deposited by chemical solution deposition,*J. Appl. Phys. 90, 1801-1808 (2001).

[15] S. Ronchin, A. Chiasera, M. Montagna, R. Rolli, C. Tosello, S. Pelli, G.C. Righini, R.R. Gonçalves, S.J.L. Ribeiro, C. De Bernardi, F. Pozzi, C. Duverger, R. Belli, and M. Ferrari, SPIE 4282, 31 (2001).

[16] G. Alombert-Goget, C. Armellini, S. Berneschi, S.N.B. Bhaktha, B. Boulard, M. Brenci, A. Chiappini, A. Chiasera, C. Duverger-Arfuso, P. Féron, M. Ferrari, R.R. Gonçalves, Y. Jestin, L. Minati, E. Moser, G. Nunzi Conti, S. Pelli, D.N. Rao, R. Retoux, G.C. Righini, G. Speranza, *Er^{3+}- activated photonic structures fabricated by sol-gel and rf-sputtering techniques,* Proceedings of SPIE Vol. 7366, 73660E-1 – 73660E-15 (2009).

[17] N. D Afify, G Dalba1 and F Rocca, *XRD and EXAFS studies on the structure of Er^{3+}-doped SiO_2–HfO_2 glass-ceramicwaveguides: Er^{3+}-activated HfO_2 nanocrystals*, J. Phys. D: Appl. Phys. 42 (2009) 115416 (11pp).

[18] S. Hendy, *Light scattering in transparent glass ceramics*, Applied Physics Letters 81 (7) (2002) 1171–1173.

[19] P. Vergeer, T. J. H. Vlugt, M. H. F. Kox, M. I. Den Hertog, J. P. J. M. van der Eerden, and A. Meijerink, *Quantum cutting by cooperative energy transfer in $YbxY1-xPO4:Tb^{3+}$*,Phys. Rev. B 71, 014119-1 – 014119-11 (2005).

[20] B. M. van der Ende, L. Aarts, and A. Meijerink, *Near-Infrared Quantum Cutting for Photovoltaics*, Advanced Materials 21, 3073-3077 (2009).

ISSN 1737-9334

7th International Conference on Control Engineering & Information Technology (CEIT-2019)
Proceedings of Engineering and Technology PET

Developing an Enhanced NAT-Traversal Approach for Collaborative Augmented Reality e-Maintenance Platforms

Allal Tiberkak[1], Abdelfetah Hentout[2], Abdelkader Bellarbi[3], Samir Benbelkacem[4], Nadia Zenati[5]
[1]University Yahia Fares of Medea, Department of Mathematics and Computer Science
Faculty of Sciences, Urban Pole, Medea, 26000, Algeria.
[2,4,5]Centre de Développement des Technologies Avancées (CDTA), Division Productique et Robotique (DPR)
BP 17, Baba Hassen, Algiers 16303, Algeria.
[3] IRIT, University of Toulouse, France
[1]tiberkak.allal@univ-medea.dz, [2]ahentout@cdta.dz, [3]abdelkader.bellarbi@irit.fr, [4]sbenbelkacem@cdta.dz,
[5]nzenati@cdta.dz

***Abstract*—This paper describes our ongoing efforts towards the development of a real-time communication module for collaborative augmented reality e-maintenance platforms. This module allows technicians and remote experts to stream video, audio and other specific structured/unstructured data application (commands, text messages, markers coordinates, virtual objects parameters, etc.) either in peer-to-peer model or using relay servers. Taking advantages from detecting local configurations of networks allows optimizing paths of data streams between technicians and experts. This is mainly done by comparing with current solutions, when technicians and experts are in the same local network, data streams would not need to be forwarded over the Internet.**

***Index Terms*—Real-time communication; Audiovisual communication; NAT traversal; Platform of e-Maintenance; Augmented reality.**

I. Introduction

The main purpose of maintenance is to slow down or avoid damages on a machine when it is in operation [1]. However, e-maintenance is the use of computing facilities to perform maintenance and the use of *ICT* (*Information and Communication Technologies*) to meet the business objectives of customers and product suppliers [2].

Two kinds of e-maintenance architectures can be distinguished: (*i*) *e-maintenance* which is operated in the production site where technicians and expert are located; and (*ii*) *tele-maintenance* which is distributed where a part is operated in the production site (used by technicians) and the other part is operated in the maintenance center (used by experts) [3].

To allow peers to exchange connection parameters, a rendezvous server is used. However, for NAT and firewall traversal, there are many techniques allowing a peer-to-peer communication over NAT and firewall. These techniques can be classified into four categories [4], [5]:

1) *Hole punching*: this technique consists in retrieving the public IP address and public port for each peer from STUN (*Session Traversal Utilities for NAT*) [6] servers, and sending them to the other peer via the rendezvous server. Consequently, each peer would know how to reach the other one. In many cases, this technique does not work; for example, in case of a symmetric NAT, the firewall denies UDP, incoming UDP packets and TCP connections. Finally, the hole punching techniques are not able to detect multiple-level NAT;
2) *Relaying*: it allows peers to use a relay servers to communicate with each other. SOCKS (*Socket Secure*) [7] is used to make connections that are not allowed by the firewall or NAT. SOCKS client connects to SOCKS server, and SOCKS server connects to requested peers. Another technique is based on TURN (*Traversal Using Relays around NAT*) [8] server. In this case, a peer requests the TURN server to allocate a channel; then, the peer sends the parameters of the allocated channel to the other one. Finally, the last peer uses the channel over the TURN server to send data to the first one;
3) *Explicitly cooperate with NAT and firewalls*: some solutions allow peers to cooperate with the NAT to perform port opening and port mapping between the couples *(public IP address, public port)* and *(private IP address, private port)*; then, each peer sends public IP address and port to the other peers. Among these solution, we cite *UPnP-IGDP* (*UPnP Internet Gateway Device Protocol*) [11], *NAT-PMP* (*Nat Port Mapping Protocol*) [12], and *PCP* (*Port Control Protocol*) [13]. Another solution, *ALG* (*Application-Level Gateway*) [14], plays the role of a proxy between peers and NAT. ALG can detect opened port and port mapping in order to use them on the profit of the peers.
4) *Combination of techniques*: the technologies ICE (*Interactive Connectivity Establishment*) [9] is used mainly by WebRTC [10] to allow peers to communicate. It uses STUN servers to make *Hole punching* in the network. If this operation failed, the two peers use a TURN server as a relay. This technique uses automatically the TURN server when the hole punching is field; however,

ISSN 1737-9334

sometimes there is more preferment solutions such as one of the two peers are behind multiple-level NAT connected to the same NAT as the other peer ($T3$ and $E4$ as illustrated by Figure 3) or one the NAT and the firewall allows reconfiguration such as port mapping and port opening;

The aim of this paper is to describe our ongoing efforts towards the development of a module that enables real-time communication between technicians and experts for a collaborative platform. This latter is at the same time a e-maintenance and a tele-maintenance platform [15]. This module should offer the streaming of video, audio and structured/non-structured data such as commands and messages. It should also transfer another kinds of data related to AR that consist of markers (glued labels on machines) coordinates and virtual objects (graphics add to pictures of machines) parameters.

Compared to the existing solutions, the main contribution of this work consists of developing a module that explores all possible techniques to ensure NAT-traversal. Additionally, this module chooses the best peer-to-peer path that passes through minimum number of network equipments.

The rest of this paper is organized as follows. Section II summarizes the existing solutions for communication between experts and technicians in e-maintenance platforms. Section III gives an overview on the considered e-maintenance platform; additionally, it illustrates the requirements related the communication between technicians and experts, mainly those of NAT-traversal. Section IV describes the proposed solution that consists of exploiting all NAT-traversal techniques and taking into account the network configuration. Finally, section V concludes the paper and draws up future works.

II. Related work

Many research works have tried to solve the problem of communication between experts and technicians. Some solution are based on a centralized entity (VPN server or services provider); other solutions are peer to peer such as those based on RTP or *WebRTC* (*Web Real-Time Communication*) [10]. The recent solutions of the literature are summarized in what follows.

Fritscher et al. [16] proposed a collaborative platform to control industrial robots. It offers three video streamed from the technician to the expert: the first provides overview of the facility, the second captures the details of the assembly machine, and the third is captured by the camera of the technician mobile device. The platform also provides the possibility of augmenting the reality by drawing virtual objects on the live videos (by expert and/or technician). The communication between technicians and experts is ensured via a VPN by using *OpenVPN*. This platform is tested on a factory located in Germany while the VPN gateway is in Brussels. Results illustrated that this platform requires from $300kbit/s$ to $3Mbit/s$ per video stream, and 5 $seconds$ to adapt the videos according to the available bandwidth.

Benbelkacem et al. [17] used Web Services architecture for collaborative control of shared interactive augmented scenes. This platform is composed of two sites: (*i*) *Site 1* for group of users working together and (*ii*) *Site 2* for automotive design experts. Additionally, web services are deployed on IIS (Internet Information Services) platform from Windows 8. The authors implemented four web services as illustrative examples: 3D translation web services, 3D rotation web services, 3D zoom web services and 3D visualization web services.

Mourtzis et al. [18] setup a platform on the cloud called $CARM^2 - PSS$ (*Cloud-Based Augmented Reality Remote Maintenance Through Shop-Floor Monitoring: A Product-Service System*). This platform consisted of monitoring service and *Augmented Reality* (*AR*) remote maintenance service. This last service allowed to exchange data between technician (at production plant) and remote expert (at maintenance department that is $600km$ far from production plant). The platform proposed five services: create technical reports, perform diagnosis, generate AR scenes, send AR scenes and overall application to technician, and check if the maintenance task is performed.

Bottecchia et al. [19] proposed a system allowing workers to help each other in the maintenance of broken machines. The platform permitted to point object by augmenting the reality by circles, arrows, etc.; sketching the elements of a scene using hands; adding animation to indicate action to do on the broken machine. The audiovisual communication between the team workers is ensured by the protocol RTP using *Live555 C++ library* (it is an open source project that implements the protocols RTP/RTCP, RTSP and SIP; it also implements *MPEG*, *H.265*, *H.264*, *H.263+* and other codecs [20]).

Fang et al. proposed an assistance system architecture that allowed experts to remotely assisting operators [21]. This architecture is composed of operators, remote experts and web servers. Furthermore, it permitted experts to augment the reality by adding virtual objects to captured video in order to guide and assist operators. However, audiovisual communication between the two peers (expert and operator) is done via WebRTC (expert station is a web application; operator station is a mobile Android application). Besides, the architecture offer a white-board to guarantee visual assistance to operators.

It can be noticed that the aforementioned solutions are not optimal; indeed, they are based on central points such as VPN [17], services provider [18], and cloud [19]. When technicians and experts are located in the same factory and connected to the same local network, the data will be forwarded from the source station to a central point (from Germany to Brussels in [17]) before arriving to destination. Therefore, the best solution is to use peer-to-peer communication such as the solution proposed in [18], [19] and [21]. Nevertheless, these solutions did not take into account the network configuration to enhance performances. Sometimes, solutions could forward data to a central point (in case of WebRTC); however, they may avoid this if they are able to take into account the network configuration.

ISSN 1737-9334

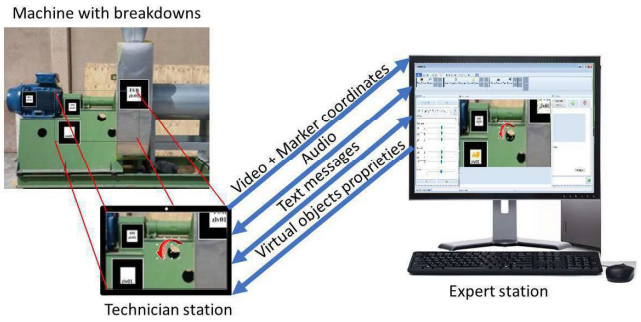

Fig. 1: Distributed e-maintennace platform.

III. Overview

The proposed e-maintenance platform is mainly composed of two stations: (*i*) *Technician station* used by technicians and (*ii*) *Expert station* used by experts. When a technician is facing a troubleshooting that he cannot solve alone, he should be able to ask for help from a list of available experts. Therefore, the platform uses two modules (as illustrated by Figure 1): an *AR module* and a *Communication module*.

- *AR module*: it extracts the markers coordinates from the video, allows the experts to add 3D virtual objects into the video and augments it on the technician station (with 3D virtual objects added by the experts) in order to guide technicians;
- *Communication module*: it streams video on the machine with breakdowns (captured by the technician station) and markers coordinates (extracted by the technician station from the video frames) to the expert station, ensures bidirectional audio communication and text messaging between technicians and experts, communicates the proprieties of the 3D virtual objects added by the experts to the technicians station.

This paper focuses only on the communication module. This module has to ensure as possible the communication between technician and expert stations wherever they are located on the network. As illustrated by Figure 1, two kinds of communication channels are needed:

- *Channels for streaming the video and the coordinates of markers from the technician station to the expert station and for bidirectional streaming of audio*: these channels should ensure best delay and less consumption of resources; they are neither needed to ensure packets order nor to avoid packets lost. The best option is to use RTP (Real-Time Transport Protocol) on UDP; but it is possible to use TCP;
- *Channels for text messaging and data transporting about 3D virtual objects*: these channels have to be reliable and avoid packets loss. The best protocol is TCP; however, UDP can be used but with ensuring packet order and retransmission of lost ones on the application layer, the protocol SCTP (Stream Control Transmission Protocol) is recommended.

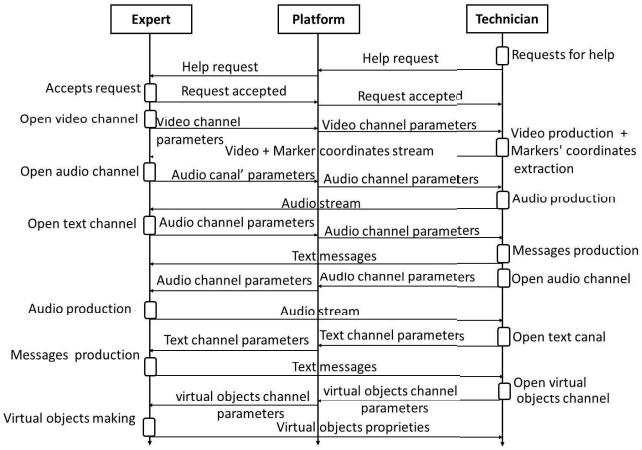

Fig. 2: Establishment of communication between technicians and experts.

As Figure 2 shows, the technician asks first for help from the expert. If the expert accepts his request, each peer (technician and expert stations) opens required channels and send their parameters (IP address and port) to the other peer.

Figure 3 presents possible locations of technicians and experts stations on the network:

- They can have public IP addresses such as $T1$ and $E1$ but located behind different firewalls ($T1$ behind $F1$, $E1$ behind $F2$);
- One of them can have a public IP address and the other is being behind NAT and firewall ($T1$ is behind $F1$, $E2$ is behind NAT $(F2, N2)$);
- Both are connected to the same NAT and firewall that are connected to Internet ($T2$ and $E2$ are both behind the NAT $(F2, N2)$ that is connected directly to Internet);
- Each of them is behind a firewall and NAT that are not the same ($T2$ is behind the NAT $(F3, N3)$, $E3$ is behind the NAT $(F4, N4)$);
- One of them is connected directly (without NAT) to Internet via a firewall and the other is connected to multiple-level NAT ($T1$ has a public IP address and is behind $F1$, $E4$ is behind the NAT (F5, N5) that is behind the NAT $(F4, N4)$);
- One of them is behind one NAT that is connected directly to Internet and the other is connected to multiple-level NAT ($T2$ is behind the NAT $(F3, N3)$ that is connected directly to Internet, $E4$ is behind the NAT $(F5, N5)$ that is behind the NAT $(F4, N4)$);
- One peer is connected to NAT that is connected directly to Internet and the other peer is connected to multiple-level NAT that is connected to the same NAT than first peer ($E3$ is behind the NAT $(F4, N4)$, $T3$ is behind the NAT $(F6, N6)$ that is behind the NAT $(F4, N4)$);
- Both peers are connected to multiple-level NAT. They are not behind the same second-level NAT but are connected to the same first-level NAT ($E4$ is behind the second level-NAT $(F5, N5)$ that is behind the first-level

ISSN 1737-9334

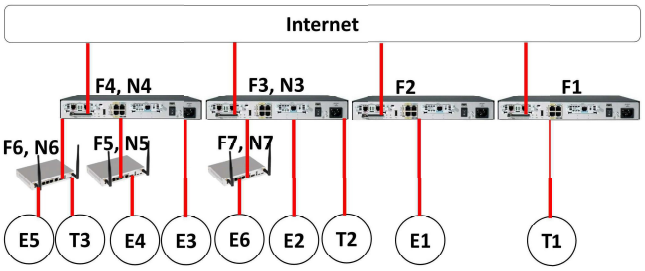

Fig. 3: Technicians and experts location inside the network.

NAT $(F4, N4)$, $T3$ is behind another second-level NAT $(F6, N6)$ that is also behind the same first-level NAT $(F4, N4)$);

- Both peers are connected to multiple-level NAT and to the same second-level NAT ($E5$ and $T3$ are behind the second-level NAT $(F6, N6)$ that is behind the first-level NAT $(F4, N4)$);
- Both peers are connected to multiple-level NAT but neither to the same second-level NAT nor to the same first-level NAT ($T3$ is behind the second-level NAT $(F6, N6)$ which is behind the first-level NAT $(F4, N4)$, $E6$ is behind another second-level NAT $(F7, N7)$ that is behind another first-level NAT $(F3, N3)$);

The objective is to allow each technician and expert to communicate over the optimal multimedia channels.

IV. Description of the Proposed Solution

The proposed solution exploits all techniques listed in the previously section to deal with all possible situations and find the best way to enable communication between technicians and experts. As Figure 4 illustrates, ALG platform is integrated on each peer, STUN and TURN servers are setup on each NAT level, and a rendezvous server (or signaling server) is setup on Internet, called RDV in figure 4. The configuration of each terminal (technician and expert) with IP address and port of each server is done manually. It is noted that ALG platform in the proposed solution should implement all the protocols of UPnP-IGDP, NAT-PMP, PCB in addition to those of classical ALG.

To illustrate how channels establishment is done, we assume that the port mapping on each NAT is as shown in Table I. This table gives information on channels (TCP or UDP) that can be opened by each peers (one channel by technician Ti or expert Ei). This configuration will be used as illustrative examples in the rest of this section.

As a general rule, if *Peer A* wants to receive data from *Peer B*, it opens a channel and sends its parameters to *Peer B*. However, if *Peer A* cannot open the channel because of NAT behavior or firewall configuration, it asks *Peer B* to initiate communication. If it is impossible to open a direct channel, both *peers A* and *B* communicate over the TURN server. Generally, *Peer A* cannot open a channel when the firewall denies incoming UDP datagrams (datagrams from peers never communicated with *Peer A*) and incoming TCP connections.

A. Possible technician-expert location cases

Some distinguishable cases that a technician Ti and an expert Ei can face aiming to establish channels between them are given in what follows. Other cases are not cited because each of them is similar to the presented ones; for example, $(T1, E3)$ is similar to $(T1, E2)$, $(T1, E5)$ is similar to $(T1, E4)$, $(T1, E6)$ is similar to $(T1, E4)$, $(T2, E1)$ is similar to $(T1, E2)$, $(T2, E5)$ is similar to $(T2, E4)$, $(T2, E6)$ is similar to $(T2, E4)$, $(T3, E1)$ is similar to $(T1, E4)$ and finally $(T3, E2)$ is similar to $(T2, E4)$.

1) Communication between $T1$ and $E1$: Both peers $T1$ and $E1$ are behind a firewall without NAT and both have a public IP address. First, each of them uses ALG algorithms to check unusable opened ports in the firewall; if no opened port exists, they try to open ports for each channel (TCP or UDP depending on the channel). If ALG algorithms does not work, each peer uses the servers STUN1 and STUN2 to make hole punching:

- *Both peers made a TCP and UDP hole punching*: each peer sends the parameters of each channel to the other peer;
- *Only one peer made a TCP or UDP hole punching*: the corresponding peer opens channel required by both peers ($T1$ and $E1$) and sends these parameters to the other one. The second peer uses the channel reserved for it to receive data and the other channel to send data;
- *Only UDP hole punching is made*: if only UDP channels can be opened, both peers use SCTP for reliable channels rather than TCP;
- *Both peers could not make neither TCP nor UDP hole punching*: in this case, each peer allocates channel in TURN1 server and sends the allocated channels parameters (within local IP address and port of each channel) to the other peer. The communication between peers and TURN1 can be done over UDP or TCP depending on the channel usage (reliable or not) and the possibility of UDP use.

It is noted that in case of direct communication between the application $T1$ and $E1$ is possible, each of them knows that it has public IP address and port. Thus, it sends only public IP address and port (local IP address and local port) for each channel; in this example, $T1$ sends $41.77.180.1 : 1000$ and $E1$ sends $41.77.180.2 : 4000$ for the corresponding channel in the example.

2) Communication between $T1$ and $E2$: The particularity of this case compared to the previous one is that $E2$ is behind a NAT. When it makes a hole punching, it retrieves two parameters of each channel: (*i*) private IP address and private port (in the illustrative example, $10.0.0.2 : 5100$), and (*ii*) public IP address and public port ($41.77.180.3 : 5000$). First, $T1$ tries to reach $E2$ using the private IP address and private port. In this case, the operation will fail because $T1$ and $E2$ are not connected to the same sub-network; thus, $T1$ uses the public IP address and public port.

ISSN 1737-9334

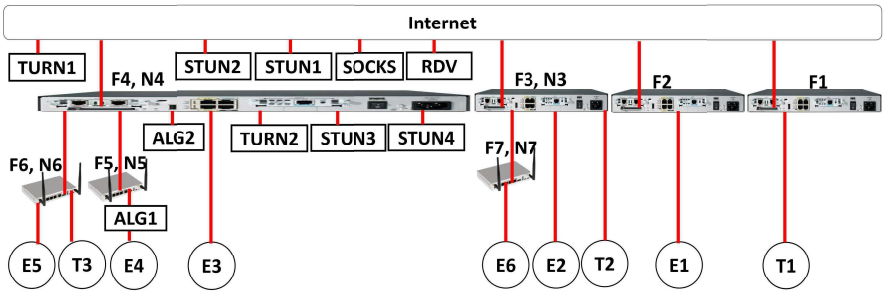

Fig. 4: Description of the proposed solution.

TABLE I: Configuration of the network illustrated in Figure 4

Peers	First-level NAT				Second-level NAT			
	Inside		Outside		Inside		Outside	
	IP address	Port	IP address	Port	IP address	Port	IP address	Port
T1	41.77.180.1	1000	41.77.180.1	1000	-	-	-	-
T2	10.0.0.1	2100	41.77.180.3	2000	-	-	-	-
T3	192.168.0.1	3100	10.0.0.5	3200	10.0.0.5	3200	41.77.180.4	3000
E1	41.77.180.2	4000	41.77.180.2	4000	-	-	-	-
E2	10.0.0.2	5100	41.77.180.3	5000	-	-	-	-
E3	10.0.0.3	7100	41.77.180.4	7000	-	-	-	-
E4	192.168.0.2	8100	10.0.0.4	8200	10.0.0.4	8200	41.77.180.4	8000
E5	192.168.0.3	9100	10.0.0.5	9200	10.0.0.5	9200	41.77.180.4	9000
E6	192.168.0.4	10100	10.0.0.6	10200	10.0.0.6	10200	41.77.180.1	10000

3) Communication between $T1$ and $E4$: In this case, $E4$ is behind a two-level NAT; so, it can use ALG1 or STUN3 and STUN4 to make a hole punching on the first-level NAT $(F5, N5)$ and ALG2 or STUN1 and STUN2 to make a hole punching on the second-level NAT $(F4, N4)$. Thus, $E4$ retrieves three parameters for each channel: local IP address and port $(192.168.0.2 : 8100)$ offered by the second-level NAT, IP address and port $(10.0.0.4 : 8200)$ offered by the first-level NAT, and the public IP address and public port $(41.77.180.4 : 8000)$. $T1$ tries to reach $E4$ using its local parameter which will fail because they are not connected the same second-level NAT; therefore, $T1$ tries to reach $E4$ using the first-level NAT parameters that will also fail, and finally $T1$ reaches $E4$ using public parameters.

In case $E4$ cannot make a hole punching in the second NAT and $T1$ cannot make a hole punching on the firewall, the communication will be done over TURN1.

4) Communication between $T2$ and $E2$: The peers $T2$ and $E2$ are connected to the same NAT. Each of them sends its local parameters of each channel $(10.0.0.1 : 2100$ for $T2$, $10.0.0.2 : 5100$ for $E2)$ and the public parameters $(41.77.180.3 : 2000$ for $T2$, $41.77.180.3 : 5000$ for $E2)$ or TURN1 parameters depending on the possibility to make a hole punching. Both peers $T2$ and $E2$ guess that they are connected to the same NAT; this is because their local IP addresses are similar. In such a case, they will try to communicate over local parameters because they are connected to the same NAT $(F3, N3)$; here, the communication successes and they will not need to use other parameters.

5) Communication between $T2$ and $E3$: As the same situation as in case of $T2$ and $E2$, $T2$ and $E3$ send their local and global (or TURN1) parameters $(10.0.0.1 : 2100$ and $41.77.180.3 : 2000$ for $T2$; $10.0.0.3 : 7100$ and $41.77.180.4 : 7000$ for $E3)$. They try to use local parameters to communicate but they will fail because $T2$ and $T3$ are not in the same local network even local IP addresses are similar. In such a case, they will make use of global parameters or server TURN1 depending on NATs configuration $(F3, N3)$ and $(F4, N4)$.

6) Communication between $T2$ and $E4$: This case is similar to that of $T1$ and $E4$. However in this case, $T2$ has two parameters $(10.0.0.1 : 2100,\ 41.77.180.3 : 2000)$ and $E4$ has three parameters $(192.168.0.2 : 8100,\ 10.0.0.4 : 8200,\ 41.77.180.4 : 8000)$ for each channel. $T2$ and $E4$ do not communicate using local parameters of $E4$ because they are not similar to that of $T2$. However, they try to communicate over local parameters of $T2$ because its IP address is similar to that offered by the NAT $(F4, N4)$ to $E4$ ($(F4, N4)$ is the first-level NAT of $E4$); this communication will fail because the two peers $T2$ and $E4$ are not connected to the same NAT. The fact that IP address offered by NAT $(F4, N4)$ to $E4$ and local IP address of $T2$ are similar, $E4$ concludes that they are both connected to the NAT $(F4, N4)$. As a consequence, it tries to establish the communication over TURN2 by allocating channels and sending their parameters to $T2$; unfortunately, the connection of $T2$ to the server TURN2 will also fail. Consequently, they can only communicate over public parameters or server TURN1.

7) Communication between $T3$ and $E3$: When $T3$ and $E3$ exchange the parameters of opened channels over the server

ISSN 1737-9334

RDV, they discover that the local IP address of $E3$ (10.0.0.3) is similar to that offered to $T3$ (10.0.0.5) by NAT $(F4, N4)$. If they cannot communicate with each other directly, they will try to use the server TURN2. In this case, they can communicate over TURN2 because they are all connected to the same NAT. Therefore, they do not need to use neither public nor TURN1 parameters.

8) Communication between $T3$ and $E4$: Both $T3$ and $E4$ are behind multiple-level NAT. When each of them receives parameters of channels opened by the other one, they conclude that they are connected to the same NAT because their local IP addresses are similar (92.168.0.1 for $T3$, 192.168.0.2 for $E4$). However, they cannot communicate via local parameters because they are not connected to the same NAT ($T3$ is connected to $(F6, N6)$ and $E4$ is connected to $(F5, N5)$); additionally, they cannot communicate over the local server TURN because there is no TURN server at this level. Per contra, they can communicate over parameters offed by the NAT $(F4, N4)$ because they have similar IP addresses (10.0.0.5 for $T3$, 10.0.0.4 for $E5$) and both peers are connected to the same NAT. If the NATs $(F5, N5)$ and $(F6, N6)$ do not allow hole punching, $T3$ and $E4$ will communicate over TURN2.

9) Communication between $T3$ and $E5$: $T3$ and $E5$ are connected to the same second-level NAT. In such a case, when they receive the parameters of opened channels and try to communicate over local parameters as they have similar IP addresses (192.168.0.1 for $T3$, 192.168.0.3 for $E5$), the communication will obviously succeed because both are connected to the same second-level NAT $(F6, N6)$ and they will not need to use other parameters.

10) Communication between $T3$ and $E6$: Both $T3$ and $E6$ are connected to the multiple-level NAT. However, they are not behind the same first-level NAT ($T3$ is behind NAT $(F4, N4)$ and $E6$ is behind NAT $(F3, N3)$). Thus, the only way to communicate is over public parameters ($41.77.180.4 : 3000$ for $T3$, $41.77.180.1 : 10000$ for $E6$) or over the server TURN1.

B. Discussion

It can be noticed that the proposed peer-to-peer communication approach takes a great advantage from the possibility of reconfiguring the network devices (such as NAT and Firewall) and locating the expert and the technician inside the network. Additionally, knowing that our solution is attended to operate in private environments, reconfiguring some network devices is not forbidden.

V. Conclusions and future works

This paper presented the development of a real-time communication module between technician and expert stations for an e-maintenance platform using application and signaling servers. This module takes into account the network configuration to offer best performances, mainly NAT traversal. Normalized technique for NAT and firewall traversal are listed; some of them require NAT and firewall reconfiguration while others do not. The paper also listed the cases where technicians and experts can be located on the network. For each case, a procedure is proposed to allow technicians and experts to communicate with each other. It is clear that this solution allows forwarding data over the best path between expert and technician terminals. This is advantageous, especially when both of them are located in the same private network.

Future perspectives will aim to extend this solution for e-health applications while taking into account WHO recommendations.

References

[1] B. Mechin, *Maintenance: concepts et définitions*. Ed. Techniques Ingénieur, 2007.
[2] R. Kour, R. Karim, A. Parida, and U. Kumar, "Applications of radio frequency identification (rfid) technology with emaintenance cloud for railway system," *International Journal of System Assurance Engineering and Management*, vol. 5, no. 1, pp. 99–106, 2014.
[3] A. Rachidi, B. Dakkak, A. Talbi, and A. Khatory, "La réalité augmentée au service de télémaintenance et de e-maintenance industrielle."
[4] B. Ford, P. Srisuresh, and D. Kegel, "Peer-to-peer communication across network address translators." in *USENIX Annual Technical Conference, General Track*, 2005, pp. 179–192.
[5] "Nat traversal," https://en.wikipedia.org/wiki/NAT_traversal#Techniques, wikipedia.
[6] D. Wing, P. Matthews, R. Mahy, and J. Rosenberg, "Session traversal utilities for nat (stun)," 2008.
[7] M. Leech, M. Ganis, Y. Lee, R. Kuris, D. Koblas, and L. Jones, "Rfc 1928: Socks protocol version 5," RFC, IETF, March, Tech. Rep., 1996.
[8] P. Matthews, R. Mahy, and J. Rosenberg, "Traversal using relays around nat (turn): Relay extensions to session traversal utilities for nat (stun)," 2010.
[9] M. Boucadair, R. Penno, and D. Wing, "Universal plug and play (upnp) internet gateway device-port control protocol interworking function (igd-pcp iwf)," 2013.
[10] S. Cheshire, M. Krochmal, and K. Sekar, "Nat port mapping protocol (nat-pmp)," *Work in Progress*, 2008.
[11] A. Ripke, J. Quittek, R. Silva, T. Dietz, and R. Winter, "Port control protocol (pcp) third-party id option," 2016.
[12] P. Srisuresh and M. Holdrege, "Ip network address translator (nat) terminology and considerations," 1999.
[13] J. Rosenberg and C. Holmberg, "Interactive connectivity establishment (ice): A protocol for network address translator (nat) traversal," 2018.
[14] A. Bergkvist, D. C. Burnett, C. Jennings, A. Narayanan, and B. Aboba, "Webrtc 1.0: Real-time communication between browsers," *Working draft, W3C*, vol. 91, 2012.
[15] S. Benbelkacem, N. Zenati-Henda, F. Zerarga, A. Bellarbi, M. Belhocine, S. Malek, and M. Tadjine, "Augmented reality platform for collaborative e-maintenance systems," in *Augmented reality-some emerging application areas*. IntechOpen, 2011.
[16] M. Fritscher, F. Sittner, D. Aschenbrenner, M. Krauß, and K. Schilling, "The adaptive management and security system for maintenance and teleoperation of industrial robots," *IFAC-PapersOnLine*, vol. 49, no. 30, pp. 6–11, 2016.
[17] S. Benbelkacem, N. Zenati-Henda, H. Belghit, A. Bellarbi, and S. Otmane, "Extended web services for remote collaborative manipulation in distributed augmented reality," in *2015 3rd International Conference on Control, Engineering & Information Technology (CEIT)*. IEEE, 2015, pp. 1–5.
[18] D. Mourtzis, A. Vlachou, and V. Zogopoulos, "Cloud-based augmented reality remote maintenance through shop-floor monitoring: a product-service system approach," *Journal of Manufacturing Science and Engineering*, vol. 139, no. 6, p. 061011, 2017.
[19] S. Bottecchia, J.-M. Cieutat, and J.-P. Jessel, "T.A.C: Augmented Reality System for Collaborative Tele-Assistance in the Field of Maintenance through Internet." in *AH'2010 (Augmented Human)*, Apr. 2010, pp. 1–7, iSBN: 978-1-60558-825-4. [Online]. Available: https://hal.archives-ouvertes.fr/hal-00585435
[20] "Live networks, inc," http://www.live555.com/, Live Networks, Inc.
[21] D. Fang, H. Xu, X. Yang, and M. Bian, "An augmented reality-based method for remote collaborative real-time assistance: from a system perspective," *Mobile Networks and Applications*, pp. 1–14, 2019.

ISSN 1737-9334

Modeling and performance analysis of a solar Photovoltaic Panels - Using Matlab/Simulink

Halim EDDAHBI[1], Mohamed KHAFALLAH[2]
Energy and Electricals Systems Laboratory
Hassan II University of Casablanca, ENSEM
Casablanca, Morocco
[1]halim.eddahbi@gmail.com
[2]mohamed.khafallah@univh2c.com

Abstract— ***This paper presents a modeling and simulation, in Matlab/Simulink environment of Photovoltaic (PV) arrays. The main objective here is to achieve a circuit based simulat ion model of a Photovoltaic (PV) cell in order to estimate the electrical behavior of the practical cell with respect to change in environmental parameters like irradiation and temperature. The modeling of PV array serve as a fundamental component for any research activity related with PV system. The results reveal that the array output is nonlinear in nature and nearly constant current up to open circuit voltage and the power has maximum pick with respect to the voltage for particular environmental condition.***

Keywords-Photovoltaic (PV), Solar panel, maximum power point (MPP), Maximum Power Point Tracking (MPPT), Modeling, Simulation, MATLAB

Nomenclature:

Ipv: Solar cell current (A).
Vpv: Solar cell output voltage (V).
Io: Diode saturation current (A).
Rs: Solar cell series resistance (Ω).
Eg: Energy band gap (ev).
n: Ideality factor (between 1 and 2).
q: Electron charge (°C).
k: Boltzmann constant (J/K).
G: irradiance (W/m²).
T: Cell temperature in Kelvin (K).
Tref: Reference cell temperature (K)
I_L: Light generated current (A).
Icc: Short circuit current (A).
Voc: Open circuit voltage (V).

I. INTRODUCTION

The solar radiation seems to be one of the most promising renewable energy sources and can be directly converted into electricity using the photovoltaic (PV) devices, solar cells. Photovoltaic panels are the fundamental power conversion unit. For given environmental conditions, there is Maximum Power Point (MPP), an operating point on the V-I characteristics, where maximum power output is achieved. Therefore, at the MPP the efficiency will be optimized. There are lots of researches about proposing the MPP tracking algorithms and designing the MPP tracker [1], [2], [3]. The ability to protect output characteristics of a photovoltaic module is very important for the design of MPP tracking and control strategy. Numerous methods have been proposed for modeling the PV panel and extracting the panel's parameters [4]. The performance of the PV panels is evaluated under standard test condition (STC), where an average solar spectrum at AM1.5 is used [5], the irradiation of 1000W/m² and the module temperature of 25°C .

In this paper, a photovoltaic panel modeling method and simulation will be presented. The parameters for the PV model are based on values provided from the manufacturer's datasheet. The proposed model is similar to a single diode model with a series resistance. But the parameters used in proposed model are obtained from only the datasheet measured at STC and the model does not need iteration routine to extract the parameters of I-V characteristics. So, this model is suitable for ISF modeling and Matlab/Simulink modeling when developing and designing MPPT algorithm. This paper also provides the Simulink modeling of the photovoltaic model performance and some simulation results.

II. OPERATION OF A PV CELL

There are different techniques for the direct conversion of sunlight into electricity, the best known is the photovoltaic conversion made using semiconductor materials such as silicon (Si), germanium (Ge) selenium (Se) where the semiconductor compounds such as gallium arsenide (GaAs), cadmium telluride (CdTe). GaAs solar cells are very expensive in their manufacture, their use is today mainly limited to space applications.

The majority of Photovoltaic cells are made from crystalline silicon because it has the characteristic of being non-toxic unlike cadmium or selenium, in addition, it achieves remarkable conversion efficiencies, it constitutes about 28% of the bark terrestrial in the form of compounds (silicates, silica), making it an almost inexhaustible source.

The semiconductor solar cell is a device for delivering an electric current into an external load when it is exposed to light. Its operating principle is as follows:

When the cell is exposed to solar radiation, photons of energy (Eph = hv) penetrating the solar cell transmit their energy to the atoms of the junction. If this energy is sufficiently high, it can pass the electrons of the valence band to the conduction band of the semiconductor material and thus create electron-hole pairs.

ISSN 1737-9334

The electrons (charges N) and the holes (charges P) are then kept separated by an electric field which constitutes a potential barrier. If a charge is placed across the cell, the electrons in zone N join the holes in zone P via the external connection, giving rise to a potential difference and an electric current flows. Figure1

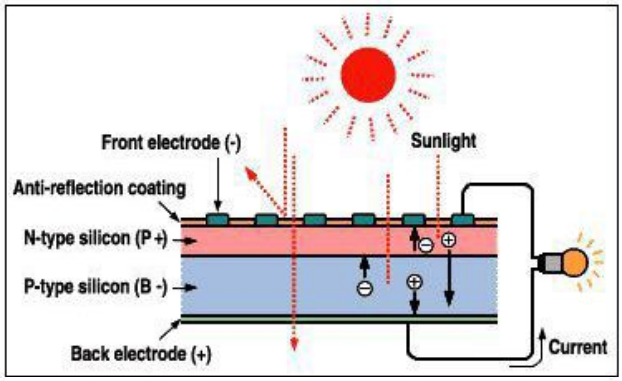

Fig 1: Physical structure of PV cell

III. SOLAR RADIATION

The sun is a star among many others. It has a diameter of 1390000 km, about 50 times that of the earth. It is composed of 80% hydrogen, 19% helium and 1% of a mixture of 100 elements, almost all the chemical elements known since Langevin and Perrin, based on the theory of relativity. Einstein, came up with the idea about 60 years ago that it is nuclear fusion energy that gives the sun its power, it is now admitted that the sun is a hydrogen thermonuclear bomb .

Helium transforming every second 564 million tons of hydrogen into 560 million tons of helium, the reaction being in its core at a temperature of about 25 million degrees Celsius. Thus, every second, the sun is lightened by 4 million tons dispersed in the form of radiation.

Its light, at a speed of 300000 km / s, takes about 8 minutes to reach the earth, its spectral distribution of the atmosphere is presented a maximum for a wavelength of about 0.5 µm, the black body temperature on the surface of the sun is about 5780 ° k [4]

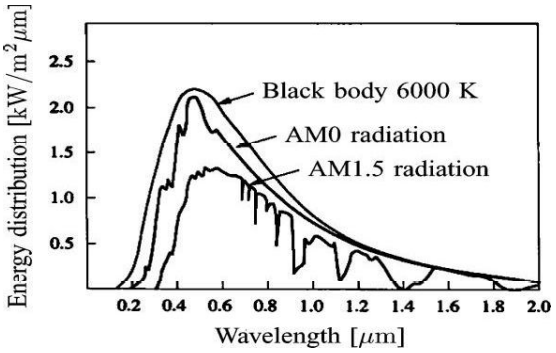

Fig. 2. Spectral distribution of the black body radiation and the Sun radiation in the extraterrestrial space (AM0) and on Earth's surface (AM1.5). [6]

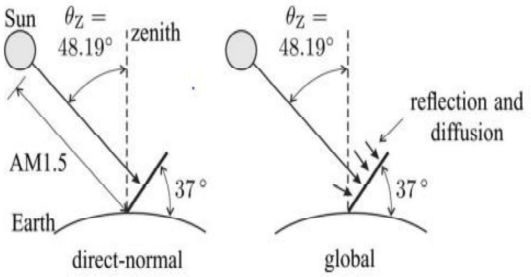

Fig. 3. Illustration of the AM1.5 path and the direct-normal and global incident radiations on a Sun-facing surface at 37◦ tilt.

IV. PV GENERATOR MODELING

A. Ideal PV Cell

In the literature, a photovoltaic cell is often depicted as a current generator with a behavior equivalent to a current source shunted by a diode. To take into account real phenomena, model is completed by two resistors in parallel and series *Rs* and *Rp* as shown in figure 4 .

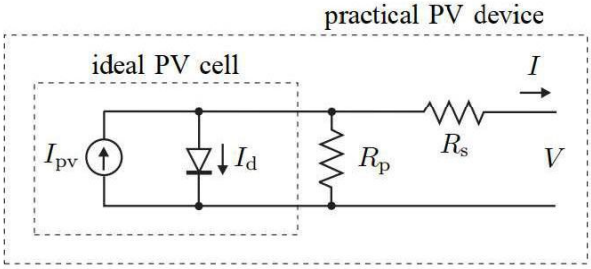

Fig. 4: PV generator model with a single diode and two resistors

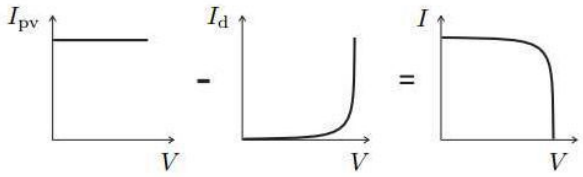

Fig 5: Characteristic I-V curve of the photovoltaic cell. The net cell current I is composed of the light-generated current Ipv and the diode current Id.

The basic equation from the theory of semiconductors that mathematically describes the I–V characteristic of the ideal PV cell is

$$I = I_{pv,cell} - I_d \quad (1)$$

$$I_d = I_{0,cell}\left[exp\left(\frac{qV}{akT}\right) - 1\right] \quad (2)$$

$$I = I_{PV,cell} - I_{0,cell}\left[exp\left(\frac{qV}{akT}\right) - 1\right] \quad (3)$$

where Ipv,cell is the current generated by the incident light (it is directly proportional to the Sun irradiation), Id is the Shockley diode equation, Io, cell is the reverse saturation or leakage current of the diode, q is the electron charge

ISSN 1737-9334

($1.60217646 \times 10^{-19}$ C), k is the Boltzmann constant ($1.3806503 \times 10^{-23}$ J/K), T (in Kelvin) is the temperature of the p–n junction, and a is the diode ideality constant

B. Modeling the PV Array

The PV field consists of modules connected in series and in parallel to obtain the desired power. Each module is itself composed of cells. For the modeling of the PV field, we will therefore start from the basic element which is the cell.

Nowadays there are several electric models of the cell: one model has a diode, two diodes, and three diodes.

The diode model offers a good compromise between simplicity and precision: it seems very suitable for our study. This model consists of photo-current, diode, parallel resistance, and series resistance .

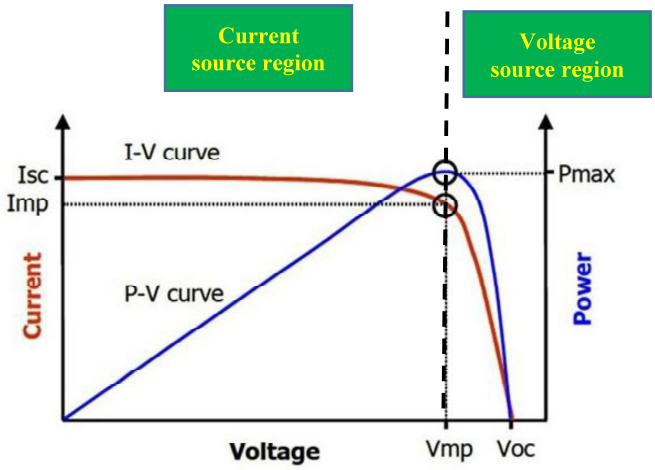

Fig. 6: Characteristic I–V and P-V curve of a practical PV device and the three remarkable points: short circuit (0, Isc), MPP (Vmp , Imp), and open circuit (Voc , 0).

The equation of the current characteristic of the solar cell is given by equation (4)

$$I = I_{pv} - I_0 \left[exp\left(\frac{V+R_s I}{aV_t}\right) - 1 \right] - \frac{V+R_s I}{R_p} \qquad (4)$$

where Iph is the photo-current, Io the saturation current, Rs the series resistance of the cell, Rp the parallel resistance of the cell, a the ideality factor of the diode and Vt is the thermal voltage.

The photovoltaic current Ipv is linearly dependent on the irradiance (G) and is also influenced by the temperature T according to the following equation:

$$I_{pv} = \left(I_{pv,n} + K_I \Delta T\right) \frac{G}{G_n} \qquad (5)$$

is the photovoltaic current generated at nominal conditions (= 298.15 K and 1000 W/m²),.ΔT = T-Tn and Ki coefficient of variation of current as a function of temperature

$$I_{pv,n} = \frac{R_P + R_s}{R_p} I_{sc,n} \qquad (6)$$

The diode saturation current Io and its dependence on the temperature may be expressed by as shown [7], [8], [9]–[10]:

$$I_0 = I_{0,n} \left(\frac{T_n}{T}\right)^3 exp\left[\frac{qE_g}{ak}\left(\frac{1}{T_n} - \frac{1}{T}\right)\right] \qquad (7)$$

where Eg is the bandgap energy of the semiconductor (Eg = 1.12 eV) for the polycrystalline Si at 25 ◦C [11], [7]), and Io,n is the nominal saturation current:

$$I_{0,n} = \frac{I_{sc,n}}{exp\left(\frac{V_{oc,n}}{\alpha V_{t,n}}\right) - 1} \qquad (8)$$

with Vt,n being the thermal voltage of Ns series-connected cells at the nominal temperature Tn .

The saturation current Io of the PV cells that compose the device depend on the saturation current density of the semiconductor

The nominal open-circuit condition, with V = Voc,n , I = 0, and Ipv ≈ Isc,n .

The value of the diode constant a may be arbitrarily chosen. Many authors discuss ways to estimate the correct value of this constant [12], [11]. Usually, $1 \leq a \leq 1.5$ and the choice depends on other parameters of the I–V model.

The PV model described in the previous section can be improved if (7) is replaced by :

$$I_0 = \frac{I_{sc,n} + K_I \Delta T}{exp\left(\frac{V_{oc,n} + K_V \Delta T}{aV_T}\right) - 1} \qquad (9)$$

where: Voc,n corresponds to nominal voltage vacuum and Kv to coefficient of variation of the voltage as a function of temperature.

C. Photovoltaic panel parameters identification

In our case, simulated panels are "ISF240" with a peek power of 240W. Properties of solar panel, according to the technical specification sheet, are shown table I

TABLE I
ELECTRICAL CHARACTERISTICS DATA OF THE ISF240 SOLAR AT 25 °C, 1.5AM, 1000W/M
OF ENERGY AND ELECTRICALS SYSTEMS LABORATORY THE NATIONAL SCHOOL OF ELECTRICITY AND MECHANICS – MOROCCO

Maximum Power (Pmax)	240W
Short-circuit current (Isc)	7.75 A
Open-circuit voltage (Voc)	37.5 V
Voltage at Pmax (Vmp)	30.4 V
Current at Pmax (Imp)	7.91 A
KV) Temperature coefficient of Voc	-0.0036V/K
(KI) Temperature coefficient of Isc	0.0053A/K

Unfortunately, not all the parameters are given in the data sheet. The values for Rs and Rp are missing and have to be found in

ISSN 1737-9334

another way. When taking a look at the formula for the maximum power output, we see that these parameters are easily extractable.

$$P_{max,m} = V_{mp}\left\{I_{pv} - I_0\left[exp\left(\frac{q}{kT} * \frac{V_{mp}+R_s I_{mp}}{aN_s}\right) - 1\right] - \frac{V_{mp}+R_s I_{mp}}{R_p}\right\} \quad (10)$$

$$R_p = V_{mp}\left(V_{mp} + I_{mp}R_s\right)/\left\{V_{mp}I_{pv} - V_{mp}I_0 exp\left[\frac{\left(V_{mp}+I_{mp}R_s\right)}{N_s\alpha}\frac{q}{kT}\right] + V_{mp}I_0 - P_{max,e}\right\} \quad (11)$$

Imp and Vmp are respectively current and voltage of photovoltaic panel at maximum power point. Pmax,m is maximum power deduced via model identification procedure and Pmax,e is the experimental maximum power indicated by the panel manufacturer under nominal conditions

To find Rp value, we have to find a value of Rs so that Pmax,m is equal to Pmax,e This is possible with an iterative algorithm. For this purpose, we can use the procedure described by MG Villalva. [13] and represented by the flowchart in Figure 7.

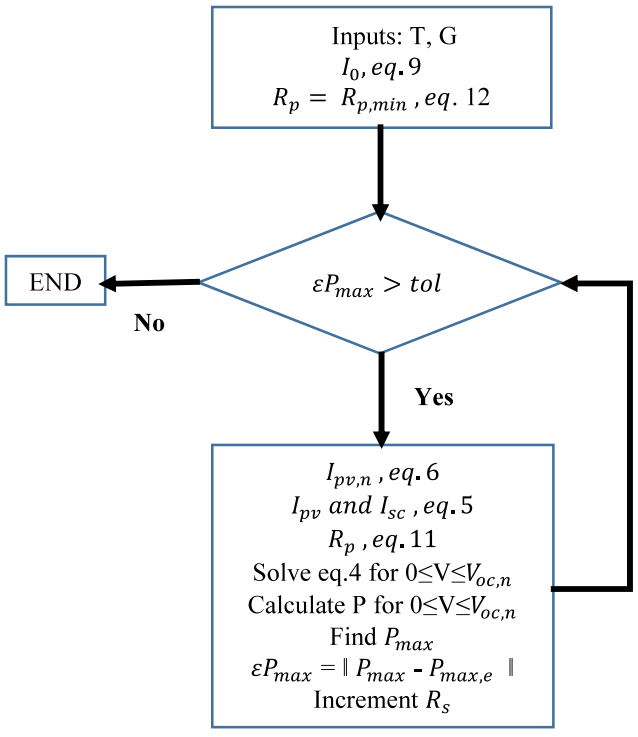

Fig. 7: Iterative algorithm to find the Rs and Rp parameters

To compute this algorithm, initial values for Rs and Rp are needed. The value for Rs,min is fixed to zero and Rp,min is found by substituting Rs by zero in the equation (10):

$$R_{p,min} = \frac{V_{mp}}{I_{sc,n}-I_{mp}} - \frac{V_{oc,n}-V_{mp}}{I_{mp}} \quad (12)$$

Using the procedure, we obtain the following values for Rs and Rp:

Rs = 0.409 Ω and Rp = 158.774 Ω

V. SIMULATION RESULTS

The power system is simulated in Matlab/Simulink power system toolbox software. In this work, the simulation model for the full PV power system components is designed (shown in Figure 8)

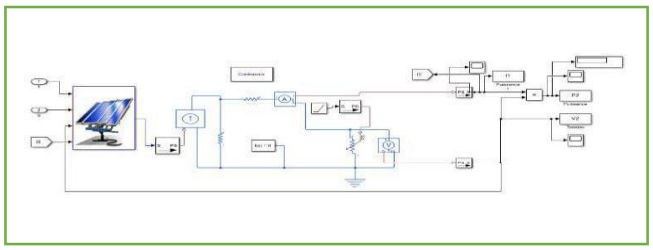

Fig. 8: Schematic of the complete system under Simulink

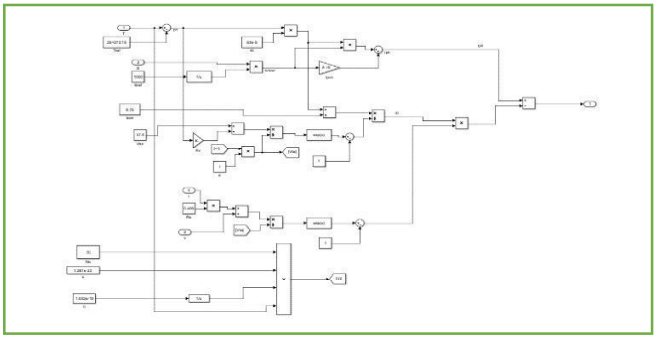

Fig. 9: Model of the equivalent circuit of a PV field under Simulink

Figure (10) shows the evolution of the generated power of the module as a function of the voltage at fixed temperature and illumination. Note that the power increases linearly up to the maximum value (240.1W) and then decreases rapidly.

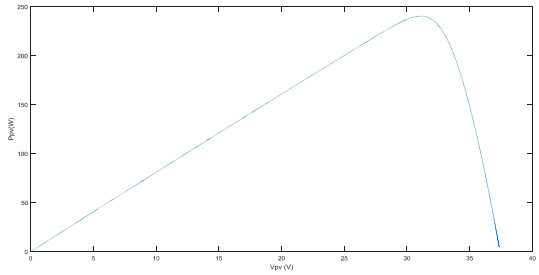

Fig. 10: Evolution panel power as a function of the voltage across

Figure (11) shows the evolution of the generated current of the module as a function of the voltage at fixed temperature and illumination. It is noted that the current remains constant up to V = 30.4V and then decreases rapidly until it is canceled.

ISSN 1737-9334

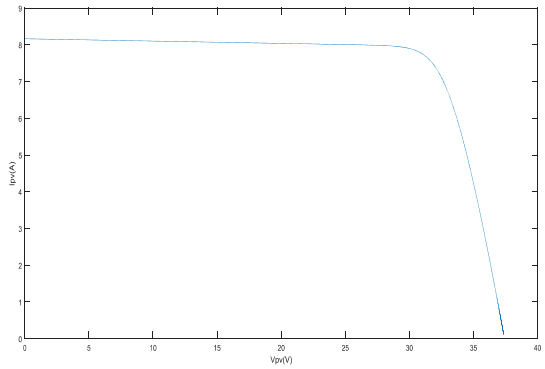

Fig. 11: Evolution of the current generated by the photovoltaic panel as a function of the voltage across

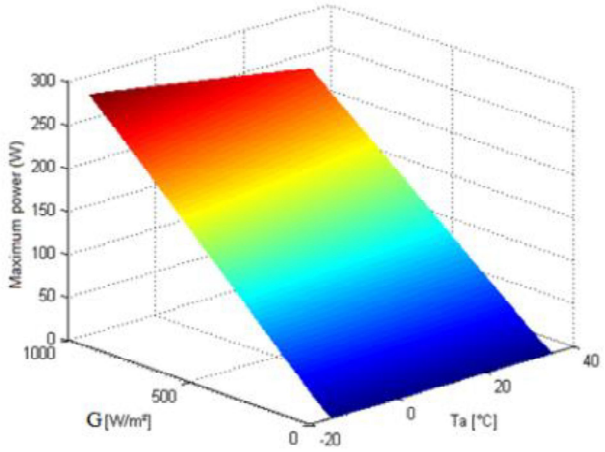

Fig. 12: Evolution of the maximum power of the photovoltaic panel "ISF240" depending on the ambient temperature (Ta) and irradiance (G)

Figure (13) shows the evolution of the power of the module as a function of the voltage at fixed temperature and variable illumination, it is found that the increase in illumination results in an increase in power.

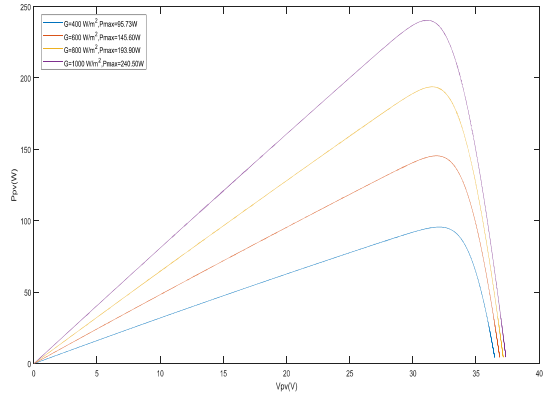

Fig. 13: Effect of the irradiation on P-VPV characteristic of ISF240 PV module at T= 25°C

FIG. (14) shows the evolution of the generated current of the module as a function of the voltage (same variation range) of output at fixed temperature and variable illumination. the increase in illumination causes an increase in the current.

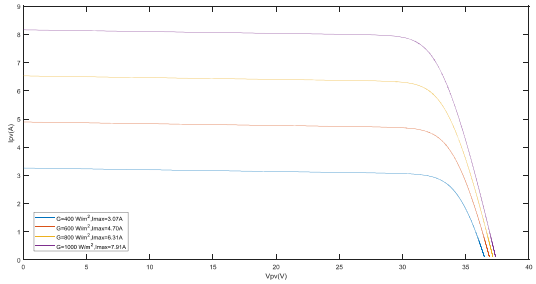

Fig. 14: Effect of the irradiation on I-V PV characteristic of ISF240 PV module at T= 25°C

Figure (15) shows the evolution of the power generated by the module as a function of the voltage at fixed illumination and variable temperature, it is found that the increase in temperature causes a decrease in power, we notice also the maximum voltage reached across the module decreases

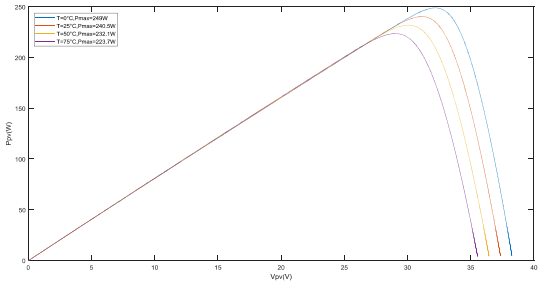

Fig. 15: Effect of the temperature on P-V PV characteristic of ISF240 PV module at G = 1000 W/m²

Figure (16) shows the evolution of the generated current of the module as a function of the voltage at fixed illumination and variable temperature, it is found that the increase in temperature causes a relatively constant current, we also note the maximum voltage reached at the terminals of the module decreases

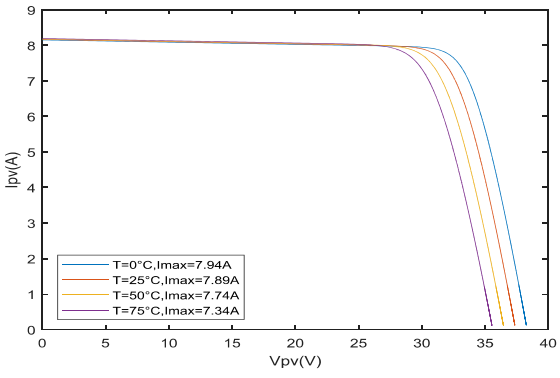

Fig. 16: Effect of the temperature on I-V PV characteristic of ISF240 PV module at G = 1000 W/m²

ISSN 1737-9334

VI. CONCLUSION

In this paper, photovoltaic solar energy comes from the direct transformation of part of the solar radiation into electrical energy. This energy conversion is done by the photovoltaic cell based on a physical phenomenon called photovoltaic effect. Voltage generated may vary depending on the material used to manufacture the cell. The association of several cells in series and / or parallel gives rise to a photovoltaic module which has a nonlinear current-voltage characteristic having a point of maximum power.

The performance of a photovoltaic module is strongly influenced by the climatic conditions, especially the solar irradiation and the temperature of the module. We chose the one-diode model to simulate the operation of the photovoltaic module for different irradiation and temperature conditions. The main interest of this model lies in its simplicity and its ease of implementation from the technical characteristics given by the manufacture .

REFERENCES

[1] T. Esram and P. L. Chapman, "Comparison of photovoltaic array maximum power point tracking techniques," IEEE Trans. Energy Convers., vol. 22, no. 2, pp. 439–449, Jun. 2007

[2] N. Femia, G. Petrone, G. Spagnuolo, and M. Vitelli, "Optimization of perturb and observe maximum power point tracking method," IEEE Trans. Power Electron., vol. 20, no. 4, pp. 963–973

[3] V. Salas, E. Olias, A. Barrado, and A. Làzaro, "Review of the maximum power point tracking algorithms for stand-alone photovoltaic systems," Solar Energy Mater. Solar Cells, vol. 90, no. 11, pp. 1555–1578, Jan. 2006.

[4] W. Xiao, W.G. Dunford, and A. Capal, "A Novel Modeling Method for Photovoltaic Cells," 35th Annula IEEE Power Electronics Specialists Conference, Aachen, Germany, pp.1950-1956, 2004

[5] M.Blhadj ''Modélisation d'un système de captage photovoltaïque autonome '' Mémoire de Magister Centre Universitaire de Bechar 2007-2008

[6] H. J. Moller, ¨ Semiconductors for Solar Cells. Norwood, MA: Artech House, 1993

[7] W. De Soto, S. A. Klein, and W. A. Beckman, "Improvement and validation of a model for photovoltaic array performance," Solar Energy, vol. 80, no. 1, pp. 78–88, Jan. 2006.

[8] Q. Kou, S. A. Klein, and W. A. Beckman, "A method for estimating the long-term performance of direct-coupled PV pumping systems," Solar Energy, vol. 64, no. 1–3, pp. 33–40, Sep. 1998.

[9] R. A. Messenger and J. Ventre, Photovoltaic Systems Engineering. Raton, FL: CRC Press, 2004

[10] K. H. Hussein, I. Muta, T. Hoshino, and M. Osakada, "Maximum photovoltaic power tracking: An algorithm for rapidly changing atmospheric conditions," in Proc. IEE Proc.-Generation, Transmiss. Distrib., Jan. 1995, vol. 142, pp. 59–64

[11] G. Walker, "Evaluating MPPT converter topologies using a matlab PV model," J. Elect. Electron. Eng., Australia, vol. 21, no. 1, pp. 45–55, 2001

[12] C. Carrero, J. Amador, and S. Arnaltes, "A single procedure for helping PV designers to select silicon PV module and evaluate the loss resistances," Renewable Energy, vol. 32, no. 15, pp. 2579–2589, Dec. 2007.

[13] M. G. Villalva, J. R. Gazoli, E. Ruppert F., "Modeling and circuitbased simulation of photovoltaic arrayes", Brazilian Journal of Power Electronics, vol. 14, n° 1, pp. 35-45, 2009

ISSN 1737-9334

Design of a circular SIW second order filter

Imane BADAOUI[#1], Naima AMAR TOUHAMI[*2], Dahbi EL KHAMLICHI[#3]

[#]*Laboratory of Information System and Telecommunications*
Faculty of Sciences, Abdelmalek Essaadi University, MOROCCO
[1]badaoui1987@gmail.com

Abstract—**In this paper a second order circular substrate integrated waveguide filter is presented with integrating some slots shapes to enhance the coupling between the resonators. Good results were achieved in the electromagnetic simulation of a substrate integrated waveguide band pass filter having 0.1dB pass band ripple, the bandwidth of the filter is about 15% the return loss is about 28dB at 9 GHz**

***Keywords*— Substrate integrated waveguide, coupling structures, slots.**

I. INTRODUCTION

Microwave filters play a very important role in telecommunications field whether in receiving or broadcasting in the most popular applications such as mobile communication, GPS, satellite, GE, radar, etc... for this raison, waveguide technology is widely used which immediately gives very high quality in filtering function. [1].

There are many kinds of waveguide filters that are cited and described in literatures among them filters evanescent modes, E-plan filters and Filter resonator-coupled [2][3] which present our case of study. This kind of filters are made of a series of resonators duplicated to achieve high Q filters. Despite the advantages offered by the waveguides, they stay bulky, expansive and difficult to be integrated in planar circuits. Those limitations were the main reason to find a new concept which combines between high performances of waveguides and the compact aspect of planar circuits specially in high frequencies.

Substrate integrated waveguide presents an alternative solution that guarantees a lossless transmission with low cost fabrication and small size [4]. This technology combines the advantages of planar circuits and high performances of the waveguide; it consists of two rows of metallic vias which guarantee a guided transmission of the electromagnetic waves because those rows of vias play a role of metallic walls [5]. Those characteristics make this technology a fertile area to design innovative circuits such as filters couplers power dividers and antennas [6].

Different topologies of filters, including cross-coupled filters can be achieved with this coupling technique [7]–[10]. However, the design of filters with particular electrical responses can be hard to achieve when the only couplings to be used are magnetic ones. For instance, a cross coupling between the first and the third resonators of a third-order filter creates a transmission zero [11] located above the passband when the cross coupling and the direct couplings of the filter are of the same nature. On the other hand, the transmission zero is below the bandpass if they differ. Several methods to achieve electric coupling exists [12], [13], and in this letter, we propose to create a novel topology of mixed coupling between integrated cavities exploited as an electric coupling.

II. SUBSTRATE INTEGRATED WAVEGUIDE CIRCULAR RESONATOR

waveguides are known among the most powerful transmission media, which exist in two famous forms; rectangular and circular. In this part of work a substrate integrated circular cavity will be reported.

The resonant frequency of TE and TM modes for the circular cavity with metallic vias can be calculated by the expressions bellow

$$f_{nmp} = \begin{cases} \frac{C}{2\pi\sqrt{\mu_r \varepsilon_r}} \sqrt{\left(\frac{\mu'_{mn}}{R}\right)^2 + \left(\frac{p\pi}{h}\right)^2} \\ \frac{C}{2\pi\sqrt{\mu_r \varepsilon_r}} \sqrt{\left(\frac{\mu_{mn}}{R}\right)^2 + \left(\frac{p\pi}{h}\right)^2} \end{cases} \quad (1)$$

Where c presents the velocity of light in the vacuum, R is the equivalent radius of the circular cavity

$\mu_r \varepsilon_r$ are respectively the permeability and permittivity of the utilised substrate. In this work the TE010 mode present the dominant mode of the SIW cavity

$$f_{TM010} = \frac{0.383C}{R\sqrt{\mu_r \varepsilon_r}} \quad (2)$$

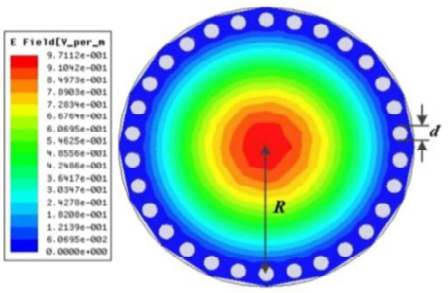

Fig1. The electric field distribution of TM_{10} mode of a circular cavity resonator

ISSN 1737-9334

The proposed filter is based on a x-band circular resonator responding to the required frequency (10Ghz) so the radius of the resonator is calculated by using formula (2). After a parametric study we achieved the results presented in fig.3

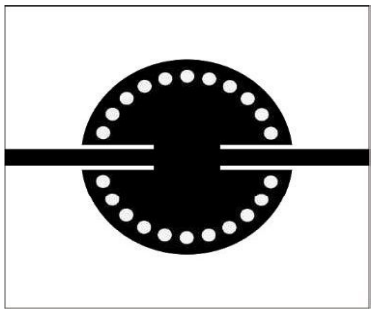

Fig2. Substrate integrated waveguide circular resonator

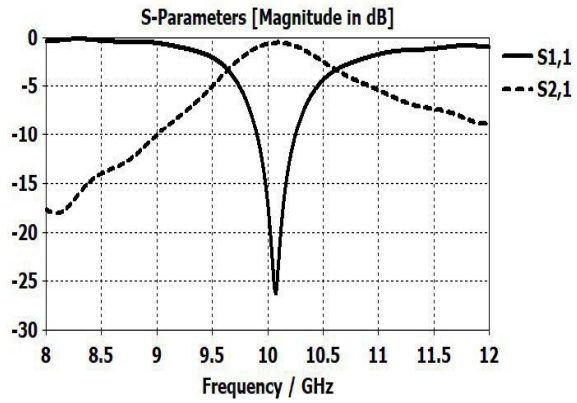

Fig3. Insertion and return loss of SIW circular resonator

III. DESCRIPTION OF THE COUPLING STRUCTURE

The structure and the coupling topology of the proposed SIW second-order filter are shown in Fig4. The RT/duroid 6006, with Ɛr=6.15, tanδ=0.0019 and thickness h=0.635mm, is chosen for all simulations. In this paper with positive coupling between the two resonators.

The I/O feed lines are 50Ω microstrip lines and the coplanar waveguide (CPW) slots are located to convert the quasiTEM mode to TM mode.

The resonators coupling was made from a grounded coplanar line etched on the upper face. This GCPW line is excited by both electric and magnetic fields of the TM mode existing within the circular cavities. There is propagation along the GCPW line, and it causes an excitation of the TM in the second cavity.

The electric field of the TM mode is vertically polarized and it is collinear with a component of the GCPW E-field. The magnetic field of the TM is circular within the cavity; under the line, it is collinear with the H-field of the quasi-TEM mode of the GCPW. Thus, E and H fields are both implicated in the

establishment of the coupling. Between the two cavities in the side wall is required to enable the propagation along the GCPW line.

Fig. 4(a and b) presents respectively the top and the bottom view of the coupling topology between two substrate integrated circular cavities.

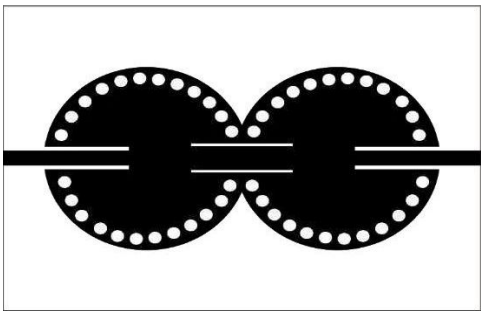

Fig4.(a) Substrate integrated waveguide circular second filter (top view)

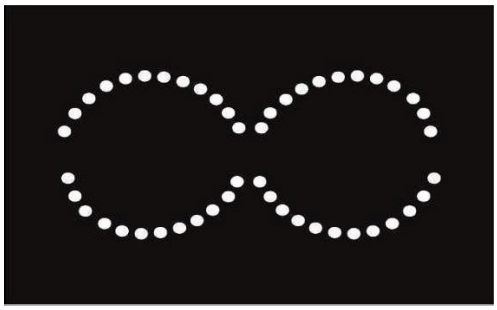

Fig4.(b) Substrate integrated waveguide circular second filter (bottom view)

This coupling was characterized by simulating this structure; the symmetry plan between the two cavities was replaced, at first, with an electric boundary, and then with a magnetic boundary. On condition to respectively denote f and f the resonant frequencies of the whole structure, then the coupling coefficient, is expressed as:

$$k = \frac{f_e^2 - f_m^2}{f_e^2 + f_m^2} \qquad (3)$$

where, in the case of an electric coupling and for a magnetic coupling.

Table 1 present the different parameters of the designed filter:

ISSN 1737-9334

TABLE1: PARAMETERS OF THE DESIGNED FILTER

Parameter	Value (mm)
R	5
P	1
Via-radius	0.4
Slot-length	5
Slot-width	0.3
h	0.653
feed-line	3

After a parametric study of the slot coupling dimensions, we achieved the results presented in Fig5

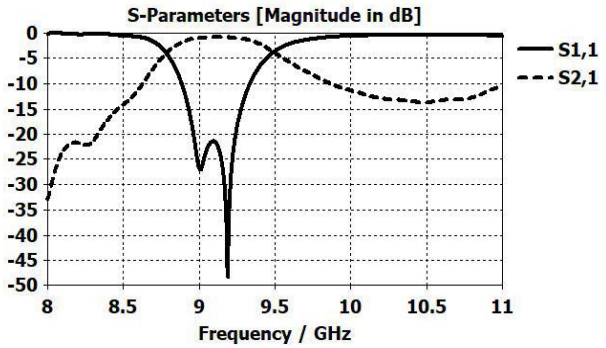

Fig5. Insertion and return loss of SIW second order filter

It can be seen that the results presented in Fig5 are in agreement with our filter specifications, the bandwidth of the filter is about 15%, the insertion loss around f0 = 9.75 GHz is approximately -0.1 dB which due to performant material utilized, the return loss in the pass-band is better than --45 dB.

This filter could be integrated in the received devises of the satellite transponders due to compact size and also for its high Q.

IV. CONCLUSION

Further to the design of the topology of electric coupling introduced in this paper, a second-order filter. Among our perspective is to develop those results by including other resonators to achieve a magnetic in-line couplings and electric cross coupling design then the fabrication process. Moreover, this topology allowed us to get, for the filter, an electrical response characterized by the existence of a transmission zero located below the bandpass. It would have been impossible to meet this specification with a filter using only magnetic couplings. Thus, the introduction of electric couplings is highly beneficial by allowing more possibilities of design.

REFERENCES

[1] Y.Lahcen, T.Abdelwahed, K. Mohamed, Z.Jamal, M.Angel. “Ku-band waveguide bandpass filter with iris radius”. International Conference on. IEEE, p. 1435-1438, Sep 2014.

[2] G. Matthaei, L. Young, L, & Jones, E. M. T. Microwave filters, impedance-matching networks, and coupling structures (Vol. 5). (1964).

[3] N. Marcuvitz "Waveguide Handbook" Peter Peregrinus Ltd On behalf of The Institution of Electrical Engineers, Polytechnic Institute of New Work, 1986

[4] X.Li, Z.Shao, C. Jiang You. “X - band substrate integrated waveguide bandpass filter using novel defected ground structure cell”. Microwave and Optical Technology Letters, vol. 57, no 5, p. 1156-1160, March 2015

[5] Zhan, X., Tang, Z., Wu, Y. Zhang. “Substrate integrated waveguide dual-mode dual-band filter”. Microwave Journal 57, 94–102 March (2014).

[6] W. Che, L. Geng, K. Deng, and Y. L. Chow, "Analysis and experiments of compact folded substrate-integrated waveguide," IEEE Trans. Microw. Theory Tech., vol. 56, no. 1, pp. 88-93, Jan 2008.M. Shell.

[7] J.-S. Hong and M. J. Lancaster, “Couplings of microstrip square open-loop resonators for cross-coupled planar microwave filters,” IEEE Trans. Microw. Theory Tech., vol. 44, no. 12, pp. 2099–2109, Dec. 1996

[8] 44444444444444444444444444444444

[9] 44444444444444444444444444444444

[10] X. Chen, W. Hong, T. Cui, Z. Hao, and K. Wu, “Substrate integrated waveguideelliptic filter with transmissionline insertedinverter,” Electron. Lett., vol. 41, no. 15, pp. 851–852, Jul. 2005.

[11] B. Potelon, J.-C. Bohorquez, J.-F. Favennec, C. Quendo, E. Rius, and C. Person, “Design of Ku band filters based on substrate integrated circularcavities(SICCs),”inIEEEMTT-SInt.Dig,SanFrancisco,CA, Jun. 2006, pp. 1237–1240.

ISSN 1737-9334

Miniaturized koch-fractal Antenna Folded-Slot

Bouchra EZZAHRY[#1], Naima AMAR TOUHAMI[*2], Tajeddin ELHAMADI[#3]

[#]*Abdelmalek Essaadi University, Faculty of Science, BP 2121 M'Hannech II, 93030 Tétouan.*
[1] bouchramebl@gmail.com
[2] Nai_amar@yahoo.fr
[3]tajeddinelhamadi@gmail.com

***Abstract*— In this paper the fractal iteration technique has been applied to obtain the second iterative of folded slot antenna, this fractal antenna has been designed on substrate Rogger RT6002 with dielectric constant =2.94 and substrate thikness h=0.76mm . The simulation and optimisation are performed using CST. The result shows that the operating frequency decrease from 5GHz to 2.6GHz**

***Keywords*— Antenna, fractal, koch, substrate, frequency, folded-slot, return loss, radiation pattern.**

I. INTRODUCTION

Antennas are considered to be the largest components of integrated low-profile wireless communication systems, therefore antenna miniaturization is a necessary task in achieving an optimal design for integrated wireless communication systems. Variety of techniques have been proposed to improve performance of microstrip antennas. These include the use of stacked microstrip antennas, air gaps, compact meandering geometries, fractal-shapes as well as insertion of shorting pins. [1]

Fractals mean broken or irregular fragments. Fractals describe a complex set of geometries ranging from selfsimilar/self-affine to other irregular structure. [2] Fractals are generally composed of multiple copies of themselves at different scales and hence do not have a predefined size which makes their use in antenna design very promising. Fractal antenna engineering is an emerging field that employs fractal concepts for developing new types of antennas with notable characteristics. The unique features of fractals such as self-similarity and spacefilling properties enable the realization of antennas with interesting characteristics such as multi-band operation and miniaturization. [3]

II. PAGE LAYOUT

Koch fractal geometry was originally introduced by a Helge von Koch in 1904. The Koch geometry can be generated using an iterative function system (IFS) represented by a set of affine transformations. The geometric implementation of the Koch iteration technique is fairly straightforward. One starts with a straight line, called the initiator. This is partitioned into three equal parts, and the segment at the middle is replaced with two others of the same length. This is the first iterated version of the geometry and is called the generator. The process is reused in the generation of higher iterations [4], [5].

- Theory of koch fractal technique:

the application of Koch fractal iterations to a folded-slot antenna is done by the following steps:

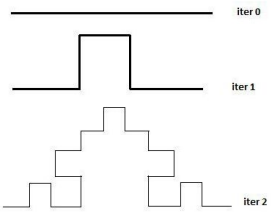

First Koch iteration is applied to a slot of length e by dividing the slot into three segments of length e/3 and replacing the middle segment by three segments of length e/3 intersecting at an angle of 90.

The same process is applied to obtain the second Koch iteration folded-slot antenna.

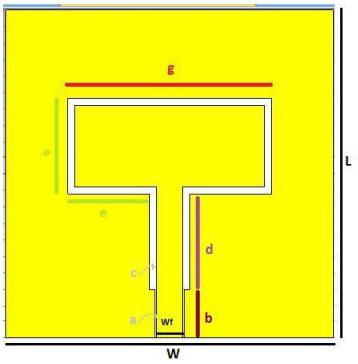

Fig. 1 Schematic layout of a simple folded-slot antenna

dimensions	values	
a	0.1	
b	3	length of CPW feed line
c	0.4	The width of the slot
d	5.8	length of quarter wave transformer.
e	5	the Koch iteration length
g	11.6	
Wf	1.6	The width of CPW feed line

TABLE 1. THE VALUES OF PARAMETERS OF THE ANTENNA

Fig. 1 shows a folded-slot antenna used. it is employed over a single-slot antenna to scale down the radiation resistance and hence enable impedance matching to a 50Ω feed. Originally, we have taken this antenna wich is initiator for the koch fractal, it is printed on only one side of rogger RT6002

ISSN 1737-9334

microwave substrate with the substrate thikness of 0.76mm and the dielectrique constante of 2.94. The antenna is matched to a 50 CPW feed line using a quarter wave transformer of length d. The dimensions are shows on table 1.

This initiator folded-slot antenna is designed on an area of 40 mm × 30 mm to operate at the frequency of 8.24GHz. Fig.3 present the first iteration koch fractal folded-slot antenna and Fig.4 present the second iteration koch fractal folded-slot antenna.

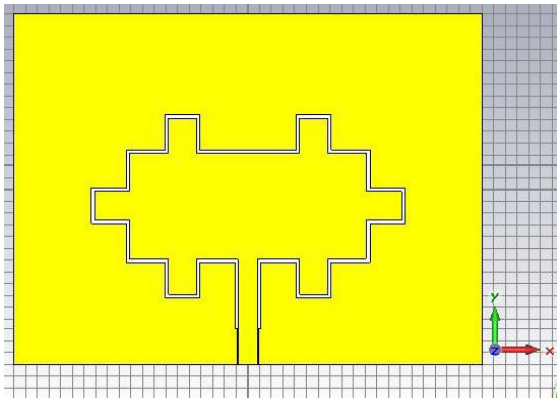

Fig 2. Schematic layout of a simple folded-slot antenna

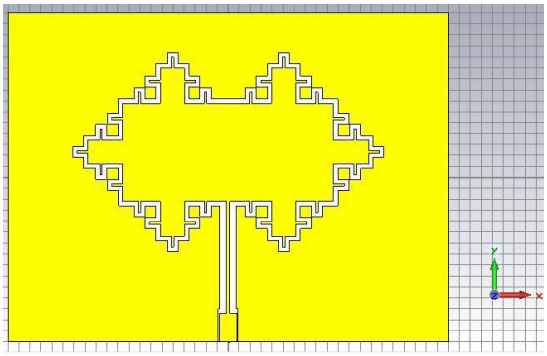

Fig 3. Schematic layout of a simple folded-slot antenna

We used Cst simulate for simulate this fractal sfolded slot antenna, after the simulation we obtain for the simple floded slot antenna, the measured return loss is around 35 dB at the operating frequency of 5 GHz. The bandwidth of the antenna is about 600 MHz.

for the first iteration Koch fractal antenna, the measured return loss is around 16 dB at the operating frequency of 3.6GHz. The bandwidth of the antenna is about 400 MHz. For the second iteration Koch fractal antenna, the measured return loss is about 25 dB at the operating frequency of 2.6GHz. The bandwidth of the antenna is about 100 MHz.

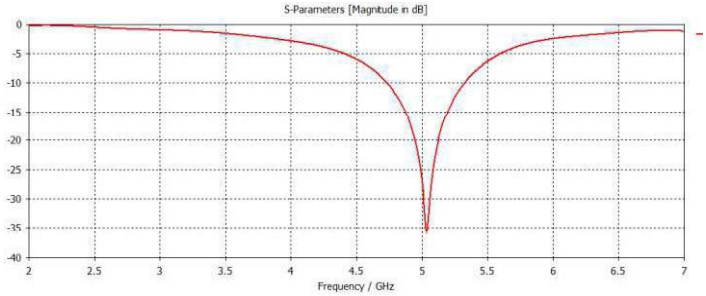

(a)

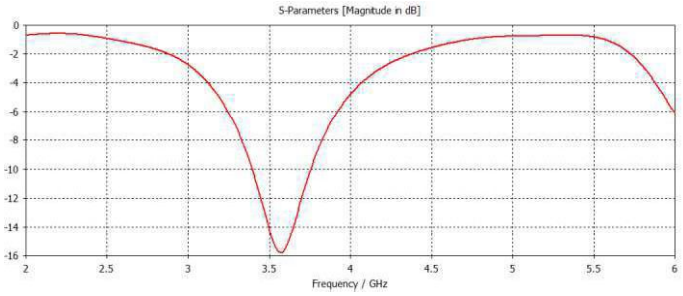

(b)

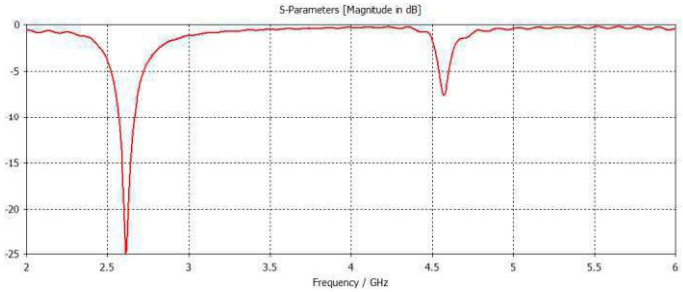

(c)

Fig 4. Return loss for the: (a) simple folded-slot antenna (b) first iteration.(c) second iteration.

The measured radiation patterns for the simple folded-slot, first iteration Koch fractal folded-slot, and second iteration folded-slot antennas measured at the corresponding operating frequencies 5GHz, 3.6GHz and 2.6 GHz, respectively, are shown in Fig. 5.

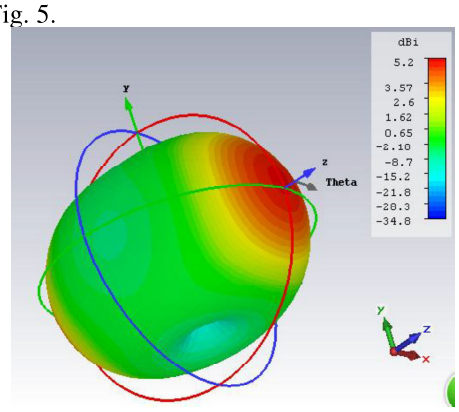

(d)

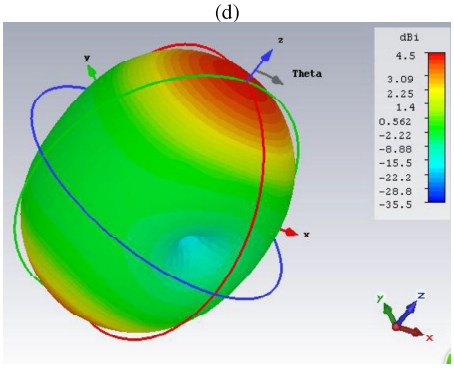

(e)

ISSN 1737-9334

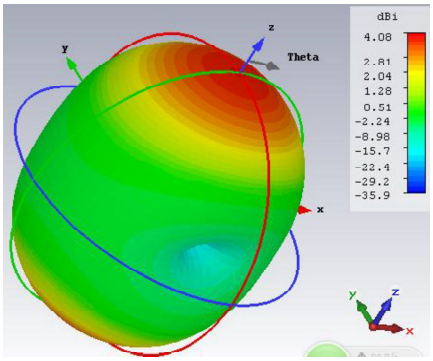

(f)

Fig. 5 Radiation Pattern of fractal antenna: (a) at 5GHz (b) at 3.6 GHz (c) at 2.6GHz

III. CONCLUSIONS

This paper presents the Koch iteration technique has been applied to obtain fractal versions of a folded-slot antenna.

It is shown that for the simple antenna, the measured return loss is around 35 dB at the operating frequency of 5 GHz, for the first iteration Koch fractal antenna, the measured return loss is around 25 dB at the operating frequency of 2.6 GHz and for the second iteration Koch fractal antenna, the measured return loss is about 30 dB at the operating frequency of 7.33 GHz. This result found that the resonant frequency of the fractal antenna lowered greatly from the simple antenna to the 2nd itération of koch fractal antenna.

REFERENCES

[1] [1] Koziel, S., Saraereh, O., Jayasinghe, J. W., & Uduwawala, D. (2017, December). Local optimization of a Sierpinski carpet fractal antenna. In 2017 IEEE International Conference on Industrial and Information Systems (ICIIS) (pp. 1-5). IEEE.

[2] [2] J. Gianvittorio, "Fractal Antennas: Design, Characterization and Applications," Ph.D. dissertation, Dep. Elec. Eng., University of California at Los Angeles, Los Angeles, 2000.

[3] [3] C. Puente, J. Romeu, R. Pous, J. Ramis, and A. Hijazo, "Small but long Koch fractal monopole," Inst. Elect. Eng. Electron. Lett., vol. 34, no. 1, pp. 9–10, Jan. 1998.

[4] [4] D. H. Werner and S. Ganguly, "An overview of fractal antenna engineering research," IEEE Antennas Propagat. Mag., vol. 45, no. 1, pp. 38–57, Feb. 2003.

[5] [5] K. J. Vinoy, "Fractal Shaped Antenna Elements for Wide and Multi-Band wireless Applications," Ph.D. dissertation, Dep. Elec. Eng., Pennsylvania State University, University Park, 2002.

ISSN 1737-9334

Study and design of Microwave oscillator For Wi-Fi application

EL ftouh H. [#1], El Bakkali M.[#1], Amar T. N.[# 1], Zakriti A.[*2], Mchbal A.[#1]

#1Department of physics, Laboratory of Information System and Telecommunication, Abdelmalek Essaâdi, Tetouan Morocco

elftouhhanae@hotmail.fr

Elbakkalimoustapha91@gmail.com

nai_amar@yahoo.f

aicha.mchbal8@gmail.com

**Ensaté*

Abdelmalek Essaâdi, Tetouan Morocco

zakriti.work@gmail.com

***Abstract*— the aim of this paper is to use a new design of a negative resistance microwave oscillator in order to fabricate oscillator with very good performance. In this study the concept of oscillator using distributed resonator and micro -strip circuit elements improve performances of our structure. The oscillator produces a sinusoidal signal of 1.7V amplitude at 2.4 GHz for load impedance of 50 Ω.**

***Keywords*—** *Oscillator, Negative resistance oscillator, Resonator*

I. INTRODUCTION

Oscillator is an electronic device used for the purpose of generating a signal. They are often found in computers, wireless receivers and transmitters, and audio-frequency equipment, and music synthesizers. They provide the signal source for all microwave systems, including both transmitters and receivers.

They can be found in any electronic system since (GSM, radio communication, spacial communication, radar, electronic war and instrumentation) it is up to them to create the electrical signal in different frequency ranges. Then the quality of any system depends directly on the performance of the oscillator. [1]

A microwave oscillator has four separates blocks: Resonator for choosing the frequency of oscillation, a transistor (active device) which operates at the desired frequency, polarization and instability blocks. The block diagram of the microwave oscillator with its different parts is shown in Fig.1. [2]

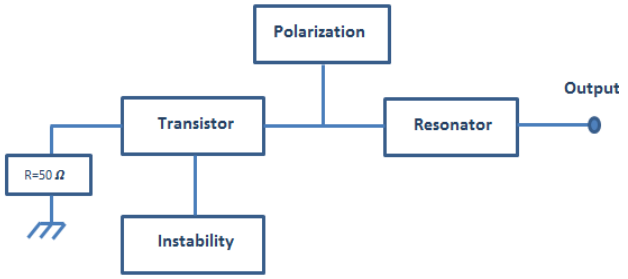

Fig. 1. Block diagram of an oscillator.

II. BIAS NETWORK

Bias network is a component with three ports. A low frequency port used to inject the polarization, a high frequency port, a high frequency port used to inject the radiofrequency signal, and a third used as an output where the radiofrequency plus Direct courant (DC) signal is recovered [3].

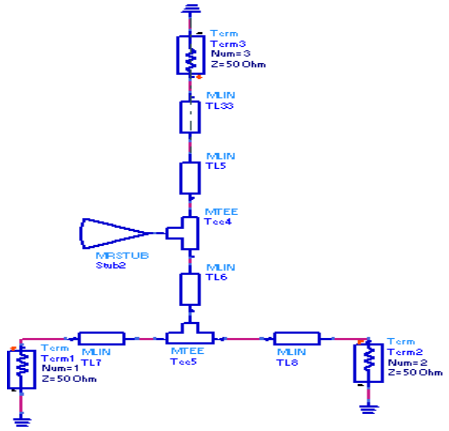

Fig. 2. Polarization circuit.

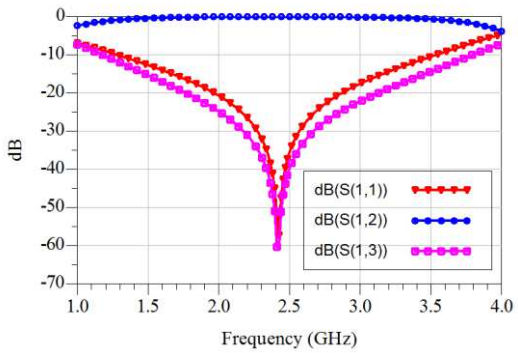

Fig. 3. Evolution of S-parameters as a function of frequency

ISSN 1737-9334

Fig. 3 shows the simulation results of S parameters. We can observe at 2.4GHz the inverse gain S12 is equal to 0 dB, that is to say the signal is transmitted totally S11, with adaptation inferior to -50 dB and isolation S13 for about -60 dB.

III. Study of Stability and Resonator

The S-parameter formulation was introduced by Kurokawa, Brodway and Hauri which states that: for absolute stability [4], two conditions must apply:

$$K<1 \text{ and } B<0$$

K and B are respectively the stability factor and measurement stability:

$$K = \frac{1-|S_{11}|^2-|S_{22}|^2+|S_{11}S_{22}-S_{12}*S_{21}|}{2|S_{12}S_{21}|} > 1$$

$$B=1+|S_{11}|^2-|S_{22}|^2-|\Delta|^2$$

With $\Delta= S_{22}S_{11-} S_{12} S_{21}$

In practice K<1 is taken by the vast microwave community as the condition for absolute stability. [4,5]

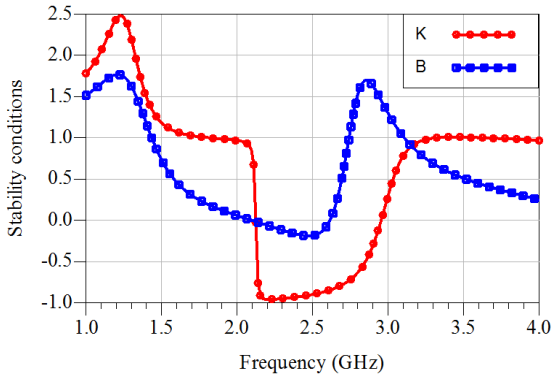

Fig. 4 Frequency response for both of stability factor and stability measure K and B respectively

As shown in Fig. 4, at 2.4 GHz the two conditions are satisfied.

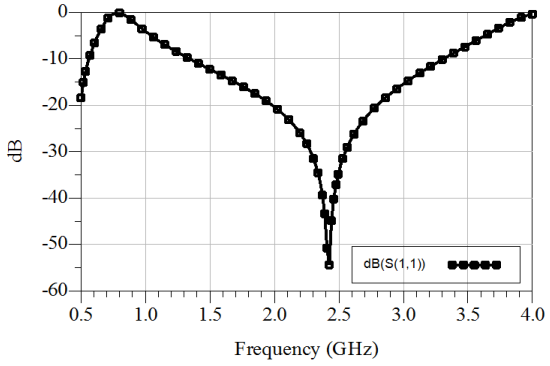

Fig. 5 Simulation of S_{11} parameter

As shown in Fig.5, the simulation of S11 parameter of the proposed resonator is less than -50 dB that shows a very good adaptation. This circuit is used mainly to set the desired frequency to the load

IV. Global Topology of Negative Resistance Oscillator

After analysing each block of the oscillator, Fig.6 shows the final layout of an oscillator capable of generating a signal characterized by a frequency of 2.4 GHz for Wi-Fi application.

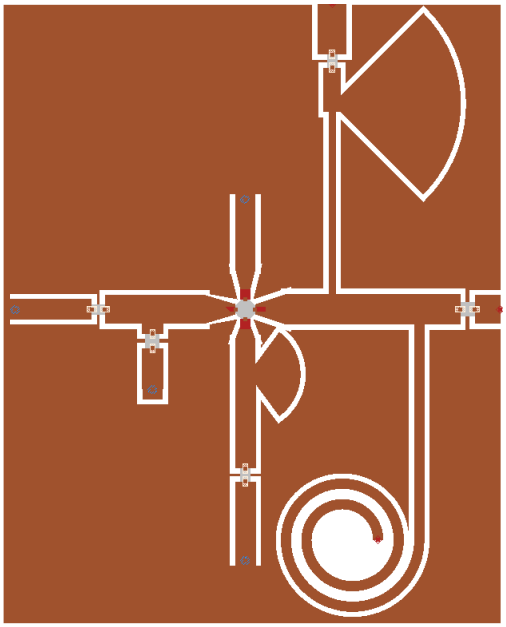

Fig. 6 Layout of a negative resistance oscillator (4.8x6cm^2)

V. Results and Discussions

We want to know the performance of our circuit for quality of the signal and output power, for that Fig.7 and Fig.8 show successively the typical output spectrum of the oscillator and the time domain of the output signal. The oscillation frequency is 2.4 GHz, Which used for Wi-Fi application. The oscillator delivers an output power of 12.297 dBm.

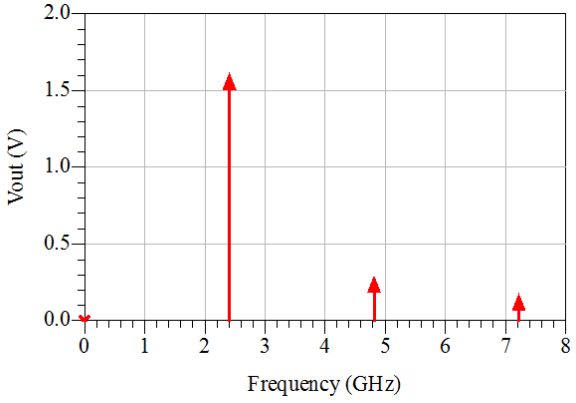

Fig. 7 Oscillator output power spectrum

ISSN 1737-9334

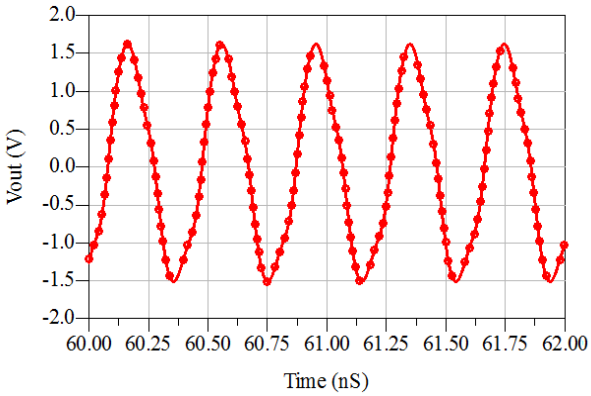

Fig. 8 Output signal in time domain of the oscillator at 2.4 GHz

VI. CONCLUSION

In this paper we have developed a negative resistance oscillator dedicated to Wi-Fi applications. This circuit offers unconditional stability and provides output power equal to 12.297dBm at the resonance frequency of 2.4GHz. This circuit has been designed by Advanced Design system simulator (ADS) and adjusted by using a theoretical step and optimization tools applied on matching impedance, resonator, active device and bias networks.

REFERENCES

[1] Ayoub Malki*1, Jamal Zbitou2, Larbi El Abdellaoui3, Mohamed Latrach4, Abdelali Tajmouati5, Ahmed Errkik6, "Design of Negative Resistance Oscillator with Rocord Low Phase Noise," TELKOMNIKA, Vol.16, No.2, April 2018, pp. 586~593.

[2] Bhavanabenakaprasad, Salah sharabi, K. Elgaid. RF and Microwave oscillator design using p-HEMT transistor. International journal of scientific and research publication. 2014; 4(8): 1-7.

[3] EL BAKKALI, Moustapha, AMARTOUHAMI, Naima, ELFTOUH, Hanae, et al. Design of 5.2 GHz Low Noise Amplifier for Wireless LAN. Procedia Manufacturing, 2019, vol. 32, p. 739-744.

[4] D.J.H. Maclean, "Broadband Feedback Amplifiers", Research Studies Press, 1982.

[5] A. Platzker and W. Struble, "Rigorous Determination of The Stability of Linear N-node Circuits From Network Determinants and The Appropriate Role of The Stability Factor K of Their Reduced Two-Ports", 3rd International Workshop on Integrated Nonlinear Microwave and Millimeterwave Circuits, pp. 93-107.

ISSN 1737-9334

Optimization of physical flows: Calculation of handling load
Case of a Moroccan multinational

Anas LAASSIRI[#1], Abdelfettah SEDQUI[*2]

[#] *Innovative Technologies Laboratory, University of Abdelmalek Essaadi, ENSAT Tangier, Morocco*

[1] Laassiri.Anas@gmail.com

[2] Abdelfettah.Sedqui@gmail.com

***Abstract*— the general framework of this project is the Lean Management, its main objective is to quantify the necessary human resources that ensure handling, storage and shipping. Then, the standardization of operations and creation of logistics procedures, simplifying the physical flow by conducting a study of establishing new flow solutions to optimize efficiency of logistics human resources. Project management and process followed to achieve these missions have allowed achieving the predefined objectives and finding solutions to various problems, such as achieving logistics cost reduction, improving the interne physical flows and the Odette Service Rate.**

***Keywords*— 5G, Lean Management, SMB, R&R, Handling, Physical Flow, Standard Work**

I. INTRODUCTION

A company placed in a competitive environment can only survive by fulfilling the complete satisfaction of its customers while reducing costs. However, in the face of an increasingly demanding customers and increased competition, the company must evolve to remain competitive. Therefore, flexibility, efficiency and reliability are among the determining criteria to guarantee the performance of its Supply Chain in order to maintain and conquer shares of the automobile market.

It is in this context that all companies have embarked on a project to improve their physical flows and the efficiency of their operations, in order to meet their need to grow in performance, to align strategically with their vocation and reduce logistics costs. Achieving such a goal can only be done by removing all the obstacles to performance and productivity. That is, chasing away all kinds of waste and making the entire value chain Lean. Handling load calculation is one of the most complex problems given the variability of the data (input, output, internal, volume, cadence flow) and the fact of defining this load remains a means of IT decision support in order to to decide on the assignment which we treated in our article [1] and whose method was quoted briefly.

The rest of this article is distributed as follows. The first part of this work deals with the industrial and problematic context, and the second part explains the SMB method and its approach. The last part implements the defined approach.

II. PRESENTATION OF THE PROBLEMATIC AND OBJECTIVES

A. Problematic and context

The problem addressed is a concrete case of the problems encountered every day in the industry in general and the automotive industry in particular. Towards the end of this article, we need to find an answer to the following question:

- How many forklift operators will we need for handling?

The answer to this question constitutes the input for the allocation problem that we treated in the article [1] The problem treated is purely dynamic, since the machine cadences change from one shift to another this implies the variation of the handling load

B. Objective

Through this work, we must:

• For the static case: define the logistics workforce ensuring internal handling in a period that we define: equal to a shift,

• For the dynamic case: development of a decision support system which enables the handling load of the store / workshop to be known at all times.

III. SMB METHOD AND CHRONO-ANALYSIS

A. Definition and state of the art

As already dealt with by [1] the problem of calculating the logistic handling load is rarely addressed in the literature. Below the methods and principle adopted in this article

1) SMB

La The basic handling standard or SMB is a method which aims to define a time allotted for each handling operation used to standardize it and measure productivity. This through a

ISSN 1737-9334

breakdown into elementary tasks of any handling or storage operation, the basic operating times are obtained thanks to universal standardized universal times, or as in our case using the Chrono-analysis method, - or timing , which is a method of analysis of working time. The purpose of Chrono-analysis is to define the production time that can be held by the entire active population for a given activity. In our case it is handling. Then the increases in these times depending on each handling situation (rest coefficient and rolling index). In our case, we adapted a purely logistical method to a production workshop context and we used it as basic input data for the bin packing problem, thus providing the handling load for each production machine in dividing the allocated handling time by the required time.

2) Chrono Analysais

It is a method of analysis of working time. The purpose of the Chrono-analysis is to define the production time that can be held by the entire working population for a given activity. In our case it's handling

3) R&R

• Repeatability: the variation of successive measurements obtained on the same mesurande under the same conditions;

• Reproducibility: the measurement variation obtained on the same mesurande by varying a condition.

A. Formalization of the problematic

1) Notation

We define the following variables:

T.O.B.C: temps timed basic operating time
F : output frequency
T.O.R : Real operating time
I_R : Driving index
I_p : Course index
T.E : Execution time
C_R : Rest coefficient
T.A : Allotted time
T_E : Engagement rate
D : Distance
E : Logistics workforce
T_R : Temps Required time

For each handling activity, we will define the time allocated and thus the corresponding handling load: the times of our problem are defined as follows:

- T.O.B.C = t_{chrono} x D x F
- T.O.R = T.O.B.C x (1+ I_R ouI_p)
- TE = T.O.R x (1+C_R)
- TA = TE x T_E
- E = $\frac{TA}{T_R}$

The resolution process is defined as follows:

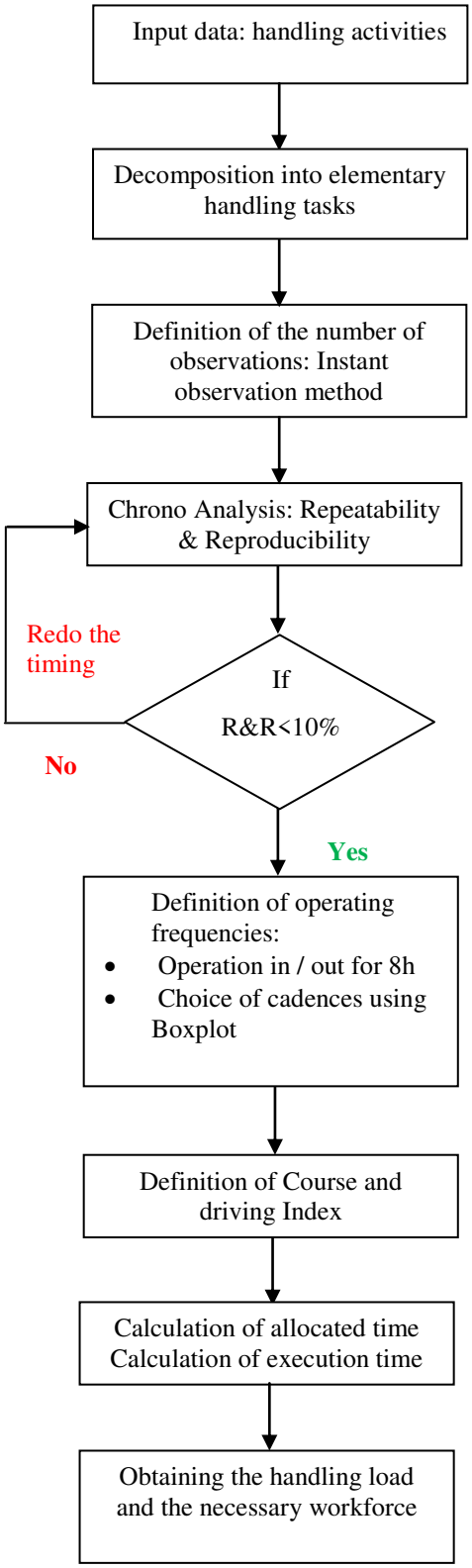

Figure 1 : Resolution process

ISSN 1737-9334

IV. IMPLEMENTATION OF THE METHOD: CASE OF A MOROCCAN MULTINATIONAL COMPANY

B. *Input data*

- Handling activities
- Means of handling
- Type of operations
- Machine output frequency
- Average distance between two machines

C. *Resolution process*

After having identified the various handling operations carried out by forklift operators in all production areas, we have broken down these tasks into elementary handling and movement tasks.

To take into account the R&R factors, we used the instant observation method to define the number of timing operations:

Let N be the total number of observations to be made, let P be the desired Percentage of engagement set at 80%, and S the desired precision rate that we set at 45%.

$$N = \frac{4 \times (1 - P)}{S^2 \times P} = 5$$

For each observation, it was necessary to observe all the basic operations carried out by the operator for a period fixed at 3:30 a.m. per day, from 9:00 a.m. to 11:30 a.m. and from 2:00 p.m. to 3:30 p.m.

After the timing, we used the MSA tool on Mini tab to validate the timed data. We did a Gage R&R analysis <Cross gage R&R> because we conducted a study with 2 operators, where each operator performs 5 times

Source	StdDev (SD)	Study Var (6 * SD)	%Study Var (%SV)
Total Gage R&R	0.37664	2.2599	8.77
Repeatability	0.30933	1.8560	7.20
Reproducibility	0.21488	1.2893	5.00
Part-To-Part	4.27987	25.6792	99.62
Total Variation	4.29642	25.7785	100.00

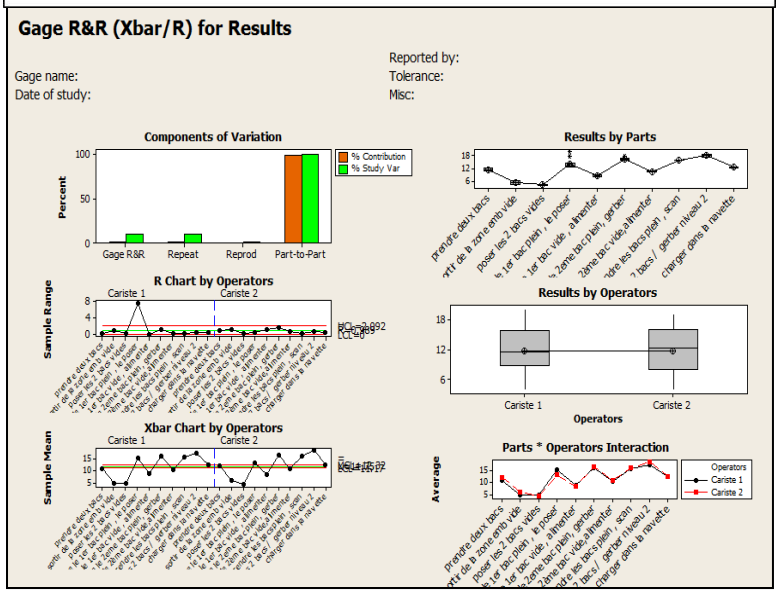

We have obtained an Index which is less than 10% however our results are reliable.

For the frequency of operations, we used the mustache box to see the distributions of all the cadences of the molds of a machine, in order to select the Max (median, average) since we want to represent the calculation scenario most penalizing in terms of handling load:

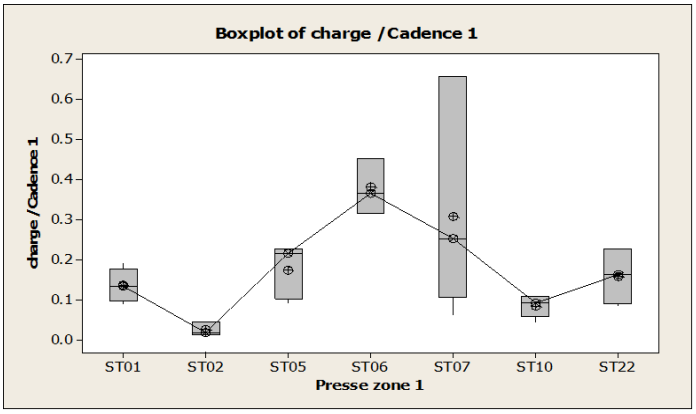

After defining the output frequencies, it remains for us to define the course and driving indices according to each situation:

- The course indices applicable to the operator's travel operations alone
- The driving indices applicable to the operator's travel operations with machine

The most recurrent are:

- E: brightness;
- S: soil defect;
- D: density of staff;
- C: Crossing aisles

The next step is to calculate the execution time and the time allocated to the operation, setting a commitment rate of 85%. Results are as follows:

		Calcul de charge & Affectation		
Zone/Cariste		Presse	charge_cariste	charge_manutentionnaire
Production Zone1	Cariste 1 +Manut	ST01	100%	61%
		ST05		
		ST22		
		ST10		
		ST06		
	Cariste 4	ST07	37%	0%
		ST02		
Production Zone 2	Cariste 2	ST19	84%	0%
		ST15		
		ST17		
		ST11		
		ST12		
		ST14		
	Manut	ST12	0%	10%
		ST11		
		ST14		
Production Zone 3	Cariste 3	ST08	100%	0%
		ST13		
		ST03		
		ST16		
		Mur-Q		
	Cariste 4	ST20	21%	
	Cariste 2	ST18	16%	

ISSN 1737-9334

Petit train	Cariste 4	Zone prod	49%	0%	
Expedition	Cariste 5		146%	0%	
	Manut		0%	21%	
Totel_charge			553%	92%	
Effectif			6	1	
Cariste	1	2	3	4	5
Zone	Zone 1	Zone 2	Zone 3	petit train	Expedition

Figure 4 : Handling load calculation

- We note that the handling load between the different production areas is not balanced, and there are people who have a load greater than 100%, therefore, the resolution of the allocation problem is necessary.
- The number of resources required is 7 people.

- For the dynamic case, we have developed an automated Excel sheet, "Load calculation" is an application developed in Excel, which will allow us, based on the SMB analysis sheets already developed and configured, to calculate the load operators for each press depending on the frequency of output from its molds (output) and its position in the factory (distance between zones). All this presented with a simple interface which contains three headings, distinguishing between the forklift operators of production, shipping, and a categorized "other (small train, handler ...)". This calculation will be used later to feed input data from the forklift truck assignment application. The main advantage of this application is to provide an instant load of the production island, which is a powerful decision support tool, to react if there is an excess load or an imbalance at the level of the operator's load and make the necessary adjustments so as not to have a press stop.

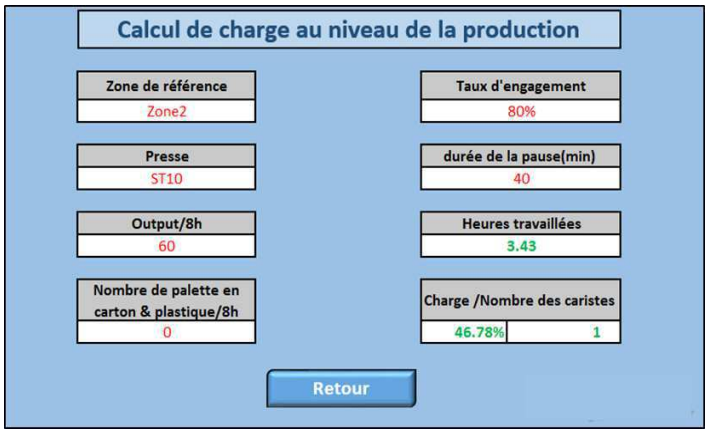

Figure 5 : Handling calculation interface

The output data of the application are: the handling load, the number of forklift operators required and the number of hours worked.

V. Conclusion & Perspectives

The complexity of the project lies in the point of modeling the situation of the factory physical flow, and the adaptation of a purely logistical method (SMB) to a context which is the physical flow <flow of finished products>. several variations and difficult to master and to be able to quantify the logistical labor necessary to ensure both the evacuation and supply tasks of the press as well as loading and unloading the Semi-trailers for shipment. Despite all these constraints, we have solved the problem due to the lack of load calculation. We have been able to calculate the manpower necessary to ensure the handling activities in the static and dynamic case. Future research should revolve around solving the resource allocation problem in order to balance the handling load.

References

[1] A. Laassiri and A. Sedqui, "Dynamic dimensioning of logistics resources : Case of production workshop: Analogy with the problem of bin-packing Moroccan multinational company," 2019 International Colloquium on Logistics and Supply Chain Management (LOGISTIQUA), Montreuil - Paris, France, 2019, pp. 1-8. doi: 10.1109/LOGISTIQUA.2019.8907270 URL: http://ieeexplore.ieee.org/stamp/stamp.jsp?tp=&arnumber=8907270&isnumber=8907237

[2] AIAG, Measurement Systems Analysis Reference Manual, 4th edition, 2010, http://www.amazon.com/Measurement-Systems-Analysis-MSA-AIAG/dp/B004Z0V40G.J. Breckling, Ed., *The Analysis of Directional Time Series: Applications to Wind Speed and Direction*, ser. Lecture Notes in Statistics. Berlin, Germany: Springer, 1989, vol. 61.

[3] Bortfeldt, Andreas, et Gerhard Wäscher. « Container Loading Problems - A State-of-the-Art Review ». FEMM Working Papers. Otto-von-Guericke University Magdeburg, Faculty of Economics and Management-avril2012. https://ideas.repec.org/p/mag/wpaper/120007.html.

[4] Aghezzaf E.H. (2007). Production planning and warehouse management in supply networks with interfacility mold transfers, European Journal of Operational Research, 182, pp. 1122-1139.

[5] Aksin, O.Z.,Karaesmen,F.,Ormeci,E.L., (2005). On the interaction between resource flexibility and flexibility structures. In: Proceedings of the Fifth International Conference on Analysis of Manufacturing Systems— Production Management, Zakynthos, Greece,May.

[6] [Smidts, 1994] Smidts, C. (1994). Probabilistic dynamics: a comparison between continuous event trees and a discrete event tree model. Reliability Engineering & System Safety, 44(2):189–206.

[7] [Taylor, 2004] Taylors, D.A. (2004). Supply Chain: A Manager's Guide. Boston: Addison-Wesley.

[8] [Tayur et al., 1999] Tayur, S., Ganeshan, R. et Magazine, M. (1999). Quantitative models for supply chain management. Kluwer Academic Publishers.

ISSN 1737-9334